THE UNIVERSITY *of* EDINBURGH

Ground borne vibrations

from high speed trains

David P. Connolly

Doctor of Philosophy

The University of Edinburgh

2013

Declaration

This thesis, the work discussed and results shown were undertaken solely by me unless otherwise stated within the text. Furthermore, it has not been submitted for any other degree or professional qualification.

David P. Connolly

The University of Edinburgh, 2013

Abstract

A consequence of high speed rail transportation is the generation of elevated ground borne vibrations. This thesis presents several original contributions towards the prediction of these vibrations.

Firstly, a new three dimensional finite element model capable of vibration prediction was developed. Its main feature was its ability to model complex track geometries while doing so through a fully coupled vehicle-track-soil system. Model output was compared to experimental results obtained during this thesis and also to independent data sets. It was shown to predict velocity time histories, vibration frequency spectrums and international vibration descriptors with high accuracy.

An appraisal of the suitability of a finite difference time domain modelling approach for railway vibration prediction was also undertaken. This resulted in the development of a new 'higher order' perfectly matched layers absorbing boundary condition. This condition was found to offer higher performance in comparison to current alternative absorbing boundary conditions.

Field work was then undertaken on high speed lines with varying embankment conditions in Belgium and England. Vibration data was recorded up to 100m from each track and geophysical investigations were performed to determine the underlying soil properties. The results were used for numerical model validation and also to provide new insights into the effect of various

embankment conditions on vibration propagation. It was found that embankments generate higher frequency excitation in comparison to non-embankment cases and that cuttings generate higher vibration levels than non-cuttings.

Once validated the finite element model was used to provide new insights into the effect of train speed, embankment constituent materials and railway track type on vibration levels. It was found that the shape and magnitude of ground vibration increased rapidly as the train's speed approached the Rayleigh wave speed of the underlying soil. It was also found that ballast, slab and metal tracks produced similar levels of vibration and that stiffer embankments reduced vibration levels at distances near and far from the track.

Two vibration mitigation techniques were also explored through numerical simulation. Firstly, an analysis was undertaken to determine the ability of a new modified ballast material to actively isolate vibration within the track structure. Secondly, wave barrier geometries were investigated to optimise their performance whilst minimising cost. It was found that barrier depth was the most influential parameter, whereas width had little effect. Additionally, geometry optimisation was found to result in a 95% cost saving in comparison to a base case.

Using a vast array of results generated using the previously developed finite element model, a new empirical prediction model was also developed, capable of quickly assessing vibration levels across large sections of track.

Unlike currently available empirical models, it was able to account for soil properties in its calculation and could predict a variety of international vibration metrics. It was shown to offer increased prediction performance in comparison to an alternative empirical model.

Contents

Nomenclature

A	Acceleration
B	Strain matrix
b	Buoyancy
b_r	Bending stiffness of rail
c	Material constant used in the constitutive equation
D	damping ratio
d_{max}	PML absorption parameter coefficient at PML extremity
d	Displacement of element nodes
E	Young's modulus
e0	Soil void ratio
F_{wr}	Wheel/rail interaction force
f	Force
f_s	Sleeve friction
f_{0i}	FE PML coefficient
g	Gravity
h	Rail vertical profile

I_p	Soil plastic limit
j	Imaginary number ($\sqrt{-1}$)
$\tilde{J}$	'Correction PML' field dependant factor
kH	Hertzian spring constant
KB_f	Vibration metric (based on moving average)
KB_{max}	Absolute maximum value of KB_f
k	Stiffness
k2	Coefficient function of relative density
L	Number of PML layers
$\tilde{M}$	'Correction PML' field dependant factor
m	Mass
m_r	Mass per unit length of rail
N	Finite element shape function
N	SPT 'N-value'
RA, RB, RE, RF	Higher order PML coefficients
p	FE PML coefficient
q_t	Corrected cone tip resistance

q_c	Cone penetrative resistance
R	PML reflection coefficient
r	Rail irregularity
s	PML stretching function
s_e	Stiffness of elastic foundation
S	Rail vertical profile (power spectral density)
t	Time
U	Displacement
U_c, V_c, A_c	Displacement, velocity and acceleration of car body
U_b, V_b, A_b	Displacement, velocity and acceleration of bogie
U_w, V_w, A_w	Displacement, velocity and acceleration of wheel
V	Velocity
VdB	Velocity decibels
V_{rb}	Bending wave speed in rails
V_p, V_s, V_r	Soil wave velocities (compressional, shear and Rayleigh)
X	Global horizontal direction (direction of train passage)
Y	Global horizontal direction (direction perpendicular to train passage)

Z	Global vertical direction
α	Rayleigh damping coefficient (mass proportional)
α_{max}	PML absorption parameter coefficient at PML extremity
β	Rayleigh damping coefficient (stiffness proportional)
$\boldsymbol{\varepsilon}$	Strain
ζ	Local z direction coordinate
η	Local y direction coordinate
κ_{max}	PML absorption parameter coefficient at PML extremity
λ	Lame's first parameter
u	Poisson's ratio
μ	Shear modulus (lames second parameter)
ξ	Local x direction coordinate
ρ	Density
$\boldsymbol{\sigma}$	Stress
σ	Effective stress
ν_{rms}	Root mean square velocity amplitude
ν_0	Background vibration level
Φ	Spatial frequency

ψ	Integration control parameter
ω, ω_1, ω_n	Frequency
ϖ	Integration control parameter

List of Tables

List of Figures

Chapter 1. An introduction to high speed rail ground vibration modelling

1.1 Background

High speed rail is witnessing an explosion in investment, with countries such as the UK, China and America investing hundreds of billions of pounds into their networks, year upon year.

This investment has facilitated exponential increases in train speeds with a Japanese train currently holding the world record of 581 km/h. These technological advances are moving train velocities into the same realm as those encountered by commercial planes such as the Boeing 737 (750 km/h). Increasing train speeds coupled with strong sustainability characteristics mean that high speed rail is replacing both road and air travel in many parts of the world. This is particularly true for short/moderate distances (typically less than 600 km) because high speed trains are efficient at moving high volumes of passengers in short time periods.

Figure 1 – Proposed track infrastructure by country (2025) (International Union of Railways, 2011)

A side effect of these elevated velocities is that excessive ground borne vibration levels may be generated. This is particularly true for cases where the train speed becomes comparable with the Rayleigh wave velocity of the underlying soil (El Kacimi, Woodward, Laghrouche, & Medero, 2013). Increased vibration levels can be problematic for both the railway track structure and also the local environment.

Related to the track structure, elevated vibrations cause safety concerns. For example, if the train wheel and the rail loose contact due to large deflection, it is theoretically possible for the train to derail. Similarly, large vibrations in the ballast cause increasingly rapid degradation, thus increasing maintenance costs. Related to the local environment, high amplitude vibrations can cause buildings to vibrate, thus generating internal noise. This noise and vibration can make buildings untenable.

When planning a new high speed rail line it is important that vibration levels can be quickly and accurately determined across the entire proposed network. If vibration levels are not correctly predicted then large financial expenditure may result from unexpected abatement measures, speed restrictions and legal action arising from real estate losses.

1.2 Thesis objectives

Although high speed rail generates ground borne vibrations that can cause negative effects within the track structure and the local environment, this thesis focuses on the local environment. There were five objectives:

1. Develop a numerical model capable of predicting vibration levels from high speed trains for the use in detailed vibration assessments.

2. Develop an empirical model capable of predicting vibration levels at the preliminary assessment stage. This model will make use of rudimentary soil properties and will be able to perform quickly and with high accuracy.

3. Perform experimental investigations on high speed rail lines. Use results to gain better understanding of ground borne vibration from trains and to validate both the detailed and preliminary stage prediction models.

4. Use numerical modelling techniques to investigate vibration isolation techniques and to develop a greater understanding of high speed rail vibrations

5. Investigate the suitability of finite difference time domain modelling techniques for railway vibration simulation. In addition, to develop a new perfectly matched layer absorbing boundary condition with the aim of improving the computational efficiency of the finite difference approach.

Chapter 2. Literature review

2.1 The effects of high speed rail ground vibration

An example of the problems caused by excessive ground-borne vibrations is the case of the Gothenburg to Kungsbacka line in Sweden (Holm, Andreasson, Bengtsson, Bodare, & Eriksson, 2002). In this situation a new high speed line was laid next to an existing freight line and shortly after opening vibration levels were measured to be ten times greater on the high speed line in comparison to the freight line. These high vibration levels were a safety concern and lead to imposed speed restrictions and other countermeasures. Processes such as this are both disruptive and expensive. Elevated vibration levels have also been observed on other lines such as (Rainer & Pernica, 1988) in Canada, where vibrations were found to be destructive at distances up to 250m from the track. (Asmussen, 2012) provides an additional review of European sites at which negative vibration impacts from high speed rail lines have been recorded.

In addition to safety concerns related to elevated track vibration, there are significant social, environmental and economic concerns.

2.1.1 Social effects

Elevated vibration levels can cause distress to nearby inhabitants in the form of sleep deprivation, structural vibration/damage and internal structural noise. Ground vibration may also compromise the ability of some businesses to perform mission critical tasks. This can lead to the degeneration of local areas

and job losses due to the closure of vibration sensitive sites, e.g. manufacturing plants, schools and hospitals.

Equally, if a high speed rail line is subject to excessive vibration then passenger comfort is compromised, thereby reducing the ability of passengers to work, sleep and eat onboard, thus diminishing the overall attractiveness of rail transportation.

2.1.2 Environmental effects

Excessive high speed rail ground vibrations are often encountered in regions characterised by low soil strength. In such cases mitigation measures must be taken, such as performing ground injection/strengthening or installing wave barriers, which can lead to an increase in the projects' carbon footprint.

If excessive vibration occurs inside the track structure then high speed locomotives require increased traction to maintain speed. This results in reduced operation efficiency, high fuel consumption and increased emissions.

Elevated vibration levels can also cause an unnecessary increase in train and track degradation, meaning that degenerated track components such as the ballast and sub-grade will lose strength and have to be replaced more frequently, thus depleting raw materials. Similarly, if train carriages are subject to excessive vibration then they will require more frequent repairs and replacement of components. This in turn shortens their life span and requires extra natural resources to manufacture new carriages.

2.1.3 Economic effects

If vibration levels are large they can make buildings close to the line untenable. In these cases the high speed rail project sponsor is often required to purchase these structures and demolish them. In the case of HS2 (HS2, 2012) this distance is at least 60m on either side of the track. If vibration levels are found to be large at distances greater than this then it is likely that compensation will be paid to the residents.

Mitigation measures can be deployed to reduce vibration levels, however if used in close proximity to the track structure (e.g. rail pads), then the lines will require closure for extensive periods. Similarly, vibration abatement in the far field (e.g. trenches) requires extensive restructuring of the surrounding soil. Both options are economically intense, for example, 170km of Swiss track has been identified as having excessive vibration and the expected mitigation cost is €1200 million (Asmussen, 2012).

If vibration is problematic for factories reliant on vibration sensitive equipment then there is a high likelihood of negative economic impact. For instance component repair costs, machinery downtime and unnecessary use of human resources puts financial strain on businesses.

If a railway track is frequently exposed to high amplitude vibrations, it can cause an increase in track degradation. This will require the track to receive greater maintenance and renewal, therefore rapidly escalating the project's total lifecycle costs. Similarly, if excessive vibration is observed then rail operators will typically impose speed restrictions, resulting in delays. For many

high speed rail travellers, lost time is costly because these routes typically connect business hubs thus meaning that a high percentage of trips are business related.

2.2 Vibration generation mechanisms

Railway vibration if generated through two primary mechanisms, quasi-static excitation and dynamic excitation. Quasi-static excitation is caused by the static train load generating a localised deflection around the wheel. This deflection moves as the wheel passes over the track and generates forces with periodic time delays due to factors such as sleeper spacing and train characteristics.

Quasi-static excitation is typically dominant at low frequencies (0-20Hz). For conventional train speeds quasi-static excitation is dominant up to roughly a quarter of a wavelength from the track (Thompson, 2009). This distance can potentially be large because these low frequencies result in long wavelengths (e.g. <5Hz for bogie passage). As train speed increases quasi-static vibrations start to propagate to greater distances from the track.

Dynamic excitation is generated primarily due to wheel/rail contact and propagates at higher frequencies in comparison to quasi-static excitation (Knothe & Grassie, 1993). It is sometimes separated into 'parametric excitation' and 'wheel/rail unevenness excitation'. Wheel/rail unevenness excitation arises from roughness or irregularities on either the wheels or rails.

Unevenness may occur in the wheel during the manufacturing process or from track debris during operation. Unevenness in the rail may occur from changes in stiffness such as abutments.

Parametric excitation results from periodic changes in track stiffness. It can arise from sources such as rail joints and sleeper spacing. It is becoming an increasingly less influential factor in the generation of dynamic excitation due to the prolific use of continuously welded rails and improved track maintenance.

2.3 Vibration propagation

The forces generated due to quasi-static and dynamic excitation mechanisms propagate through the track and soil as seismic waves. These waves are categorised as either body waves or surface waves. Surface waves travel along a structures (i.e. soil) surface and decay exponentially with depth. Body waves propagate primarily beneath the soil surface. Wave propagation characteristics are shown in Figure 2.1.

Compressional waves (P-waves) propagate in a longitudinal direction and travel faster than all other types of waves. Shear waves (S-waves) propagate in a transverse direction and although they travel faster than Rayleigh waves, they always travel slower than P-waves. Rayleigh waves are the slowest type of seismic wave. Although other types of waves are theoretically possible (e.g. Lamb waves in layers and Stoneley waves at interfaces), compressional, shear and Rayleigh are the most common and are

the focus of this research. Furthermore, an emphasis is placed on the propagation of Rayleigh waves as they transmit approximately two thirds of the total excitation energy (Rayleigh waves≈67%, S-waves≈26%, P-waves≈7%). Therefore they are most likely to cause negative effects in both the railway track and nearby structures.

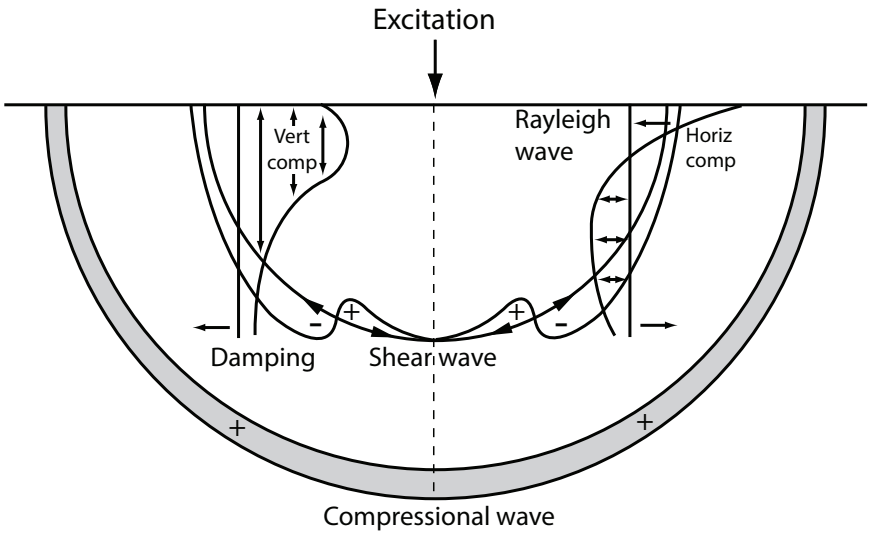

Figure 2.1 – Seismic wave propagation (slice view)

2.4 Soil material properties

There are a wide variety of parameters used to classify soil material such as liquid limit, particle size distribution, over-consolidation ratio…etc. For the purpose of describing wave propagation many of these physical properties are either irrelevant or better described using alternative parameters. For numerical analysis wave propagation can be efficiently described using four main material properties and their derivatives:

Density – The mass divided by the unit volume of a material. Density typically increases with depth because lower soil layers tend to have experienced elevated consolidation and therefore the solid particles are more tightly packed together.

Poisson's ratio – When a material is compressed using a force in a single direction, Poisson's ratio defines the degree to which the material expands in the other two directions. This is the ratio of expansion to the contraction caused by the compression. Some of the tests in this thesis have been formulated to determine compressional (V_p) and shear wave (V_s) velocities. If these are known, Poisson's ratio can be calculated using Equation 2.1:

$$\upsilon = \frac{V_p^2 - 2V_s^2}{2(V_p^2 - V_s^2)} \qquad \text{Equation 2.1}$$

Sudden increases of Poisson's ratio within a soil are often due to the presence of the water table. This is particularly true for clays which when fully saturated become incompressible (i.e. $\upsilon \approx 0.5$). In this case the P-wave speed increases dramatically because the wave speed becomes more representative of the water rather than the soil. On the other hand the S-wave velocity remains unchanged because water has no shear strength and thus the wave speed remains representative of the soil. Changes in wave speed with respect to Poisson's ratio are shown in Figure 2.2. It can be noticed that Poisson's ratio also has an effect on Rayleigh wave speed. This effect is minor because the Rayleigh wave speed can never exceed the shear wave speed. Therefore

Rayleigh wave speed is usually located in the range of 85-95% of the S-wave velocity.

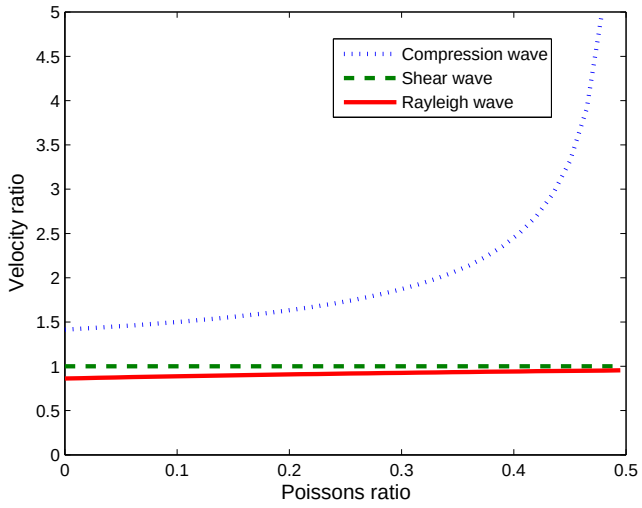

Figure 2.2 - The effect of Poisson's ration on seismic wave speeds

Young's modulus – A measure of the stiffness of a material. It is calculated using the tangent modulus of the initial, linear portion of the stress-strain curve. Many of the tests and correlations presented in this chapter have been designed to calculate shear modulus (μ) which is related to Young's modulus via:

$$E = 2\mu(1 + \upsilon) \qquad \text{Equation 2.2}$$

At large strains soils behave non-linearly because shear modulus depends highly of strain. Although large strains may occur in geotechnical engineering applications such as pile driving, blasting or on off-shore oil rigs, in case of ground vibration from railways, soil particle deformation is typically very small in comparison to its dimensions. The magnitude of strain

experienced by the soil during train passage is therefore low (10^{-5} %) and can be modelled using 'small strain' theory. This allows for the soil to be considered as a linear elastic material and for the shear modulus to be considered to be equal to the 'maximum shear modulus'. The shear modulus is related to the shear wave speed using Equation 2.3.

$$V_s = \sqrt{\frac{\mu}{\rho}} \qquad \text{Equation 2.3}$$

Damping – A measure of the rate at which energy is reduced as it disperses and passes through a material. These forms of attenuation are known as geometrical and material damping respectively. Damping is defined using a damping ratio (a ratio of critical damping) and typically has a non-linear relationship with frequency. When using FE modelling, 'Rayleigh damping' is commonly used to define the damping ratio as a function of both stiffness and mass damping. Regarding in-situ soils, damping is typically greatest in the upper layers and reduces with depth. This is because stiffer soils are generally located at greater depth and damping ratio decreases with increasing stiffness.

2.4.1 Rayleigh waves

Rayleigh waves transmit two thirds of wave energy (depending on frequency (Wolf, 1994)) and are thus potentially more destructive than their compressional and shear wave counterparts. It is seen in Figure 2.3 that Rayleigh waves move in an elliptical pattern against the direction of

propagation, a.k.a, 'retrograde' motion. Therefore Rayleigh waves are characterised by both a vertical and horizontal component. Also notice that only the near surface particles are disturbed and the lower particles are unaffected. This is because Rayleigh waves decay rapidly with depth as seen in Figure 2.3 where typical decay profiles are plotted for various Poisson's ratio values. From this figure it can be concluded that Rayleigh waves propagate in a surface region with a depth of approximately one wavelength.

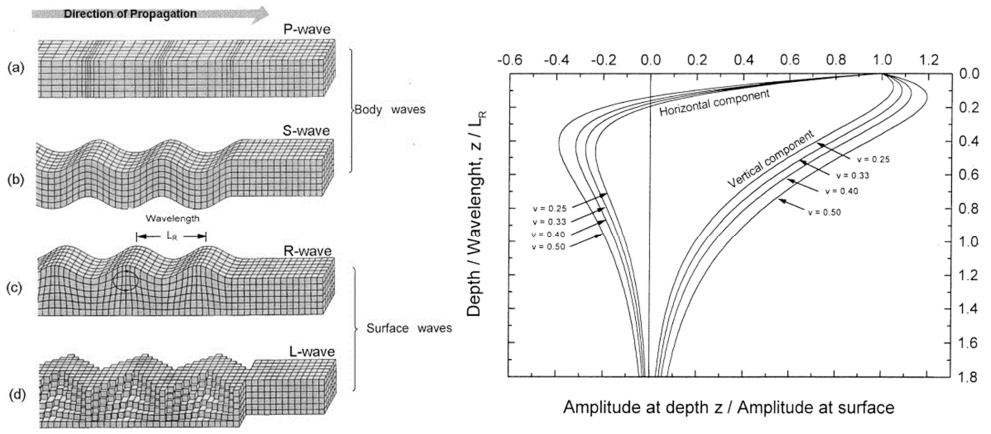

Figure 2.3 – (a) Left: Body and surface wave propagation characteristics, (b) Right: Rayleigh wave decay (Athanasopoulos, Pelekis, & Anagnostopoulos, 2000)

Although Rayleigh waves decay rapidly with depth from the ground surface, they propagate to greater distances than P-waves and S-waves. Therefore, locations close to the excitation (i.e. near a railway track) will be subject to Rayleigh, shear and compressional wave energy whereas locations far from the track will experience a greater percentage of Rayleigh energy. This attenuation of Rayleigh energy has been shown to be relatively frequency independent for S-wave values ranging from 140-1000m/s. Some relationships

between Rayleigh attenuation coefficients and S-wave velocities are presented by (Athanasopoulos et al., 2000).

Rayleigh wave speed can be calculated analytically using the formulas presented in (Rahman & Barber, 1995). Despite this, these formulations are unwieldy and three separate equations are required to calculate Rayleigh wave speed for the Poisson's ratios typically associated with soil (0.15-0.5). Therefore, more straightforward approximations have been presented by (Bergmann, 1948), (Brekhovskikh & Godin, 1998), (Briggs & Kolosov, 1992), (Malischewsky, 2005), (Rahman & Michelitsch, 2006). These approximations are shown in Figure 2.4 and for the purpose of estimating railway vibrations, all formulas provide adequate approximations.

It should be noted that each of these formulations use Poisson's ratio to calculate the ratio of the Rayleigh wave speed to the S-wave speed. The formula for P-wave (V_p) and S-wave (V_s) speed are shown in Equation 2.4 and Equation 2.3 respectively. Lames parameters can be calculated using Equation 2.5 and Equation 2.6 (or Equation 2.3). For the work undertaken in this thesis the classical relationship proposed by (Bergmann, 1948) was used to evaluate Rayleigh wave velocity (V_R) (Equation 2.7).

$$V_p = \sqrt{\frac{\lambda+2\mu}{\rho}} \qquad \text{Equation 2.4}$$

$$\lambda = \frac{\upsilon E}{(1+\upsilon)(1-2\upsilon)}$$ Equation 2.5

$$\mu = \frac{E}{2(1+\upsilon)}$$ Equation 2.6

$$V_R = \frac{0.87 + 1.12\upsilon}{1+\upsilon}$$ Equation 2.7

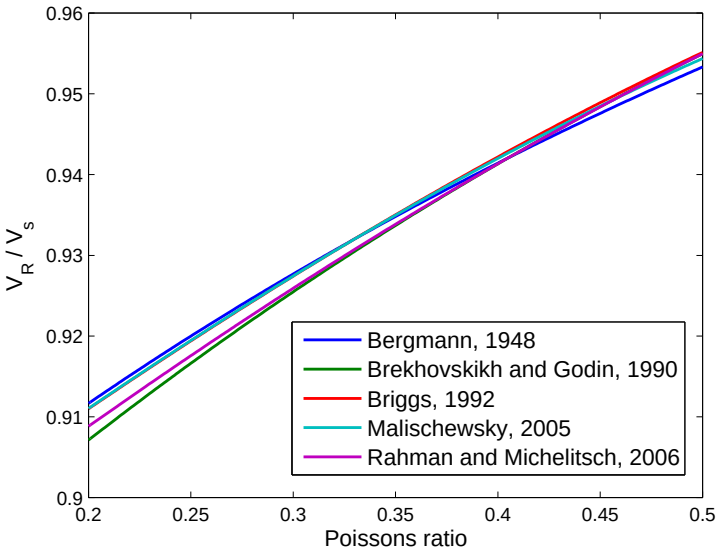

Figure 2.4 – Rayleigh wave speed approximations

2.5 Prediction of ground borne vibrations

In an attempt to better understand and predict railway vibrations, researchers have developed ground borne vibration prediction models. Two

primary types of prediction model exist, both of which are used at different stages of the overall assessment campaign. The first type is used during preliminary assessment for the purpose of quickly assessing vibration levels for long sections of track (sometimes known as a scoping model). These models are usually based on empirical relationships.

The second type is used to perform detailed assessments for individual locations and can be used at any stage of the project, even to assess mitigation measures post-construction. Typically these are numerically based models based on techniques such as the finite element method (FEM) and/or boundary element method (BEM). The original scoping model is typically used to identify locations where the detailed model should be deployed.

2.6 Seismic wave propagation due to moving loads

The first step for researchers in attempting to predict vibration levels was to analyse the problem of a moving load and the resulting seismic response. A moving load can be approximated as a series of point loads acting at different locations at different instances of time. Therefore the response observed at a certain location is a function of all the seismic waves generated at all excitation points, arriving at the receiver at a moment in time. To first understand the response of a material to a single, stationary load, (Lamb, 1904) investigated the response of an elastic half-space due to static point and line loads. Exact analytical solutions were developed and later expanded upon by (Aki & Richards, 2002) to calculate the characteristics of P, S and Rayleigh waves

caused by static loading. These solutions provided the foundation for early analytical train/track railway prediction models.

Lamb's work was extended to loads moving through an unbounded elastic body (i.e. no free surface, thus no surface wave propagation) by authors such as (Fryba, 1972). Fryba acknowledged the relationship between the moving load speed and the natural wave speed of the material upon which it was traversing. It was shown that if 'V' was equal to the speed of the moving load, 'V_s' was the shear wave speed of the ground/half-space and 'V_p' was the compressional wave speed, there were 3 distinct velocity regimes:

1. The subsonic case - The load moves at a speed less than the shear wave speed of the material constituting the half-space. ($V < V_s$)
2. The transonic case - The load moves at a speed greater than the shear wave speed but less than the compressional wave speed. ($V_s < V < V_p$)
3. The supersonic case – The load moves at a speed greater than the compressional wave speed. ($V < V_p$)

This unbounded elastic body solution was reformulated by (Payton, 1967) for a moving line load on an elastic half-space (an infinitely deep soil layer with a flat free surface). The presence of a free surface caused the generation of Rayleigh surface waves and the author was able to show that when the load reached a speed equal to the Rayleigh wave speed, the displacement would become infinitely large. As Rayleigh waves are dominant during train passage, this result was of concern to the railway industry.

Figure 2.5 shows the strong relationship between train speed, Rayleigh wave speed and vibration levels. This data was collected experimentally on European high speed lines where the train speed was close to the soil Rayleigh wave speed. The horizontal axis shows normalised train speed which is equal to the train speed divided by the Rayleigh wave speed. Therefore a normalised train speed of 1 is equivalent to the train travelling at the soil Rayleigh wave speed (critical velocity). The vertical axis is a measure of vibration described by the dynamic displacement divided by the static displacement. It can be seen that when the normalised train speed exceeds 0.5, vibration levels (expressed as displacements) start to grow rapidly. A generalised relationship between speed and displacement can be described using a cubic polynomial and is also shown in the figure.

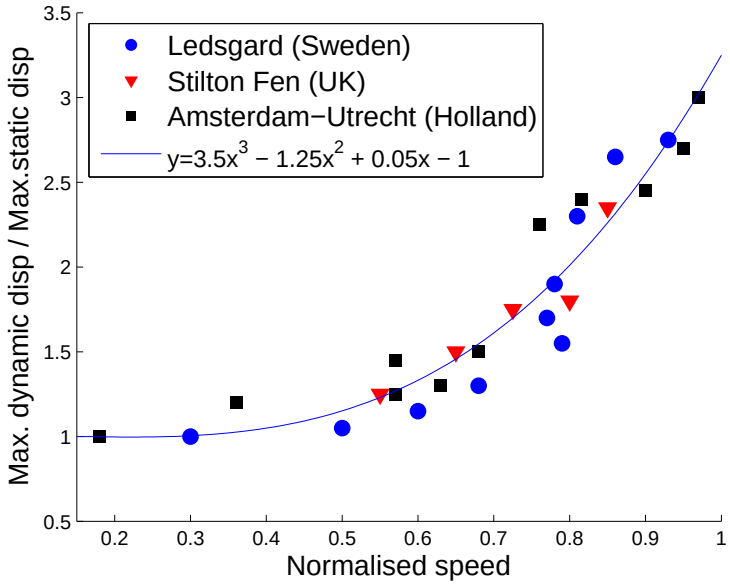

Figure 2.5 – The effect of Rayleigh wave speed on vibration levels (replicated from (Banimahd, 2008))

2.7 Modelling track vibration characteristics

Modelling train passage requires simulating seismic wave propagation through a track structure and into the ground. Rather than attempt to simulate vibration levels at distances from the track, early railway approaches focused primarily on vibration levels within the track structure. This was of primary concern to railway track operators and designers. When attempting to model track vibration, the complex wavefields generated by the 3D track geometries (e.g. sleepers) are difficult to model, particularly using analytical expressions. Additionally, cases where the half-space is directly subjected to loading (Fryba, 1972), (Payton, 1967) are not a realistic approximation of the train/track/ soil problem.

To overcome these challenges, early analytical approaches simplified the track structure by making assumptions regarding the track geometry. These simplifications typically involved describing the rail as a beam resting on an elastic foundation. This elastic foundation was used to describe the track or a combination of the track and soil. These methods were useful for investigating the low frequency characteristics of the track (Knothe & Grassie, 1993).

One of the most straightforward approaches to track modelling is to use a Euler beam resting on a continuous support ((Timoshenko, 1953), (Patil, 1987) and (Kenney, 1954)). The use of a continuous support is intended to simulate the entire track and neglects the effect of sleepers. Despite this, it has been shown to be a reasonable approximation at frequencies below 500 Hz

(Knothe & Grassie, 1993). To overcome this, sleeper effects can be modelled through the use of a discontinuous support (Mead, 1970), thus facilitating superior accuracy at higher frequencies.

Further increases in model accuracy were achieved by modelling the rail as a Timoshenko beam rather than a Euler beam. Timoshenko beams account for additional degrees of freedom (shear forces) in comparison to Euler beams and have been used in railway applications by (Suiker, De Borst, & Esveld, 1998), (Chen, 2001) and (Kargarnovin, 2004). A review of the interaction between various beams and plates with underlying soil was investigated by (Auersch, 2008a).

The track foundation model has also been shown to have an effect on model accuracy. Early models used Winkler (Auersch, 1996) or viscoelastic (Metrikine & Popp, 2000) foundations, however recently elastic half-space models have been shown to offer increased accuracy (Knothe & Wu, 1998).

Lastly, it should also be noted that alternative approaches to calculating track vibration characteristics have been proposed. These include (Nielsen & Igeland, 1995) and (X Lei & Noda, 2002) who proposed a FE method capable of modelling a discretely supported rail. A key advantage of the FE method is that it can be used to model non-linear effects (e.g. wheel-rail contact), however it can be subject to wave reflections due to model truncation. Another alternative approach was proposed by (Mazilu, Dumitriu, Tudorache, & Sebeşan, 2011) who used Green's functions to study track vibration.

2.8 Analytical modelling of free field vibration

In recent years researchers have attempted to predict vibration levels outwith the track structure (in the 'free field'). This research has been driven by the desire to quantify vibration effects on local communities, rather than the effect of vibrations on track quality, and is the focus of this research. This task is potentially more challenging than predicting the vibration characteristics of a simplified track structure because the soil must be modelled. Soil modelling is complex due to its unbounded nature and its complex (and often unknown) 3D stratification.

Modern analytical models have attempted to reduce the assumptions associated with early prediction models (Jones, 2010), while accurately modelling soil vibration at large track offsets. Like many of the aforementioned track models, they are typically formulated in the frequency and/or wavenumber domain for the purpose of reducing computational requirements. They often combine various forms of the aforementioned 'beam on elastic foundation' models, with receptence methods (Sheng, 1999a) and/or Green's functions to aid in the prediction of far field vibrations (Schevenels et al. 2007, Bode 2002).

One example is a model proposed by (Krylov, Dawson, Heelis, & Collop, 2000) and later revised by (Degrande & Lombaert, 2001). This frequency domain model used Lamb's problems to approximate the soil's Green's function and then the superposition of Rayleigh waves generated by all sleepers to

calculate the response for a given receiver. Unlike some other models, it was able to account for the effect of individual sleepers and two soil layers; a situation that is more common than a homogenous soil. Once again it was shown that large amplification of ground vibration levels was possible if the Rayleigh wave speed was equal to the train speed.

Another approach was outlined by (Karlstrom & Bostrom, 2006) who modelled the rails using Euler-Bernoulli beams and used anisotropic Kirchhoff plates to simulate the sleepers. The soil was modelled as a stratified half space comprised of linearly viscoelastic layers. The solution was calculated using Fourier transforms and resulted in a model with low computational requirements, thus allowing far field simulation. The model was validated using a combination of field results and previously developed numerical models.

(Sheng, 2004) developed a coupled train-track-soil model for calculating vibration levels due to vertical track irregularities. The model was based on calculating receptances (displacement amplitude per force applied) for both the vehicle and the track system. The soil was modelled as a layered half space using the approach described in (Sheng, 1999b). The final model was then used to model the vibration characteristics of several types of railway track.

(Xia, Cao, & De Roeck, 2010) proposed a similar method to (Sheng, 2004) for describing the multibody vehicle and track. A significant difference was that Green's functions were used to calculate the ground response. It was concluded that a critical speed exists for high speed rail/tracks and is close to the Rayleigh

wave velocity of the soil. Unfortunately the model was not verified or validated against any field measurements to determine its accuracy.

(Cao, Cai, Sun, & Xu, 2011) used inverse Fourier transform methods to analyse a poroelastic half space subject to a moving train in the frequency-wavenumber domain. The train was modelled using a multibody approach and wheel/rail interaction was simulated using a Hertzian contact spring. It was found that dynamic loads have a high contribution towards the vibration of a poroelastic medium and that the vibrations generated by a moving train increase in proportion with the primary suspension stiffness of the vehicle. The model was validated using results from another train vibration model (Sheng, 2004) and a strong correlation was exhibited.

(Salvador, Real, Zamorano, & Villanueva, 2011) expanded on the work of (Koziol, Mares, & Esat, 2008). Notable improvements include the implementation of a Timoshenko beam and the ability to model non-harmonic loads. The train, track and soil equations were developed in the frequency-wavenumber domain and solved using the Fourier transform. The final time domain solution was found using Fourier series techniques. Model results were compared with experimental results and found to have high accuracy. Despite this, only one field measurement was taken using a single acceleration transducer. Therefore despite the strong conclusions that were drawn, the model cannot be considered to be fully validated because of the small sample size of field measurements used.

Another alternative semi-analytical approach for modelling underground railways was also proposed by (Hussein & Hunt, 2007)and (Jones, 2010). The Pipe-in-Pipe (PiP) method was used to model the tunnel pipe using thin-shell theory and the soil pipe using elastic continuum theory. Both pipes were concentric, coupled pipes and the soil was considered as a full-space. The PiP approach was advantageous over other numerical methods because its computational requirements were very low meaning simulations could be performed rapidly. Despite this, as the model was only capable of simulating wave propagation within a soil full-space, the contribution of Rayleigh waves was ignored.

2.9 Numerical modelling of free field vibration

2.9.1.1 2D models

Two dimensional numerical modelling reduces the number of calculations required in comparison to three dimensional numerical modelling, thus significantly reducing computational expense. As computational requirements are a significant challenge in large scale numerical modelling of train passage, researchers have bypassed this challenge by reducing the problem to two dimensions.

(Balendra, Chua, Lo, & Lee, 1989) used a two dimensional, plane strain, finite element (FE) method to investigate the transmission of vibration from a subway, through the ground and into a building above. It was found that in the

high frequency range, a floating slab track can provide strong vibration isolation capabilities. More recently, (L. A. Yang, Powrie, & Priest, 2009) used a two dimensional FE model to investigate stress changes in the track bed of a ballasted railway. Analysis was undertaken using the commercial FE software ABAQUS and it was shown that dynamic analyses (instead of static analyses) must be undertaken when modelling train speeds which are greater than 10% of the Rayleigh wave speed. It was also shown that at train speeds greater than the Rayleigh wave speed, the stresses due to dynamic effects increase significantly.

2.9.1.2 2.5D models

A disadvantage of 2D railway modelling is that one dimension must be ignored (typically the axis parallel to the direction of train passage). In an attempt to provide a better approximation for the vibration response along the ignored axis, 2.5D models have also been developed. The concept of 2.5D modelling is that the modelling domain is considered as 2D while the excitation is considered as 3D. The advantage of 2.5D modelling is that the computational requirements to execute a 2.5D model are lower than those required to execute a 3D model, and assuming the structure is invariant in one direction, the accuracy of a 2.5D model is similar to a 3D one.

Hanazato et al. (Hanazato, T, Ugai, Mori, & Sakaguchi, 1991) used a 2.5D model combined FE and the extended thin layered element model to simulate railway vibrations. Similar to (L. A. Yang et al., 2009), it was found that the

dynamic components of the excitation were dominant in comparison to the static components.

Yang et al. (Y. Yang, 2003) also used a 2.5D method to investigate the propagation of ground vibrations in layered soils generated by train passages at various speeds. The model was implemented using the FE method and the unbounded soil domain was terminated using an infinite element solution. This prevented spurious reflections from the truncated domain.

An alternative approach was proposed by (François, Schevenels, Thyssen, Borgions, & Degrande, 2012) which coupled a 2.5D FE approach with a 2.5D boundary element (BE) method to prevent boundary reflections. It was used to investigate the effect of layered soils on structures located near a railway line such as a road, embedded tunnel, a dyke and a wave barrier. A similar approach has been proposed by (Lombaert & Degrande, 2009).

2.9.1.3 3D models

Although 2.5D models are capable of achieving accuracy levels similar to that of 3D models, this accuracy is highly dependant on the wavenumber sampling. If high accuracy is required then sampling must also be high, thus making the computation requirements comparable to 3D modelling techniques. Additionally, model properties and geometry must be assumed to be invariant in one axis (usually the direction of train passage). This means that periodic components such as sleepers and non-continuous structures (e.g. buildings) close to the line cannot be modelled. Instead, only continuous tracks such as embedded rail tracks can be modelled.

As mentioned previously, two types of model are used in a vibration prediction study. First a scroping model is used to assess vibration levels quickly and with low accuracy. Then a more detailed model is used to assess vibration levels with higher precision. The use of 2.5D modelling falls between the requirements of these assessment approaches because it is too computationally intense to be practical for preliminary studies, and not flexible enough to be used in detailed investigations.

3D models avoid many of the assumptions associated with 2.5D modelling by explicitly modelling the third dimension. This allows for realistic modelling of nearly any track structure and surrounding area (e.g. buildings). Galvin et al. (Galvin, Romero, & Domínguez, 2010a) used a coupled FE/BE method approach where the track was modelled using the FE method and the unbounded domain was accounted for by the BE method. The FE sub-model allowed for highly accurate modelling of the track and could account for changes in track geometry and dynamic excitation. Despite this, the BE sub-model was dependent on the availability of the Green's functions for the medium (e.g. (Luco & Apsel, 1983)). As the Green's function was used to determine the fundamental solution of the differential equations that were used to describe wave propagation in the medium, the 3D soil had to be defined using a 1D soil layer profile. Similar challenges faced methods proposed by O'Brien et al. (O'Brien & Rizos, 2005) and Chebli et al. (Chebli, Othman, Clouteau, Arnst, & Degrande, 2008).

A pure FEM solution was utilised by (Banimahd, Kennedy, Woodward, & Medero, 2010) and (Kouroussis, Verlinden, & Conti, 2009a). A challenge presented by this approach was that absorbing boundary conditions had to be implemented at model boundaries to prevent spurious waves contaminating the solution space. (Kouroussis et al., 2009a) employed ABAQUS' infinite element library to absorb these waves. Absorption performance was enhanced for excitations at the centre of the sphere by modelling the soil as a spherical domain. Despite this, the performance of the absorbing boundary condition decreased as the distance between excitation and boundary was reduced. Therefore when the excitation location deviated from the central position, performance degraded.

A disadvantage of ABAQUS' modelling capabilities was its difficulty in simulating displacement defined loads, which are pivotal in modelling a realistic contact condition between wheel and rail. (Powrie, Yang, & Clayton, 2007) and (Hall, 2003) employed static and moving point loads respectively but the weakness of these techniques was that they were unable to simulate dynamic excitation effects. (Kouroussis, Verlinden, & Conti, 2011a) proposed an alternative solution by separating the modelling approach into two sub-models, one for the multibody vehicle simulation and one for soil modelling. Although this approach was capable of simulating quasi-static and dynamic excitation mechanisms, the models were solved independently, meaning that only first order interaction effects were accounted for.

2.10 Empirical prediction models

Empirical prediction models rely on using a combination of previous outcomes and correlations to predict vibration levels quickly and efficiently. The volume of assumptions that underpin many empirical models is large meaning that accuracy is sacrificed for low computational demand. Therefore empirical models are most commonly used in the early stages of vibration prediction to identify potential problem areas that require more in depth investigation, perhaps using a 3D numerical model.

An empirical model based on energy considerations was outlined by (Trochides, 1991). The model was validated using a 1:10 physical scale model and shown to provide estimates reliable enough for design purposes. An alternative semi-empirical model was presented by (Madshus, Bessason, & Harvik, 1996), in which the problem was broken down into three main components: the vibration creation region (source), the propagation region and the reception region (receiver). A statistical approach was then used to predict both vibration levels and confidence limits.

(Federal Railroad Administration, 2012) developed a vibration prediction model that allows the user to predict vibration levels at various distances from the track, due to trains passing at different speeds. Vibration values were calculated by starting with a generalised vibration propagation curve and then adjusting depending on the train speed and track setup. These adjustment factors were derived from vibration data collected on many railway lines. A similar approach is outlined by (Kuppelweiser & Ziegler, 1996) who

presented a semi-empirical model (VIBRA-1) to calculate vibration levels based upon a database of vibration data already collected on Swiss railways (VIBRA-3).

An alternative approach was proposed by (Rossi & Nicolini, 2003) who presents a model capable of predicting root mean square (RMS) velocity vibration levels. A calibration factor was used to validate the output against previously recorded results. In a similar manner to (Federal Railroad Administration, 2012), (Rossi & Nicolini, 2003) ignored the use of geotechnical properties for vibration prediction purposes. Instead it was assumed that the underlying soil was a 'compressed high-density' soil. Soil properties have been shown to have a significant effect on vibration levels ((Kouroussis, Conti, & Verlinden, 2012) and (Auersch, 2008b)), thus ignoring them, even for preliminary studies, can potentially affect model accuracy. This is particularly true in situations where the train speed approaches the Rayleigh wave speed of the underlying soil.

2.11 Field measurement

Field measurement refers to either the collection of train passage data on existing lines for use with statistical analysis, or the use of direct field measurements at proposed sites to estimate vibration levels.

The collection of train passage data has been undertaken by (Okumura & Kuno, 1991) who performed recordings at 79 Japanese railway sites.

Regression analysis was used to show that receiver distance from the track was the most influential parameter and that when train speeds are much lower than the soil Rayleigh wave speed, train speed was not an influential parameter.

(Kouroussis, 2005) performed train passage recordings on a Belgian high speed rail site and found that the dominant frequency components generated due to train passage were in the 0-50Hz range. Similar investigations were performed by (Degrande & Schillemans, 2001a) who recorded train passages of different speeds at another Belgian test site, before it commenced commercial operation. It was found that speed played a role in increasing vibration levels and shifted the frequency spectrum to a higher range.

In an attempt to combine field measurements with empirical modelling, (Melke & Kraemer, 1983) proposed a model comprising of analytical techniques, laboratory tests and in-situ measurements. The advantage of this was that soil properties were included in the modelling process, thus increasing model accuracy. (Federal Railroad Administration, 2012) also presented a second prediction model based upon the work by (Nelson & Saurenman, 1987) and (Bovey, 1983), which relied on in-situ measurements. This method relied on summing the 'force density level' (FDL) due to a train passing over the track and the 'line source transfer mobility' (LSTM) of the soil, to calculate the vibration level. Therefore although neither the physical track nor soil properties were measured directly, their response to excitation was measured and could thus be used to determine vibration levels with high accuracy. Despite this, it was possible under certain soil conditions that the calculation of

the FDL was dependent upon the underlying soil (i.e. the LSTM). Therefore this decoupled approach has limitations if the contrast between soil and subgrade material properties is high (i.e. soft soil). The accuracy of decoupled track/soil submodels has been investigated by (Kouroussis, Verlinden, & Conti, 2011b) using a numerical approach.

(Verbraken, Lombaert, & Degrande, 2011) expanded on this work by developing a hybrid vibration prediction method based upon (Federal Railroad Administration, 2012). Instead of performing in-situ experiments to calculate the FDL and LSTM, they were calculated numerically. The advantage of this was that access to the site was not required and that the simulations could be performed efficiently. Despite this, for a given site (e.g. layered soil) it is difficult to calculate the LSTM accurately without prior field work, thus making it hard to justify.

2.12 The practical application of vibration prediction models

When planning a new high speed rail route environmental assessments are required to predict noise and vibration levels due to both line operation and construction. When predicting operational vibration, various combinations of the aforementioned approaches have been used.

(Federal Railroad Administration, 2005) and (Federal Railroad Administration, 2012) has gained wide acceptance in recent years and has been used to assess operational ground vibration levels due to tram passage in

Edinburgh, Scotland (Pouillon, Rys, Samyn, & Vanhonacker, 2009). Analysis involved the use of experimental investigations to calculate the LSTM and combining it with FDL measurements calculated numerically. This approach allowed for a high accuracy calculation of vibration levels within a sensitive urban area without the need for intrusive geotechnical investigations such as drilling boreholes. Despite this, undertaking this procedure in an urban area meant that it was possible for the LSTM results to be contaminated by background vibration due to cars, buses, etc.

(Federal Railroad Administration, 2012) was also used to calculate vibration levels for the City Rail Link in (Whitlock, Fitzgerald, & Peakall, 2012). Instead of using in-situ experiments to calculate FDL and LSTM, the more straightforward empirical method was preferred. This allowed the consultant to predict the vibration levels using just numerical simulations rather than field work. Despite this, accuracy was sacrificed because the effect of soil properties on vibration levels was ignored.

Crossrail is an underground railway project under construction in London, UK. Operational vibration prediction was undertaken using finite difference time domain simulations (RPS, 2004). This allowed for full 3D modelling of the domain and for arbitrary soil properties (including soil layering and anisotropy) to be accounted for. This was important for this project because its close proximity of the line to a river meant that changing water levels were a concern. Therefore the numerical model was used to assess vibration levels subject to a variety of water level test cases.

2.13 Thesis outline

Chapters 2 and 3 outline the development of 3D FE models capable of predicting railway vibration levels, using the commercial FE software packages ABAQUS and LSDYNA. The models overcome accuracy and coupling challenges that have been faced by other researchers and are shown to have high accuracy prediction capabilities in chapter 8.

Chapter 5 investigates the application of the finite difference time domain modelling method for railway vibration prediction. Although it is found to be less suitable than the FE method, a new absorbing boundary condition is developed for the FDTD method with higher performance than other current alternatives.

Chapter 6 outlines the development of a neural network prediction model based upon results obtained from the ABAQUS model outlined in chapters 2 and 3.

Chapter 7 presents a review of techniques to determine soil parameters for use with numerical models. As it is not always possible to undertake geophysical investigations, emphasis is placed on empirical correlations between in-situ tests and soil properties. Several new correlations between standard penetration test results and shear wave velocity are proposed.

Chapter 8 describes a series of experiments undertaken on high speed lines in the UK and in Belgium. The collection methodology describes the recording of vibration levels and the determination of soil parameters.

Chapter 9 uses the experimental results from Chapter 8 to validate the two detailed FE models developed in Chapters 2 and 3, and the neural network model outlined in Chapter 6. The FE models are both shown to predict vibration levels and frequency content with high accuracy. The neural network model is also shown to have high prediction accuracy and to outperform a commonly used alternative model.

Chapter 10 outlines the use of the detailed FE models to investigate the effect of embankment stiffness, Rayleigh wave speed and railway track structure on vibration propagation. It is shown that soft embankments generate higher levels of vibration and Rayleigh wave speed has a large effect on vibration magnitudes. It is also shown that slab track produce slightly reduced levels of vibration in comparison to metal and ballasted tracks.

Chapter 11 presents an analysis of vibration mitigation methods. A newly developed recycled rubber ballast is found to offer significant vibration isolation, particularly for thick ballast layers. Wave barriers are also investigated and it is found that the optimisation of their geometries can facilitate large vibration isolation for a reduced cost.

2.14 Conclusions

The deployment of high speed rail technology has grown rapidly over the last 30 years. This demand for new infrastructure has brought an increased desire to deploy high speed rail lines through urban environments.

One of the key environmental concerns related to high speed rail is the level of the elevated ground-borne vibration levels, and their impact on the local, and often urban environment. In an attempt to identify these vibration levels before lines are constructed, various researchers have developed techniques to predict them. This shift in train speed is reflected in the change of focus of railway vibration modelling. Early research focused on predicting the vibration characteristics solely within the track structure however in recent times there is a greater desire to predict vibration levels in the free field. This thesis focuses on the latter.

The methods used to predict vibrations include analytical techniques, numerical simulation, empirical techniques, in-situ experiments, and hybrid approaches which combine aspects of several of these methods. Vibration assessment projects can have vastly different objectives thus making the application of one particular modelling technique more suitable than another. This is reflected in the fact that a wide variety of techniques have been used to predict vibration levels on real world projects.

This thesis aims to develop several new prediction models that are capable of predicting free field vibration levels, either more accurately or more efficiently than previous works. In doing so it aims to provide better

understanding of ground-borne vibrations from trains and to investigate methods to protect against it.

Chapter 3. Finite element model development

3.1 Introduction

The finite element (FE) method is a numerical technique used to approximate the solution of a complex domain that otherwise could not be solved using analytical expressions. The domain is broken into a finite number of smaller parts (elements), each with simple geometries, and the laws of physics are applied to each element. The combination of the behaviour of all elements is used to approximate the solution of the entire domain.

FE methods have been used extensively in engineering to perform structural analysis (Jofriet & McNeice, 1971), crash testing analysis (Cheng, Thacker, Pilkey, Hollowell, & Reagan, 2001), and to investigate vibration propagation from railways (see Chapter 1). A strength of the FE method is its ability to model complex geometries. This is advantageous for railway modelling because the small dimensions associated with railway components such as the rail can be modelled precisely, while at the same time, modelling the large dimensions associated with the soil can be done using larger elements.

The aim of this thesis was to develop numerical models for the purpose of investigating railway vibration. Rather than develop new FE software from scratch it was decided to take advantage of the vast body of underlying numerical techniques already present commercial codes. This way, mesh creation, part interactions and absorbing boundary conditions could be defined in a straightforward manner without the associated physical programming challenges. Similarly, commercial codes have pre-defined routines to optimise the parallelisation of computations and their element libraries have been extensively verified. Taking advantage of these features meant that a focus was placed on tailoring the general purpose FE codes for railway vibration modelling rather than investigating FE programming. This allowed for a more powerful and accurate model to be developed.

Despite these advantages, a shortcoming of currently available commercial codes is that they have not been purposely built for railway applications. Therefore there were challenges, particularly associated with the definition of moving loads, in adapting them for railway modelling. The solution to these problems and the general development of the FE model is discussed in this chapter and in Chapter 4.

3.2 The finite element method – an overview

Commercial FE packages ABAQUS and LSDYNA were chosen to develop (pre-process) the FE railway model due to their ability to model complex geometries using a graphical user interface (GUI) and their advanced meshing

capabilities. They were also used as FE solvers because of their ability to utilise multiple processors thus maximising computational efficiency.

Although each FE code was not coded directly, the development of a reliable vibration prediction model using commercial software required a strong understanding of FE principles. Therefore the key principles are now recapitulated. Theory is provided in the context of 3D FE modelling because the majority of modelling work was performed in three dimensions (3D).

3.2.1 Key assumptions

In the case of railway vibration, the magnitude of strain experienced by the soil is small. Deformations are also small and can be considered to have a linear relationship with loading. This allows for the problem to be treated as 'linear elastic'. This means that deformation is linear, and the deformation of a solid (e.g. the soil) disappears when loading is removed, meaning the solid will revert back to its original state.

It was also assumed that all model components were 'isotropic', meaning that material properties were uniform properties in all directions. For an isotropic material, if a force is applied in one direction, the deformation will be identical to another case where the force is applied in a different direction.

For moving load problems such as that for high speed train passage, the problem is a dynamic one. This is because the solution variables (e.g. velocity, stress) are a function of time.

3.2.2 Shape functions

The finite element method is based upon dividing a domain into smaller parts. As an example, the domain in Figure 3.1 (left), can be divided into a finite number of elements, each with 24 degrees of freedom (DOF's). For the majority of modelling in this thesis, elements were chosen to be of regular shape and size thus making calculation more straightforward. Although each element in the global domain can be defined using a global coordinate system, it is more convenient to use a local coordinate system, especially when considering complex element geometries. This local coordinate system has coordinates (0,0,0) in the centre of the element, and each node of the element is referenced from this point using a shape function. The global coordinate system can be defined in three directions using x, y and z, and the local system can be defined using ξ, η, and ζ.

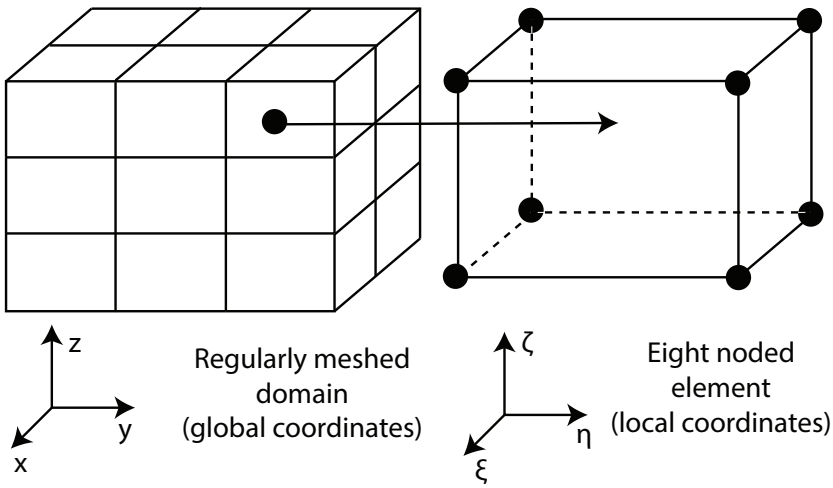

Figure 3.1 – FE meshing process, (a) left: a regularly meshed domain constructed from (b) Right: eight noded elements

With a local coordinate system established, the displacement within each element can be expressed as a function of the nodal displacements (**U**).

$$\boldsymbol{U} = \boldsymbol{N}(x, y, z)\boldsymbol{d}_e \qquad \text{Equation 3.1}$$

Where $\boldsymbol{d}_e$ represents nodal displacements and **N** is a shape function which helps to interpolate element behaviour between nodes in areas where there are no points to define the mesh. Shape functions exist for each different type of finite element. For a regular 3D isotropic element the shape function varies linearly in each direction and is defined as:

$$N_i = \frac{1}{8}(1 + \xi\xi_i)(1 + \eta\eta_i)(1 + \zeta\zeta_i) \qquad \text{Equation 3.2}$$

3.2.3 Strain matrix calculation

There are six stress and six strain components at each point in a 3D solid. The stress and strain tensors respectively are:

$$\boldsymbol{\sigma} = \left[\sigma_{xx}\ \sigma_{yy}\ \sigma_{zz}\ \sigma_{yz}\ \sigma_{xz}\ \sigma_{xy}\right]^T \qquad \text{Equation 3.3}$$

$$\boldsymbol{\varepsilon} = \left[\varepsilon_{xx}\ \varepsilon_{yy}\ \varepsilon_{zz}\ \varepsilon_{yz}\ \varepsilon_{xz}\ \varepsilon_{xy}\right]^T \qquad \text{Equation 3.4}$$

Where ^{T} means transpose and strain is equal to the change in displacement divided by unit length. The relationship between strain and displacement can be expressed as:

$$\boldsymbol{\varepsilon} = \boldsymbol{LU} \qquad \text{Equation 3.5}$$

Where $\boldsymbol{U}$ represents displacement and $\boldsymbol{L}$ is a matrix of partial derivate operators. Using this equation in combination with Equation 3.1 gives:

$$\boldsymbol{\varepsilon} = \boldsymbol{LNd}_e \qquad \text{Equation 3.6}$$

$$\boldsymbol{LNd}_e = \boldsymbol{Bd}_e \qquad \text{Equation 3.7}$$

Cancelling $\boldsymbol{d}_e$ gives:

$$\boldsymbol{B} = \boldsymbol{LN} \qquad \text{Equation 3.8}$$

$\boldsymbol{B}$ is known as the strain matrix which is defined in terms of derivatives with respect to the global coordinate system. As the shape functions are defined in terms of natural coordinates $\boldsymbol{B}$ must be solved using the chain rule of partial differentiation.

3.2.4 Element matrices

Once the shape functions and strain matrix have been calculated then both displacements and strains can be expressed in terms of nodal coordinates. Similarly, the stiffness and mass vectors can be found using:

$$\boldsymbol{k}_e = \int_{Vol_e} \boldsymbol{B}^T \boldsymbol{c} \boldsymbol{B} dV \qquad \text{Equation 3.9}$$

$$\boldsymbol{m}_e = \int_{Vol_e} \rho \boldsymbol{N}^T \boldsymbol{N} dV \qquad \text{Equation 3.10}$$

Where Vol_e represents the volume of the element and **c** is the constitutive matrix, a form of Hooke's law, which relates stresses to strains. For the case of train passage modelling, all materials were assumed to be fully isotropic. Therefore the constitutive matrix reduced to:

$$\boldsymbol{c} = \begin{bmatrix} c_{1_1} & c_{1_2} & c_{1_2} & 0 & 0 & 0 \\ & c_{1_1} & c_{1_2} & 0 & 0 & 0 \\ & & c_{1_1} & 0 & 0 & 0 \\ & & & (c_{1_1} - c_{1_2})/2 & 0 & 0 \\ & symm & & & (c_{1_1} - c_{1_2})/2 & 0 \\ & & & & & (c_{1_1} - c_{1_2})/2 \end{bmatrix}$$

Where

$$c_{1_1} = \frac{E(1+\upsilon)}{(1-2\upsilon)(1+\upsilon)}$$

$$c_{1_2} = \frac{E\upsilon}{(1-2\upsilon)(1+\upsilon)}$$

It can also be seen that c_{1_1} and $c_{1_2}$are related to shear modulus:

$$\frac{c_{1_1} - c_{1_2}}{2} = \frac{E}{2(1+\upsilon)} = \mu$$

3.3 Gauss integration

As shown previously, strain is defined using a local coordinate system. This makes the integration of the stiffness and mass matrices difficult. Therefore these integrals are solved using a Gauss integration scheme.

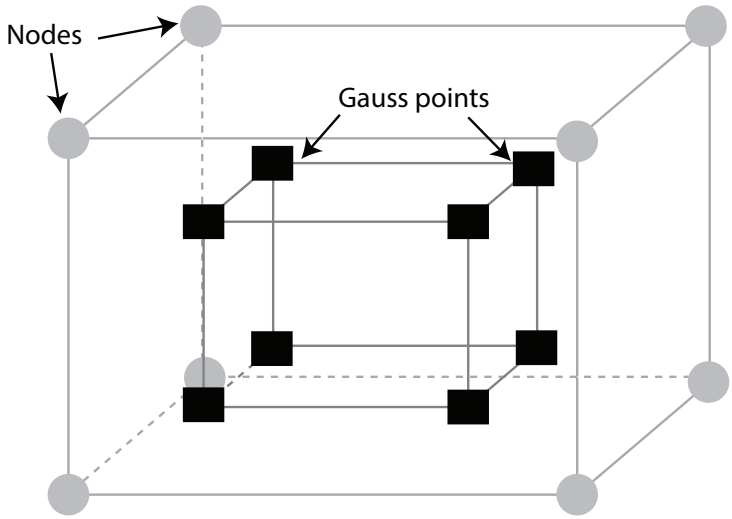

Figure 3.2 – Gauss point locations

Equation 3.11 shows the gauss integration equation for a 3D element. It is the summation of the integrand evaluated at each Gauss point (Figure 3.2) multiplied by the associated weight coefficients. Exact Gauss point locations and weightings can be found in (Liu & Quek, 2003).

$$I = \int_{-1}^{1} \int_{-1}^{1} \int_{-1}^{1} f(\xi, \eta, \zeta) d\xi d\eta d\zeta \qquad \text{Equation 3.11}$$

Finally, after the mass and stiffness matrices have been calculated, the force matrix is calculated. Assuming a force is applied on a surface between nodes a and b, the force vector is:

$$\boldsymbol{f}_e = \int_l [\boldsymbol{N}]^T|_{(a-b)} \begin{Bmatrix} f_{sx} \\ f_{sy} \\ f_{sz} \end{Bmatrix} dl \qquad \text{Equation 3.12}$$

3.3.1 Material damping

Before the equations of motion can be solved the damping matrix must also be assembled. (Caughey, 1960) proposed that material damping could be defined as a function of the mass and stiffness matrices. This is known as Rayleigh damping and is expressed as:

$$\boldsymbol{C} = \alpha \boldsymbol{M} + \beta \boldsymbol{K} \qquad \text{Equation 3.13}$$

Where α is the mass proportional damping coefficient and β is the stiffness proportional damping coefficient. α and β are often determined experimentally using:

$$\alpha = \frac{2D\omega_1\omega_n}{\omega_1 + \omega_n} \qquad \text{Equation 3.14}$$

$$\beta = \frac{2D}{\omega_1 + \omega_n} \qquad \text{Equation 3.15}$$

Where ω_1 is the first natural frequency of the system and ω_n is the highest natural frequency. *D* is the damping ratio which is expressed as a fraction of critical damping. If the damping ratio is equal to 1.0 then the system is critically damped, meaning it will return to equilibrium as quickly as possible without residual oscillation. If the damping ratio is zero then the system is

undamped. Damping ratio can be expressed in terms of Rayleigh damping using α and β.

$$D = \frac{1}{2}\left(\frac{\alpha}{\omega} + \beta\omega\right) \qquad \text{Equation 3.16}$$

It can be seen that mass proportional damping attenuates low frequency response whereas stiffness damping attenuates higher frequency response. The relationship between α, β and Rayleigh damping is illustrated in Figure 3.3.

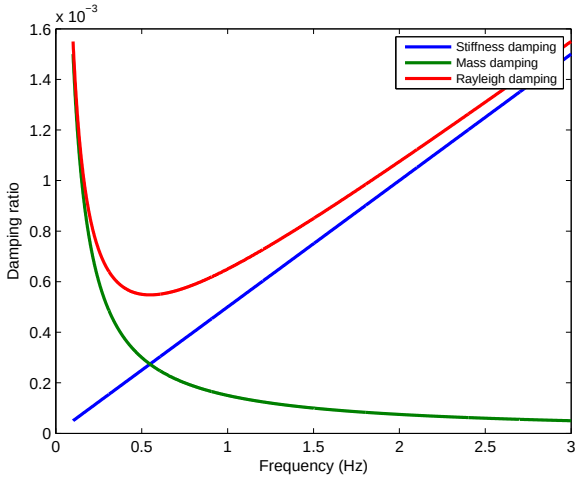

Figure 3.3 – Rayleigh damping characteristics

3.3.2 Numerical integration

Once the matrices have been developed for each element in the modelling domain, they are assembled to form a global system of equations. This takes the form of:

$$\boldsymbol{KU} + \boldsymbol{CV} + \boldsymbol{MA} = \boldsymbol{F} \qquad \text{Equation 3.17}$$

Where **V** and **A** are the global velocity and acceleration matrices respectively. Similarly, **K, C, M** and **F** are the global stiffness , damping, mass,

and force matrices. An explicit central difference integration scheme (Smith & Griffiths, 1997) was then used to solve the global system:

$$\begin{aligned} \mathbf{X}_{t+1} &= \mathbf{X}_t + \Delta t \mathbf{V}_t + 0.5\Delta t \mathbf{X}_t \\ \mathbf{A}_{t+1} &= \mathbf{M}^{-1}\left(\mathbf{F}_{ext} - \mathbf{C}\mathbf{X}_t - \mathbf{K}\mathbf{X}_{t+1}\right) \\ \mathbf{V}_{t+1} &= \mathbf{V}_t + 0.5\Delta t\left(\mathbf{A}_t + \mathbf{A}_{t+1}\right) \end{aligned} \qquad \text{Equation 3.18}$$

Where Δt is the integration timestep.

3.3.3 Timestep criterion

Explicit integration methods are conditionally stable. This means that unlike implicit methods, the timestep used for integration must be lower than a critical threshold. If the timestep is larger than this value at any stage of the simulation then the simulation is likely to develop errors. Eventually these errors will grow causing the simulation to loose stability.

For this reason, timesteps used for explicit simulations are typically several magnitudes less than those used for implicit simulations. The critical timstep, which must not be exceeded is calculated based upon the time taken for the fastest stress wave propagating in the domain to traverse the smallest element in the mesh. Therefore it becomes clear that in the case of railway ground vibration modelling, the cell size used to mesh the rail is a key factor in determining the critical timestep. To maintain consistency, trial and error analyses were used and the choice of a timestep of 1.5e-5 seconds was chosen because it was found to provide stable results for all FE simulations.

3.4 Development of a 3D railway track model

3.4.1 Track modelling

Track geometry and material properties were modelled in accordance with the UK Channel Tunnel Rail Link (O'Riordan & Phear, 2001) and International union of Railways (International union of Railways, 1994) specification. Fifty metres of track was modelled using 77 sleepers placed at 0.65m centres. The model was symmetrical in the track direction, so only half of all track components and half of the supporting soil were modelled.

The graphical user interface (GUI) available through the commercial FE software used to develop the track/soil model made it straightforward to model the rails and sleepers. This was a key advantage of using a GUI because defining complex geometries and part interactions was important for accurately describing the transfer of forces from train wheels, through the track and into the soil. Rather than attempt to model these complex geometries, they were simplified by transforming them into 2D problems by (Nielsen & Igeland, 1995) and (Knothe & Grassie, 1993). Similarly, (El Kacimi et al., 2013) and (Thornely-Taylor, 2004) used geometry simplifications in three dimensions to model the track. Therefore in an attempt to achieve higher levels of accuracy by more closely approximating the physical problem, the complex geometries were modelled explicitly.

The rail was modelled as a continuously welded solid rectangular section with dimensions 0.153m x 0.078m, laid at 1.435m gauge. Timoshenko beam elements 0.1m in length were used in preference to Euler beam elements due to

their additional degrees of freedom. This approach allowed shear forces to be modelled, thus providing a more accurate transmission of high frequency forces into the track structure.

Each sleeper was formed from reinforced concrete with dimensions 0.242m x 0.2m x 2.42m. The sleeper sections were supported by a ballast layer, a subballast layer and a subgrade layer as shown in Figure 1. Track material properties are provided in Table 9.1.

All track components (excluding the rail) were modelled using 8 noded solid cuboid elements, approximately 0.2m in length along each axis. The edges of the ballast, subballast and subgrade layers located at the ends of the track were terminated with an absorbing boundary condition. This prevented reflections occurring inside the track structure due to the truncation of components.

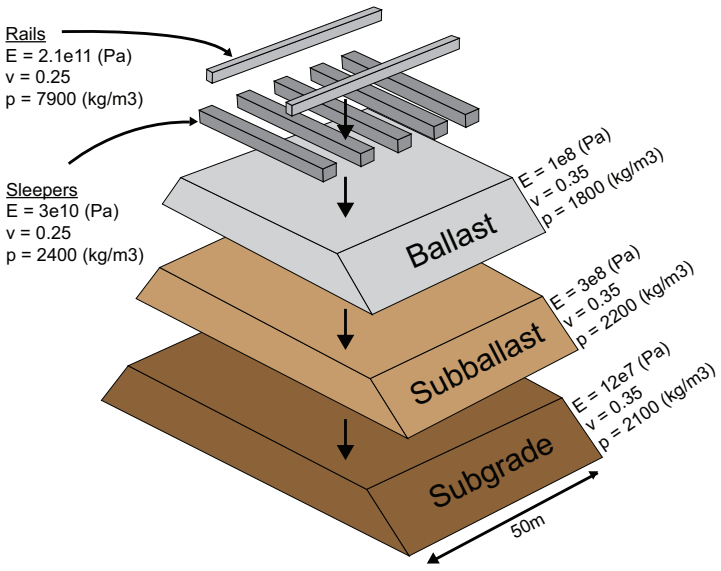

Figure 3.4 – Track properties

3.4.2 Contact between track components

Contact was defined using 'tie constraints'. For all contacts except between rail and sleepers, 'surface to surface' criteria was used. This formulation helped to avoid stress noise at the interface. Tieing was performed by dividing the contact surfaces into master and slave surfaces. Master surfaces were chosen as the surface with a coarser mesh, so for the contact between subgrade and soil, the top surface of the soil was the master surface. For contacts where the mesh sizes at each surface were identical, the lower surface was used as the master. The default ABAQUS position tolerance criterion was used to determine which nodes/surfaces would be tied. Defining the slave and master surfaces correctly allowed ABAQUS to interpolate stresses and displacements across the interface accurately.

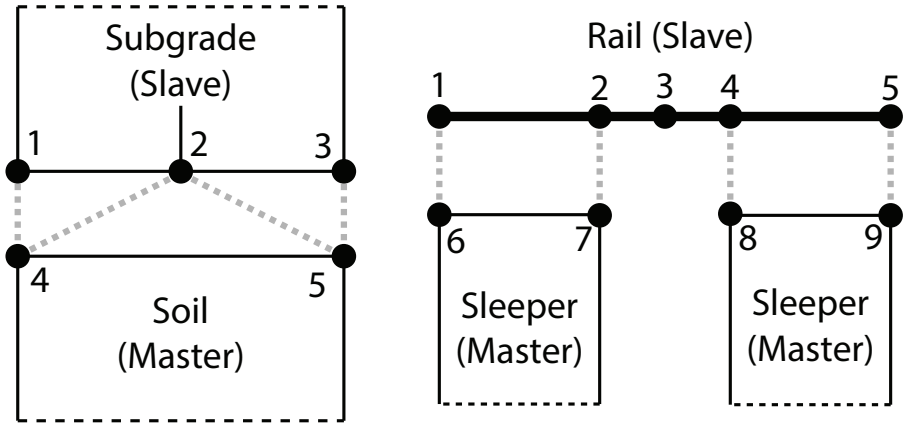

Figure 3.5 – Tie constraints: (a) Left: Surface to surface, (b) Right: node to surface

For the contact between rail and sleeper, a 'node to surface' tie constraint was used. This constraint is typically used to define interfaces between complex surfaces, such as was the case, due to the discontinuous nature of the sleepers.

An example of 'node to surface' and 'surface to surface' constraints is shown in Figure 3.5.

3.4.3 Vehicle modelling

To model each train the carriages were broken down into their three primary components: the wheels, bogies and cars. In a similar manner to the track components, the vehicle was symmetrical in the longitudinal direction. In addition, it was assumed that each car was also symmetrical in the direction of vehicle movement meaning each car could be divided into two separate spring-damper systems. This approach reduced computational demands and has previously been shown to produce similar results to modelling the carriages as a single body (Galvin et al., 2010a). Each quarter carriage was thus modelled using a multi-body spring-damper system where the carriage mass, $\overline{m}_c = m_c/8$, and the bogie mass, $\overline{m}_b = m_b/4$. The cars and bogies were modelled as rigid bodies and were connected via a primary and secondary suspension system (Figure 3.6). This resulted in the following equations of motion similar to that of Equation 3.17.

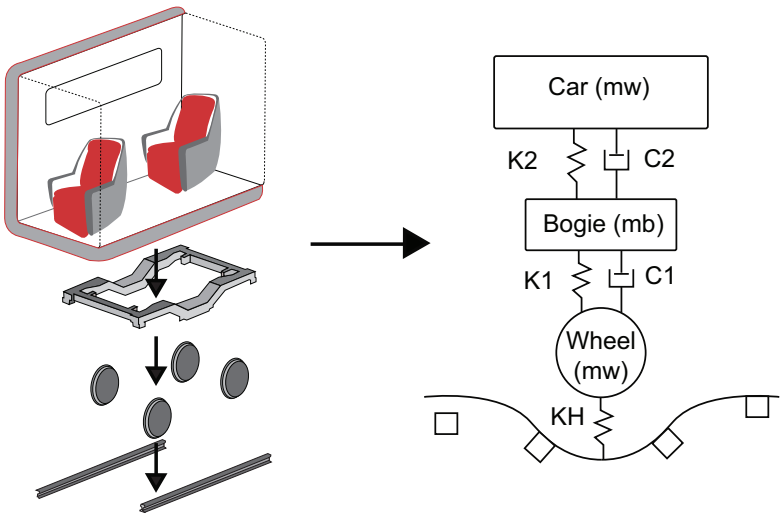

Figure 3.6 – Vehicle modelling, (a) Left: Thalys Vehicle, (b) Right: Simplified model

$$\begin{bmatrix} k_2 & -k_2 & 0 \\ -k_2 & k_1+k_2 & -k_1 \\ 0 & -k_1 & k_1 \end{bmatrix}\begin{bmatrix} U_c \\ U_b \\ U_w \end{bmatrix} + \begin{bmatrix} c_2 & -c_2 & 0 \\ -c_2 & c_1+c_2 & -c_1 \\ 0 & -c_1 & c_1 \end{bmatrix}\begin{bmatrix} V_c \\ V_b \\ V_w \end{bmatrix} + \begin{bmatrix} \bar{m}_c & 0 & 0 \\ 0 & \bar{m}_b & 0 \\ 0 & 0 & \bar{m}_w \end{bmatrix}\begin{bmatrix} A_c \\ A_b \\ A_w \end{bmatrix} = \begin{bmatrix} \bar{m}_c \cdot g \\ \bar{m}_b \cdot g \\ \bar{m}_w \cdot g + F_{wr} \end{bmatrix}$$

Equation 3.19

Where U_i, V_i and A_i were displacement, velocity and acceleration respectively, with i $\in (c, b, w)$. Subscripts c, b and w denote the multi-body component (i.e. car, bogie or wheel). Values for mass, stiffness and damping associated with a variety of high speed train locomotives are found in Chapter 8. The final FE model is visualised in Figure 3.7.

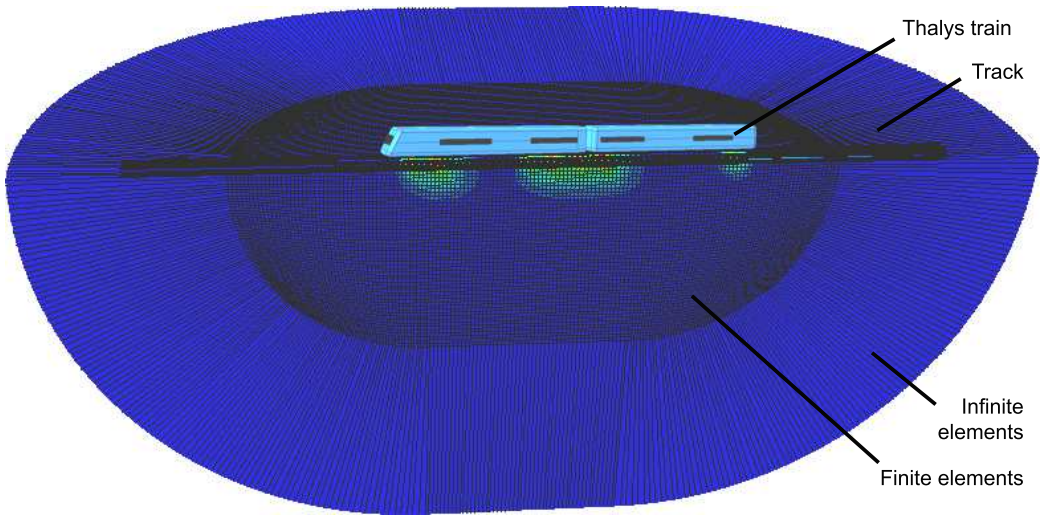

Figure 3.7 – Visualisation of final FE model

3.4.4 Wheel-rail coupling

The wheel and rail were coupled using a non-linear Hertzian contact spring (Johnson, 1985). This allowed the force exerted from the train wheels at a given timestep to be a function of the wheel displacement and rail displacement. If the wheel was not touching the rail then no force was exerted:

$$F_{wr} = k_H(u_w - u_r - r)^{1.5}, \quad u_w - (u_r + r) < 0 \qquad \text{Equation 3.20}$$

$$F_{wr} = 0, \quad u_w - (u_r + r) > 0$$

$F_{wr,}$ represents the wheel/rail interaction force and k_H is the Hertzian constant which is related to the geometry and material properties of the wheel and rail. A value of $k_{H,} = 9.4\text{x}10^9$ N/m$^{1.5}$ was assumed.

'r', represents the rail surface irregularity. This accounted for geometric defects caused by train operational effects such as train braking and track debris. Irregularities introduce high frequency excitation into the system in addition to the low frequency content generated due to the bogie passage excitation frequencies. Figure 3.8 shows an example of rail irregularity. The combination of quasi-static and dynamic excitation has been shown to play an important role in the propagation of railway vibration (Sheng, Jones, & Thompson, 2003), (Lombaert & Degrande, 2009), (Auersch, 2005).

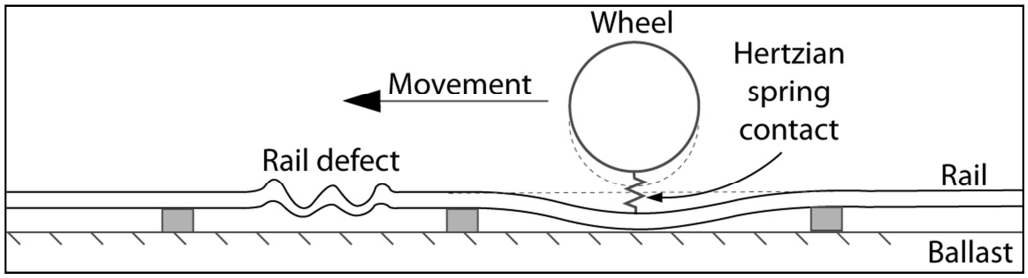

Figure 3.8 – Wheel/rail contact

To allow for a flexible yet accurate representation of the overall rail irregularity, an irregularity scale was implemented according to (Garg & Dukkipati, 1984). This scale had six quality classes ranging from 'good' to 'very poor' quality track irregularity. Each track class was based upon a large body of data collected by (FRA, 2013). As the numerical model was only capable of simulating vertical excitation, only the vertical profile was used to describe the track irregularity, i.e. lateral alignment was ignored.

The vertical profile, power spectral density (PSD) as outlined by (Garg & Dukkipati, 1984) was described as:

$$S_{zz}(\phi) = \frac{A\phi_2^2(\phi^2 + \phi_1^2)}{\phi^4(\phi^2 + \phi_2^2)} \qquad \text{Equation 3.21}$$

Parameters		Track classes					
Symbol	Units	1	2	3	4	5	6
A	10^{-6}m	1.6748	0.954	0.53	0.2968	0.1675	0.0954
φ_1	$10^{-3}m^{-1}$	23.294	23.294	23.294	23.294	23.294	23.294
φ_2	$10^{-2}m^{-1}$	13.123	13.123	13.123	13.123	13.123	13.123

Table 3.1 – Track class parameters

Where φ_1 and φ_2 are the lower and upper cutoff spatial frequencies, and A was a roughness constant (Table 3.1). It should be noted that the wavelength range was limited to between 1.5m and 300m, in accordance with (Garg & Dukkipati, 1984). To convert the PSD to a physical profile expressed in terms of the track position, Fourier series was used (Kouroussis, Verlinden, & Conti, 2009a):

$$h(x) = \sum_k \sqrt{2\,\Delta\phi\, S_{zz}(k\Delta\phi)\cos(k\Delta\phi x + \varphi_k)} \qquad \text{Equation 3.22}$$

Where *x* was position, $\Delta\varphi$ was the spatial frequency step and ϕk was a random number uniformly generated between π and $-\pi$. Figure 3.9 and Figure

3.10 show the PSD and random unevenness associated with each of the six quality classes respectively.

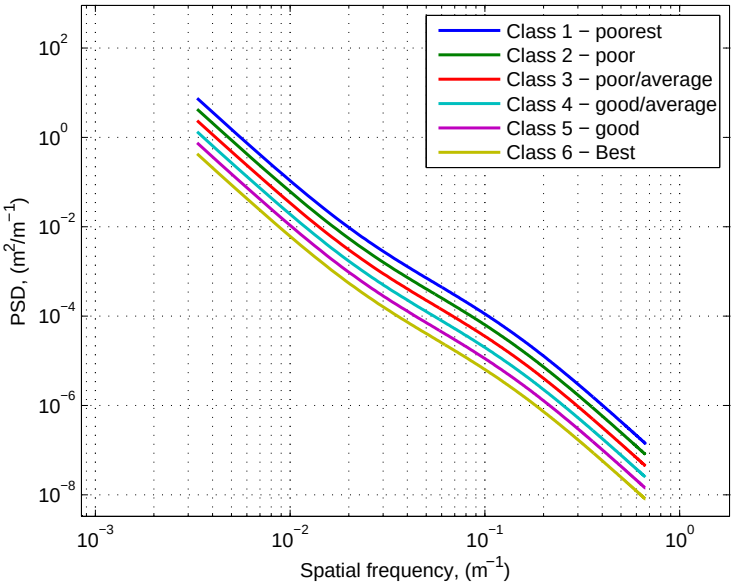

Figure 3.9 – Power spectral density for all classes (Garg & Dukkipati, 1984)

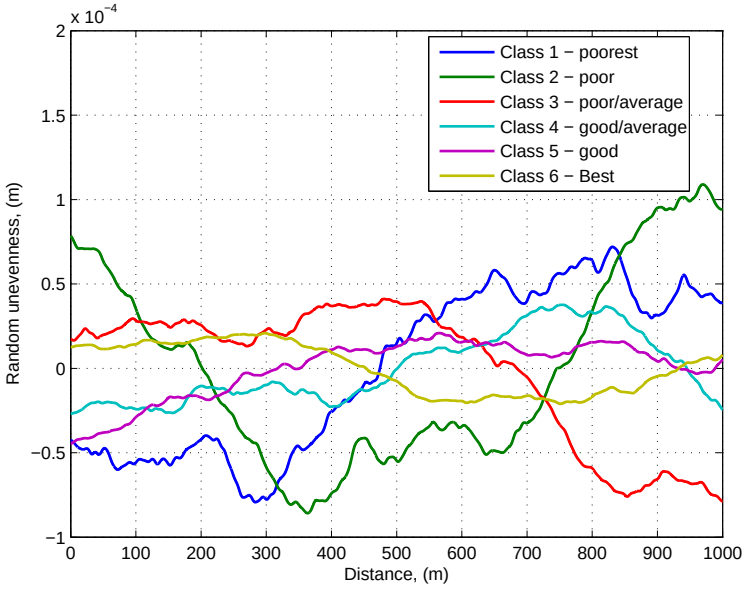

Figure 3.10 – Rail irregularity for all classes (Garg & Dukkipati, 1984)

3.4.5 Vehicle integration scheme

In additional to the default ABAQUS explicit solver, an integration scheme was required to solve the equations of motion for the vehicle. To determine the most suitable integration scheme, the explicit central differencing scheme was tested against an alternatively proposed scheme described by Equation 3.23 (Zhai, 1996):

$$\boldsymbol{U}^{t+1} = \boldsymbol{U}^{t} + \Delta t\boldsymbol{V}^{t} + (0.5 + \psi)\Delta t^{2}\boldsymbol{A}^{t} - \psi\Delta t^{2}\boldsymbol{A}^{t-1}$$

$$\boldsymbol{V}^{t+1} = \boldsymbol{V}^{t} + (1 + \varpi)\Delta t\boldsymbol{A}^{t} - \varpi\Delta t\boldsymbol{A}^{t-1} \qquad \text{Equation 3.23}$$

$$\boldsymbol{A}^{t+1} = \boldsymbol{M}^{-1}(\boldsymbol{F}_{ext}^{t+1} - \boldsymbol{C}\boldsymbol{V}^{t+1} - \boldsymbol{K}\boldsymbol{A}^{t+1})$$

Where ψ and ϖ were dimensionless and controlled both numerical stability and dispersion. Testing was performed using a similar example to that presented by (Smith & Griffiths, 1997) and is shown in Figure 3.11. It consisted of a three element, eight node, 2D cantilever beam, subject to a Gaussian excitation at the free end. The model timestep was held constant at 0.01s.

During testing, when performing the integration described by Equation 3.23, ψ and ϖ were set to 0.0 for the initial timestep and for all subsequent timesteps they were equal to 0.5. Each explicit scheme was compared to the (Newmark, 1959) implicit integration scheme.

Figure 3.12 shows that the response of both schemes was almost identical to the implicit scheme. Despite this, it was found that the stability

criterion for the central difference algorithm was less severe than that for (Zhai, 1996). Therefore the central differencing scheme was chosen to compute the equations of motion for the vehicle. Another advantage of this choice was that it closely followed that used within the ABAQUS solver. This made it trivial to ensure that the minimum timestep threshold was met simultaneously for both staggered schemes.

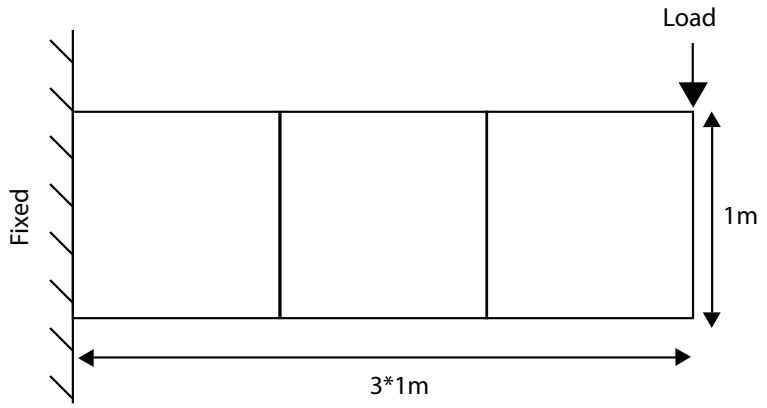

Figure 3.11 - Integration test model, Poisson's ratio=0.3, Young's modulus=1 Pa, density=1 kg/m^3

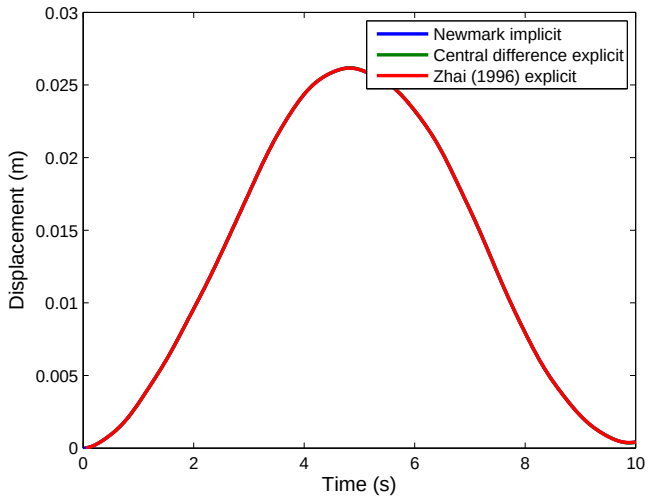

Figure 3.12 – Integration performance comparison

3.5 Conclusion

Commercial finite element software was chosen to develop a railway vibration prediction model due to its pre-programmed algorithms for mesh creation, computation parallelisation, part interactions and absorbing boundary conditions. To enable the enhancement of commercial codes it was important to understand the underlying theory of the finite element method. Therefore the key concepts required for simulating high speed train passage were outlined.

The track components were modelled explicitly in three dimensions which was made straightforward due to the graphical user interface available with the commercial software. This allowed for a more accurate description of track force propagation from wheel to soil. All track components were coupled using tie constraints and the train vehicle was modelled using a multibody approach to describe the wheel, bogie and car body. The train wheels were coupled to the rail using a non-linear Hertzian contact spring, and rail irregularity was simulated using a quality classification system derived from field experiments. Lastly, the ability of two explicit integration schemes to solve the equations of motion were tested and it was found that the traditional central differencing scheme performed best.

Chapter 4. Finite element model implementation

4.1 Background

For railway modelling applications, a strength of the FE method is its ability to model complex geometries. To enable the development of these intricate components, a graphical user interface (GUI) is desirable because it allows for the rapid construction and straightforward modification of complex meshes. Rather than develop a bespoke GUI, the commercial codes ABAQUS and LSDYNA were used to aid pre-processing. Additionally, in instances where changes were too complex to be made using the GUI, MATLAB scripts were developed to make changes directly to the input file.

ABAQUS is a general purpose FE software suite developed by Dassault Systemes. It was released in 1978 and has gained wide acceptance in with both academic and industrial applications due to its large material and element libraries, and its ability for customisation. This research used ABAQUS/CAE for pre and post-processing and ABAQUS/Explicit for model evaluation. LSDYNA is an alternative FE software suite developed by Livermore Software Technology Corporation. Although capable of implicit analysis, LSDYNA's strengths lie in its explicit analysis, thus making it useful for railway vibration applications. This research used LS-Pre-Post for pre and post-processing and the default LSDYNA solver for model evaluation.

The utilisation of commercial software for FE railway model development has also been proposed by (Kouroussis, Verlinden, & Conti, 2009b) and (Kouroussis et al., 2011b). In this series of works, a soil sub-model developed using ABAQUS was combined with a vehicle/track multi-body sub-model developed using EasyDyn (Verlinden, Kouroussis, & Conti, 2005). Although both sub-models were capable of accurate simulation, they were not coupled. Therefore their interaction was limited meaning overall model accuracy was reduced. Modelling of vibrations as generated by Maglev trains in tunnels was also simulated using LSDYNA by (Wang, Jin, & Cao, 2011).

To improve accuracy, this chapter outlines two FE implementations where the train, track and soil are fully coupled. This allowed for higher accuracy modelling of the force input from train into soil in comparison to previously developed models. Firstly, both commercial packages are evaluated to ensure they are capable of modelling the physical problem. This is undertaken via testing of element performance absorbing boundary conditions (ABC's) performance. Lastly, methods to couple the vehicle and track efficiently using each commercial software package are discussed.

4.2 Element comparison

ABAQUS and LSDYNA have large element libraries. To investigate the ability of each to simulate 3D surface wave propagation, eight noded brick elements were tested. For each software package, elements with the full number of Gauss integration points and elements with a reduced number of

Gauss integration points were tested. Reduced integration is typically used to reduce computation time because each integral can be evaluated using fewer calculations. The disadvantage of using a reduced number of Gauss points is that it can result in a loss of accuracy.

To test the ability of both commercial software package libraries to simulate wave propagation two identical numerical models were developed using ABAQUS and LSDYNA. The model geometry was that of a cube with edges 8m in length, which were terminated using an absorbing boundary condition (for ABAQUS, an infinite element solution was used and for LSDYNA, perfectly matched layers were used). The domain was meshed using $0.1m^3$ cells and two lines of symmetry were used to reduce the total number of elements by 75%. A Gaussian pulse with centre frequency 20Hz was used to excite the centre node. For the ABAQUS tests the element types used were C3D8 (non-reduced) and C3D8R (reduced). For the LSDYNA tests the element types were ELFORM=3 (non-reduced) and ELFORM=1(reduced). To compare the performance of each element type, an analytical solution to the wave equation, using the Cagniard-de Hoop technique (De Hoop, 1960) was used as a reference (Berg, Nielsen, & Skovgaard, 1994).

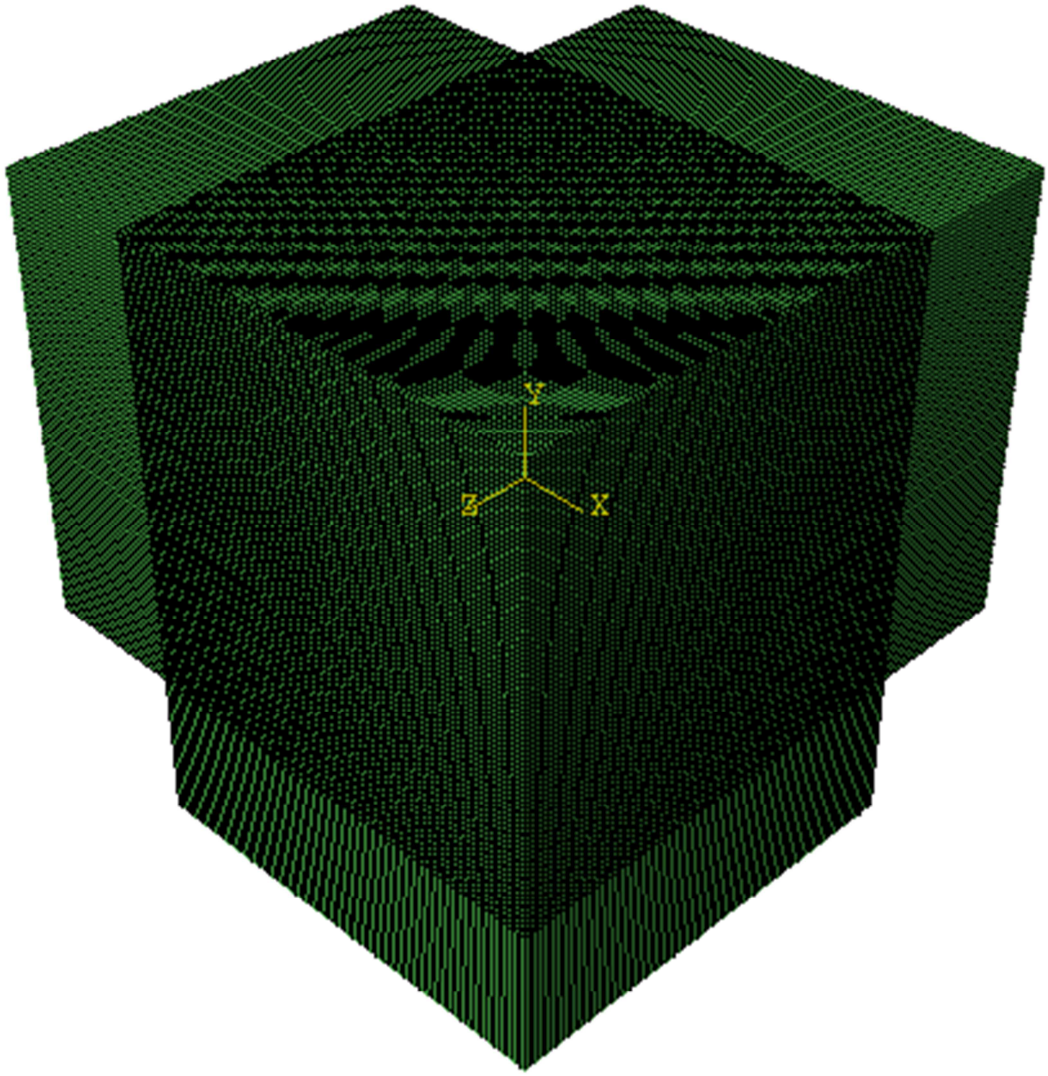

Figure 4.1 - Test domain for element comparison

Figure 4.1 shows a comparison between reduced and non-reduced elements for each commercial software package. Comparing each result to the analytical solution it can be seen that the use of reduced integration has introduced error into the solution. This is especially true for the LSDYNA reduced elements. Regarding the non-reduced elements, both ABAQUS and LSDYNA results are very similar to the analytical solution showing that they

provide high accuracy approximations to the wave propagation problem. Therefore it was concluded that the fully integrated element types were suitable for modelling ground-borne vibration whereas reduced integration elements are unsuitable.

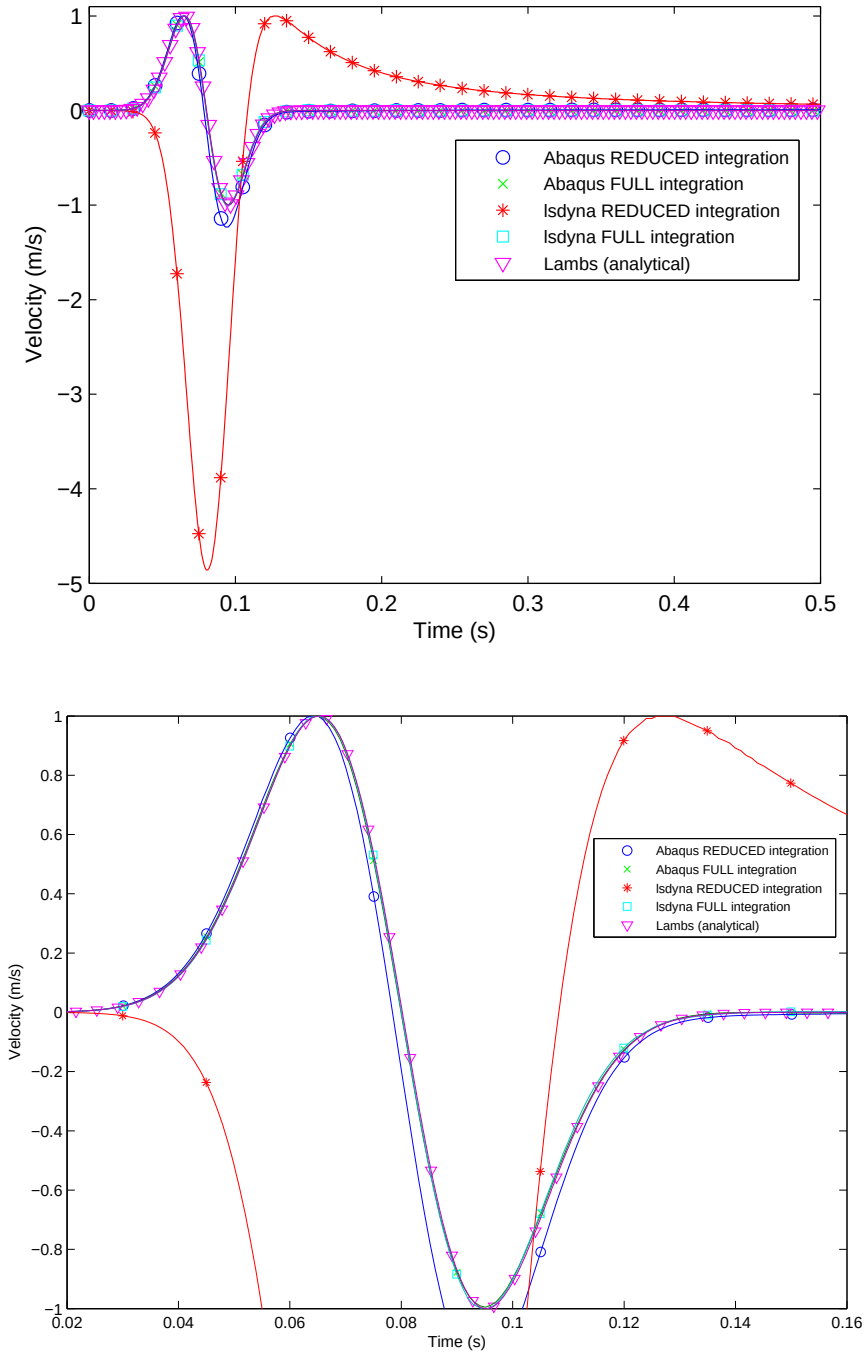

Figure 4.2 - Comparison between reduced integration and non-reduced integration elements for ABAQUS and LSDYNA (a) Top: all traces, (b) Bottom: all traces (zoomed)

4.3 Cell size comparison

The frequency spectrum associated with high speed rail vibrations is predominantly below 50Hz. Therefore it is important that the spatial step of the soil mesh is able to simulate waves propagating at frequencies below this value. Smaller element sizes are capable of resolving higher frequencies, however as element size decreases the total number of domain elements, and thus computational time increases exponentially. For a typical FE model developed as part of this research (domain size, 50x25x15m), the exponential relationship between cell size and total elements is shown in Figure 4.3. Note that it has been assumed that all cells are cubes (i.e. equal dimensions in all three directions).

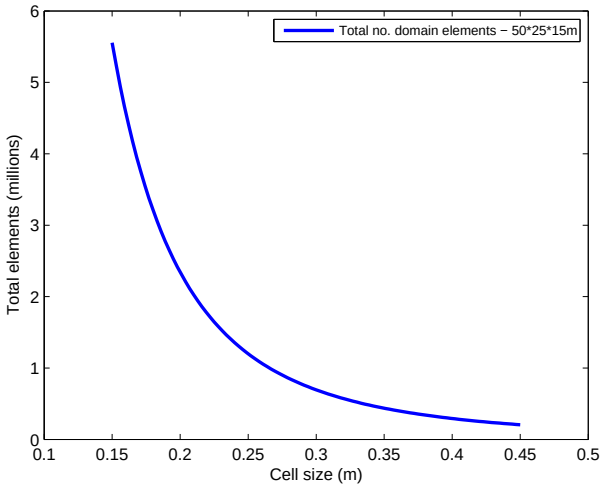

Figure 4.3 – Relationship between cell size and total elements

To test the ability of both ABAQUS and LSDYNA to resolve the aforementioned frequency spectrum, a 3D model was developed using some

typical soil material properties (Young's modulus = $8x10^7$, Poisson's ratio = 0.35, density = $2000kg/m^3$). The soil was a cube model with double symmetry and was excited at the centre using a Gaussian excitation with centre frequency 30Hz. The Gaussian pulse and subsequent frequency spectrum are shown in Figure 4.4. It can be seen that the majority of frequency content was below 50Hz with only a small percentage above this value. Therefore the excitation had a similar frequency range as that due to a high speed train.

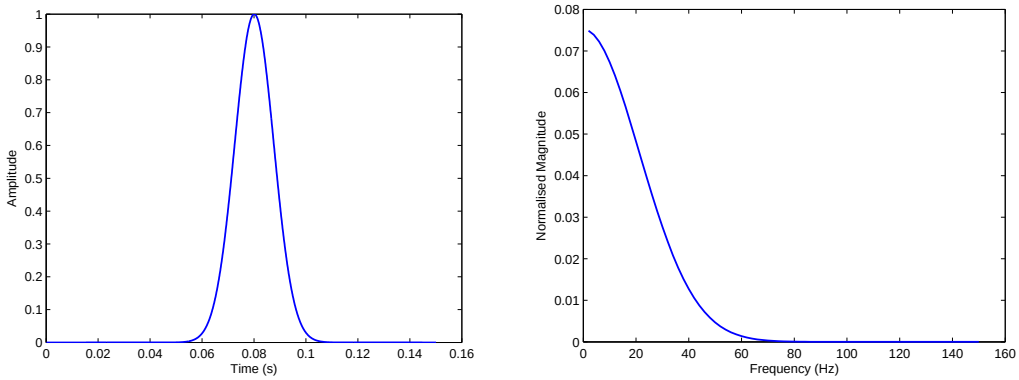

Figure 4.4 – (a) Left: Gaussian pulse time history, (b) Right: Gaussian pulse frequency spectrum

Figure 4.4 shows the resulting traces for three different mesh sizes, at a distance 1.2m from the excitation. All three sizes resolve the wave propagation reasonably well, although the 0.3m case has a performance benefit over the 0.4 case. Additionally, the 0.2m case does not offer significant benefit compared to the 0.2m case. Therefore, to minimise computational requirements, an element size of 0.3m was chosen.

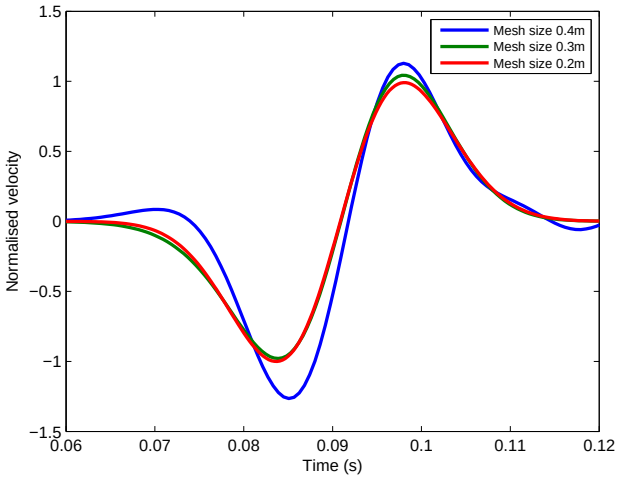

Figure 4.5 - Element size comparison

4.4 Absorbing boundary conditions

The FE method uses volume discretisation (meshing) to solve the partial differential equations associated with wave propagation. This discretised domain cannot extend to infinity due to computational constraints so must be truncated. A shortcoming of this truncation is that it acts to reflect waves back into the modelling space, thus contaminating the solution. One approach is to place this boundary at a great distance from the solution space, however this is inefficient and results in excessive computation requirements.

An alternative solution is to use an absorbing boundary condition (ABC). ABC's attempt to extrapolate from interior grid points to the boundary grid points in such a way as to mimic a condition where the mesh boundary is located at infinity. A vast body of research exists in this area and is covered in Chapter 5. The commercial FE codes used in this research have in-built

absorbing boundary conditions. To test their performance and applicability to ground borne vibration problems, each was tested.

4.4.1 Infinite elements (ABAQUS)

Infinite elements use decay functions to modify FE shape functions, thus simulating an infinity condition. Their development was first outlined by (Bettess & Zienkiewicz, 1977) and since then a variety of follow-up (Bettess, 1992) and alternative infinite element formulations have been proposed. The performance of a selection of these formulations was investigated by (Astley, 2000).

4.4.2 Maximising infinite element performance

Infinite element performance is high for one dimensional problems where plane waves impinge orthogonally at the model boundary. Therefore they offer very high absorption for 1D problems. For more complex problems, such as the case of 3D ground vibration modelling where the wavefield is a combination of surface and body waves, propagating at a range of frequencies, performance is lowered. One reason for this loss in performance is that the waves are not impinging orthogonally at the absorbing boundary thus causing higher levels of reflection.

In an attempt to improve absorption performance, rather than use a typical cuboid shaped domain, a half-spherical shaped domain was tested. It was proposed that a half-spherical shaped domain would more closely match

the spherical propagation characteristics of seismic waves (Figure 2.1). If the propagation and domain geometries were similar then a higher percentage of waves would impinge orthogonally at the boundary and therefore higher absorption rates would be achieved (Figure 4.6).

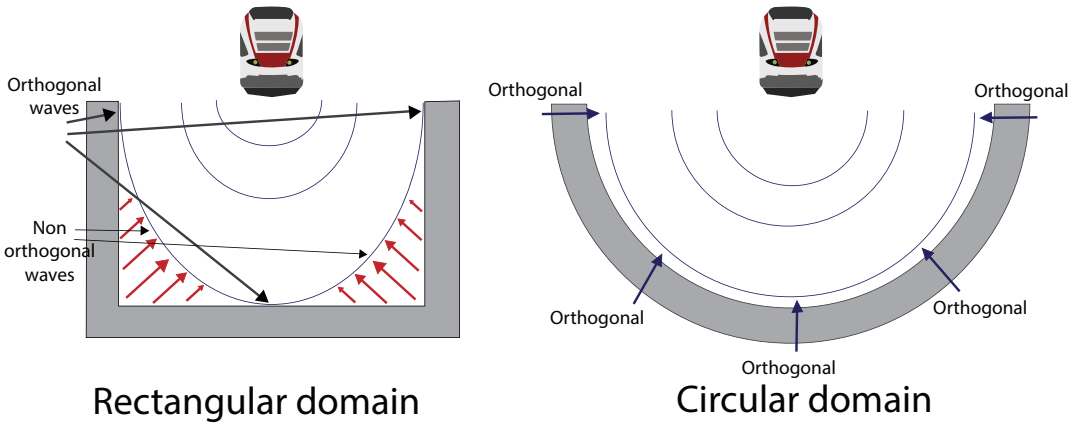

Figure 4.6 - Rectangular vs circular domains

To create a spherical domain bounded by infinite elements required the utilisation of both ABAQUS and MATLAB. First a spherical domain was created and meshed in ABAQUS. This mesh was created one element larger than the domain size required. The ABAQUS input file was then edited directly using a MATLAB script for the purpose of converting this additional layer of elements into infinite elements.

The MATLAB script first located the outermost layer of elements in the input file and changed their type to infinite elements. Then it identified the outermost model nodes and extrapolated the coordinate system to shift the nodes to a distance of 50% of the global model domain (Figure 4.7). This was

required to optimise infinite element performance (Hibbitt, Karlsson, & Sorensen, 2010). Lastly, the node numbering scheme was changed because infinite elements are numbered differently from finite elements.

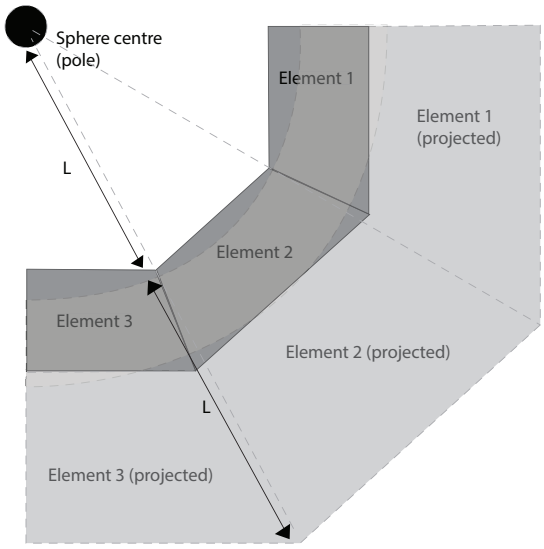

Figure 4.7 - Node projection procedure for infinite element creation in a circular domain

To compare the performance of the spherical domain against a rectangular domain, a rectangular model similar to Figure 4.1 was tested against 3D rectangular domain with the geometry of an eighth of a sphere. To maintain consistency, although both models had different dimensions, overall domain volume was constant between models. Figure 4.8 shows a comparison in performance between the two domains. Although reflections are visible at 0.3s for both models, the circular model was found to offer a slight increase in performance over the rectangular one. Therefore it can be concluded that

under circumstances where domain size is of key importance, a circular domain may prove beneficial.

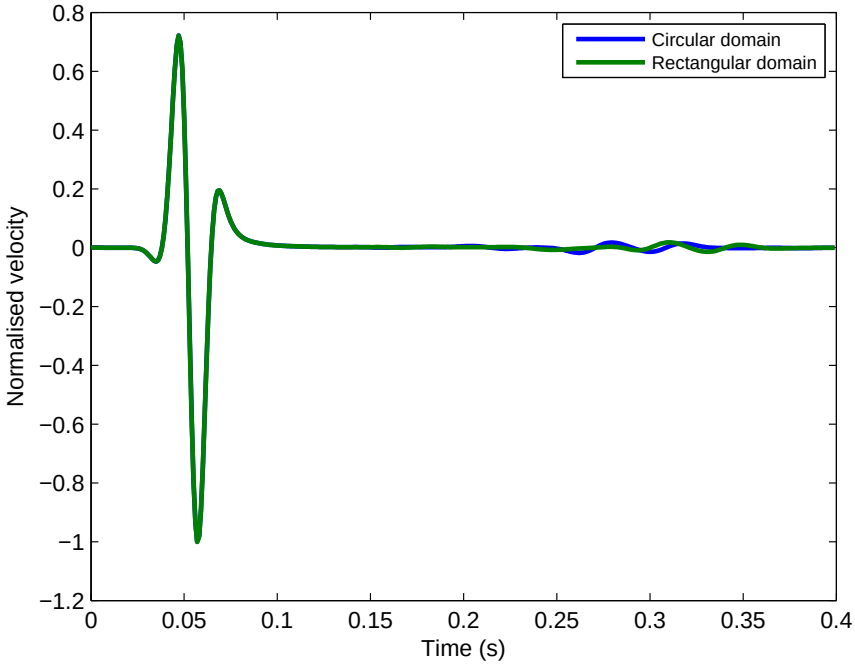

Figure 4.8 - Velocity trace histories for rectangular and circular domains

4.4.3 FE perfectly matched layer implementation (LSDYNA)

Perfectly matched layers (PML) is often considered the most efficient form of absorbing boundary for seismic applications such as finite difference time domain (FDTD). It was initially developed for FDTD modelling however has been recently adapted to FE modelling (Basu, 2009), (Basu, 2003). It works by stretching the coordinate system, within the PML region, in complex space. This serves to rapidly damp all waves, independent of their frequency within this zone. It is termed 'perfectly matched layers' because it consists of a series of layers, each with identical material properties to the modelling domain. The

only variation between layers is the value of the stretching function which is chosen to maximise attenuation.

PML has been implemented in LSDYNA using the formulation described by (Basu, 2009). This implementation requires the original FE equations to be written in the frequency domain. Then a stretching function is applied in the frequency domain before moving back to the time domain. The stretching function was chosen as:

$$s(x_i') = [1 + f_i^e(x_i')] + \frac{1}{i\omega}[f_i^p(x_i')\left(\frac{V_s}{L}\right)] \qquad \text{Equation 4.1}$$

Where L was the PML depth, *Vs* was the shear wave speed, ω was frequency and $i = \sqrt{-1}$. The attenuation functions f_i^e, f_i^p, were chosen to be equal to f_i:

$$f_i(x_i') = f_{0i}\left(\frac{x_i}{L_{Pi}}\right)^p \qquad \text{Equation 4.2}$$

The values of f_{0i} and p were chosen to be 9 and 1 respectively. These values were been shown to be optimal for the PML depth used for all simulations in this research (8-10 perfectly matched layers) (Basu, 2009).

The LSDYNA PML formulation was tested against ABAQUS's infinite element solution and the results are shown in Figure 4.9. For this example, tests were performed by exciting a cluster of nine nodes at the centre of a doubly symmetric domain with dimensions x=24m, y=24m, z=8m, using a 30Hz

Gaussian pulse. The domain was bounded by 10 layers of PML and the observation point was 1.5m from the model centre.

It was found that both models initially produced similar results and the initial arrivals were nearly identical. Despite this, after the first arrival it was clear that the infinite element solution did not absorb the outgoing waves as efficiently. This can be seen by the disturbances after approximately 0.15 seconds. Therefore it was concluded that the PML formulation was capable of higher absorption, which was similar to the findings presented in (Basu, 2009).

Despite this, when investigating an appropriate absorbing boundary condition, computational requirements must also be considered. The PML solution in LSDYNA consisted of 10 layers of elements surrounding the modelling domain whereas the infinite element solution in ABAQUS consists of a single layer. Therefore less calculations need to be performed for the infinite element approach.

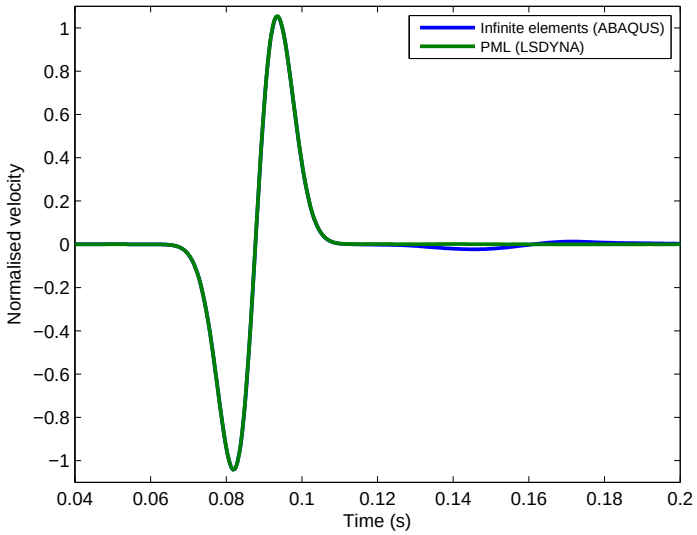

Figure 4.9 - Absorption performance - PML vs infinite elements

4.5 Moving excitation

ABAQUS moving loads are typically defined using the VDLOAD FORTRAN subroutine. This subroutine defines the distribution of non-uniform load magnitudes as a function of time and position, at a set of predefined nodal points. Despite this, it was not possible to directly implement a displacement defined load in this manner because VDLOAD prohibits access to the real time displacement values of the loading surface.

To overcome this, the VDLOAD subroutine was combined with additional codes to provide it with these displacement values. This facilitated coupling between the wheel and rail, an essential requirement for defining the non-Hertzian contact condition.

Once the rail displacement was obtained, the equations of motion for the cars, bogies and wheels were computed within the VDLOAD subroutine in a staggered manner with respect to the ABAQUS solver. The entire process is shown in Figure 4.10.

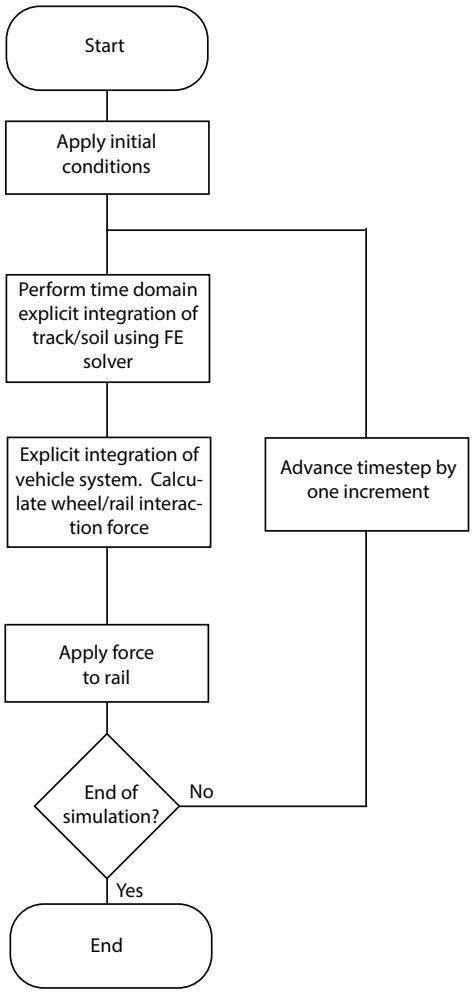

Figure 4.10 - FEM model execution process

Note the application of initial conditions during the first timestep. Initial conditions were applied to all vehicle components to simulate a realistic inter-coupled system from the start of the simulation. This meant that rather than the

car, bogie and wheel starting from stationary positions, they were already in motion, thus aiding to simulate the train 'fading' into the model.

To determine suitable initial conditions, the vehicle system was redeveloped in MATLAB and run for a long period of time to allow the multi-body response to become steady. The conditions at this moment of time were chosen as initial conditions for the final model. Realistic boundary conditions for the rail displacement were determined by subjecting the track/soil ABAQUS model to a moving point load and recording the rail response.

LSDYNA provided a more straightforward method for defining a multi-body moving load. Solution variables such as displacements, velocities and accelerations are directly accessible from the 'loadud' function within the native 'dyn21.f' file. Therefore the extraction of variables, explicit integration and application of the load were all undertaken in one step within the 'dyn21.f' file.

4.5.1 Moving point load vs. moving fully coupled load

The performance between a fully coupled multi-body excitation and a moving point load of 150 kN (typical train loading force) is compared in Figure 4.11. Both responses were similar in both timing and magnitude. Despite this, for the case of the point load, each bogie passage was more pronounced and the overall passage pattern was much clearer in comparison to the coupled case. For the coupled system it was clear that the there was a wider spectrum of frequencies being input to the system. The point load was able to simulate key

frequencies such as the bogie and axle passage frequencies, but was unable to account for the excitation caused by mechanisms such as the car bounce. Therefore it was concluded that the fully coupled excitation mechanism was capable of simulating the physical problem with greater accuracy in comparison to the point load.

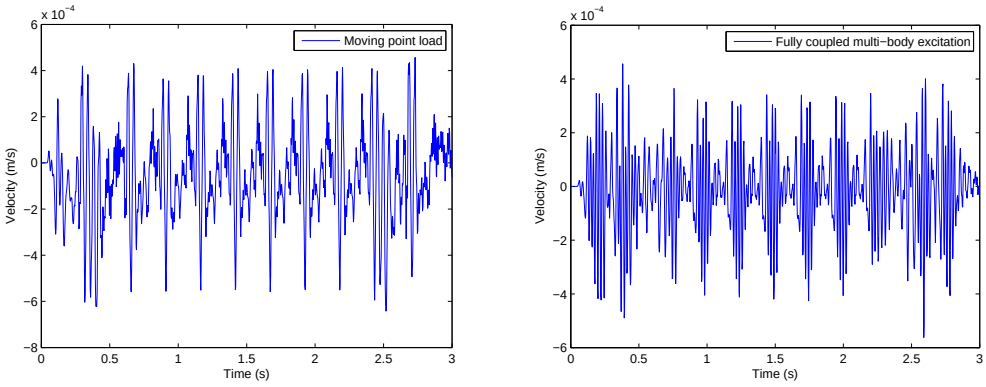

Figure 4.11 - Load type comparison. (a) Left: point load, (b) Right: multi-body load

4.6 Conclusions

The applicability of the general purpose commercial FE software codes ABAQUS and LSDYNA to model high speed railway vibrations was investigated. First the performance of various 3D element types was investigated and it was determined that for both packages the full complement of Gaussian integration points was required for accurate modelling of soil vibration.

Investigations were also undertaken to determine the maximum allowable cell size required to accurately model the frequency range of excitation from a high speed train line. This cell size was calculated to be 0.3m.

The performance of the native absorbing boundaries available in both ABAQUS and LSDYNA were compared. ABAQUS utilises an infinite element solution which was shown to be satisfactory for the required modelling domain. Additionally, infinite element performance was enhanced through the implementation of spherical domain geometry. LSDYNA offers a PML solution to the unbounded domain problem which was shown to have higher absorption performance than the infinite element solution available in ABAQUS, albeit with higher computational cost. Therefore it was concluded that the absorbing boundaries available in both packages were suitable for the current problem.

Lastly, the implementation of moving sources in each software package was discussed. LSDYNA offers for a more straightforward implementation of a multi-body excitation whereas ABAQUS requires the application of a multi-step process. The performance benefit achieved through using a multi-body excitation in comparison to a point load was also shown.

Chapter 5. Finite difference model development

5.1 Background

Finite difference time domain modelling (FDTD) is commonly used for solving wave propagation problems, particularly in the field of electrodynamics. It is also used in elastodynamics, where it is used as an efficient technique to enable the execution of full waveform seismic inversions (e.g. for oil/gas exploration). It is chosen for such applications because it uses a 'strong' formulation of the wave equation which makes computation more efficient than the FE method. When performing computationally expensive tasks such as large scale seismic modelling, execution speed becomes a major factor in the choice of the modelling tool.

FDTD modelling has been used by (Ketcham, Moran, Lacombe, Greenfield, & Anderson, 2005) to model moving excitations for the purpose of vehicle tracking applications. In a series of works, the seismic response of several types of multibody vehicles was modelled using finite difference techniques, both in the presence of a flat free surface and also topography. Although the approach was proven to accurately predict the presence of such vehicles, the wheels were uncoupled with the model surface. This is a major limitation of adapting this modelling approach directly to railway applications because it is vital that the train wheel is coupled to the track. If not then dynamic excitation is ignored.

The application of FDTD techniques to railway vibration modelling is relatively novel. Instead, a much greater number of FE related modelling approaches have been documented. Despite this, one of the few approaches was undertaken by (Katou, Matsuoka, Yoshioka, Sanada, & Miyoshi, 2008). In this study a 3D staggered grid FD method was used to simulate the passing of a Shinkansen train. Rather than couple the wheels to the rail, experimental work was undertaken to determine a realistic source function. To do so strain gauges were attached to the wheels of a Shinkansen locomotive and the time histories recorded. Therefore, rather than coupling a multi-body excitation source to the track, time histories were used directly as model input excitation. These excitation time histories were used to excite a track model derived from (Krylov, 2001), which was then used to excite the FDTD model.

A disadvantage of this approach was that the train, track and soil were essentially decoupled thus reducing accuracy. Furthermore, it is expensive and impractical to rely on experimental data obtained from the running wheels of a train as input data. Lastly, a shortcoming of the modelling approach was that a low performance absorbing boundary was used. This meant that a relatively large domain was modelled, resulting in a computational time of 11 days per 1.6 seconds of train passage.

Another alternative FDTD approach was outlined by (Thornely-Taylor, 2004) to investigate railway vibrations generated by underground railways. Once again a low performance absorbing boundary was used and rather than create a long section of track, a shorter model was connected end-to-end so that

when the train passed through one end of the model, it would start again at the other end. An advantage of this modelling approach in comparison to (Katou et al., 2008) was that the track was modelled explicitly and the moving excitation was coupled to the track. The model was thus fully coupled and capable of achieving higher accuracy.

The aim of this chapter is to investigate the suitability of the FDTD method for ground vibration modelling from high speed rail. This suitability is compared to the FE approach outlined in previous chapters. A key advantage of the FDTD method is that the absorbing boundary technology is more advanced and has higher performance than similar techniques available in the FE method. Therefore for the purpose of tailoring the applicability of the FDTD method to railways, a new high performance PML condition is also developed.

5.2 The applicability of FDTD to railway vibration modelling

When modelling ground-borne vibration propagation from high speed rail lines, there are three distinct modelling components: the vehicle, the track and the soil. The soil domain is much larger in volume in comparison to vehicle and track components meaning a high percentage of the overall calculation time is spent computing the soil response. Computational time becomes a limiting factor when the domain is large (e.g. for railway problems with unbounded domains) meaning it is important that the soil response can be calculated efficiently.

The FD method uses the 'strong' form of the wave equation and approximates the derivatives at a distinct set of grid points. In comparison, the FE method calculates the exact operators but approximates the solution basis functions and the problem is solved for the interior grid points. Because the FD method has less calculation points (e.g. no Gauss integration points) element calculations can be performed faster.

Additionally, FD methods rely on regular sized grids and thus can be broken up efficiently for parallel processing purposes. This means that a particular domain can be divided into a number equal to the number of processors and the overall computational burden shared between each core. Parallel processing can significantly reduce computational times. Although parallelisation is also possible using the FE method it is typically not as efficient or straightforward due to larger variance in cell size and cell types.

Lastly, FD methods typically offer higher performance absorbing boundary conditions in comparison to FE methods. This is because FD methods have traditionally been used for wave propagation and therefore there has been greater incentive to solve such boundary problems. Perfectly matched layers (PML) are currently considered the optimal solution as they offer high attenuation performance. This means that the boundary can be placed closer to the modelling domain without contamination, thus reducing overall domain size. A reduced domain size results in lower computational cost.

5.3 The equations of motion

Considering a two dimensional domain, the equations of motion ('strong form') used to describe wave propagation are in directions x (horizontal) and z (vertical) are:

$$\rho \frac{\partial^2 u_x}{\partial t^2} = \frac{\partial \sigma_{xx}}{\partial x} + \frac{\partial \sigma_{xz}}{\partial z} \qquad \text{Equation 5.1}$$

$$\rho \frac{\partial^2 u_z}{\partial t^2} = \frac{\partial \sigma_{xz}}{\partial x} + \frac{\partial \sigma_{zz}}{\partial z} \qquad \text{Equation 5.2}$$

$$\sigma_{xx} = (\lambda + 2\mu) \frac{\partial \upsilon_x}{\partial x} + \lambda \frac{\partial \upsilon_z}{\partial z} \qquad \text{Equation 5.3}$$

$$\sigma_{zz} = (\lambda + 2\mu) \frac{\partial \upsilon_z}{\partial z} + \lambda \frac{\partial \upsilon_x}{\partial x} \qquad \text{Equation 5.4}$$

$$\sigma_{xz} = \mu \left(\frac{\partial \upsilon_z}{\partial x} + \frac{\partial \upsilon_x}{\partial z} \right) \qquad \text{Equation 5.5}$$

Where υ_i represents displacement in the i direction ($i \in \{x,z\}$), and μ and λ are lames coefficients. σ_{ii} represents the stress components and ρ is density. To formulate these relationships into a set of first order differential equations, they were differentiated with respect to time and then the time differentiated displacements were substituted by the velocity components:

$$\frac{\partial v_x}{\partial t} = b \left(\frac{\partial \sigma_{xx}}{\partial x} + \frac{\partial \sigma_{xz}}{\partial z} \right) \qquad \text{Equation 5.6}$$

$$\frac{\partial v_z}{\partial t} = b\left(\frac{\partial \sigma_{xz}}{\partial x} + \frac{\partial \sigma_{zz}}{\partial z}\right) \qquad \text{Equation 5.7}$$

$$\frac{\partial \sigma_{xx}}{\partial t} = (\lambda + 2\mu)\frac{\partial v_x}{\partial x} + \lambda\frac{\partial v_z}{\partial z} \qquad \text{Equation 5.8}$$

$$\frac{\partial \sigma_{zz}}{\partial t} = (\lambda + 2\mu)\frac{\partial v_z}{\partial z} + \lambda\frac{\partial v_x}{\partial x} \qquad \text{Equation 5.9}$$

$$\frac{\partial \sigma_{xz}}{\partial t} = \mu\left(\frac{\partial v_z}{\partial x} + \frac{\partial v_x}{\partial z}\right) \qquad \text{Equation 5.10}$$

Where v is velocity and b is buoyancy, the inverse of density. Then using a standard staggered grid (SSG) finite difference technique (Figure 5.1 - (Virieux, 1986) and (Graves, 1996)), the equations of motion were approximated. Using a Taylor expansion and assuming a homogenous material, the equations were written in a discrete form as:

$$v_{x_{i+\frac{1}{2},j}}^{k+1/2} = v_{x_{i+\frac{1}{2},j}}^{k-1/2} + b\frac{\Delta t}{\Delta x}\left(\sigma_{xx_{i+1/2,j}}^{k} - \sigma_{xx_{i-1/2,j}}^{k}\right) + b\frac{\Delta t}{\Delta z}\left(\sigma_{xx_{i,j+1/2}}^{k} - \sigma_{xz_{i,j-1/2}}^{k}\right) \qquad \text{Equation 5.11}$$

$$v_{z_{i+\frac{1}{2},j+1/2}}^{k+1/2} = v_{z_{i+\frac{1}{2},j+1/2}}^{k-1/2} + b\frac{\Delta t}{\Delta x}\left(\sigma_{xx_{i+1,j+1/2}}^{k} - \sigma_{xx_{i,j+1/2}}^{k}\right) + b\frac{\Delta t}{\Delta z}\left(\sigma_{xx_{i+1/2,j+1}}^{k} - \sigma_{xz_{i+1/2,j}}^{k}\right) \qquad \text{Equation 5.12}$$

$$\sigma_{xx}^{k+1}{}_{i+\frac{1}{2},j} = \sigma_{xx}^{k}{}_{i+\frac{1}{2},j} + (\lambda + 2\mu)\frac{\Delta t}{\Delta x}\left(\nu_{x_{i+1,j}}^{k+1/2} - \nu_{x_{i,j}}^{k+1/2}\right) + \lambda\frac{\Delta t}{\Delta z}\left(\nu_{z_{i,j+1}}^{k+1/2} - \nu_{z_{i,j}}^{k+1/2}\right) \quad \text{Equation 5.13}$$

$$\sigma_{zz}^{k+1}{}_{i+\frac{1}{2},j} = \sigma_{zz}^{k}{}_{i+\frac{1}{2},j} + (\lambda + 2\mu)\frac{\Delta t}{\Delta x}\left(\nu_{x_{i,j+1}}^{k+1/2} - \nu_{x_{i,j}}^{k+1/2}\right) + \lambda\frac{\Delta t}{\Delta z}\left(\nu_{z_{i+1,j}}^{k+1/2} - \nu_{z_{i,j}}^{k+1/2}\right) \quad \text{Equation 5.14}$$

$$\sigma_{xz_{i,j+1/2}}^{k+1} = \sigma_{xz_{i,j+1/2}}^{k} + \mu\frac{\Delta t}{\Delta x}\left(\nu_{x_{i,j+1}}^{k+1/2} - \nu_{x_{i,j}}^{k+1/2}\right) + \mu\frac{\Delta t}{\Delta z}\left(\nu_{z_{i+1,j}}^{k+1/2} - \nu_{z_{i,j}}^{k+1/2}\right) \quad \text{Equation 5.15}$$

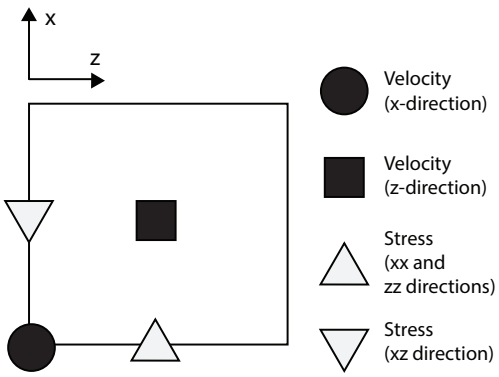

Figure 5.1 – Standard staggered grid stencil

Where i and j were equivalent to the x and z coordinate axes respectively.

5.4 Numerical stability

To maintain numerical stability it was imperative that Equation 5.16 was met, where V_p is the minimum compressional wave velocity across the whole grid.

$$V_p \Delta t \sqrt{\frac{1}{\Delta x^2} + \frac{1}{\Delta z^2}} < 1 \qquad \text{Equation 5.16}$$

5.5 Material interfaces and free surface

Free surface boundary conditions were chosen carefully to ensure model stability. This is important in FDTD modelling because when averaging velocity or stress components across an air/earth interface, numerical dispersion can occur. In FDTD modelling, there are a wide range of techniques used to model a free surface boundary condition (Lan & Zhang, 2011), however the two most commonly used types are the 'vacuum' formulation and the 'zero-stress' formulation. For this work the vacuum formulation was used because it provided a more straightforward implementation of surface topography.

5.5.1 Vacuum formulation

The vacuum formulation was achieved by setting all velocities, Lame's parameters and density close to zero above the free surface. This approach was

attractive because it could be used to model topography and the original finite difference equations remained unchanged. The disadvantage of the vacuum formulation was that only second order FD schemes could be used due to the discontinuity across the air/earth interface. If higher order operators were used then instabilities were introduced due to the presence of a low density zone.

5.5.2 Material averaging

To smooth contrasting material interfaces such as a free surface condition or soil layering, parameter averaging was required. For this purpose, arithmetic averaging was used to calculate profiles for density and Lame's first parameter, however for the shear modulus, harmonic averaging was used ((Graves, 1996), (Bohlen & Saenger, 2006)):

$$\rho_{z(i+\frac{1}{2},j)} = \frac{\rho_{(i,j)} + \rho_{(i+1,j)}}{2} \qquad \text{Equation 5.17}$$

$$\rho_{z(i,j+\frac{1}{2})} = \frac{\rho_{(i,j)} + \rho_{(i,j+1)}}{2} \qquad \text{Equation 5.18}$$

$$\lambda_{(i+\frac{1}{2},j+\frac{1}{2})} = \frac{\lambda_{(i,j)+}\,\lambda_{(i+1,j)+}\,\lambda_{(i+1,j+1)+}\,\lambda_{(i,j+1)}}{4} \qquad \text{Equation 5.19}$$

$$\mu_{(i+\frac{1}{2},j+\frac{1}{2})} = \frac{4}{\mu^{-1}{}_{(i,j)}\,\mu^{-1}{}_{(i+1,j)+}\,\mu^{-1}{}_{(i+1,j+1)+}\,\mu^{-1}{}_{(i,j+1)}} \qquad \text{Equation 5.20}$$

5.6 Absorbing boundary conditions

Maximising absorbing boundary performance can lead to reduced domain sizes and increased computational efficiency. As computational efficiency is one of the key factors for choosing FDTD techniques to model high speed rail ground vibrations, it was important that absorbing boundary performance was optimised.

Early FDTD absorbing boundaries included 'one way wave equations' (Higdon, 1986) and 'damping zone' (Cerjan, Kosloff, Kosloff, & Resheq, 1985) approaches. Although these techniques generally perform well for waves arriving perpendicular to the boundary (e.g. 1D domains), their performance is reduced for waves impinging at low angles of incidence.

(Berenger, 1994) introduced a 'Perfectly matched layer' (PML) technique to absorb electromagnetic waves based upon a series of finite layers, each with identical material properties, that gradually damped outgoing waves. This gradual damping was implemented through a stretching of the spatial coordinates inside the PML region. It offered high performance and was capable of absorbing waves independent of arrival angle. (Chew & Weedon, 1994) quickly extended the PML to include a stretching of both real and imaginary spatial co-ordinates thus offering the potential for additional absorption.

Using a similar implementation to electromagnetics, (Chew & Lui, 1996) adapted the PML condition to offer absorption for seismic waves. Despite this, spurious reflections were encountered for evanescent and low frequency waves. These shortcomings were addressed through the implementation of frequency

dependant damping applied using the complex frequency shifted PML (C-PML). C-PML techniques have been developed for elastic (Martin, Komatitsch, & Ezziani, 2008), poroelastic (Martin et al., 2008) and anisotropic media (Becache, Ezziani, & Joly, 2003).

Early PML formulations (Collino & Tsogka, 2001) were implemented using an artificial splitting of velocity and stress fields. This splitting procedure made PML implementation in traditional FDTD codes challenging because two different sets of equations are required for each PML and non-PML region (i.e. one for stresses and one for velocities). In addition, such implementations were not 'well-posed' (Abarbanel & Gottlieb, 1997).

To avoid field splitting, convolution terms (Komatitsch & Martin, 2007), auxillary differential equations and integral terms (F. Drossaert & Giannopoulos, 2006) have been proposed. As convolution is generally regarded as computationally inefficient, recent focus has shifted to auxillary differential equation (ADE) and integral term implementations.

(Martin, Komatitsch, Gedney, & Bruthiaux, 2010) outlined a non-convolutional ADE PML approach where a fourth-order Runge-Kutta scheme was used in conjunction with eighth order Holberg space discretization. This formulation was shown to have increased accuracy over the traditional ADE-PML implementation and to be stable for up to 100,00 timesteps. Additionally the authors investigated the potential to extend this ADE-PML condition to higher order PML's but concluded that no significant performance benefit was capable.

(W. Zhang & Shen, 2010) built on the work of (Martin et al., 2010) and outlined a similar ADE-PML fourth-order Runge-Kutta scheme that resulted in a complete set of first order differential equations. This meant that the same FDTD implementation could be used to solve both the ADE C-PML equations and the interior domain equations.

An alternative approach was outlined by (F. Drossaert & Giannopoulos, 2006) through the use of a recursive integration technique (RIPML). This technique used an extended trapezoidal rule to integrate the time derivatives thus negating the requirement to split the fields or use an ADE formulation. The RIPML required an equal amount of computational memory in comparison to split formulations and slightly less memory than an ADE implementation.

Meanwhile, (Correia & Jin, 2005) and (Giannopoulos, 2011) proposed a higher order PML implementation for Maxwell's equations. The additional degrees of freedom proved to offer superior absorption in comparison to traditional first order PML methods. This was in contrast to (Martin et al., 2010) who concluded that higher order PML's offered no significant benefit for elastic waves. Therefore for the purpose of maximising absorption, a new PML condition for the seismic wave equation was developed based upon the higher order PML implementation for electrodynamics. An additional aim was to offer this higher performance using a more straightforward implementation.

5.6.1 Implementing PML through a correction technique

Perfectly matched layers attenuate wave energy by simultaneously stretching the coordinate system and by applying a decay function. To achieve this attenuation the original equations of motion (Equation 5.6 - Equation 5.10) were multiplied by a stretching function ($1/s_x$). Then after translating the new equations into the frequency domain, the two-dimensional frequency domain elastodynamic velocity-stress equations took the form:

$$i\omega\tilde{v}_x = b\left(\frac{1}{s_x}\frac{\partial\tilde{\sigma}_{xx}}{\partial x} + \frac{1}{s_z}\frac{\partial\tilde{\sigma}_{xz}}{\partial z}\right) \qquad \text{Equation 5.21}$$

$$i\omega\tilde{v}_z = b\left(\frac{1}{s_x}\frac{\partial\tilde{\sigma}_{xz}}{\partial x} + \frac{1}{s_z}\frac{\partial\tilde{\sigma}_{zz}}{\partial z}\right) \qquad \text{Equation 5.22}$$

$$i\omega\tilde{\sigma}_{xx} = (\lambda + 2\mu)\frac{1}{s_x}\frac{\partial\tilde{v}_x}{\partial x} + \lambda\frac{1}{s_z}\frac{\partial\tilde{v}_z}{\partial z} \qquad \text{Equation 5.23}$$

$$i\omega\tilde{\sigma}_{zz} = (\lambda + 2\mu)\frac{1}{s_z}\frac{\partial\tilde{v}_z}{\partial z} + \lambda\frac{1}{s_x}\frac{\partial\tilde{v}_x}{\partial x} \qquad \text{Equation 5.24}$$

$$i\omega\tilde{\sigma}_{xz} = \mu\left(\frac{1}{s_x}\frac{\partial\tilde{v}_z}{\partial x} + \frac{1}{s_z}\frac{\partial\tilde{v}_x}{\partial z}\right) \qquad \text{Equation 5.25}$$

Where the frequency domain velocity components were denoted by $\tilde{v}$ and the frequency domain stress components by $\tilde{\sigma}$. λ and μ were the lames coefficients and b was buoyancy.

s_x and s_z were the PML stretching functions (in x and z directions respectively), which served to stretch the domain coordinates to aid absorption:

$$s_{u_i} = \kappa_{u_i} + \frac{d_{u_i}}{\alpha_{u_i} + j\omega} \qquad \text{Equation 5.26}$$

κ_{u_i}, d_{u_i}, and α_{u_i} were attenuation coefficients used to describe the loss within the PML region ($u, \in \{u, v\}$ and $i \in \{x, z\}$). Additionally, the variable transform ψ_u was defined:

$$\psi_u = \frac{1 - s_u}{s_u} = \frac{1}{s_u}\left(\frac{1 - s_u}{1}\right) = \frac{1}{s_u} - 1 \qquad \text{Equation 5.27}$$

Or

$$\frac{1}{s_u} = (1 + \psi_u) \qquad \text{Equation 5.28}$$

Rearranging equations Equation 5.21 - Equation 5.25 in terms of ψ_u gave

$$i\omega\tilde{v}_x = b\left((1 + \psi_x)\frac{\partial\tilde{\sigma}_{xx}}{\partial x} - (1 + \psi_z)\frac{\partial\tilde{\sigma}_{xz}}{\partial z}\right) \qquad \text{Equation 5.29}$$

$$i\omega\tilde{v}_z = b\left((1 + \psi_x)\frac{\partial\tilde{\sigma}_{xz}}{\partial x} - (1 + \psi_z)\frac{\partial\tilde{\sigma}_{zz}}{\partial z}\right) \qquad \text{Equation 5.30}$$

$$i\omega\tilde{\sigma}_{xx} = (\lambda + 2\mu)(1 + \psi_x)\frac{\partial\tilde{v}_x}{\partial x} - \lambda(1 + \psi_z)\frac{\partial\tilde{v}_z}{\partial z} \qquad \text{Equation 5.31}$$

$$i\omega\tilde{\sigma}_{zz} = (\lambda + 2\mu)(1 + \psi_z)\frac{\partial\tilde{v}_z}{\partial z} - \lambda(1 + \psi_x)\frac{\partial\tilde{v}_x}{\partial x} \qquad \text{Equation 5.32}$$

$$i\omega\tilde{\sigma}_{xz} = \mu\left((1 + \psi_x)\frac{\partial\tilde{v}_z}{\partial x} - (1 + \psi_z)\frac{\partial\tilde{v}_x}{\partial z}\right) \qquad \text{Equation 5.33}$$

Examination revealed that the stretched velocity/stress equations were analogous to an addition of field dependant variables $\tilde{J}$ and $\tilde{M}$ to the original

unstretched components. Therefore Equation 5.29 - Equation 5.33 were rearranged and rewritten with the addition of the field dependant variables.

$$i\omega\tilde{v}_x = b\left(\frac{\partial\tilde{\sigma}_{xx}}{\partial x} + \frac{\partial\tilde{\sigma}_{xz}}{\partial z}\right) + b(\tilde{J}_{xx} + \tilde{J}_{xz}) \qquad \text{Equation 5.34}$$

$$i\omega\tilde{v}_z = \tilde{b}\left(\frac{\partial\tilde{\sigma}_{xz}}{\partial x} + \frac{\partial\tilde{\sigma}_{zz}}{\partial z}\right) + b(\tilde{J}_{xz} + \tilde{J}_{zz}) \qquad \text{Equation 5.35}$$

$$i\omega\tilde{\sigma}_{xx} = (\lambda + 2\mu)\frac{\partial\tilde{v}_x}{\partial x} + \lambda\frac{\partial\tilde{v}_z}{\partial z} + \left((\lambda + 2\mu)\widetilde{M}_{xx} + \lambda\widetilde{M}_{xz}\right) \qquad \text{Equation 5.36}$$

$$i\omega\tilde{\sigma}_{zz} = (\lambda + 2\mu)\frac{\partial\tilde{v}_z}{\partial z} + \lambda\frac{\partial\tilde{v}_x}{\partial x} + \left((\lambda + 2\mu)\widetilde{M}_{zz} + \lambda\widetilde{M}_{zx}\right) \qquad \text{Equation 5.37}$$

$$i\omega\tilde{\sigma}_{xz} = \mu\left(\frac{\partial\tilde{v}_z}{\partial x} + \frac{\partial\tilde{v}_x}{\partial z}\right) + \mu\left(\widetilde{M}_{zx} + \widetilde{M}_{xz}\right) \qquad \text{Equation 5.38}$$

Where $\tilde{J}$ and $\widetilde{M}$ were given by

$$\tilde{J}_{xu} = \psi_u\frac{\partial\tilde{\sigma}_{xu}}{\partial u} \qquad \text{Equation 5.39}$$

$$\widetilde{M}_{xu} = \psi_u\frac{\partial\tilde{v}_v}{\partial u} \qquad \text{Equation 5.40}$$

with $u,\ v \in \{x, z\}$ and $u \neq v$.

Velocity and stress values of the stretched coordinates in the PML region (i.e. where $\psi_u \neq 0$) could therefore be calculated through an addition of $\tilde{J}$ and $\widetilde{M}$ to previously calculated values. This meant that the PML could be implemented in existing scripts without revision of the original code.

5.6.2 Development of a higher order PML

A new PML formulation based on N[th] order stretching was then developed. It was anticipated that higher order stretching would provide additional degrees of freedom that could facilitate higher absorption performance. Using the 'correction PML' implementation, the higher order PML was developed and implemented in a more straightforward manner.

5.6.2.1 Stretching function definitions

For brevity, only the derivation of J_{xz} is outlined. All other J_{uu} and M_{uu} can be found analogously. Firstly, combining Equation 5.27 and Equation 5.39 lead to:

$$\tilde{J}_{xz} = \left(\frac{1}{s_u} - 1\right)\frac{\partial \tilde{\sigma}_{xu}}{\partial u} \qquad \text{Equation 5.41}$$

Then, assuing *u=z*, and rearranging resulted in:

$$\frac{\partial \tilde{\sigma}_{xz}}{\partial z} = s_z\left(\tilde{J}_{xz} + \frac{\partial \tilde{\sigma}_{xz}}{\partial z}\right) \qquad \text{Equation 5.42}$$

Additionally, for Nth order stretching the overall stretching function was defined as:

$$s_u = \prod_{i=1}^{N} s_{u_i} \qquad \text{Equation 5.43}$$

Meaning that the overall stretching function was the product of all other stretching functions from 1 to N. When combined with Equation 5.42, this yielded:

$$\frac{\partial \tilde{\sigma}_{xz}}{\partial z} = \left(\prod_{i=1}^{N} s_{z_i}\right)\left(\tilde{J}_{xz} + \frac{\partial \tilde{\sigma}_{xz}}{\partial z}\right) \qquad \text{Equation 5.44}$$

This overall stretching function was described using different stretching functions for three different sets of *N* (and different sets of *i*). To facilitate this a function Ψ_{xz_i} was defined for $i \in [1, N-1]$:

$$\Psi_{xz_i} = \left(\prod_{m=i+1}^{N} s_{z_m}\right)\left(\tilde{J}_{xz} + \frac{\partial \tilde{\sigma}_{xz}}{\partial z}\right) \qquad \text{Equation 5.45}$$

Using equations Equation 5.44 and Equation 5.45 to eliminate $\tilde{J}_{xz}$, lead to:

$$\frac{\partial \tilde{\sigma}_{xz}}{\partial z} / \Psi_{xz_i} = s_{z_i} \qquad \text{Equation 5.46}$$

For *i=1* (i.e. the first order stretching function) this was equivalent to:

$$\Psi_{xz_1} = \frac{1}{s_{z_1}} \frac{\partial \tilde{\sigma}_{xz}}{\partial z} \qquad \text{Equation 5.47}$$

Then combining Equation 5.42 and Equation 5.47, resulted in the stretching functions for $i \in [2, N-1]$:

$$\Psi_{xz_i} = \frac{1}{s_{z_i}} \Psi_{i-1} \qquad \text{Equation 5.48}$$

and finally, combining Equation 5.42 and Equation 5.48 resulted in the stretching function for *i=N*:

$$\left(\tilde{J}_{xz} + \frac{\partial \tilde{\sigma}_{xz}}{\partial z}\right) = \frac{1}{s_{z_N}} \Psi_{xz_{N-1}} \qquad \text{Equation 5.49}$$

5.6.2.2 Domain transformation

The stretching functions (Equation 5.47, Equation 5.48 and Equation 5.49) had previously been defined in the frequency domain. To implement them within a time domain finite difference model they had to also be formulated in the time domain.

To facilitate this tranformation, firstly the stretching function s_{y_1} (Equation 5.26) was substituted into Equation 5.47 giving:

$$\kappa_{z_1} \Psi_{xz_1} + \frac{d_{z_1}}{\alpha_{z_1} + i\omega} \Psi_{xz_1} = \frac{\partial \tilde{\sigma}_{xz}}{\partial z} \qquad \text{Equation 5.50}$$

With the intention of solving for $\Psi_1$in the time domain, both sides were then multiplied by $(\alpha_{z_1} + i\omega)$

$$(\alpha_{z_1}\kappa_{z_1} + d_{z_1})\Psi_{xz_1} + i\omega\kappa_{z_1}\Psi_{xz_1} = \alpha_{z_1}\frac{\partial \tilde{\sigma}_{xz}}{\partial z} + i\omega\frac{\partial \tilde{\sigma}_{xz}}{\partial z} \qquad \text{Equation 5.51}$$

To prime Equation 5.51 for transformation it was rearranged and similar terms were grouped together,

$$\Psi_{xz_1} = \frac{1}{\kappa_{z_1}}\frac{\partial \tilde{\sigma}_{xz}}{\partial z} + \frac{1}{i\omega}\left[\frac{\alpha_{z_1}}{\kappa_{z_1}}\frac{\partial \tilde{\sigma}_{xz}}{\partial z} - \frac{(\alpha_{z_1}\kappa_{z_1} + d_{z_1})}{\kappa_{z_1}}\Psi_{xz_1}\right] \quad \text{Equation 5.52}$$

The relationship $\frac{1}{i\omega}\tilde{A}(w) = \int_0^t A(t)\delta t$ was then be used to make the transform trivial. Finally, the stretching function could be expressed as the time domain formulation:

$$\Psi_{xz_1} = \frac{1}{\kappa_{z_1}}\frac{\partial \sigma_{xz}}{\partial z} + \int_0^t \frac{\alpha_{z_1}}{\kappa_{z_1}}\frac{\partial \sigma_{xz}}{\partial z} - \frac{(\alpha_{z_1}\kappa_{z_1} + d_{z_1})}{\kappa_{z_1}}\Psi_{xz_1}\ \delta t \quad \text{Equation 5.53}$$

5.6.2.3 Application of the extended trapezoidal rule

The time domain integral term in Equation 5.53 was solved using the extended trapezoidal rule. Although alternative integration techniques may have been more accurate, for PML applications they have been found to require additional memory and are thus undesirable (F. H. Drossaert & Giannopoulos, 2007).

Using the traditional velocity-stress FDTD grid that was staggered in both space and time as described earlier, the application of the extended trapezoidal rule resulted in:

$$\Psi_{xz_1}^{n+\frac{1}{2}} = \frac{1}{\kappa_{z_1}} \frac{\partial \sigma_{xz}^{n+\frac{1}{2}}}{\partial z} +$$

$$\sum_{p=0}^{n-1} \left[\frac{\alpha_{z_1} \Delta t}{\kappa_{z_1}} \frac{\partial \sigma_{xz}^{p+\frac{1}{2}}}{\partial z} - \frac{\left(\alpha_{z_1} \kappa_{z_1} + d_{z_1}\right) \Delta t}{\kappa_{z_1}} \Psi_{xz_1}^{p+\frac{1}{2}} \right] \quad \text{Equation 5.54}$$

$$+ \frac{\Delta t}{2} \frac{\alpha_{z_1}}{\kappa_{z_1}} \frac{\partial \sigma_{xz}^{n+1/2}}{\partial z}$$

$$- \frac{\Delta t}{2} \frac{(\alpha_{z_1} \kappa_{z_1} + d_{z_1})}{\kappa_{z_1}} \Psi_{xz_1}^{n+1/2}$$

rearranging yielded:

$$\left(1 + \frac{\Delta t}{2} \frac{(\alpha_{z_1} \kappa_{z_1} + d_{z_1})}{\kappa_{z_1}}\right) \Psi_{xz_1}^{n+1/2}$$

$$= \left(\frac{1}{\kappa_{z_1}} + \frac{\Delta t}{2} \frac{\alpha_{z_1}}{\kappa_{z_1}}\right) \frac{\partial \sigma_{xz}^{n+1/2}}{\partial z}$$

$$+ \sum_{p=0}^{n-1} [\frac{\alpha_{u_1} \Delta t}{\kappa_{u_1}} \frac{\partial \sigma_{xz}^{p+1/2}}{\partial z} \quad \text{Equation 5.55}$$

$$- \frac{(\alpha_{z_1} \kappa_{z_1} + d_{z_1}) \Delta t}{\kappa_{z_1}} \Psi_{xz_1}^{p+1/2}]$$

Which was then solved for $\Psi_{xz_1}^{n+1/2}$

$$\Psi_{xz_1}^{n+1/2} = \frac{2+\Delta t\alpha_{z_1}}{2\kappa_{z_1}+\Delta t(\alpha_{z_1}\kappa_{z_1}+d_{z_1})}\frac{\partial\sigma_{xz}^{n+1/2}}{\partial z} + \frac{2\kappa_{z_1}}{2\kappa_{z_1}+\Delta t(\alpha_{z_1}\kappa_{z_1}+d_{z_1})}\sum_{p=0}^{n-1}\left[\frac{\alpha_{z_1}\Delta t}{\kappa_{z_1}}\frac{\partial\sigma_{xz}^{p+1/2}}{\partial z} - \frac{(\alpha_{z_1}\kappa_{z_1}+d_{z_1})\Delta t}{\kappa_{z_1}}\Psi_{xz_1}^{p+1/2}\right] \quad \text{Equation 5.56}$$

Thus allowing $\Psi_{xz_1}^{n+1/2}$ to be obtained

$$\Psi_{xz_1}^{n+1/2} = \frac{2+\Delta t\alpha_{z_1}}{2\kappa_{z_1}+\Delta t(\alpha_{z_1}\kappa_{z_1}+d_{z_1})}\frac{\partial\sigma_{xz}^{n+1/2}}{\partial z} + \frac{2\kappa_{z_1}}{2\kappa_{z_1}+\Delta t(\alpha_{z_1}\kappa_{z_1}+d_{z_1})}\Phi_{xz_1}^{n-1/2} \quad \text{Equation 5.57}$$

The value of the previous time integral was held by the summation memory variable Φ_{xz_1}.

$$\Phi_{xz_1} = \sum_{p=0}^{n-1}\left[\frac{\alpha_{z_1}\Delta t}{\kappa_{z_1}}\frac{\partial\sigma_{xz}^{p+1/2}}{\partial z} - \frac{(\alpha_{z_1}\kappa_{z_1}+d_{z_1})\Delta t}{\kappa_{z_1}}\Psi_{xz_1}^{p+1/2}\right] \quad \text{Equation 5.58}$$

Φ_{xz_1} was updated after the correction procedure of the FDTD field variables, but at the same time instance and within the same computational loop. This was written as:

$$\Phi_{xz_1}^{n+1/2} = \Phi_{xz_1}^{n-1/2} + \frac{\alpha_{z_1}\Delta t}{\kappa_{z_1}}\frac{\partial \sigma_{xz}^{n+1/2}}{\partial z} - \frac{\Delta t(\alpha_{z_1}\kappa_{z_1} + d_{z_1})}{\kappa_{z_1}}\Psi_{xz_1}^{n+1/2} \quad \text{Equation 5.59}$$

The undesirable $\Psi_{xz_1}^{n+1/2}$ term was eliminated from the update of $\Phi_{xz_1}^{n+1/2}$ through substitution of Equation 5.57 into Equation 5.59, resulting in:

$$\Phi_{xz_1}^{n+1/2} = \frac{2\kappa_{z_1} - \Delta t(\alpha_{z_1}\kappa_{z_1} + d_{z_1})}{2\kappa_{z_1} + \Delta t(\alpha_{z_1}\kappa_{z_1} + d_{z_1})}\Phi_{xz_1}^{n-1/2} - \frac{2d_{z_1}\Delta t}{(2\kappa_{z_1} + \Delta t(\alpha_{z_1}\kappa_{z_1} + d_{z_1}))\kappa_{z_1}}\frac{\partial \sigma_{xz}^{n+1/2}}{\partial z} \quad \text{Equation 5.60}$$

Upon inspection of Equation 5.60, it was seen than for $i \in [2, N-1]$ (i.e. for all three stretching functions Equation 5.47, Equation 5.48 and Equation 5.49), Ψ_{xz_i} could be calculated in an analogous manner to Ψ_{xz_1} resulting in

$$\Psi_{xz_i}^{n+1/2} = \frac{2 + \Delta t\alpha_{z_i}}{2\kappa_{z_i} + \Delta t(\alpha_{z_i}\kappa_{z_i} + d_{z_i})}\Psi_{xz_{i-1}}^{n+1/2} + \frac{2\kappa_{z_i}}{2\kappa_{z_i} + \Delta t(\alpha_{z_i}\kappa_{z_i} + d_{z_i})}\Phi_{xz_i}^{n-1/2} \quad \text{Equation 5.61}$$

correspondingly, the previous time integrals, Φ_{xz_i} for $i \in [2, N]$ were updated:

$$\Phi_{xz_i}^{n+1/2} = \frac{2\kappa_{z_i} - \Delta t(\alpha_{z_i}\kappa_{z_i} + d_{z_i})}{2\kappa_{u_i} + \Delta t(\alpha_{z_i}\kappa_{z_i} + d_{z_i})}\Phi_{xz_i}^{n-1/2} - \frac{2\sigma_{z_i}\Delta t}{(2\kappa_{z_i} + \Delta t(\alpha_{z_i}\kappa_{z_i} + d_{z_i}))\kappa_{z_i}}\Psi_{xz_{i-1}}^{n+1/2} \quad \text{Equation 5.62}$$

Furthermore, through application of the same principles used to arrive at Equation 5.61 and Equation 5.62, Equation 5.49 was used to provide an overall formulation for J_{xz}:

$$J_{xz}^{n+1/2} = \frac{2 + \Delta t\alpha_{z_N}}{2\kappa_{z_N} + \Delta t(\alpha_{z_N}\kappa_{z_N} + d_{z_N})}\Psi_{xz_{N-1}}^{n+1/2} + \frac{2\kappa_{z_N}}{2\kappa_{z_N} + \Delta t(\alpha_{z_N}\kappa_{z_N} + d_{z_N})}\Phi_{xz_N}^{n-1/2} - \frac{\partial\sigma_{xz}^{n+1/2}}{\partial z} \quad \text{Equation 5.63}$$

5.6.2.4 N^{th} order stretching

Because Ψ_{xz_i} was merely a function of both $\partial\sigma_{xz_1}/\partial z$ and Φ_{xz_1}, Ψ_{xz_i} could be eliminated from Equation 5.63. Finally, the creation of four new variables, RA_{z_i} RB_{z_i}, RC_{z_i} and RD_{z_i} resulted in the compact formula to describe stretching for a PML of any order:

$$J_{xz}^{n+1/2} = \{(\prod_{q=1}^{N} \mathrm{RA}_{\mathrm{z_q}}) - 1\}\frac{\partial \sigma_{xz}^{n+1/2}}{\partial z} + \sum_{i=1}^{N-1} \{(\prod_{q=i+1}^{N} \mathrm{RA}_{\mathrm{z_q}})\mathrm{RB}_{\mathrm{z_i}}\Phi_{xz}^{n-1/2}\} + \mathrm{RB}_{\mathrm{z_N}}\Phi_{xz_N}^{n-1/2} \quad \text{Equation 5.64}$$

where $i \in [2, N-1]$.

Similarly, due to the same relationship between Ψ_{xz_i}, $\partial \sigma_{xz_1} / \partial z$ and Φ_{xz_1}, Ψ_{xz_i} could be eliminated from the summation memory variable. For a PML of any order this was equivalent to:

$$\Phi_{xz_i}^{n+1/2} = \mathrm{RE}_{\mathrm{z_i}}\Phi_{xz_i}^{n-1/2} - \mathrm{RF}_{\mathrm{z_i}}\{(\prod_{q=1}^{i-1} \mathrm{RA}_{\mathrm{z_q}})\frac{\partial \sigma_{xz}^{n+1/2}}{\partial z} + \sum_{m=1}^{i-1} (\prod_{q=m+1}^{i-1} \mathrm{RA}_{\mathrm{z_q}})\mathrm{RB}_{\mathrm{z_m}}\Phi_{xz_m}^{n-1/2}\} \quad \text{Equation 5.65}$$

Also where $i \in [2, N-1]$.

RA_{z_i} $\mathrm{RB}_{\mathrm{z}_i}$, $\mathrm{RC}_{\mathrm{z}_i}$ and $\mathrm{RD}_{\mathrm{z}_i}$ were defined by:

$$\mathrm{RA}_{\mathrm{z_i}} = \frac{2 + \Delta t \alpha_{z_i}}{2\kappa_{z_i} + \Delta t(\alpha_{z_i}\kappa_{z_i} + d_{z_i})} \quad \text{Equation 5.66}$$

$$\mathrm{RB}_{\mathrm{z_i}} = \frac{2\kappa_{z_i}}{2\kappa_{z_i} + \Delta t(\alpha_{z_i}\kappa_{z_i} + d_{z_i})}$$

$$\mathrm{RE}_{z_i} = \frac{2\kappa_{z_i} - \Delta t(\alpha_{z_i}\kappa_{z_i} + d_{z_i})}{2\kappa_{z_i} + \Delta t(\alpha_{z_i}\kappa_{z_i} + d_{z_i})}$$

$$\mathrm{RF}_{z_i} = \frac{2\sigma_{z_i}\Delta t}{(2\kappa_{z_i} + \Delta t(\alpha_{z_i}\kappa_{z_i} + d_{z_i}))\kappa_{z_i}}$$

5.6.3 First order implementation

Theoretically, Equation 5.64 can be used to define an N[th] order PML, where $N \in \mathbb{R}$. When N=1, Equation 5.64 results in a first order PML implementation. In this case the PML formulation defaults to a similar formulation as presented by (F. Drossaert & Giannopoulos, 2006), albeit with the application of the new correction technique.

$$J_{xz}^{n+1/2} = \{\mathrm{RA}_{z_1} - 1\}\frac{\partial \sigma_{xz}^{n+1/2}}{\partial z} + \mathrm{RB}_{z_1}\Phi_{xz_1}^{n-1/2} \qquad \text{Equation 5.67}$$

followed by the update of Φ_1

$$\Phi_{xz_1}^{n+1/2} = \mathrm{RE}_{z_1}\Phi_{xz_1}^{n-1/2} - \mathrm{RF}_{z_1}\frac{\partial \sigma_{xz}^{n+1/2}}{\partial z} \qquad \text{Equation 5.68}$$

5.6.4 Second order implementation

When N=2, Equation 5.64 results in the second order formulation:

$$J_{xz}^{n+1/2} = \{\mathrm{RA}_{z_1}\mathrm{RA}_{z_2} - 1\}\frac{\partial \sigma_{xz}^{n+1/2}}{\partial z} + \mathrm{RA}_{z_2}\mathrm{RB}_{z_1}\Phi_{xz_1}^{n-1/2} + \mathrm{RB}_{z_2}\Phi_{xz_2}^{n-1/2} \quad \text{Equation 5.69}$$

followed by the updates for Φ_{xz_2} and Φ_{xz_1}

$$\Phi_{xz_2}^{n+1/2} = \mathrm{RE}_{z_2}\Phi_{xz_2}^{n-1/2} - \mathrm{RF}_{z2}\{\mathrm{RA}_{z_1}\frac{\partial \sigma_{xz}^{n+1/2}}{\partial z} + \mathrm{RB}_{z_1}\Phi_{xz_1}^{n-1/2}\} \quad \text{Equation 5.70}$$

$$\Phi_{xz_1}^{n+1/2} = \mathrm{RE}_{z_1}\Phi_{xz_1}^{n-1/2} - \mathrm{RF}_{z_1}\frac{\partial \sigma_{xz}^{n+1/2}}{\partial z} \quad \text{Equation 5.71}$$

5.7 Numerical results

5.7.1 Correction PML vs original formulation

The correction PML implementation was tested against the original recursive integration implementation as described in (F. Drossaert & Giannopoulos, 2006). Although both formulations are similar the correction version allows for a more straightforward implementation. Numerical experiments were conducted including those outlined in (F. Drossaert & Giannopoulos, 2006). Both formulations were found to perform nearly identically and due to the high similarity the resulting traces are omitted. The

only discrepancies were in the range of (1 x 10^{-15}) generated due to numerical precision errors arrising from the different implementations.

5.7.2 Correction PML vs CPML

The correction PML implementation was benchmarked against the CPML implementation as described in (Komatitsch & Martin, 2007), (Martin et al., 2010). The new formulation was tested using a homogenous, two dimensional rectangular grid identical to that also outlined in (Martin et al., 2010). The domain comprised of 101 x 641 square cells, with 10m spacing between grid points in both directions. The homogenous material was characterised by pressure wave velocity $V_p = 3300\ ms^{-1}$, shear wave velocity $V_s = 1905\ ms^{-1}$ and density $\rho = 2800$ kgm^{-3}. The staggered computational scheme was second order accurate in both space and time with a constant time step of $\delta t = 0.001s$. The grid followed that outlined by (Virieux, 1986) and was bounded on all sides by a PML region 10 cells thick.

A 8Hz excitation with the form of a first derivative of a gaussian was used to excite the velocity components in both directions at coordinate (79, 427). Recievers one, two and three were placed at (20,413), (70,227) and (81,27) respectively. Physically receiver one was located closest to the source and receiver three located furthest away (Figure 5.2).

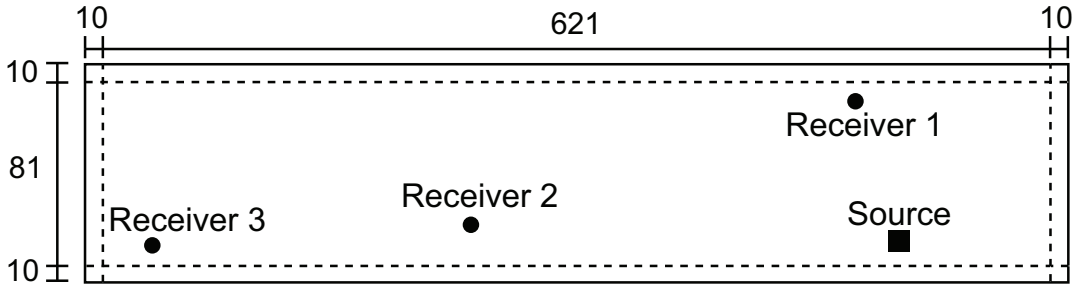

Figure 5.2 – Numerical example schematic (rotated 90 degrees)

For both implementations PML parameters were taken from (Komatitsch & Martin, 2007) who showed that using $\kappa_{max} = 7$ and $\alpha_{max} = \omega\pi$ facilitated high CFS absorption performance for this particular domain. Additionally, $d_{max} = \frac{3V_p}{2L} log \frac{1}{R}$ where V_p = compressional wave speed, L = number of PML layers and R was the reflection coefficient (R = 1 x 10^{-5}).

Once again for this example the resulting traces were similar. Therefore to facilitate a more detailed comparison of performance a metric was introduced:

$$\text{Error}_{\text{db}}|_{i,j}^{n} = 20\log_{10} \frac{\| E|_{i,j}^{n} - E_{\text{ref}}|_{i,j}^{n} \|}{\| E_{\text{ref}_{\text{max}}}|_{i,j} \|} \qquad \text{Equation 5.72}$$

Where $E_{i,j}^{n}$ represents the test trace at a point in time n and at spatial location i, j. E_{ref} represents the reference solution, and $E_{ref_{max}}$ is the maximum amplitude of the reference trace. When plotted this allows for a better visual interpretation of the errors at each point in time.

Although the error plots (Figure 5.3) allowed for easier comparison between traces, there were still large similarities between results. At some points the CPML could be seen to perform marginally better but at other points the correction PML exhibited slightly higher accuracy. This is clearly evident at receivers vx1 and vx2. Therefore it was concluded that the CPML offered very similar performance to the CPML implementation.

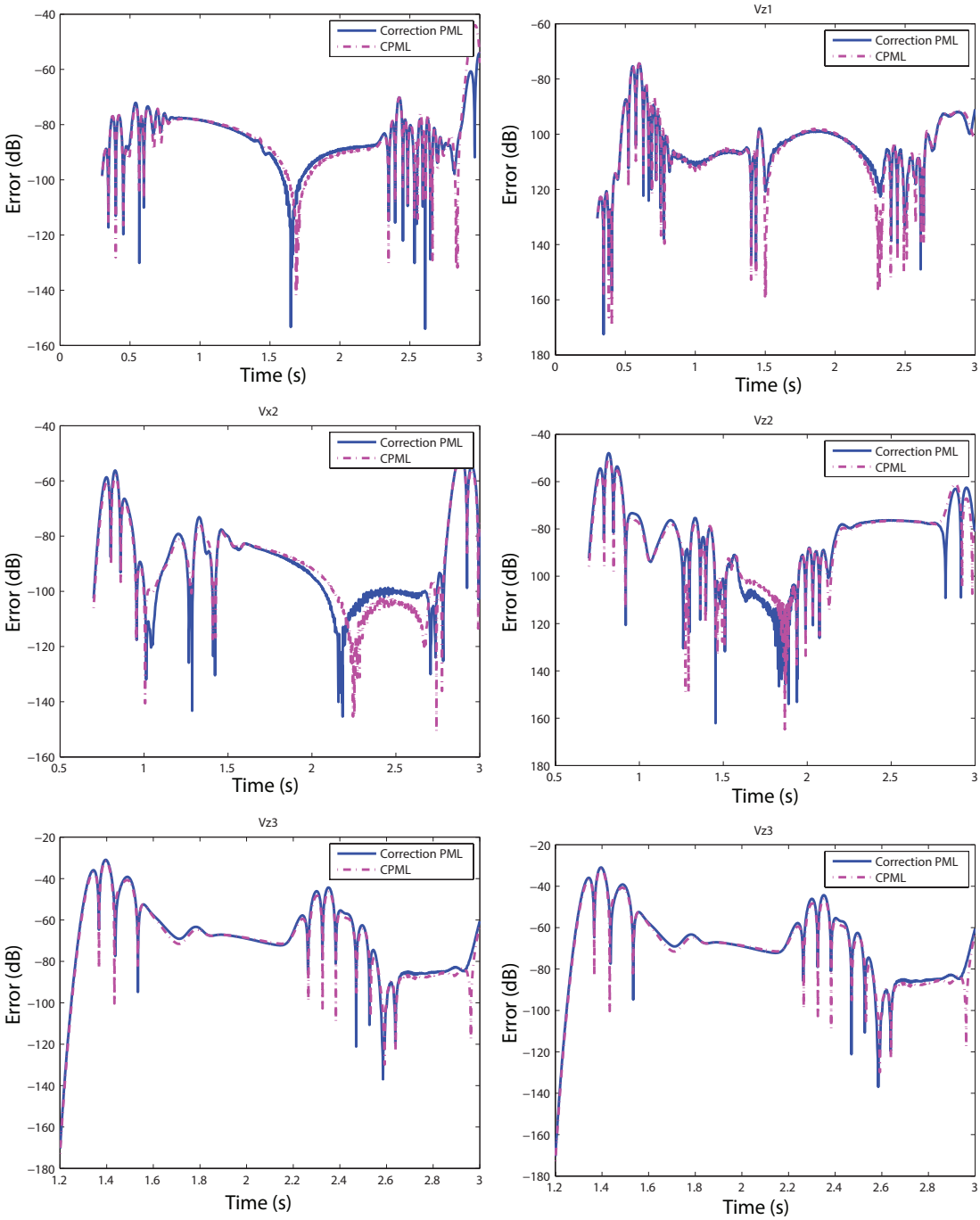

Figure 5.3 – Performance comparison - CPML vs correction PML

5.7.3 Second order PML performance – stationary excitation

To illustrate the ability of a higher order PML scheme to outperform its first order counterpart, a CFS-CFS stretching function was tested to determine

whether combining these optimised parameters with an additional CFS stretching function would offer increased performance. The second set of CFS parameters were as follows:

$$d_{max_2} = \frac{d_{max_1}}{30}$$

$$\kappa_{max_2} = 1.5 \qquad \text{Equation 5.73}$$

$$\alpha_{max_2} = 2d_{max_1}$$

Figure 5.4 - Figure 5.5 shows the resulting error plots for the furthest away receiver (receiver 3). It was found that both first order CFS formulations produced nearly identical results and that the overall error increased as the receiver distance was increased. Concerning the O2 CFS-CFS implementation, performance at receivers vx_1 and vz_1 was improved slightly but as distance increased, performance increased rapidly. Receivers vx_3 and vz_3 showed a marked improvement with on average between 10dB and 20dB less error.

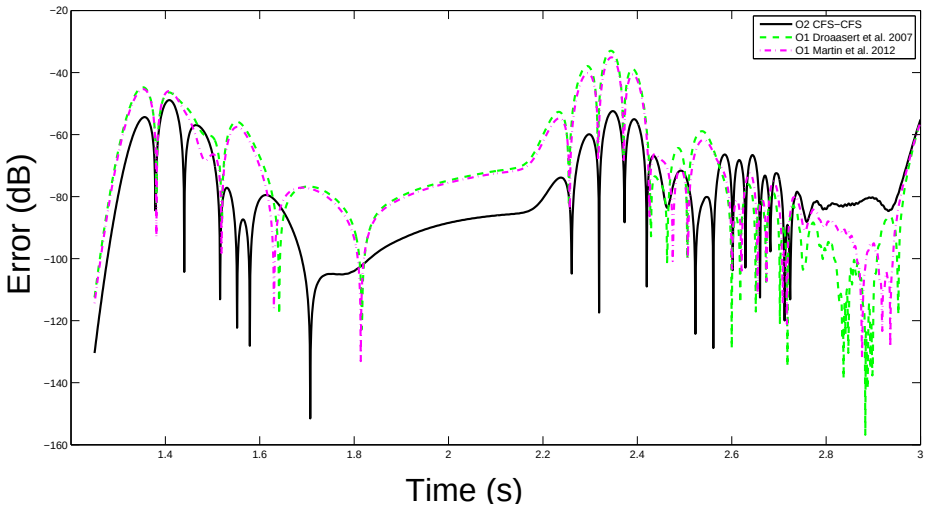

Figure 5.4 - Error comparison for receiver 3 (vx_3 - horizontal velocity component)

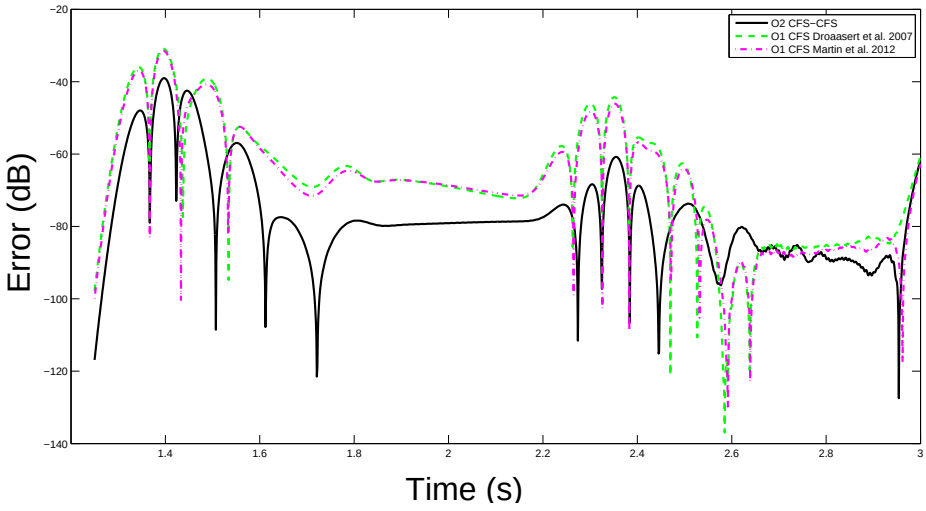

Figure 5.5 - Error comparison for receiver 3 (vz_3 - vertical velocity component)

This increase in performance was likely because the furthest away receivers were at greater distance from the excitation and very close to the PML. Therefore naturally they would be subject to a greater number of evanescent waves and waves arriving at imaginary angles in comparison to the closest receivers. PML schemes typically have degraded performance under such

conditions however the additional degrees of freedom associated with the second order PML allow it to maintain higher levels of performance in comparison to both first CFS stretching functions.

As the close receivers experienced only a low percentage of evanescent waves the first order CFS was capable of high performance absorption for these locations. Therefore there was not much scope for improvement by adding an additional stretching function for regions where the wavefield was relatively predictable.

It should be noted that attempts were also made to improve absorption performance using a combination of both the classical and CFS stretching functions. Although this case has been shown to offer the best performance in the case of electromagnetic waves, no significant performance benefits were found for the elastodynamic case.

5.7.4 Second order PML performance – moving excitation

FDTD modelling is typically used to simulate seismic wave propagation from a single stationary excitation, as examined in 5.7.3. This is a common modelling scenario for applications such as seismic exploration, and therefore the higher order PML may have extended application within this area. Despite this, for railway applications it is imperative that it can be used with moving excitations. Therefore to test the ability of the velocity-stress grid and second order PML

combination to model waves originating from a moving source, a moving point load test was undertaken.

This test was important because a moving excitation generates waves with a broad spectrum of frequencies, from a variety of spatial locations. This spectrum of frequencies and arrival angles can lead a degradation in performance for some absorbing boundary conditions. Figure 5.6 shows the ability of the PML to absorb such waves for a homogenous half-space. It is seen that the seismic waves move as expected and that they are absorbed efficiently by the PML which has attenuated all waves in the fourth screenshot.

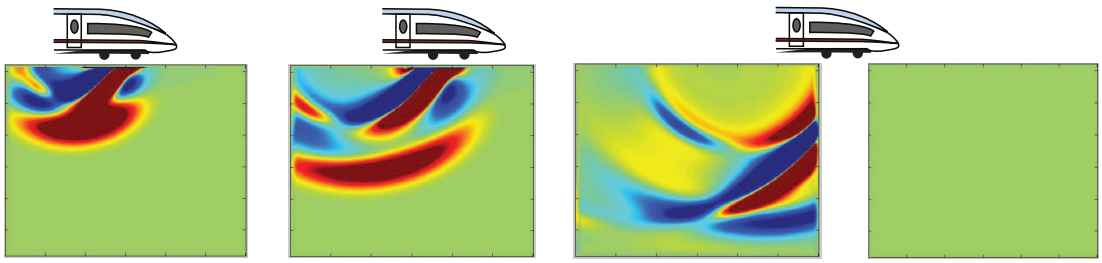

Figure 5.6 - PML perormance for a moving excitation (vertical velocity)

5.8 Track modelling

A 2D slab track was developed in conjunction with the 2D domain. An embedded concrete slab track (INNOTRACK, 2008) was chosen to eliminate the complex geometries (topography) associated with sleeper modelling, which was likely to cause numerical dispersion. The 2D model layout is shown in Figure 5.7 and the material properties used for each component are shown in Table 5.1. As the material interfaces between rail, slab and sleeper contrasted

strongly parameter averaging was used as described in 5.5.2. This was necessary for stability of the standard staggered grid (Bohlen & Saenger, 2006).

A major drawback of parameter averaging for small geometries is that averaging can greatly affect their overall material properties. This is not a concern in seismology where soil layers are typically thick and the contrast in material properties between layers is relatively low. However for the case of railway modelling, the rail was bounded by air and concrete, both with high contrasting material properties in comparison to itself. Due to its small height (0.15m), the rail was formed from only one FD element. This meant that after averaging the entire element's material properties were a hybrid combination of the air, rail and concrete. Therefore the element was no longer an accurate representation of the rail. Similar challenges were faced when modelling the concrete slab due to the contrasting properties from the rail and soil.

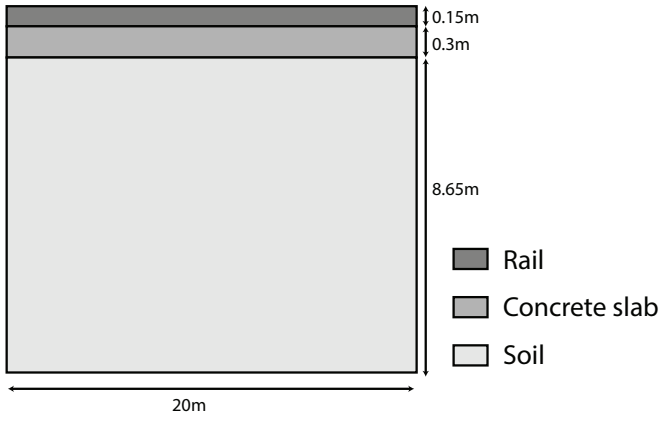

Figure 5.7 - Embedded rail slab track layout

	Material properties		
Track component	Young's modulus (MPa)	Poisson's ratio	Density (kg/m^3)
Rail	1.1E+05	0.25	7900
Slab	30000	0.4	2400

Table 5.1 - Embedded rail slab track material properties

5.9 Moving source implementation

An identical one wheel excitation mechanism as that outlined in Chapter 4 was used to model the moving vehicle. Once again it was coupled to the rail using a non-linear Hertzian spring. Numerous attempts were made to ensure an efficient coupling between the wheel and the rail however excessive dispersion and high frequency contamination was found for all cases. One possible reason for this was that due to the necessary material property averaging of the SSG, the coupling could not be made directly with the rail.

5.10 Limitations and recommendations for future work

The FDTD modelling technique was shown to have high performance for stationary and moving point loads, in the presence of a homogenous half-space. Despite this, two main disadvantages were found thus prohibiting its use in railway vibration modelling. Firstly, at material interfaces, especially those bounding the rail and sleeper elements, parameter averaging caused the generation of hybrid material properties that did not reflect the true properties

of the track components. This in turn created problems in coupling the train loading to the rail.

Future work should focus on investigating alternative velocity-stress stencils to eliminate the need for parameter averaging. Although a solution to this problem exists and has previously facilitated the development of a railway prediction (Thornely-Taylor, 2004), it is commercially sensitive and remains unpublished (Thornely-Taylor, 2013).

Some promising possible solutions include the development of a rotated staggered grid (Saenger, Gold, & Shapiro, 2000) which may help in partially reducing the parameter averaging requirements. Additionally, techniques such as mixed grids (Hustedt, Operto, & Virieux, 2004), or FE/FD hybrid grids (Galis, Moczo, & Kristek, 2008) may be useful for railway applications, due to their ability to model finer details within the track structure, thus reducing the inaccuracies associated with parameter averaging.

5.11 Conclusions

FDTD approaches to railway vibration modelling have been proposed by (Katou et al., 2008) and (Thornely-Taylor, 2004). A shortcoming of these approaches was that low performance boundary conditions were used, thus increasing computational requirements. Therefore in an attempt to expand on these works, it was decided to develop a similar model but with high performance boundary conditions to drastically reduce computational times.

To this end, a new higher order PML condition was developed and was shown to outperform current alternative approaches. Although the new PML condition greatly aided in the absorption on seismic waves from a moving source, it also performed well for stationary excitations. Therefore it is applicable outside the railway industry, particularly in fields such as seismic exploration.

Despite this elevated PML performance, the ability of the FDTD standard staggered grid method to model railway track geometries and excitation was unsatisfactory. It was found that parameter averaging between material interfaces was required to maintain numerical stability, and this lead to a model that provided a poor representation of the physical problem. It also led to difficulties in coupling a moving multi-body excitation to the track.

The work undertaken by (Thornely-Taylor, 2004) suggests that it is possible to overcome these material property averaging challenges, however the solution remains unpublished. Therefore for the purpose of this research, after careful deliberation, it was decided that the drawbacks of the SSG FDTD approach were too challenging to take the development of the FDTD model any further. Instead, future work focused on using the FE method due to its ability to model complex geometries and material interfaces without material parameter averaging.

Chapter 6. Artificial intelligence model development

6.1 Background

The FE models developed in Chapter 4 are shown later to have high accuracy prediction abilities regarding ground borne vibration levels from trains. This makes them useful for performing detailed vibration studies at vibration critical locations. To identify possible critical locations and to undertake a generalised vibration study of a new line, a preliminary study (also known as scoping) is undertaken.

To perform a preliminary study, vast sections of track must be analysed in a short time frame, meaning the use of a prediction model with low computation requirements is vital. If a fully 3D model was used to perform such an analysis, the associated computer run times would be impractical for commercial use. Additionally, the number of inputs required to deploy a scoping model must be few and availability of these parameters must be high. Although a model may have high prediction accuracy and run quickly, if it requires highly detailed geotechnical information that is only obtainable through field experiments, then the collection of data becomes the limiting factor.

A scoping model was developed by the Norwegian Geotechnical Institute (Madshus et al., 1996) to predict vibration levels (and confidence limits) in

buildings close to railway lines. The model was based upon a statistical analysis of measured vibration levels at a variety of test sites in Norway and Sweden. Using this model, the frequency weighted r.m.s. (root mean square) velocity levels were predicting using:

$$V = F_v \cdot F_R \cdot F_B = (V_T \cdot F_s \cdot F_D)F_R \cdot F_B$$

Where F_v is the basic vibration function including the contribution from V_T, F_s and F_D. V_T is the vibration level at a reference distance of 15m from the track, F_s is the speed factor and F_D is the distance factor. F_R is a track quality factor and F_B is the building amplification factor. Each factor had a default value of 1.0 and was increased/decreased depending on specified criteria. The model was used for predicting vibration levels on a high speed rail track between Oslo and Oslo airport.

(Rucker & Auersch, 1999) presented a vibration model capable of predicting vibration levels at distances from the track and inside nearby buildings. The methodology was based on calculating three transfer functions, one for the vehicle/track excitation, one for the wave propagation through the soil and one for the transfer of vibration into the building. The transfer function for the track is calculated using FE methods and wave propagation is calculated using the thin layer method. Lastly, the transfer of vibration into structures is calculated using a combination of theoretical and experimental results. The final prediction program was implemented within a graphical user interface, however was not compared to any experimental results.

(Bahrekazemi, 2004) presented an alternative empirical model to estimate one second r.m.s vibration values. Experimental work was undertaken to record railway vibration levels at four Swedish test sites (Kahog, Partille, Ledsgard and Sabylund). The results were used to develop a model that predicted vibration levels based upon train speed, receiver distance, vibration attenuation and wheel force. The model was verified using data from the same four sites, which was deliberately excluded from the model development. Finally the model was implemented within a Geographical Information System (GIS) to aid usability.

A shortcoming of the model was that during the experimental field work, the majority of train speeds recorded were between 75-130 km/h. Although a small number were higher, a maximum speed of 200 km/h was recorded, which is lower than the velocities typically experienced on commercial high speed rail lines. Therefore the relationships developed in this work were only valid for lower speed trains. Additionally, the curve fitting used in this work was linear, thus possibly over simplifying the relationship between model variables and predicted r.m.s. values.

(Federal Railroad Administration, 2012) and (Rossi & Nicolini, 2003) also proposed empirical models for preliminary study purposes. (Rossi & Nicolini, 2003) proposed a model based upon making assumptions about wave propagation and (Federal Railroad Administration, 2012) outlined a model developed solely using ground-borne acceleration data obtained through field experiments. These experiments involved the recording of 88 train passages on

eight lines across Sweden, France and Italy. The results were statistically analysed to determine correlations between a discrete number of track setups. The final model approximated vibration levels on a velocity log scale and was straightforward to use. This ease of use meant that the model gained wide acceptance and is commonly used on commercial projects.

Although (Federal Railroad Administration, 2012) was based upon a statistical analysis of field recordings from a large number of tests sites, because the soil properties were not investigated at these test sites, the model ignored nearly all soil characteristics. Therefore, factors such as Rayleigh wave speed were not considered in the vibration prediction. The only exception to this was if the track was characterised as resting on soil conditions that 'promoted efficient vibration' such as rock.

Soil properties have previously been shown to contribute significantly to the levels of ground vibrations experienced by receivers close to railway tracks ((Kouroussis et al., 2012), (Lombaert, Degrande, & Clouteau, 2001), (Auersch, 2008b)). This is particularly the case for trains travelling close to the underlying Rayleigh wave speed. Thus, ignoring soil properties is likely to reduce the accuracy of a prediction model.

Another drawback of (Federal Railroad Administration, 2012) was that it could only be used to predict VdB (vibration decibels) values. Although VdB is acceptable in a few isolated vibration standards, particularly in America, there are many countries where this metric is not applicable.

This chapter outlines the development of an empirical model that is capable of predicting high speed rail vibrations using rudimentary soil properties. The aim was to develop a model that could use existing borehole data to quickly assess long lengths of track in a short period of time. The model would be straightforward to use and not require significant railway engineering or geotechnical experience. An additional aim was to include the ability to predict a wide range of vibration metrics (section 6.4), thus making it universally applicable. A Neural Network, machine learning approach was used for model development.

6.2 Background of artificial neural networks

Artificial neural networks (ANN) is a form of artificial intelligence inspired by the biological network of the brain which aims to find patterns and relationships between input and output variables. It is a statistical tool inspired by biological behaviour where a network of artificial neurons and connectors are used to model complex global behaviour. It is typically used to find underlying relationships for problems where no formal mathematical theories exist. The key advantage of a neural network is its ability to instantaneously predict the solution to a problem without the resources required to model the physical domain using techniques such as FE.

The first stage in developing an ANN is to expose it to a large number of previous outcomes. This allows it to use pattern recognition to train itself using input and output data. Once the network has been trained its ability to predict

the existing data using these recognised patterns is evaluated. If the prediction ability is strong then it is further tested against data it has never been exposed to.

ANN techniques have been used in wave propagation modelling to predict vibration levels from blasting in the mining industry ((Monjezi, Ghafurikalajahi, & Bahrami, 2011), (Khandelwal & Singh, 2006), (Dehghani & Ataee-pour, 2011)), to investigate the performance of 2D trenches to isolate railway vibration (Hung & Ni, 2007), to relate railway track geometry to vehicle performance (Li, Meddah, Hass, & Kalay, 2006) and to estimate shear wave velocities of soils from geophysical tests (Nazari, Saljooghi, Shahbazi, & Akbari, 2010).

6.3 Development of an artificial neural network

The purpose of the proposed ANN model was to provide high speed rail planners with a method to assess vibration levels without prior geotechnical experience. Therefore it was important that existing elementary borehole information (or other geotechnical information) could be easily translated into input variables for the model. To aid translation it was important that only a minimal number of input variables would be required to use model. Thus, a sensitivity analysis was undertaken to determine the effect each FE soil property had on vibration propagation. This way, it was possible to quantify the least influential parameters and remove them from the analysis.

6.3.1 FE parameter sensitivity analysis

Density, Poisson's ratio, damping and Young's modulus play different roles in describing wave propagation. Consequently the sensitivity of wave propagation to each parameter is different. For the range of soil parameters typically found in-situ, the effect of each parameter on peak particle velocity (PPV) levels was tested.

For each test the model properties were kept constant, unless otherwise stated, with Young's modulus = 100 MPa, density = 2000 kg/m^3, Poisson's ratio = 0.35 and damping ratio = 0%. Two simulations were performed to investigate the sensitivity of each parameter on PPV. The first simulation was performed using a parameter at the lower end of that for a typical soil and the second was performed using a parameter at the upper end of that for a typical soil. The excitation shape was of the form of the first derivative of a Gaussian and the PPV results were normalised with respect to the PPV value calculated at 0.5m from the source, with respect to the lower value material parameter under investigation.

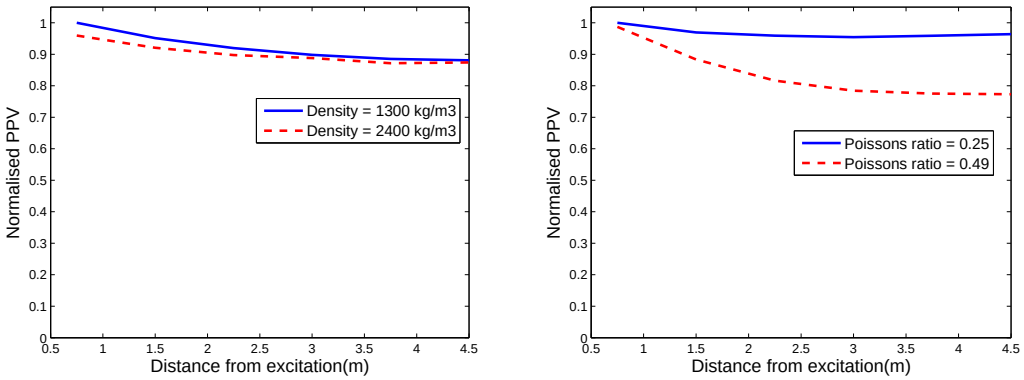

Figure 6.1 - PPV sensitivity, (a) Left: density, (b) Right: Poisson's ratio)

Figure 6.1 shows the effect of density on normalised PPV with increasing distance from the excitation point. The change in PPV between 1300 kg/m^3 and 2400 kg/m^3 is low (<5%) at all observation points. Therefore it can be concluded that the range of densities commonly found in-situ have a low effect on vibration amplitudes.

Figure 6.1 also shows the effect of Poisson's ratio on normalised PPV. At low distances from the excitation the difference between Poisson's ratio values is also low, however it increases with distance. At distances greater than 3m from the excitation the difference between results becomes relatively constant (~20%). Therefore, although it has a greater affect than density, the typical range of Poisson's ratio values for soils have a low impact on vibration levels.

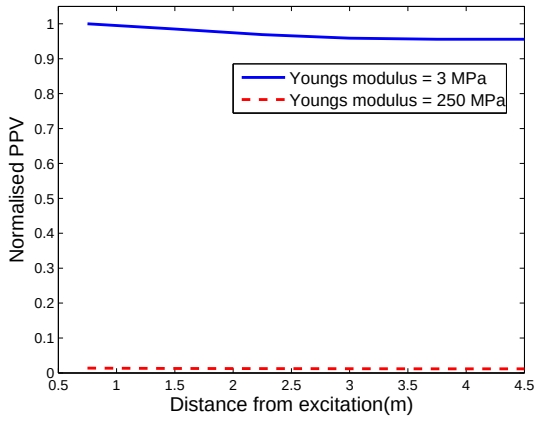

Figure 6.2 - PPV sensitivity to Young's modulus

Figure 6.2 shows the effect of Young's modulus on PPV levels. There is a distinct change in PPV when the Young's modulus is changed from 3MPa to 250MPa. The discrepancy is relatively constant and greater than 95%. This difference is much greater than that for Poisson's ratio and density. Therefore it can be concluded that the range of Young's modulus values for typical soils has a much more dominant effect on vibration levels than the typical ranges for Poisson's ratio and density.

This finding is relevant for both the physical tests and empirical correlations used to determine soil properties, that will be described later in this thesis. Many of these tests and correlations are used to determine shear modulus or shear wave speed. Shear modulus can be related to Young's modulus using solely Poisson's ratio and shear wave speed is related to Young's modulus using density and Poisson's ratio. This is important because density and Poisson's ratio have both been shown to have minor effects on vibration

levels. Therefore in cases where it is not possible to determine them directly, (e.g. initial vibration assessments) it is a valid assumption to make approximations for these values ((Kouroussis et al., 2012) and (Nour, Slimani, Laouami, & Afra, 2003)).

Although this sensitivity analysis focused on typical soil properties, it was also possible that the upper soil stratum may consist of rock. A variety of rock types and associated material properties are found in (Zhao, Labiouse, Dudt, & Mathier, 2010). Considering Limestone rock as an example, it has a Young's modulus of 45 GPa, a density of 2720 kg/m^3 and a Poisson's ratio of 0.3. When compared to Table 7.1 - Table 7.3, it can be seen that the Poisson's ratio of rock is similar to that of a typical soil and density is less that 50% greater than a typical soil. Therefore the changes to PPV caused by density and Poisson's ratio were likely to be small. In comparison, the shear modulus of rock is much greater than that for a typical soil. This was important because as shown in Figure 6.2, even small changes in Young's modulus have large effects on vibration amplitudes. Therefore, for the case of rock modelling it was also evident that accurate determination of the shear modulus was more important that the accurate determination of both Poisson's ratio and density.

6.4 Optimising the international compatibility of model output

The complexity of seismic wave propagation prohibited the prediction of raw time history signals using machine learning. Instead, key vibration indicators were calculated using raw ABAQUS model trace histories and then

used as the outputs/targets for neural network construction. These indicators were chosen carefully to maximise the international compatibility of the vibration prediction model. The aim was to create a network(s) that allowed planning engineers from a variety of countries to assess vibration levels using their own national standards. First a review of the current vibration guidelines proposed by a variety of countries was undertaken.

6.4.1 National and international standards

The measurement of railway vibration is dependent on whether the subject under investigation is a human or a structure. A variety of national and international standards are available for quantifying the effect of vibration on both types of subject. Ten of these are shown in Table 6.1.

Country	**Relevant standard(s)**	**Country**	**Relevant standard(s)**
Austria	ONORM 9012:2010	Spain	Real Decreto 1307/2007
Germany	DIN 4150-2:1999	Sweden	SS 460 48 61:1992
Italy	UNI 9614:1990	UK	BS 6472-1:2008, BS 7385-2:1993
Netherlands	SBR Richtlijn - Deel B (2002)	USA	FRA (2012), FTA (2006)
Norway	NS 8176:2005	International	ISO 2631-1:1997, ISO 2631-2:2003

Table 6.1 - National and international vibration standards

Each standard uses different criteria to assess vibration levels making it difficult to compare standards and to classify vibration levels universally. For example, the UK and Spain use acceleration to quantify vibration whereas Germany and America use velocity criteria. Similar differences exist between frequency weighting curves, time averaging procedures, units of measurement and metrics. Comprehensive reviews of existing standards can be found in (Griffin, 1998) and (Asmussen, 2011a).

A variety of these standards have been used in practise to successfully assess vibration levels. For example, the Docklands light rail project (URS, 2010) in London, UK used (BSI, 2008) to assess VDV (velocity dose values) in a similar manner to (Trinder & Wood, 2009). Additionally, various standards have been used at sites irrespective of project country. For example, American standards have been used on a tram-line in Edinburgh, Scotland (Pouillon et al., 2009), and on a commuter rail line in Toronto, Canada (Metrolinx, 2010).

6.4.2 Human response

Ground borne vibrations generated from high speed train passage are transmitted into buildings resulting in structural vibration. This structural vibration can impact on humans in three main ways:

1. Whole body response
2. Low frequency noise from vibrating floors and walls

3. Noise/vibration from other objects, e.g. rattling of windows, doors and furniture

Additionally, vibration is perceived differently depending on the subjects reference value of vibration. For example, an existing railway line that is upgraded to accommodate a greater number of train passages or higher speed trains will often result in elevated vibration levels. If this upgrade generates vibration levels that are less than 25% greater than the levels previously experienced, residents are unlikely to perceive the increase (Asmussen, 2012).

Train passage is also likely to generate a combination of noise and vibration. This noise may arise from vibrating floors and walls, or may arrive directly in the form of air-borne noise (e.g. generated directly from the wheel/rail contact). Researchers have investigated the relationship between noise and vibration and have found that when combined, the presence of both can affect the human perception of each individual component. (Howarth & Griffin, 1991) showed through lab tests that vibration has little effect on perceived noise levels, but that noise has an effect on perceived vibration levels. These findings are supported by (Paulsen & Kastka, 1995). In addition to lab testing, (Findeis & Peters, 2004) have shown that greater complaints arise due the presence of noise and vibration. Despite these findings, no standards or guidelines currently include noise/vibration relationships.

6.4.3 Human response metrics

As mentioned, a variety of standards and guidelines are available for the classification of vibration. In an attempt to provide results applicable to a range of standards/countries and to maintain consistency, results presented in this work are based upon velocity criteria. To assess human response to vibration, two metrics were used: KB_{max} and VdB.

KB_{max} is based on KB_f and is the weighted vibration severity signal as proposed by (ISO, 1999) to assess human discomfort to vibration. It provides a relevant metric for assessing human exposure to vibration because it uses a time-averaged signal for calculation. Therefore, rather than simply analysing the maximum of the signal, it takes account of its duration. This is important because although structural response is affected by maximum exposure, humans perceive vibration levels also as a function of time. For example, long duration vibrations cause greater human discomfort than short duration vibrations, whereas duration does not affect structural response. KB_f is calculated using:

$$KB_f(t) = \sqrt{\frac{1}{\tau}\int_0^t KB^2(\xi)e^{\frac{-t-\xi}{\tau}}d\xi} \qquad \text{Equation 6.1}$$

Where, τ=0.125s. It is based upon the calculation of a weighted velocity signal KB(t), defined by:

$$H_{KB}(f) = \frac{1}{\sqrt{1 + \left(\frac{5.6}{f}\right)^2}} \qquad \text{Equation 6.2}$$

KB_f produces a time history of vibration response, however as mentioned, time histories are impractical to predict using ANN's. Therefore the maximum value of KB_f was used (KB_{max}).

VdB (Vibration velocity level) is an American metric (Federal Railroad Administration, 2012) to assess the response of humans in buildings, to vibration. In a similar manner to $KB_{f,}$ it is based upon calculating a moving average:

$$VdB = 20 \log_{10} \frac{v_{rms}}{v_0} \qquad \text{Equation 6.3}$$

Where VdB is the velocity level expressed in decibels, and υ_{rms} is the root mean square velocity amplitude. υ_0 describes the level of background vibration and its recommended value varies depending on country. For the purposes of this research it was chosen to be 2.5×10^{-8} m/s. Once again, to aid in ANN construction and vibration analysis, VdB was assumed to be the maximum VdB value.

6.4.4 Structural response metrics

Structural response to ground excitation is affected by the frequency content of vibration and the natural frequency of the structure. Additionally,

the daily function of a structure also affects its sensitivity to vibration. For example, concert halls and hospitals housing MRI (magnetic resonance imaging) scanners will be more sensitive to vibration than an office environment.

PPV (Peak particle velocity) is often used to assess vibration levels for the purpose of determining structural response/damage. Its use is recommended by (International Standards Organisation, 1999), (BSI, 1999), (BSI, 2008) and is defined as "the maximum instantaneous velocity of a particle at a point during a given time interval". This means it is the absolute maximum velocity level of a given signal. It is commonly used in practice due to its ease of calculation.

$$PPV = max|v(t)| \qquad \text{Equation 6.4}$$

6.5 Development of an empirical homogenous half-space model

A homogenous half-space model was developed with four input parameters. Young's modulus was included as it was shown from the sensitivity analysis to have a large effect on vibration levels. Damping and distance from the track were also included because they have been shown to have large influences on vibrations ((Kouroussis et al., 2012) and (Degrande & Schillemans, 2001a)). Lastly, train speed was used as an input because it has been shown extensively that train speed can have a significant effect on vibration levels ((Krylov, 1995) and (Ju & Lin, 2004)). Density and Poisson's

ratio were held constant at 2000 kg/m^3 and 0.3 respectively. Three separate models were developed to predict each of the three output variables.

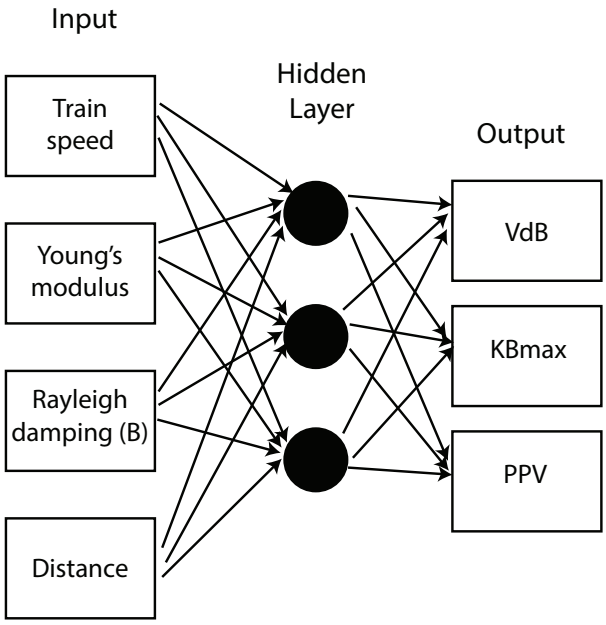

Figure 6.3 – Homogenous ANN schematic (3 output models)

To construct the database of output values, the ABAQUS model developed in Chapter 4 was computed for 92 permutations of the input parameters via ECDF (Richards & Baker, 2008). A Thalys high speed train was chosen as the excitation model and rail irregularity was ignored. For each simulation, the computational run time for a full Thalys trainset with 10 carriages (three seconds of modelling time) took approximately 50 hours. To reduce computational time the excitation model was reduced to a single driving carriage with four wheels. This reduced the run times to 10 hours. Comparisons were made between the PPV, KB and VdB results obtained from

each model and the discrepancy was found to be small (4.6%) meaning the four wheel model provided a reasonable approximation of a full Thalys trainset.

The range of values for each input parameter was chosen carefully to cover a wide range of parameters likely to be found in real life. These parameters are shown in Table 6.2. It should be noted that although the distance parameter was an input parameter for the final ANN model, it was not an explicitly defined parameter within the ABAQUS model (i.e. the other parameters were used as input for the ABAQUS model however distance was just the recording distance for output).

	Input parameters				
Train speed (km/h)	100	200	250	300	350
Young's modulus of soil (MPa)	40	80	120	180	260
Rayleigh stiffness damping coefficient of soil (s)	0.0001	0.0003	0.0005		
Distance from nearest rail (m)	3	7	9	15	19

Table 6.2 – Homogenous ANN input parameters

A 'back propagation', multilayer perceptron (MLP) neural network architecture was used to map the inputs to outputs. This meant that there was a hidden layer between the input and output nodes with several hidden nodes, and that errors were fed back through the network. The training patterns were first propagated forward through this network structure and compared against the output targets. The error was then propagated back through the network and the node weightings updated. The newly predicted outputs were then

compared against the output targets to determine the new error. This iterative procedure was used to reduce the error to an acceptable level.

To optimise performance an iterative approach was undertaken. Firstly, 5000 networks were trained and the five most accurate were analysed in greater detail to determine the optimum number of hidden layers, nodes and the optimum activation function. Typically, the optimum number of nodes was found to be similar to the number of input variables, as defined by (Heaton, 2008). Finally, using these optimised network characteristics a more precise search was performed to further reduce the error.

Although the use of more nodes and/or layers was sometimes found to increase the ability of the model to find relationships within the training data set, it was also found to cause over-fitting. An example of over-fitting is seen in Figure 6.4 where although the red polynomial curve better represents the relationships between training data points, it performs more poorly for predicting the testing data than the linear curve. Over-fitting was analysed by comparing training and testing model performance. If the testing results (and validation results) were found to have a much lower accuracy than the training results, it was likely that over-fitting had occurred. To solve the problem of over-fitting the threshold of error for each search was adjusted until testing accuracy was consistent with training accuracy.

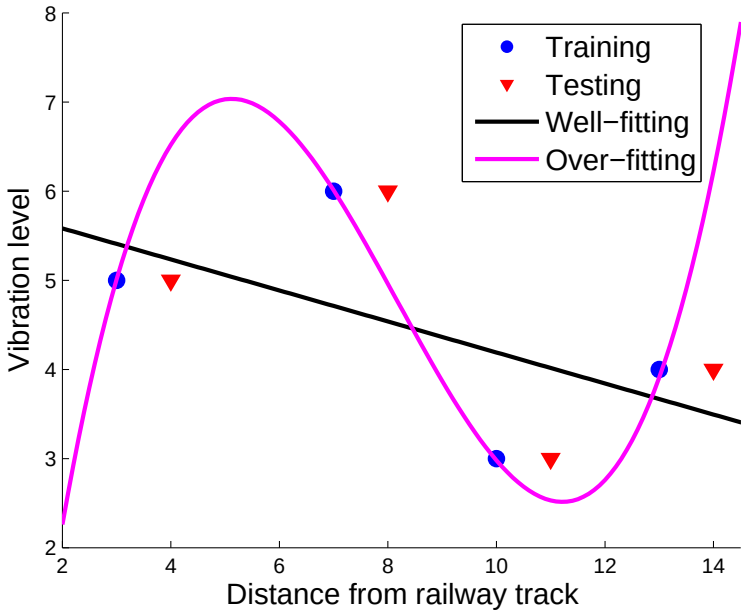

Figure 6.4 - An example of over-fitting within a neural network

6.6 Development of a two layer heterogeneous half-space model

A two layer model was developed in addition to the homogenous model to allow for more detailed soil input values to be used in the model. It was proposed that a 2 layer model would help prediction accuracy significantly, especially in cases where there was a strong contrast in soil stiffness below the ground surface.

6.6.1 Determination of input and output variables

The same input and output variables that were used for the single layer model were retained for the two layer model. The key difference was that two Young's modulus values were used instead of one for describing the soil stiffness profile. Additionally, the depth of the first layer was specified. As the

model depth was always constant at 10m, the depth of the second layer did not require specification. Once again the soil density and Poisson's ratio were held constant.

The same feed-forward neural network architecture was used as that for the homogenous model. The architecture is shown in Figure 6.5, alongside the input parameters in Table 6.3. To enable the rapid development of two layer ABAQUS models each with different layer depths and material properties, a MATLAB code was developed. This code was used to directly edit a generic ABAQUS input file and modify the required FE parameters.

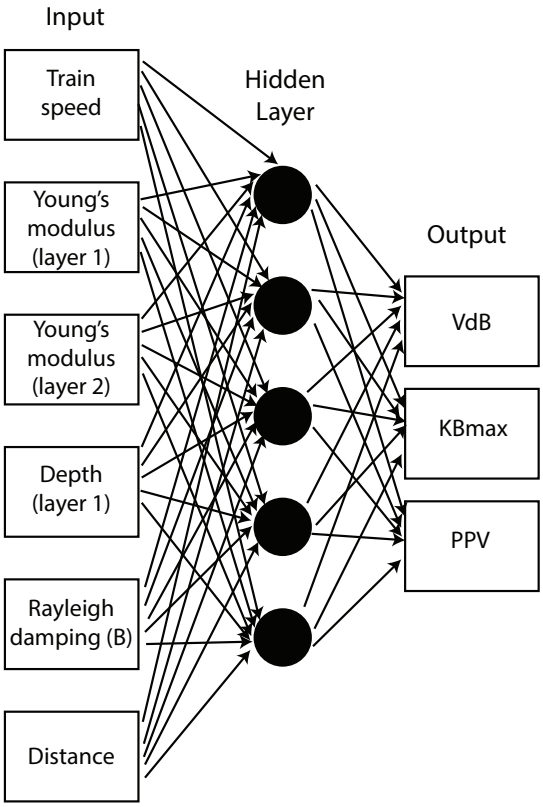

Figure 6.5 – Heterogeneous, two layer ANN model schematic (3 model outputs)

	Input parameters				
Train speed (km/h)	100	200	250	300	350
Young's modulus of top soil layer (MPa)	40	80	160		
Young's modulus of bottom soil layer (MPa)	80	160	240		
Depth of layer 1 (m)	1.5	3	5		
Rayleigh stiffness damping coefficient of soil (s)	0.0001	0.0003	0.0005		
Distance from nearest rail (m)	3	7	9	15	19

Table 6.3 – Heterogeneous, two layer ANN input parameters

The results from the homogenous model were combined with the two layer model during training. To make the homogenous results compatible with the two layer results they were converted into two layer models, with each upper and lower layer having identical material properties. For all distances, this resulted in 1350 homogenous results and 1350 two layer results. Therefore including all distances 2700 data points were used in the creation of the two layer neural network.

6.7 Weka vs statistica

Neural network development was tested using two alternative machine learning software packages. The first package to be tested was Weka (Witten & Frank, 2005) which is an open source package that utilises a gradient descent function. This allowed for the manipulation of learning rate and momentum

however only one network could be trained and tested at any one time. This made the model refinement process very time consuming.

To improve the time efficiency of model creation the alternative software package Statistica (Statsoft, 2008) was used. Statistica's ability to train multiple networks simultaneously and retain the highest performing ones was found to greatly improve the efficiency of the modelling process. To obtain best results a combination of automatic network search and custom network search algorithms were used. First the automatic search function was used, and then refined using the custom search function based upon the output from the residuals and activation functions. A comparison was made between the gradient descent, conjugate descent and Broyden–Fletcher–Goldfarb–Shanno (BFGS) training algorithms. It was found the BFGS offered highest performance.

6.8 Computational requirements

For both homogenous and two layer models the FE (ABAQUS) model was computed using the computer architecture described in (Richards & Baker, 2008). Although running on a high performance computer cluster reduced model run times, the high computational requirements were still a limiting factor in the number of times the model could executed. The total volume of simulations took approximately 28,800 core hours, however parallel processing using eight cores reduced this time by a factor of eight. The total computational workload took six months to complete.

6.9 Conclusions

Preliminary vibration scoping assessment models are used at an early stage of the railway design process. They are used to predict vibration levels across the entire line quickly and typically sacrifice speed for accuracy.

This chapter outlined the development of neural network models to predict three international vibration assessment indicators (PPV, KB_{max} and VdB). The underlying data used for the statistical analysis was generated using a FE ABAQUS model that had been validated using field experiment data.

Firstly, to assess the sensitivity of vibration levels on soil material properties a parametric study was undertaken. It was found that for the typical range of soil properties as found in the literature, Young's modulus had a large effect on PPV whereas density had a minimal effect. Additionally, Poisson's ratio had a moderate to low effect. Therefore Young's modulus, in addition to damping, was chosen to characterise the soil. Poisson's ratio and density were held constant at 0.3 and 2000kg/m^3 respectively.

This reduction of input parameters allowed for a wide variety of soil characteristics to be included in the neural network development, without requiring the execution of an unachievable number of simulations. In addition to soil properties, train speed and distance from the track were also used as input variables. Two soil models were developed: a single layer model and a two layer model. This was done to determine whether a layered soil model

would outperform a single layer model. Both models used slightly different combinations of the aforementioned soil parameters in their definition.

Although the inclusion of soil properties in the prediction process was likely to increase accuracy, it is imperative that these properties are also described accurately. Therefore the next chapter discusses techniques to obtain accurate soil data from limited soil records, to facilitate this improved prediction accuracy.

Chapter 7. Soil property determination for numerical simulation

7.1 Background

The partial differential equations associated with the FE formulation of the elastodynamic wave equation require a minimum of three known parameters: Young's modulus, Density and Poisson's ratio. In addition, although not an implicit requirement, a description of damping is required to simulate energy loss through the medium. Therefore there are four primary variables required to model wave propagation.

If a FE model is to be developed to predict vibration levels within a soil, it is imperative that the material properties of this soil are described accurately. If the soil input parameters are inaccurate then it is unlikely that the FE model will be capable of accurately predicting vibration levels.

Despite this, the level of desired accuracy depends on project purpose. For a preliminary assessment exercise, low level approximations of soil conditions, based on previous soil investigations are typically acceptable. However, for detailed design more comprehensive soil data is required. Depending on the availability of existing data, detailed design may require an additional soil investigation campaign.

One of the challenges with FE modelling is that there is discord between traditional physical testing methodologies and FE input parameters. This makes it challenging to convert test results into discrete FE parameters. This section outlines a selection of the most common testing methodologies and related empirical correlations that can be used to calculate FE input parameters. First correlations are presented between FE parameters and physical soil descriptions. Then correlations are presented for parameters obtained during traditional invasive investigation techniques. Thirdly the MASW test is discussed, and finally some practical guidelines are provided relating to the application of the aforementioned techniques in practice.

7.2 Techniques to determine FE soil parameters

7.2.1 Desktop studies

When approximating soil properties it is not always possible to undertake in-depth site investigations. In the case of railway vibration prediction, this is often true for initial assessments (scoping) due to the impractical nature of performing site investigations over large areas. Under such circumstances material properties must be determined using existing geological data, such as that from previous soil investigations, found through resources such as ("British Geological Association," 2013).

One of the most common forms of geological data is a simple classification of the underlying soil (e.g. recorded on a borehole log), recorded either in-situ by an experienced site investigation engineer or through laboratory testing. Soils are typically categorized using a classification system and this thesis focuses on the four main soil types: clay, silt, sand and gravel. The two most common soil properties used to categorise these soil types (via laboratory testing) are grading and plasticity. Grading is used to classify soils based on particle sizes as described in (BSI, 2004). Typically clay is defined as having the smallest grain size (<0.002mm), followed by silt (0.002-0.06mm), then by sand (0.06-2mm) and finally by gravel (2-60mm). Plasticity relates to the ability of a material to be irreversibly deformed (moulded). Clays and silts are described as 'cohesive' meaning they are easily moulded (high plasticity index) whereas sands and gravels are termed 'granular' or 'non-cohesive' (low plasticity index).

The underlying premise of soil classification is that soils with similar properties are grouped together. Therefore in the absence of additional information it is important that a general approximation of soil properties can be obtained from simple classification data. Several authors (Table 7.1 - Table 7.3) have presented information for this purpose, however, it should be noted that the standard deviation of material values derived from soil type descriptions is large. These potential discrepancies arise because although two soils may be classified as 'clays', it is still possible that they have vastly different material properties.

Typical correlations between Young's modulus and soil classification are presented in Table 7.1, and for density in Table 7.2. It can be seen that for all cases, that saturated soils are more dense than unsaturated soils. This is because the air voids become filled with water which has a higher density than air, thus increasing the soil overall density.

Table 7.3 presents Poisson's ratio values for common soil classifications. In a similar manner to density, Poisson's ratio increases due to saturation. This is particularly true for clays, which when saturated, carry all stresses on their pore water components thus reducing their compressibility. Once fully saturated, clays are incompressible and therefore have a Poisson's ratio of 0.5. It should also be noted that it is also theoretically possible for some heavily over-consolidated soils to be characterised by a Poisson's ratio greater than 0.5 (e.g. Boulder Clay).

It is interesting to note the deviation between maximum and minimum values for each parameter. Young's modulus varies from 3 Mpa for made ground to 137.5 MPa for sandy clay. Therefore sandy clay has a Young's modulus 45 times greater than made ground. In comparison, Poisson's ratio and density vary much less. Poisson's ratio's for soils rarely deviate from the range of 0.2-0.5, the maximum being 2.5 times greater than the minimum. Similarly, density change between the minimum value (made ground) and maximum value (sandy clay) is only 15%, also much less than that for Young's modulus.

Lastly, Figure 7.1 shows the relationship between soil type and damping ratio. Sand typically has damping ratio slightly less than 1% which is lower than gravel. Clay has the highest damping ratio and can range between 1% and 6%. It is also seen that damping ratio in the range of 1-1.2% covers all three soil types. Additional damping data, in terms of dB attenuation per meter, for saturated soils is presented by (Hamilton, 1980). Furthermore, (Stoll, 1979) shows that for sandy soils, damping is frequency dependant at frequencies lower than 43Hz, i.e. the range of interest for high speed rail ground borne vibration analysis.

Soil type	**Young's modulus (MPa)**	**Reference**
Made ground (saturated)	3	(RPS, 2004)
Silty sand	11	(Subramanian, 2011)
Sand (dense)	64.5	(Subramanian, 2011)
Sand and gravel	119.5	(Ryall, Parke, & Harding, 2000)
Clay (medium stiff)	32.5	(Subramanian, 2011)
Sandy clay	137.5	(Subramanian, 2011)

Table 7.1 – Empirical Young's modulus relationships

	Density (kg/m^3)		
Soil type	**Dry**	**Saturated**	**Reference**
Sand	1750	1850	(Carter & Bentley, 1991)
Clay	1300	1780	(Carter & Bentley, 1991)
Made ground (saturated)	-	1700	(RPS, 2004)
Sandy clay	1500	1950	(Carter & Bentley, 1991)
Silty clay	1500	1950	(Carter & Bentley, 1991)

Table 7.2 - Empirical density relationships

Soil type	**Poisson's ratio**	**Reference**
Made ground (saturated)	0.49	(RPS, 2004)
Silt	0.45	(Hemsley, 2000)
Gravel medium dense	0.28	(Prasad, 2009)
Saturated clay	0.49	(Subramanian, 2011)
Clay - unsaturated	0.3	(Subramanian, 2011)
Medium dense sand	0.33	(Das, 2008)

Table 7.3 - Empirical Poisson’s ratio relationships

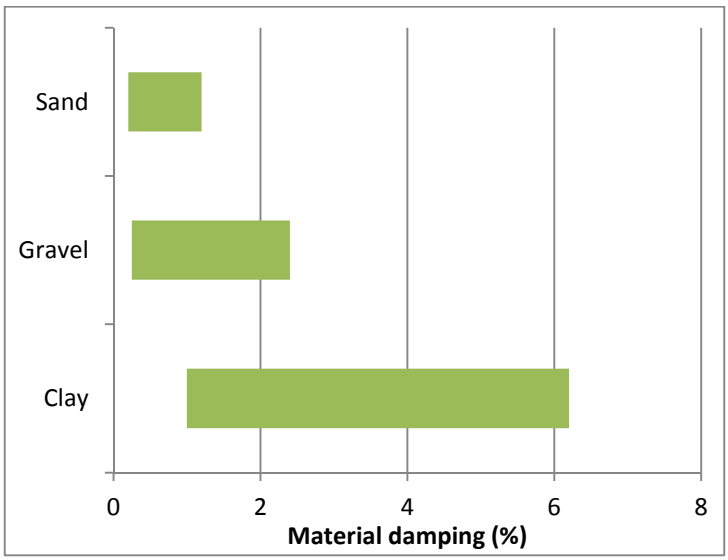

Figure 7.1 - Empirical damping relationships (Asmussen, 2011b)

7.3 Invasive soil investigation techniques

A shortcoming of using approximations based upon soil descriptions is that descriptions are independent of key parameters such as soil depth. For example, although it is likely that a soil's density will increase with depth, the use of soil descriptions will approximate the density of sand located in the uppermost crust as equal to similar sand located 30m below the surface.

To overcome this challenge it is possible to use invasive investigations to either perform in-situ tests or extract physical soil samples for laboratory testing.

7.3.1 In-situ testing

The majority of in-situ testing is undertaken using borehole techniques. This typically involves drilling into the ground and performing penetration experiments at several depths to build up a profile of the soil stratum. The two most widely used penetration experiments are the standard penetration test (SPT) and cone penetration test (CPT).

7.3.1.1 Standard penetration test

The most common type of penetration experiment is the standard penetration test (SPT) - (BSI, 2012). It is undertaken by dropping a 63.5kg (140lb) weight from a height of 760mm (30 inches) and recording the number of blows required for it to penetrate 300mm (12 inches). This number of blows is known as the 'N-value'.

An advantage of using SPT N-values to determine FE modelling properties is that the SPT test is the most widely performed test and resources such as ("British Geological Association," 2013) provide an extensive database of borehole logs. Therefore it is often possible to obtain SPT data without the financial outlay required to perform physical tests.

Additionally, a wide body of research exists for correlating SPT N-values with physical soil properties. Therefore it is possible to use SPT data to obtain soil properties that are more reliable than using soil description data. Despite this, a challenge with the SPT test is that the methodology is not performed

consistently and parameters such as the drop height can vary between countries. (Robertson, Campanella, & Wightman, 1983) presented correction factors to account for these inconsistencies although some authors have questioned whether these factors lead to more reliable results. Additionally, it should be noted that all SPT N-value correlations are based on soils experiencing low strain levels (i.e. the assumption of small strain theory).

Figure 7.2 presents correlations between SPT N-values and shear wave speeds for general soils. The overall deviation between correlations is low, apart from (Seed, Idriss, & Arango, 1983) and (Iyisan, 1996), which both seem to overestimate shear wave velocity.

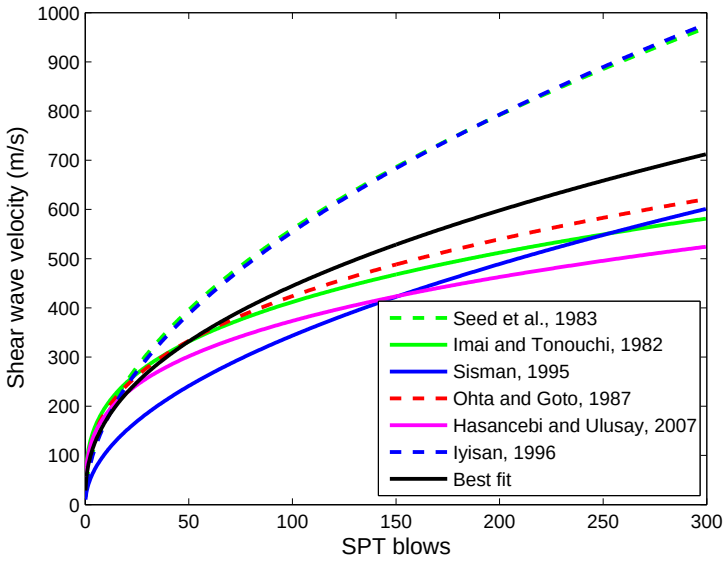

Figure 7.2 - SPT shear wave velocity correlations – all soils. (Seed et al., 1983), (Imai & Tonouchi, 1982), (Sisman, 1995), (Ohta & Goto, 1978), (Hasancebi & Ulusay, 2006), (Iyisan, 1996)

Rather than use SPT correlations to classify all generic soil types, empirical relationships have also been presented for individual soil types. Each of these is based upon whether the soil is a sand, clay or silt; information which is typically recorded when performing SPT testing.

Figure 7.3, Figure 7.4 and Figure 7.5 show relationships for sand, silt and clay respectively. For each soil type, relationships are relatively well correlated with each alternative relationship. Exceptions are the relationships proposed by (Jafari, Shafiee, & Razmkhah, 2002), which for each soil, overestimates the shear wave velocity.

In addition to the relationships shown in Figure 7.3, Figure 7.4 and Figure 7.5, authors such as (Seed, Wong, Idriss, & Tokimatsu, 1987) have proposed correlations based on a greater number of variables (e.g. soil depth) in attempt to improve accuracy.

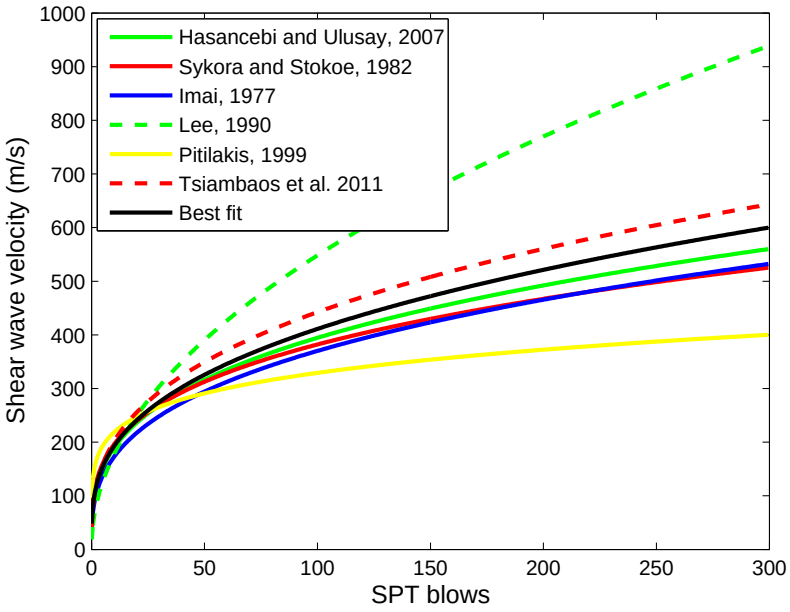

Figure 7.3 - SPT correlations – Sand. (Hasancebi & Ulusay, 2006), (Imai, 1977), (S. Lee, 1990), (S. Lee, 1990), (Pitilakis, Raptakis, Lontzetidis, & T, 1999), (Tsiambaos & Sabatakakis, 2010)

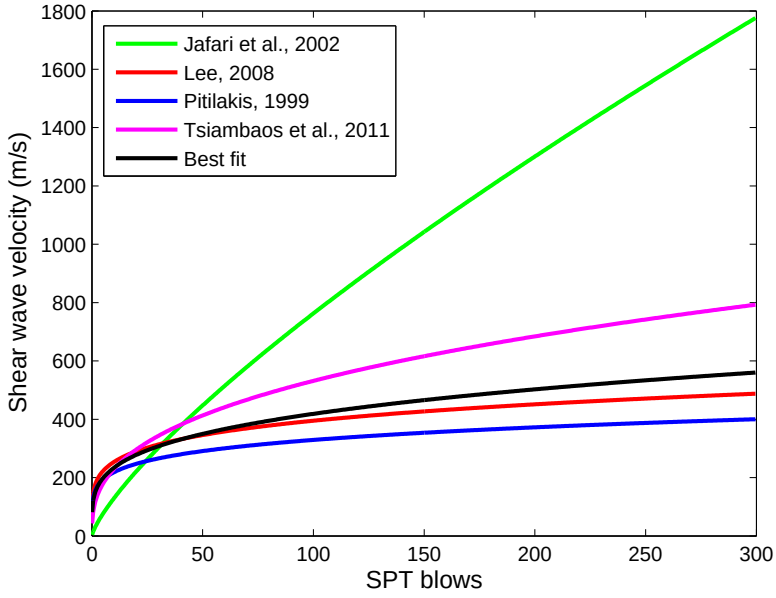

Figure 7.4 - SPT correlations – Silt. (Jafari et al., 2002), (C. Lee & Tsai, 2008), (Pitilakis et al., 1999), (Tsiambaos & Sabatakakis, 2010)

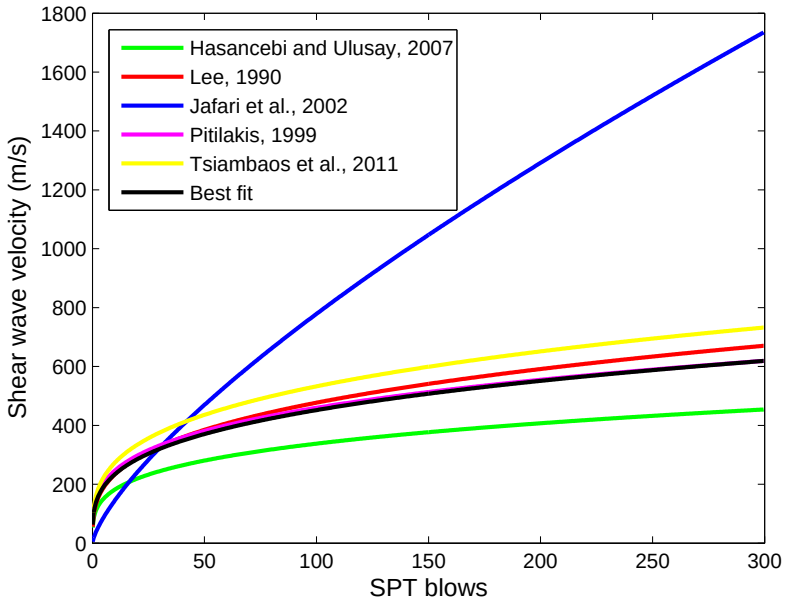

Figure 7.5 - SPT correlations – Clay. (Hasancebi & Ulusay, 2006), (S. Lee, 1990), (Jafari et al., 2002), (Pitilakis et al., 1999), (Tsiambaos & Sabatakakis, 2010)

Rather than attempt to utilise a variety of SPT relationships, one new relationship for each soil type was developed. These new relationships were best fit correlations between all other relationships and are shown using a black line in Figure 7.2 - Figure 7.5. For both the silt and clay relationships, the relationships presented by (Jafari et al., 2002) were ignored because they exhibited a poor correlation with all other proposed relationships. The new relationships are described numerically in Table 7.4 and plotted in Figure 7.6. As expected, the SPT relationships proposed for generic soil shear wave speeds have the largest standard deviation. Silts have a relatively large standard deviation and clays have the lowest at 64.5m/s.

Soil type	SPT relationship	Standard deviation (m/s)
General soils	$V_s = 62.9 \cdot N^{0.425}$	111.7
Sands	$V_s = 86.71 \cdot N^{0.3386}$	81.6
Clays	$V_s = 120.8 \cdot N^{0.2865}$	64.5
Silts	$V_s = 127.1 \cdot N^{0.2595}$	102.9

Table 7.4 - Best fit SPT 'N-value' correlations

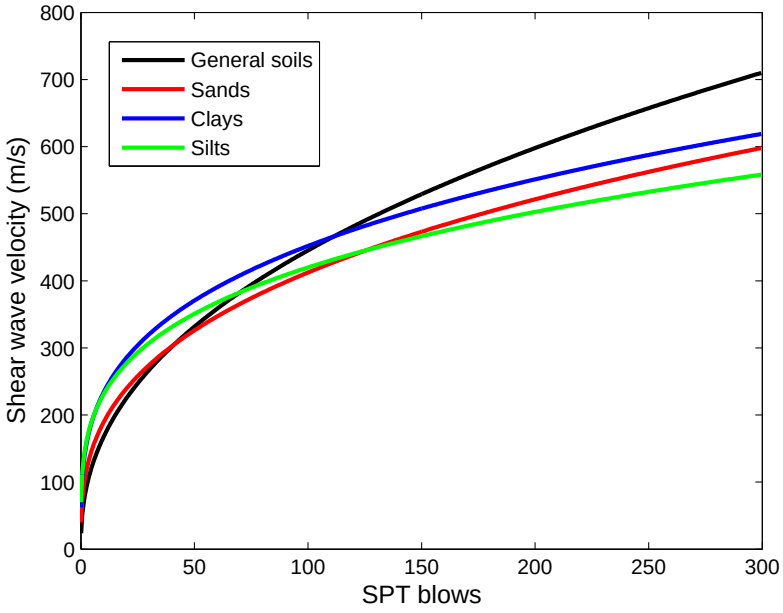

Figure 7.6 - Best fit SPT 'N-value' correlations

7.3.1.2 Cone penetration test

The cone penetration test (CPT) test is an alternative and more sophisticated penetration experiment in which a metal cone is pushed into soil and the penetrative resistance (q_c) is measured. The cone typically has a diameter of 35.7mm^2, cast at a 60^0 angle and is pushed, with the aid of a land vehicle, into the soil at a constant rate.

It addition to cone tip resistance, sleeve friction (f_s) is commonly measured. Less commonly, piezocone penetration tests are used to measure pore water pressure and sometimes seismic cone penetration tests are used to measure shear wave velocity.

Although CPT testing is becoming more widespread, SPT testing remains more common place and historical data relating to SPT N-values is more freely available. One explanation for this is that due to the force required to push the cone into soils, the CPT method can only be used for relatively soft soils. Therefore researchers such as (Chin, Duann, & Kao, 1988) have attempted to correlate CPT results with SPT N-values. This approach is not recommended for the purpose of using empirical correlations to estimate FE parameters because it creates an additional layer of uncertainty. Instead, several authors have presented formulations based directly on CPT results, a variety of which are shown in Table 7.5.

For these relationships, σ is effective stress, k2 is a coefficient function of relative density, q_t is the corrected cone tip resistance (Dejong, 2007) and e0 is void ratio. The relationships have not been plotted graphically because of their

dependence on a variety of soil parameters. This makes it challenging to make direct comparisons.

Soil property	Equation	Soil type	Reference
Shear modulus	$1000 \cdot k2 \cdot \sigma^{0.5}$	Sand	(Paoletti, Hegazy, Monaco, & Piva, 2010)
Shear wave velocity	$50 \cdot ((q_c/p_a)^{0.43} - 3)$	Sand	(Paoletti et al., 2010)
Shear wave velocity	$277 \cdot q_t^{0.13} \cdot \sigma^{0.27}$	Sand	(Baldi, Bellotti, Ghionna, Jamiolkowski, & Presti, 1989)
Shear wave velocity	$(10.1 \cdot \log(q_t) - 11.4)^{1.67} \cdot (f_s/q_t \cdot 100)^{0.3}$	General soils	(Hegazy & Mayne, 1995)
Shear wave velocity	$118.8 \cdot \log(f_s) + 18.5$	General soils	(Mayne, 2006)
Shear wave velocity	$1.75 \cdot q_t^{0.627}$	Clay	(Mayne & Rix, 1995)
Shear wave velocity	$9.44 \cdot q_t^{0.435} \cdot e_0^{-0.532}$	Clay	(Mayne & Rix, 1993)
Shear wave velocity	$1.75 \cdot qt^{0.627}$	Clay	(Mayne & Rix, 1993)

Table 7.5 – CPT empirical relationships

7.3.1.3 Laboratory testing

Lab testing involves extracting soil samples from the test site, transporting them to the lab and performing controlled experiments to determine characteristics that are difficult to obtain using in-situ tests.

A variety of lab testing methodologies are available including bender element testing, resonant column testing, ultrasonic pulse testing and more traditionally, tri-axial testing.

A major advantage of lab testing is that the samples are tested under controlled conditions and therefore allow for a more accurate determination of soil properties. Despite this, due to inevitable sample disturbances caused during soil sample extraction and transportation, the properties of a soil at the time of lab testing are not always similar to the properties of the soil in-situ.

7.3.1.4 Classical lab testing

Classical lab testing refers to tests such as the quick undrained triaxial test to determine undrained shear strength (Dickensen, 1994). They also include other tests to determine properties such as bulk density, moisture content, liquid limit and plastic limit. Although these soil properties (except density) are not required for FE simulation, correlations have been proposed to map them more closely to parameters such as Young's modulus (Asmussen, 2011b).

For vibration prediction purposes, it is sometimes the case that classical lab testing data is available in addition to existing borehole data. Therefore empirical correlations between lab data and FE parameters may be useful for validating SPT correlations. Despite this, if a new soil lab investigation is being performed then bender element and resonant column testing techniques are preferable to classical lab testing. This is because the aforementioned tests can determine FE parameters directly, rather than approximating them using empirical relationships.

One of the most common empirical relationships between lab test results and shear modulus is:

$$\mu = AF(e_0)(\sigma_0')^n \qquad \text{Equation 7.1}$$

$F(e_0)$ is a function of the void ratio, σ'_0 is the effective confining stress and n is non-dimensional. A range of suggested values based on Equation 7.1, for a range of void ratios are shown in Figure 7.7. Ip is the plasticity index associated with each sample. The effective confining stress for each relationship was assumed to be 100 kPa.

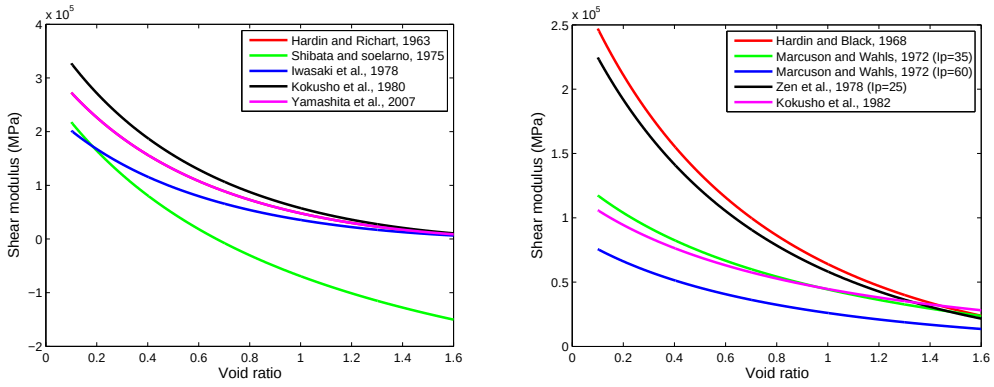

Figure 7.7 – Empirical void ratio correlations

Equation 7.1 depends solely on the prior calculation of void ratio and therefore is often used due to its ease of application. Alternatively, researchers have presented formulations which depend on additional experimentally calculated variables. For example, (Larsson & Mulabdic, 1991) outlined a correlation based upon liquid limit and undrained shear strength. Also, (Hardin & Black, 1963) presented a correlation based upon both void ratio and over-consolidation ratio (OCR). Despite this OCR is difficult to accurately determine even through lab testing thus making it difficult for practical use. Some empirical relationships for calculating OCR from CPT results are provided by (Lunne, Robertson, & Powell, 1997).

Damping can also be calculated from classical lab test results with (Kramer, 1996) suggesting it can be calculated using the hystersis loop for a soil. Alternatively, several authors propose that damping is highly correlated with normalised shear modulus. As discussed previously, vibrations generated due

to train passage are in the small strain zone thus allowing (Ishibashi & Zhang, 1993) to propose the relationship:

$$D = 0.0065(1 + e^{-0.0145I_p^{1.3}}) \qquad \text{Equation 7.2}$$

This equation is based on solely the plastic modulus (Ip) and has been shown by (Biglari & Ashayeri, 2011) to provide an accurate approximation for a range of soils. Similarly, (J. Zhang, Andrus, & Juang, 2005) present a relationship based on normalised shear modulus. Despite this, for soils undergoing small strain this results in all soils having a damping ratio equal to 0%. If true then all soils in this zone would be purely elastic which is unrealistic.

Alternative formulations have also been presented by (Rollins, Evans, Diehl, & Daily, 1998) and (Kagawa, 1993), both based on using cyclic shear strain values.

7.3.1.5 Bender element testing

Bender element testing is used to determine the compressional and shear wave speed of soil (Yamashita et al., 2007). The sample is placed within the top and bottom pedestals of triaxial testing equipment and two bender elements (receiver and transmitter) are inserted, connecting the sample to the pedestals.

An electrical current, typically in the form of a sine wave pulse, is then passed through the bender elements causing them to bend. This bending is

used to create shear and compressional waves within the soil sample. These waves are recorded and are used to calculate the wave speeds of the soil. Typically, the time difference between arrival times is used for speed calculation, although analysis of first peaks and cross-correlation methods are sometimes used.

Once the shear and compressional wave speeds have been calculated, Young's modulus, Poisson's ratio and density can be calculated. It is also possible to calculate damping ratio using bender element testing although this has not been widely accepted as a reliable technique (Karl, 2005).

7.3.1.6 Resonant column testing

The resonant column test is used to determine Young's modulus, shear modulus and damping ratio. The soil sample is confined between a (typically fixed) bottom end and a free/fixed top end which is used to both excite the sample and measure its response. Longitudinal excitation of the top is used for Young's modulus investigation and torsional excitation is used for shear modulus calculation. The sample is excited using a variable frequency which is increased until the first eigenfrequency is reached. This frequency is recorded alongside the amplitude of vibration. Assuming the soil density is known, the resonant column geometry and the constraint conditions are used to calculate shear modulus and Young's modulus.

The excitation is then switched off and the decay of free vibrations is recorded. The logarithmic decrement method can be used to determine the damping ratio from these free vibrations. Alternatively, analysis of the frequency response function calculated using the bandwidth of the resonance peak can be used. Further information regarding best practise can be found in (ASTM D4015 - 07, 2007).

7.3.2 Non-invasive techniques - MASW

Multi-channel analysis of surface waves (MASW) is a non-invasive testing technique used to identify soil layering and to calculate shear wave speeds (with the additional capability of estimating compressional wave speeds and damping ratio). It is advantageous compared to invasive tests because it does not disturb the ground meaning it can be used at sensitive sites. Additionally, it provides a continuous profile of the underlying soil, unlike the SPT which only generates data at discrete depths.

Unlike alternative non-invasive methods such as ground penetrating radar (Millard, Shaw, Giannopoulos, & Soutsos, 1998) which use high frequency radio waves to image subsurfaces, MASW uses lower frequency seismic waves. Data collection is performed by exciting the soil surface (e.g. using a hammer blow or a swept sine source) and measuring the vibration response at a variety of distances using one component (vertical) low frequency geophones.

Originally (Nazarian & Milind, 1993) and (Yuan & Nazarian, 1993) proposed the SASW method using a small number of geophones, however it is now preferential to use the MASW method (Park, Miller, & Xia, 1999), which typically requires at least 16-24 geophones. Recommended acquisition parameters are shown in Figure 7.8.

Depth (Z_{max})[1] (m)	Source (S)[2] (lb)	Receiver (R)[3] (Hz)	Receiver Spread (RS) (m)				SR Move[6] (dx)			Recording[8]				
			Length[4] (D)	Source Offset[5] (X_1)	Receiver Spacing (dx)		Lateral Resolution[7]			dt[9] (ms)	T[10] (sec)	Vertical Stack[11]		
					24-ch*	48-ch	High	Medium	Low			C	N	VN
≤ 1.0	≤ 1	4.5–100	1–3	0.2–3.0	0.05–0.1	0.02–0.05	1–2	2–4	4–12	0.5–1.0	0.5–1.0	1–3	3–5	5–10
	(1)**	(40)	(2.0)	(0.4)	(0.1)	(0.05)	(1)	(2)	(4)	(0.5)	(0.5)	(3)	(5)	(10)
1–5	1–5	4.5–40	1–15	0.2–15	0.05–0.6	0.02–0.3	1–2	2–4	4–12	0.5–1.0	0.5–1.0	1–3	3–5	5–10
	(5)	(10)	(10)	(2)	(0.5)	(0.25)	(1)	(2)	(4)	(0.5)	(0.5)	(3)	(5)	(10)
5–10	5–10	≤ 10	5–30	1–30	0.2–1.2	0.1–0.6	1–2	2–4	4–12	0.5–1.0	0.5–1.0	1–3	3–5	5–10
	(10)	(4.5)	(20)	(4)	(1.0)	(0.5)	(1)	(2)	(4)	(0.5)	(1.0)	(3)	(5)	(10)
10–20	≥ 10	≤ 10	10–60	2–60	0.4–2.5	0.2–1.2	1–2	2–4	4–12	0.5–1.0	1.0–2.0	1–3	3–5	5–10
	(20)	(4.5)	(30)	(10)	(1.5)	(1.0)	(1)	(2)	(4)	(0.5)	(1.0)	(3)	(5)	(10)
20–30	≥ 10	≤ 4.5	20–90	4–90	0.8–3.8	0.4–1.9	1–2	2–4	4–12	0.5–1.0	1.0–2.0	1–3	3–5	5–10
	(20)	(4.5)	(50)	(10)	(2.0)	(1.5)	(1)	(2)	(4)	(1.0)	(1.0)	(3)	(5)	(10)
30–50	≥ 10 (20)	≤ 4.5	30–150	6–150	1.2–6.0	0.6–3.0	1–2	2–4	4–12	0.5–1.0	1.0–3.0	1–3	3–5	5–10
	or passive	(4.5)	(70)	(15)	(3.0)	(2.0)	(1)	(2)	(4)	(1.0)	(1.0)	(3)	(5)	(10)
> 50	≥ 10 (20)	≤ 4.5	> 50	> 10	> 2.0	> 1.0	1–2	2–4	4–12	0.5–1.0	≥ 1.0	1–3	3–5	5–10
	or passive	(4.5)	(150)	(30)	(6.0)	(4.0)	(1)	(2)	(4)	(1.0)	(2.0)	(3)	(5)	(10)

Figure 7.8 – MASW recommended parameters (Park Seismic, 2013)

The input force (e.g. hammer blow) excites the soil using a spectrum of frequencies. The low frequency energy imparted into the ground penetrates deep into the soil where the layers are typically stiffer and have a lower damping ratio than the upper layers. This results in seismic waves that have high phase velocities and low attenuation. In contrast the high frequency waves have shorter wavelengths and therefore do not penetrate as deep as the low frequency waves. These upper layers typically have low stiffness's and high damping ratios, resulting in low phase velocities. These variations in phase velocity and attenuation coefficient with frequency allow for the plotting of a

ground dispersion curve. Inversion of this curve facilitates the estimation of soil parameters.

Before the MASW technique was fully established, the SASW method ((Nazarian & Milind, 1993), (Yuan & Nazarian, 1993)) was commonly used. The SASW method involves using two geophones to record a soils response due to excitation. Using the recorded vibration trace histories the phase difference for a single frequency is calculated. This is repeated for different frequencies to build up a dispersion curve.

Instead of calculating individual phase velocities first, the MASW method is used to construct a 2D dispersion curve image (typically plotted in the frequency/wavenumber domain) of the energy accumulated for a range of frequencies. Visual inspection is then used to pick the best fit dispersion curve.

Using the chosen dispersion information, inversion is performed to determine the theoretical soil properties that match the dispersion curve. This inversion problem cannot be solved directly. Instead optimisation techniques must be used in an attempt to find soil parameters that correspond best to the dispersion curve. The parameters that are optimised to match the dispersion curve are P-wave speed and S-wave speed. S-wave speed is most accurately determined because during the construction of the dispersion curve image the fundamental mode is often easiest to pick and it is dominated by S-wave energy. This is useful for FE modelling because as shown earlier, wave propagation is highly sensitive to Young's modulus, which in turn relies more heavily on S-wave speed than any other parameter.

Density is relatively insensitive to changes in the dispersion curve and therefore during the inversion process it is typically held constant at an average soil value (e.g. 2000 kg/m^3). It is also possible to use MASW results to calculate damping ratio although these techniques have not yet gained widespread acceptance (Karl, 2005). P-wave velocities can be calculated during inversion however as the fundamental mode is not dominated by P-wave energy, results are not as accurate as for S-wave calculation.

An alternative method for calculating P-wave speed is the use of refraction techniques. Refraction can be used either to validate the values calculated during the MASW inversion or to assist in parameter selection of P-wave values for the MASW optimisation procedure.

Refraction analysis is often coupled with the MASW testing procedure because the only difference between each is the post-processing approach. Therefore it is considered as a low cost solution. Instead of constructing a dispersion curve using the experimental data, the geophone responses are used to identify the first arrival of seismic waves at each location. This process is repeated for all excitation locations and the results are collated. Using Snell's law of refraction and reflection between layer interfaces the P-wave speed and layer depths are calculated.

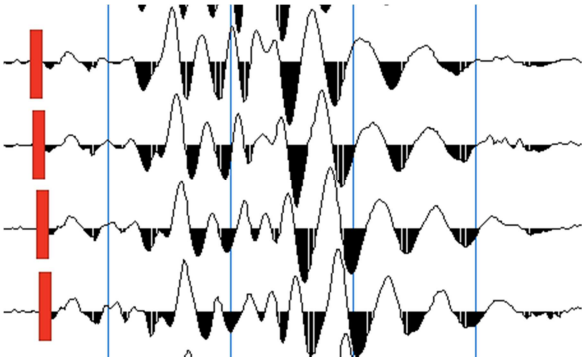

Figure 7.9 - Arrival time identification. (black line: velocity trace, red line: wave arrival)

A disadvantage of both MASW, SASW and refraction testing is that they rely on the assumption that the waves speeds and density in underlying soil increase with depth. If a low velocity zone exists then it will not be revealed because its interface will not reflect seismic waves back to the earth's surface. Although such layers are uncommon, their presence causes inaccuracies in experimental results. An additional drawback is that the parameters obtained from MASW/SASW analysis, although optimised, are non-unique. This arises because the inversion problem cannot be solved directly, and relies on optimisation techniques. Therefore it is always possible that another set of completely different parameters may describe the soil stratum equally well (Schevenels, Lombaert, Degrande, & François, 2008).

A possible alternative to overcome the challenges associated with the traditional MASW method is to post-process the results via full waveform inversion (FWI). Recent developments in FWI are outlined in (Virieux & Operto, 2009), (Tran & McVay, 2012) and (Kallivokas et al., 2013). FWI techniques

allow for a 3D ground profile to be created and can are capable of identifying low density layers. Despite this, FWI post-processing is time consuming due to the large computational demands required for 3D global optimisation (MASW testing is often undertaken prior to FWI to aid optimisation). Additionally, for small and/or shallow domains dominated by Rayleigh waves, such as is the case for railway vibration, full waveform inversion techniques are still experimental. This experimental nature combined with high computational requirements makes current FWI approaches impractical for most railway vibration applications.

7.4 Experimental cost appraisal

Some approximate cost information for the tests described in this chapter is shown in Table 7.6. Costings were calculated based upon quotes from (Holequest, 2013) and information provided by (Karl, 2005).

Test method	Comments	Cost (£ - excluding VAT)
Desktop study	e.g. Technics Group, Envirocheck, Groundsure	150
Field tests		
SPT	Based on a 12m deep profile, measurements every 1m. Includes mobilisation, labour and drilling	1000
CPT (conventional)	Based on a 12m deep profile, measurements every 1m. Includes mobilisation, labour and drilling	1150
Cross-hole test	Based on 4 x 12m deep boreholes. Includes mobilisation, labour and drilling	5500
MASW	Based on 1 day of site work and 1 day of post-processing	4000
Laboratory tests		
Resonant column test	Costings for 1 sample and 4 consolidation stages	2000
Bender element test	1 sample and 1 consolidation stage, including triaxial testing	1300
Classical lab testing	Triaxial testing, Moisture content	500

Table 7.6 – Typical geotechnical survey costs

7.5 Conclusions

A wide range of geophysical tests exist for the determination of soil properties. Some tests are more suitable for calculating the material properties necessary to describe seismic wave propagation than others.

When planning an investigation into ground borne vibration levels it is important that the project budget and aim of the study are well defined. If the purpose is an initial estimate where long sections of track are to be analysed then it will be cost prohibitive to perform soil investigations such as MASW testing or borehole drilling. Instead a desktop study in conjunction with typical soil properties and empirical correlations should be used for assessment. Such techniques are inexpensive and provide accuracy that is generally acceptable for initial estimates (e.g.(RPS, 2004)).

The most common type of existing soil data is SPT 'N values'. A variety of empirical correlations between 'N value' and shear wave velocity, for sand, clay, silt and gravel have been presented in previous literature. These correlations have been collected and combined to create four new correlations for calculating shear wave velocity from SPT 'N values'.

If the project requires a detailed prediction of vibration levels (e.g. for highly sensitive sites such as hospitals) then it is necessary to obtain a more accurate description of the underlying soil properties. If lab testing is preferred then bender element or resonant column testing is preferable to traditional lab testing (e.g. triaxial) because they can determine FE parameters directly rather than using empirical correlations. If the site is sensitive to invasive techniques then non-invasive tests such as MASW are more applicable in comparison to tests that rely on borehole drilling.

The next chapter outlines an experimental campaign performed in the absence of historical borehole information. The MASW method is chosen as the testing method to categorise the soil properties due to project constraints.

Chapter 8. Experimental work

8.1 Introduction

Experimental field data is required to validate numerical prediction models. Without validation it is difficult to assess whether a model is capable of predicting results that are similar to the physical problem. Additionally, experimental work is useful for investigating physical characteristics that are difficult to model using numerical methods (e.g. high frequency content).

(Galvin & Domínguez, 2009) collected experimental results on the Cordoba-Malaga line using accelerometers for the purpose of validating a numerical model (Galvin et al., 2010a). The underlying soil properties were determined using the spectral analysis of surface waves (SASW) method. Despite this, raw data from the tests was unpublished. Similar validation studies with unpublished data sets include (Salvador et al., 2011), (Hendry, Barbour, & Hughes, 2010), (Chatterjee et al., 2003), Rossi, (Triepaischajonsak, Thompson, Jones, Ryue, & Priest, 2011), (With, Bahrekazemi, & Bodare, 2006), and (Bowness, Lock, Powrie, Priest, & Richards, 2007).

One of the few published data sets freely available is (Degrande & Schillemans, 2001b). This data was collected on the Brussels-Paris high speed line in December 1997. The passage of nine Thalys high speed trains at variable speeds were recorded using accelerometers and then numerical integration was

used to convert the results to velocity time histories. The underlying soil stratum characteristics were obtained using SASW tests.

The physical properties of the soil at the test site chosen by (Degrande & Schillemans, 2001b) were associated with low stiffness's and low wave speeds (V_p=149m/s, V_s=80m/s, V_r=68m/s). To model these soil properties at the frequencies of interest using techniques such as the FE method, requires a very fine mesh. This becomes problematic because when modelling vibrations in the far field, the soil domain must be large. Using a small cell size to model a large domain means that the total number of cells becomes large (Figure 4.3) and the computational power required to model the problem becomes impractical. Therefore it is difficult to use the (Degrande & Schillemans, 2001b) data set to validate the previously described numerical models.

To overcome the challenges associated with (Degrande & Schillemans, 2001b) experimental investigations were performed at six locations on two separate railway networks. The first four sites were located in Belgium, close to the French border and the other two other sites were located on a line in the South-West of England. In addition to model validation, the sites in Belgium were also chosen to investigate the effects of earthworks profiles, train type, train speed and abutment presence on vibration propagation.

8.2 Test site descriptions

The following provides details regarding the geography of each test site and the tests performed. All sites were chosen carefully in an attempt to comply as closely as possible with the recommendations set out in (Asmussen, 2011c). For all tests at all sites, geophones were mounted on 150mm spikes perpendicular to the track and each 3 component sensor was aligned to the desired orientation using a spirit level. All signals were processed using a 24 channel Geode exploration seismograph and recorded using a Panasonic Toughbook CF-19.

The natural frequency of the SM-6 geophones was 4.5Hz. This meant that vibrations propagating with frequencies less than 4.5Hz were dampened due to the natural geophone characteristics. To overcome this, the signals were post-processed and a filter was applied to the frequency content between 0-4.5Hz. This filter was used to magnify the geophone response curve (Appendix A), by multiplying it by the inverse of the response curve at frequencies below 4.5Hz.

Although this post-processing step could have been avoided by using accelerometers which are better equipped to model low frequencies (i.e. below 4.5Hz), accelerometers can be greatly affected by adverse weather conditions. Geophones are more rugged than accelerometers and the recorded signal is less likely to be contaminated with spurious excitations due to wind and rain. One possible solution, as proposed by (Triepaischajonsak, 2011), is to place

upturned buckets over each sensor. Despite this, the effect of each bucket may also effect the vibration response.

8.2.1 Site 1 – Mons (at-grade)

Site 1 consisted of an at-grade railway section (Figure 8.1 and Figure 8.2) 4km south of the town of Leuze-en-Hainaut, with global coordinates (50.560914, 3.624199). The site was accessible by car but was not located near any major roads thus eliminating the effect of ambient background vibration. Similarly, the access road did not experience any additional vehicle passes throughout the duration of testing.

The track was a classically ballast track, supported by ballast, subballast and subgrade layers, with thicknesses 0.3m, 0.2m and 0.5m respectively. The rails were continuously welded UIC 60 rails with a mass of 60kg/m^3 and fixed to the prestressed concrete sleepers via Pandrol clips. The rails were also supported by railpads with thickness 0.01m. The regularity quality of the rails was assumed to be very high because grinding had been performed one week before testing.

	3 component measurements							
Distance from rail (m)	**9**	**11**	**15**	**19**	**23**	**27**	**31**	**35**
Components measured*	H1, H2, V1	H1, H2, V1	H1, H2, V1	H1, H2, V1	H1, H2, V1	H1, H2, V1	H1, H2, V1	H1, H2, V1
*H1=Horizontal component, H2=horizontal component, V1=vertical component								

Table 8.1 - Three component geophone arrangement

	1 component measurements											
Distance from rail (m)	**9**	**11**	**13**	**15**	**21**	**25**	**29**	**33**	**37**	**41**	**45**	**49**
Component measured*	V1	V1	V1	V1	V1	V1	V1	V1	V1	V1	V1	V1
Distance from rail (m)	**53**	**57**	**61**	**69**	**73**	**77**	**81**	**85**	**89**	**93**	**97**	**100**
Component measured*	V1	V1	V1	V1	V1	V1	V1	V1	V1	V1	V1	V1
*V1=vertical component												

Table 8.2 - One component geophone arrangement

Two distinct test setups were deployed, the first to record three component vibration levels at distances from 9m-35m from the closest track (Figure 8.2,Table 8.1), and the second to record vertical vibration from 9m-100m from the track (Table 8.2). The first setup comprised of 8 low frequency, 3 component, SM-6 geophones, with sensitivity 28.8 V/m/s (Appendix A). For the second setup, 24 low frequency, 1 component (vertical), SM-6 geophones, also with sensitivity 28.8 V/m/s (Appendix A) were used. In addition, 2

accelerometers were placed parallel to the track (9m from the nearest rail) to aid in train speed calculation.

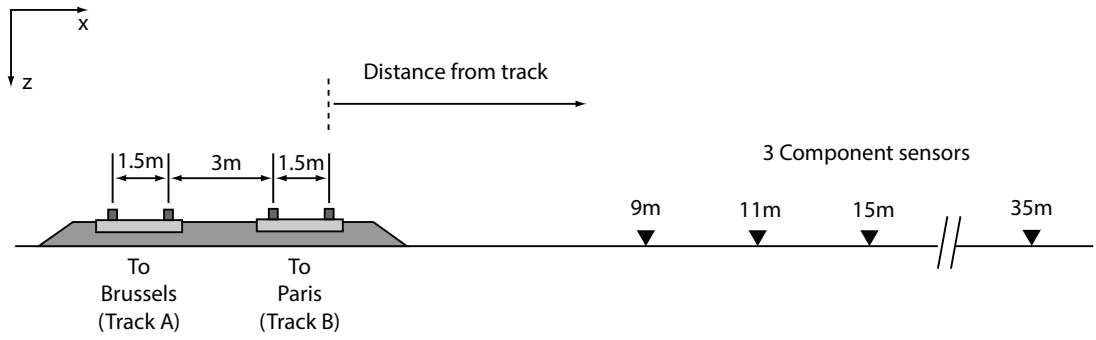

Figure 8.1 - Three component testing at site 1

Figure 8.2 - Belgian at-grade test site

8.2.2 Site 2 – Mons (embankment)

Site 2 was also located on the Paris-Brussels line, North-East of the town of Braffe, with coordinates (50.557697, 3.602763). The track configuration consisted of an embankment 5.5m high with a slope of 30 degrees. The

experimental methodology and geophone arrangement was consistent with site 1. As was the case for site 1, the testing location was situated far from any sources of background vibration such as road traffic. Embankment construction records revealed that it was constructed from a mixture of silt and clay, originating from the local area. The track components were identical to that of test site 1.

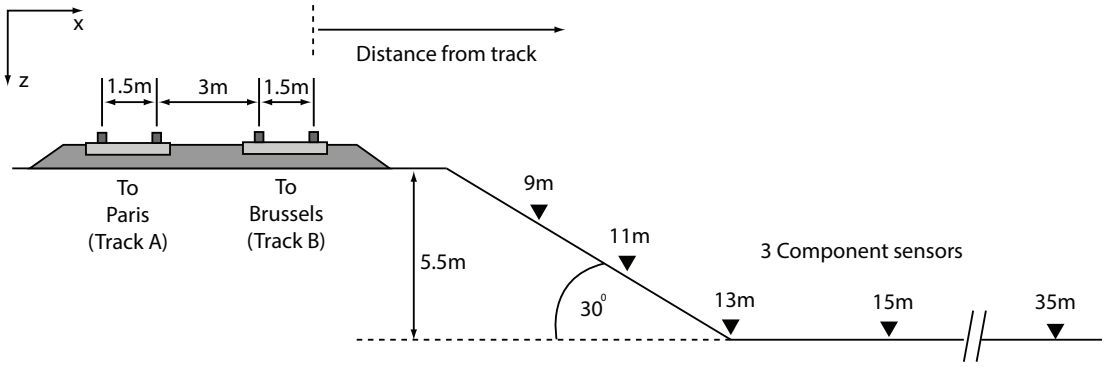

Figure 8.3 - Three component testing at site 2

Figure 8.4 - Belgian embankment test site

8.2.3 Site 3 – Mons (Cutting)

Site 3 was also located on the Paris-Brussels line, North-West of the town of Braffe, with coordinates (50.555495, 3.569042). The track configuration consisted of a cutting (excavated embankment), 7.2m high at a gradient of 25 degrees. The track components were identical that of test site 1.

Two experimental setups were used also in a similar manner to that of site 1. Despite this site 3 was situated approximately 90m from an infrequently used road. Therefore the furthest away vertical component geophones could not be placed at their required distance. Rather than adjust the spacing of all 24 geophones and making a direct comparison between results difficult, the furthest three geophones were not deployed.

On several occasions, road traffic was experienced during train passage. In this event, rather than attempting to filter the signal to remove contamination, all contaminated recordings were deleted. Only non-contaminated signals were saved, and have been included in this report.

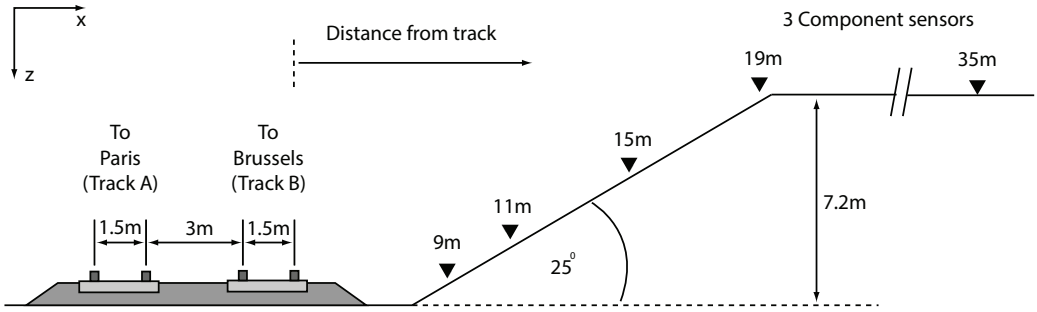

Figure 8.5 – Three component testing at site 3

Figure 8.6 - Belgian cutting test site

8.2.4 Site 4 – Mons (Abutment)

Site 4 was located approximately 100m East of site 2 and thus the track components were identical that of test site 2. The embankment was also identical to site 2 except that there was a concrete tunnel passing through the embankment and beneath the track.

This tunnel served as a minor road for car passage and is shown in Table 8.7. At this site a hybrid geophone setup was deployed, combining aspects of both of the previously described setups (Table 8.3).

	1 component measurements											
Distance from rail (m)	**19**	**19**	**19**	**20**	**23**	**23**	**23**	**25**	**25**	**25**	**28**	**31**
Component(s) measured*	H1	H2	V1	H2	H1	H2	V1	H1	H2	V1	V1	H1
Distance from rail (m)	**31**	**31**	**35**	**35**	**35**	**36**	**44**	**52**	**60**	**68**	**76**	**82**
Component(s) measured*	H2	V1	H2	H1	V1	V1	V1	V1	V1	V1	V1	V1
*H1=Horizontal component, H2=horizontal component, V1=vertical component												

Table 8.3 - Geophone arrangement

Figure 8.7 - Belgian embankment/tunnel test site

8.2.5 Site 5 – HS1 (at-grade)

Site 5 was located East of Hollingbourne, England (51.262338, 0.619311). On the side of track measurement the track was at-grade and the opposite side there was an embankment. It was assumed that the embankment on the opposite side would not greatly affect the vibration characteristics at the receivers at the near side. Therefore the test results were considered to have been undertaken on an at-grade section. As the track was part of the high speed network that connected London to Paris and Brussels, the track components were identical to that of test site 1.

South of the track was a motorway. Therefore before the train passage experiments were undertaken, measurements were performed to assess the potential contribution of motorway traffic to the vibration results. It was found that the furthest receivers from the track (and closest to the motorway) were

effected more than the receivers closest to the track. Despite this, it was concluded that these background vibrations only contributed minimally to the velocities observed due to a high speed train passage. Therefore the motorway presence was assumed to have no effect on results. Despite this, due to the close proximity of the motorway, the full array of one component receivers (Table 8.2) could not be deployed. Therefore only three component geophones were used, with the spacing as described in Table 8.1.

Figure 8.8 - English at-grade test site

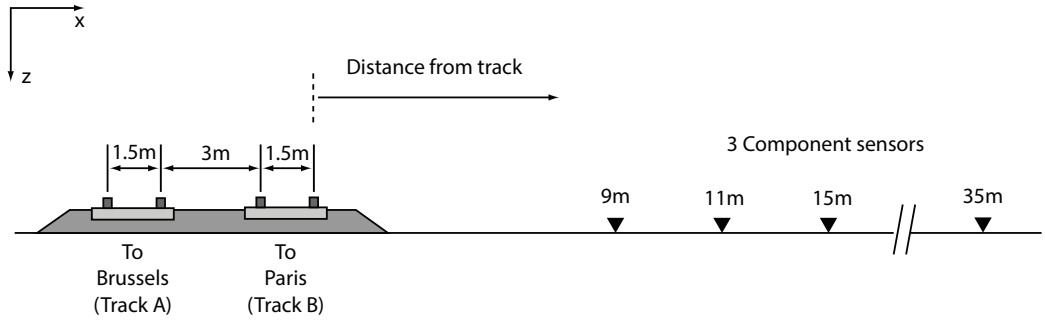

Figure 8.9 - Geophone layout at site 5

8.2.6 Site 6 – HS1 (tunnel)

Site 6 was located several hundred meters South-East of Site 5, and had global coordinates, (51.260935, 0.622144). The site was located above a 'cut and cover' tunnel (Eyehorn tunnel – Figure 8.10), close the town of Hollingbourne. The track components were identical to Site 6 and the Belgian test sites. Only three component geophone tests were performed, using the distances outlined in Table 8.1.

Figure 8.10 - Construction of the Eyehorn tunnel

8.3 Train characteristics

Six train set configurations were recorded across all six sites during the measurement campaign.

8.3.1 TGV Réseau (TGV)

TGV trainsets are manufactured by Alstom and commenced commercial operation in 1993. The TGV-R is the successor to the TGV Atlantique. During testing, each train-set consisted of two power cars at each end (Y230A), six passengers cars in the centre (Y237B) and two lateral cars (Y237A) connecting the power and passenger cars. Bogies were shared between passenger cars and the power cars had two separate bogies each (Figure 8.11). Table 8.4 shows the specification of the TGV trainset. TGV passage was recorded at sites 1-4.

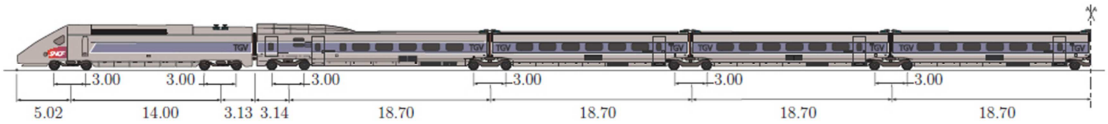

Figure 8.11 - TGV configuration

	TGV	
	Driving + central cars	**Passenger cars**
Half-car body mass (kg)	25000	17500
Bogie mass (kg)	5800	3300
Wheelset mass (kg)	1600	1750
Primary suspension stiffness (MN/m)	4.3	1.4
Primary suspension damping (kNs/m)	70	40
Secondary suspension stiffness (MN/m)	1.423	450
Secondary suspension stiffness (kNs/m)	24	120

Table 8.4 - TGV specification

8.3.2 Thalys and Thalys double (Thalys)

Thalys high speed train sets commenced operation on European high speed lines in 1998 and have a maximum commercial speed of 300 km/h. They are derived from the TGV and manufactured by Alstom. The total train length spans 200m. Double Thalys train sets use identical cars as the single Thalys, however there is twice the number of passenger cars. Thalys passage was recorded at sites 1-4.

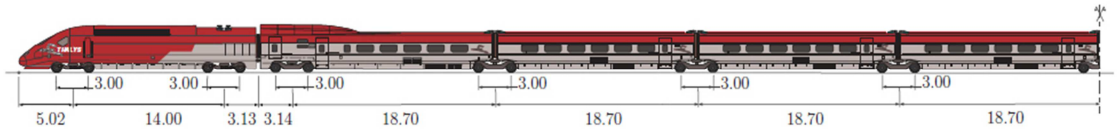

Figure 8.12 - Thalys configuration

	Thalys		
	Bogie Y230A (Driving car)	**Bogie Y237A (Lateral car)**	**Bogie Y237B (Passenger car)**
Half-car body mass (kg)	26721	14250	20426
Bogie mass (kg)	3261	1400	8156
Wheelset mass (kg)	2009	2050	2009
Primary suspension stiffness (MN/m)	2.09	1.63	2.09
Primary suspension damping (kNs/m)	40	40	40
Secondary suspension stiffness (MN/m)	2.45	0.93	2.45
Secondary suspension stiffness (kNs/m)	40	40	40

Table 8.5 – Thalys specification

8.3.3 Eurostar TransManche (Eurostar)

The Eurostar was manufactured by Alstom and has been operational since 1993. Its length of 394m makes it longer than both the Thalys and TGV and it is capable of holding 750 passengers. In common with the Thalys and TGV trainsets, wheelspacing is identical and it consists of three car types: driving cars at the ends, lateral cars next to the driving cars and passenger cars in the middle. The entire trainset consists of 20 carriages. Wheel layout is

shown in Figure 8.13 and the trainset specifications are shown in Table 8.6. Eurostar passage was recorded at all sites.

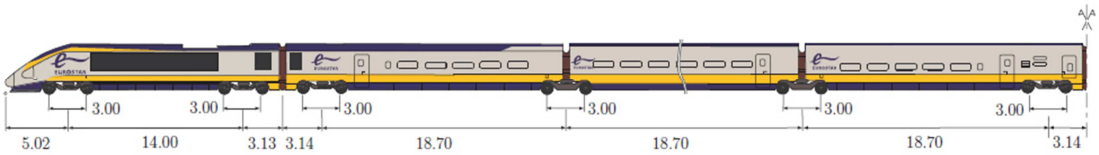

Figure 8.13 – Eurostar configuration

	Eurostar		
	Bogie Y230A (Driving car)	**Bogie Y237A (Lateral car)**	**Bogie Y237B (Passenger car)**
Half-car body mass (kg)	27083	10802	17842
Bogie mass (kg)	3075	2363	9580
Wheelset mass (kg)	2046	2046	2046
Primary suspension stiffness (MN/m)	2.63	2.07	2.2
Primary suspension damping (kNs/m)	12	12	12
Secondary suspension stiffness (MN/m)	3.26	0.61	0.91
Secondary suspension stiffness (kNs/m)	90	4	2

Table 8.6 – Eurostar specification

8.3.4 British Rail Class 395 (Javelin and double Javelin)

Javelin trainsets were designed by Hitachi specifically for the UK rail network to provide a trainset that was compatible with both the existing UK network and High Speed 1 (HS1) connecting London and Paris. They consist of

six carriages with driving pantograph trailers at each end and four passenger cars in the centre. The driving cars have an approximate weight of 47,000kg and the passenger cars had an approximate weight of 45,000kg. The total train length was 122m which is shorter than many other high speed trains, however it is possible to connect two trainsets together, thus doubling the length and number of carriages. Javelin trainsets commenced commercial operation in December 2009. Their passage was recorded at sites 5 and 6.

8.4 Train speed calculation

Approximate train speeds were obtained using tachymeter information provided by the train operator, Infrabel. In an attempt to minimise tachymeter inaccuracy train speeds were also calculated experimentally. During the field experiments, an additional accelerometer was placed close to the track. This was a pre-calibrated, IEPE Dytran 3100B accelerometer with a sensitivity of 100 mV/g. Results were recorded using a 4 channel Svantek, Svan 958 sound and vibration analyser.

The high sensitivity and low natural frequency of the accelerometer allowed for high accuracy recording of the wheel and bogie passage events. To calculate the train speed a MATLAB program was developed to automatically calculate the train speed from the recorded accelerations. First the signal was passed through a 25Hz low-pass filter to remove high frequency content associated with the track and soil excitation mechanisms (Figure 8.14). This isolated the frequencies associated with the train passage.

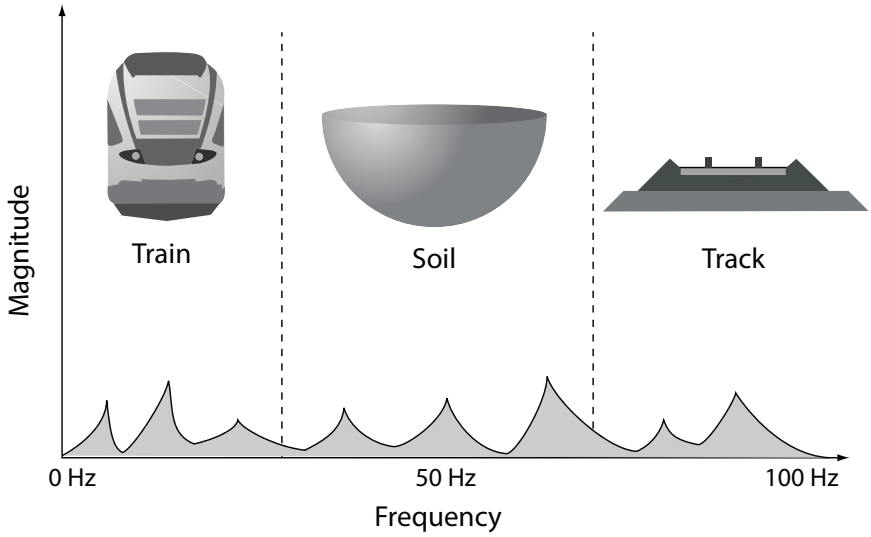

Figure 8.14 – Train, track and soil excitation mechanisms

Then a moving average was used to further isolate the wheel and bogie passage events. This made the local maxima associated with each passage clearly identifiable and they were then automatically selected (Figure 8.15). Using the wheel and bogie spacing for each trainset, the train speed was calculated.

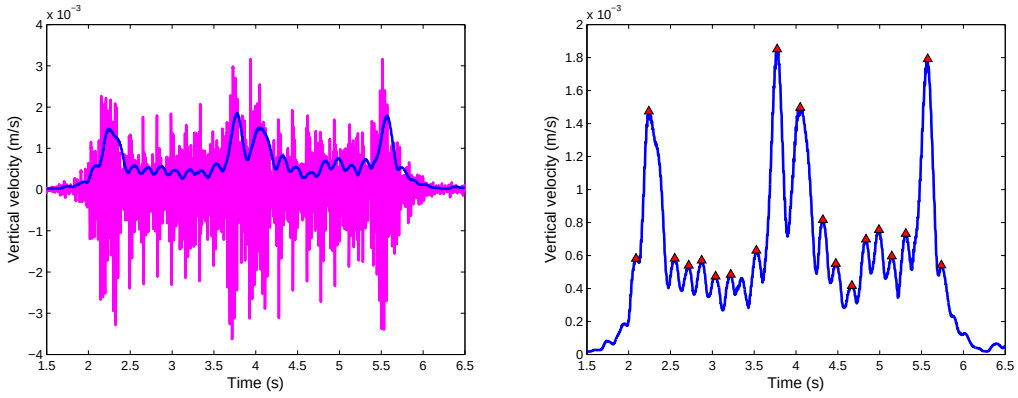

Figure 8.15 – Train speed calculation example. (a) Left: moving average, (b) Right: local maxima selection)

8.5 Passages recorded

Testing at sites 1-4 was undertaken over a three day period and 50 train passages were recorded. This consisted of 23 Thalys passages, 12 Eurostar passages and 15 TGV passages. 29 of the passages were along the nearest track to measurement and 21 were on the further away track. The analysis presented later in this chapter is based upon the results from these sites, made possible due to the similarities in soil properties, track characteristics and train configurations.

Testing at sites 5 and 6 was also undertaken over the course of three days, with a total of 31 train passages recorded. Due to the large experimental variance between the Belgian (sites 1-4) and English test sites (5-6), the English results were used solely for validation, rather than for direct comparison with those collected in Belgium.

8.6 Soil stratum characteristics

To determine the material properties of the soils at each test site, a multi-channel analysis of surface waves methods was used in conjunction with a desktop survey of existing soils data. As discussed in Chapter 7, MASW techniques are non-invasive and do not require lab testing. This was important because all test sites were located on private land, for which invasive testing

permission could not be obtained. Therefore MASW was the most attractive option.

8.6.1 Experimental setup

The MASW experimental setup is shown in Figure 8.16. Excitation was provided using a 12lb PCB 086D50 impact hammer with on-board accelerometer. The accelerometer was connected to a data acquisition unit using a microdot connector. This allowed for calculation of the input force exerted by each hammer blow. For each impact the experimental engineer stood behind the excitation location (i.e. outwith the line between the excitation location and the first sensor). This step was taken to reduce the effect of the engineers mass on the vibration propagation.

Rather than excite the ground directly, two striking/excitation plates were tested. The lighter plate (5kg) was found to 'bounce' upon impact with the hammer, thus providing poor coupling with the soil. This was important because bouncing generated secondary ground waves which made post-processing difficult. The heavier plate (15kg) provided much superior soil coupling and was used for all subsequent measurements. Alternative approaches to coupling have been presented by (Schevenels et al., 2008) and (Triepaischajonsak, 2011), who used cast in-situ concrete and 'Plaster of Paris' respectively to couple the plate and soil. Despite this, comparisons between using these coupling materials and a heavier impact plate were not performed, making their performance benefits unclear. Additionally, there are two drawbacks of using these methods. Firstly, the curing process of concrete and

'Plaster of Paris' is time consuming meaning fewer tests can be performed in the same timeframe. Secondly, casting these materials in the ground is achieved through the excavation of soil which is an invasive process. The experiments undertaken in this thesis were performed on private land, meaning it was important that disturbance to the local area was minimised. Therefore the heavier plate with no coupling material was chosen.

24 Low frequency (4.5Hz), vertical component, SM-6 geophones (Appendix A) were placed parallel to the railway track. The array was placed far enough away from the track to ensure the results were not contaminated from potential artefacts close to the line, but close enough to ensure that the soil properties were representative of those beneath the track. No MASW measurements were undertaken during train passage.

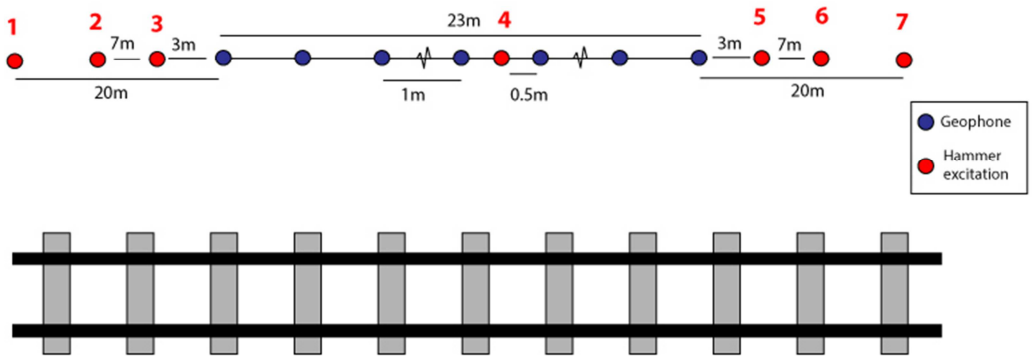

Figure 8.16 – MASW setup

Figure 8.17 – In-situ placement of geophones

Geophone spacing was 1m as recommended by (Park Seismic, 2013) and each sensor was coupled to the ground using 150mm spikes. Excitation was performed at 7 individual locations by striking an embedded metal impact plate. Six excitations were performed at each location, consisting of two steel tipped hammer impacts, two vinyl tipped hammer impacts and two rubber tipped hammer impacts (Appendix A). Therefore 42 impacts were performed at each test site. All results were amplified using a high gain and recorded using a Panasonic Toughbook in SEG-2 format. The gain was removed during post-processing.

8.6.2 Multichannel analysis of surface waves

The MASW results were analysed using Geopsy (Wathelet, 2008a) and sub-program Dinver (Wathelet, 2008b). Geopsy is a graphical user interface (GUI) capable of generating dispersion curve plots (i.e. frequency vs wavenumber) from the 24 recorded signals (Figure 8.18). To improve the

clarity of the dispersion plots, maximum amplitude criteria was used as suggested by (Triepaischajonsak et al., 2011). Although individual dispersion plots could have been calculated using MATLAB, Geopsy was advantageous because it provided a straightforward method to create dispersion plots based on multiple excitations. Additionally, the chosen curves were compatible with Dinver. Therefore the best fit dispersion curves were chosen visually and exported for use in sub-program Dinver.

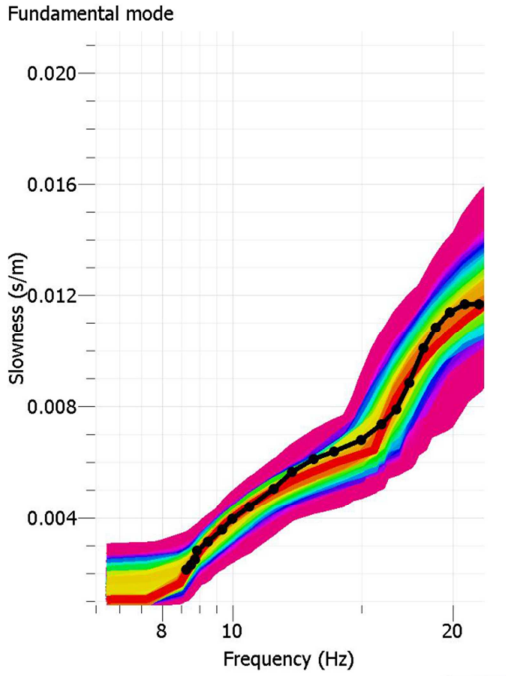

Figure 8.18 – Example experimental dispersion curve (red), and numerically predicted dispersion curve (black)

To perform the inversions using Dinver, density was held constant at 2000 kg/m^3. Shear wave speed is highly independent from density and therefore is typically held constant to increase the convergence rate and

reliability of the parameter optimisation process. The inversion process was used to calculate the layer depths and wave speeds of the underlying soil. P-wave profiles were validated using a refraction analysis, performed using the commercial seismic software package, SiesImager/2D. Sub-module PickWin was used to identify first arrivals and sub-module Plotrefa was used to calculate the P-wave velocity profile. Geopysy MASW results were found to be consistent with SeisImager results.

As an additional check, a desktop study was undertaken by comparing results to existing soil information. For sites 1-4, generalised soil maps were available describing the soil layer permutations and composition of each layer. For sites 5-6, borehole information was available. For all sites, the experimental findings were generally consistent with the existing soil records (Appendix A). Once the wave speeds had been determined with confidence, the Young's modulus was calculated using basic material property relationships.

8.6.3 Classification of soil properties

Figure 8.19 describes the soil properties associated with test sites 1-3. Each of the three sites were found to consist of three distinct layers. Each top layer consisted of silt, supported by a layer of sand which in-turn was underlain by a clay layer. As test site 4 was in very close proximity to test site 2 (Belgian embankment site), no MASW tests were undertaken and the soil properties were assumed to be identical to site 2.

The resulting soil properties were in good agreement with existing soil records from the area (Appendix A) and were also similar to those presented by (Kouroussis et al., 2011a) for previous spectral analysis of surface waves (SASW) tests undertaken on nearby soils. It is clear that the soil properties at all three sites were similar in regards to wave speed profile and layer depth/orientation. The only inconsistency was at site 3 which was underlain by a layer of clay that was stiffer than the other two sites.

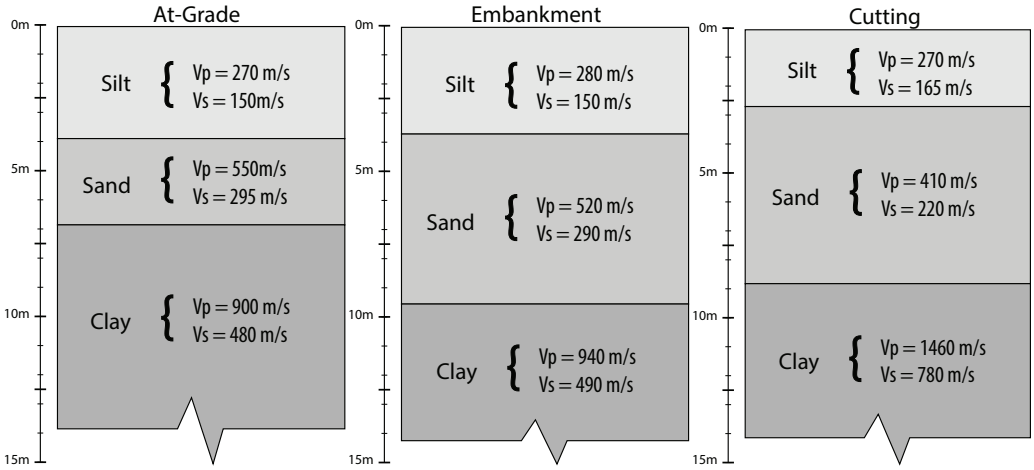

Figure 8.19 – Soil properties at sites 1-3

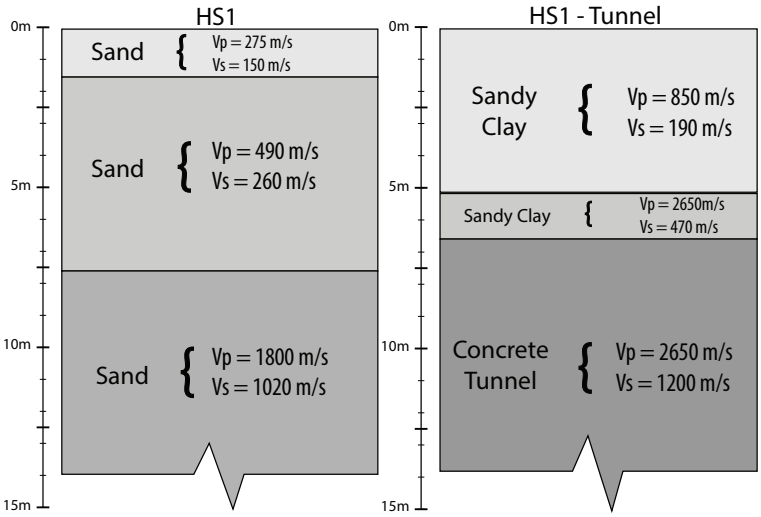

Figure 8.20 - Soil properties at sites 5-6

Site 5 consisted of three layers. Each layer was likely to be an increasingly stiff layer of 'Folkstone Beds sand' as defined in local borehole records. Site 6 was situated above a concrete tunnel section which was located 6.6m below the soil surface. Due to the large contrast in material properties and spherical geometry associated with the tunnel, the MASW tests results below this level were discarded.

8.6.4 Soil damping calculation

After the MASW technique had been applied to determine the soil layering and material properties of each test site, a 2D ABAQUS FE model was constructed using this soil information. This model had a cell size of 0.1m, was excited using a 10Hz Gaussian pulse, and used infinite elements to absorb waves impinging on the model boundary. To allow for the rapid replication of each test site based upon the soil depths and properties obtained through the MASW approach a MATLAB program was developed. This program facilitated the rapid creation of ABAQUS models for any soil layer combination directly using MATLAB.

The model was run numerous times for each test site using different damping values. The results were then compared to the field impact experiments using maximum amplitude criteria (PPV). Although Rayleigh damping is typically specified using two variables (α and β), it was found that it

was sufficient to specify damping using only one degree of freedom. Similarly each site was composed of several layers, each of which was likely to be damped slightly differently, however in the FE model each layer was assumed to be equally damped.

Figure 8.21 shows a sample damping comparison curve that was used via visual inspection to determine the damping coefficient. In this case a value of 0.00025s was found to be the most suitable choice as it yielded results most similar to the experimental ones. The final damping parameters for each site are described in Table 8.7. A similar damping calculation technique has been investigated by (Kouroussis et al., 2011a).

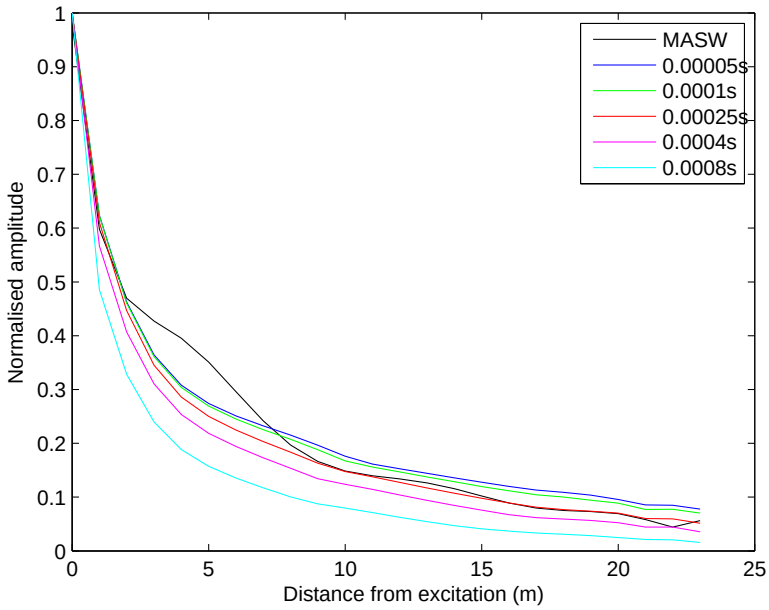

Figure 8.21 – Identification of Rayleigh damping coefficient

	Site number			
	1	2	3	4
Site description	At-grade (Belgium)	Embankment (Belgium)	Cutting (Belgium)	Abutment (Belgium)
Damping coefficient (s)	0.00025	0.0003	0.0003	0.0003

	Site number		
	6	7	
Site description	At-grade (England)	Tunnel (England)	
Damping coefficient (s)	0.0002	0.0002	

Table 8.7 – Rayleigh damping coefficients

8.7 Analysis of results

8.7.1 Three component vibration levels

Figure 8.22 shows the variation in PPV levels for the 3 embankment configurations for the case of near track train passage. For each figure the mean PPV at each location was calculated for all recorded train passages. It should be noted that the 3 subfigures should not be compared directly because each relies on a different combination of locomotive passages. It was found that for all embankment cases, vertical vibration levels (z direction) were of greater magnitude than horizontal vibration levels. Additionally, for the 'at-grade' and

embankment cases, y direction vibrations (perpendicular to the track) appeared to be slightly greater than x direction vibrations (parallel to the track). On average, for all receiver locations, x direction vibration was 61% less and y-direction was 25% less than vertical vibration levels respectively. This was consistent with results presented by (Kouroussis, 2005).

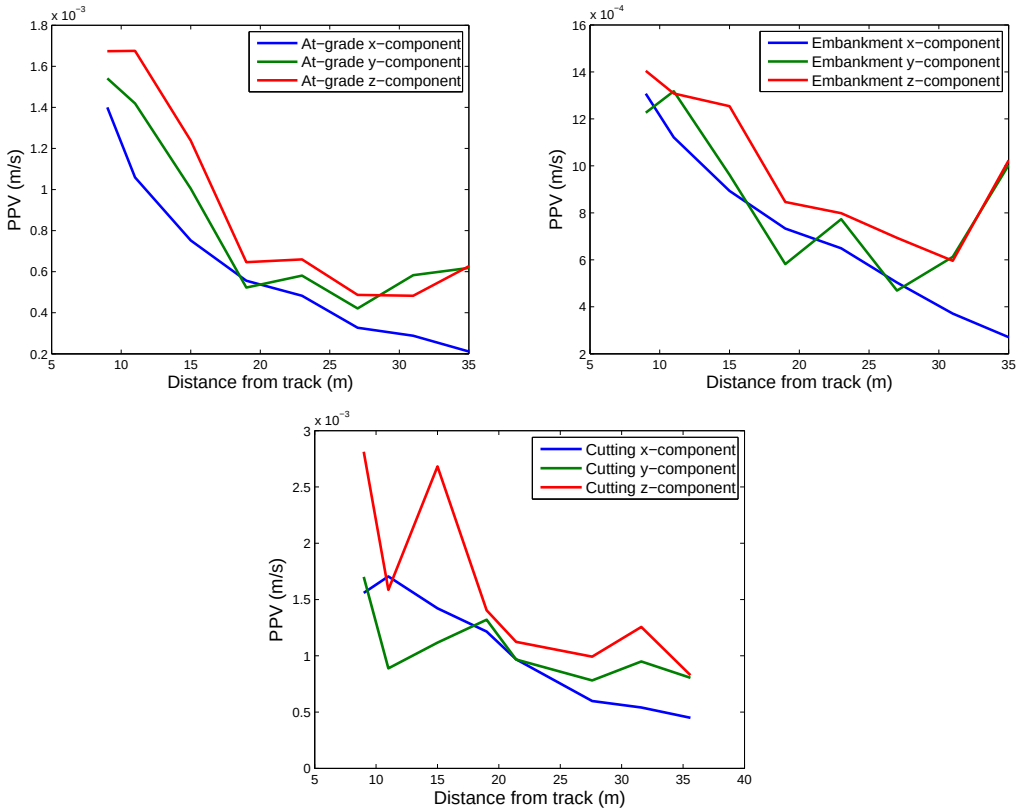

Figure 8.22 – PPV levels for three embankment cases, (a) Top left: at-grade, (b) Top right: embankment, (c) Bottom: cutting

8.7.2 The effect of earthworks profiles

Figure 8.23 shows the effect of earthworks configuration on vibration levels for a passing Thalys high speed train. Thalys passages were chosen because of their low deviance in speed, thus allowing direct comparison. For the at-grade,

embankment and cutting, the train speeds were 291, 293 and 294 km/h respectively. The at-grade and embankment cases generated similar levels of vibration, with the embankment case generating slightly lower levels. On the other hand the cutting generated higher amplitude vibrations in all 3 component directions. This was in contrast to the empirical relationships presented in (Federal Railroad Administration, 2012) which suggests that a cutting "may reduce the vibration levels slightly". This discrepancy may be explained by the minor variance in soil material parameters between test site locations.

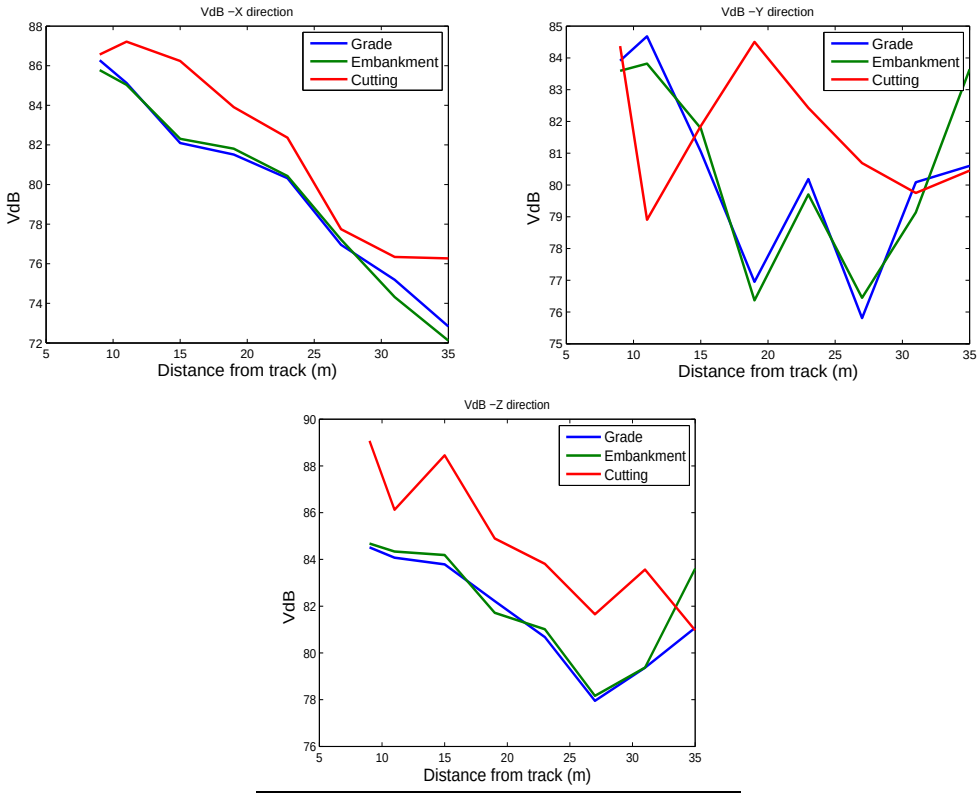

Figure 8.23 – Earthworks profile effects in three component directions, (a) Top left: x, (b) Top right: y, (c) Bottom: z

8.7.3 Near vs far tracks

Figure 8.24 compares mean PPV vertical vibration levels for all trains passing on either the near or far tracks. Again the cutting generated greatest vibration levels. Despite this, there was a strong discrepancy between the at-grade and embankment cases. For the case of the near train passages the embankment exhibited lower vibration levels than the at-grade case, consistent with (Connolly, Giannopoulos, & Forde, 2013). For the far train passage the embankment generated elevated vibration levels in comparison to the at-grade case. This is because when the far track was excited the receivers experienced the superposition of vibration from two sources: directly from the track and also from the face of the furthest away embankment.

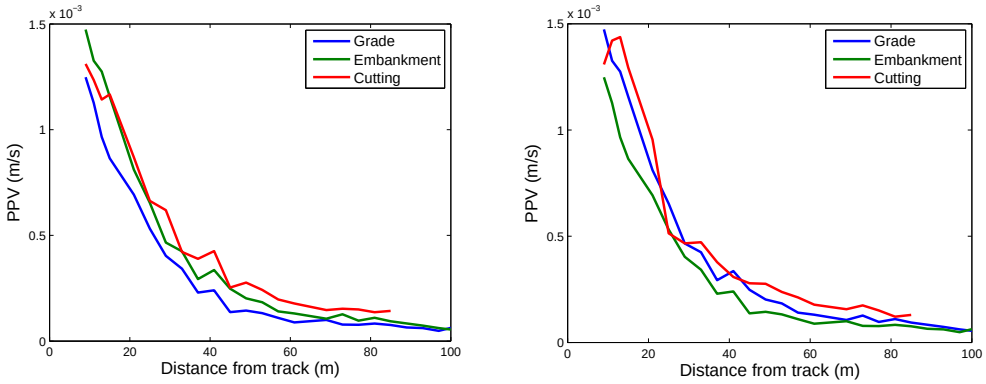

Figure 8.24 – Embankment vibration, (a) Left: near track, (b) Right: far track

8.7.4 Far field vibration vs near field vibration

It is observed from Figure 8.23 that vertical vibration levels decayed exponentially with distance from the excitation. This was as expected and was due to geometrical and material damping. For the purpose of comparing near

and far field vibration characteristics, Figure 8.25, Figure 8.26 and Figure 8.27, show how the frequency content of vertical railway vibration varies from near to the far field.

For the at-grade case (Figure 8.25) in the near field the frequency of propagating waves was predominantly between 15-30Hz, with more pronounced peaks at 27-31Hz. In the far field the dominant frequency range was generally still located between 15-30Hz although much less pronounced. A small resonant frequency at 8.8Hz was visible in the near field and was greatly magnified in the far field.

For the embankment case (Figure 8.26) in the near field the frequency range was much broader, and generally higher than the far field, with the main resonant frequency appearing at 141Hz (consistent with the sleeper passage frequency). The majority of near field frequency content was located below this peak, and similarly to the at-grade case there was a large volume of waves propagating in the 15-30Hz range. Additional zones of frequency content were also visible at 50-65 and 80-95Hz. For the far field, a large percentage of this high frequency content had dissipated and the frequency content was located between 5-30Hz. The main peak at 141Hz had disappeared and three main peaks appeared at 8.6, 17.5 and 22Hz.

These higher frequencies were in agreement with numerical results presented by (Ditzel & Herman, 2004). They were generated due to the propagating waves reflecting off the edges of the embankment structure and a proportion of them becoming trapped within the embankment. Additionally,

some higher frequencies may have been caused by the waves reflecting at the numerous horizontal interfaces of compacted material created during the embankments construction.

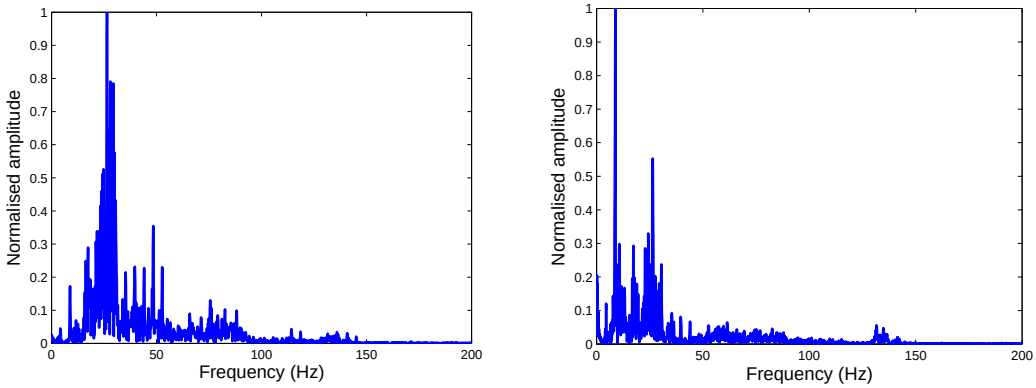

Figure 8.25 - Frequency spectrum at at-grade site, (a) Left: near, (b) Right: far

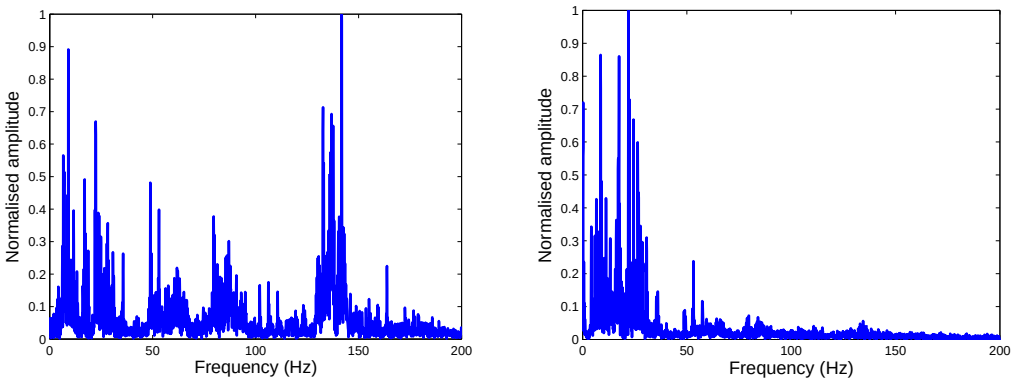

Figure 8.26 - Frequency spectrum at embankment, (a) Left: near, (b) Right: far

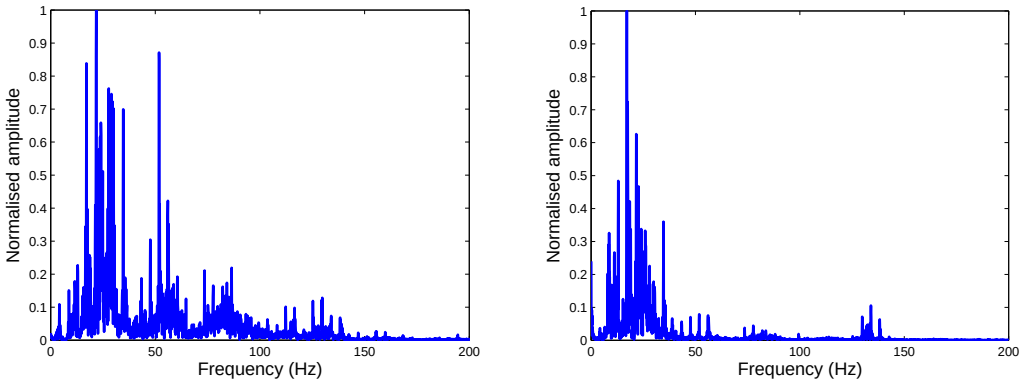

Figure 8.27 – Frequency spectrum at cutting, (a) Left: near, (b) Right: far

For the near field cutting case (Figure 8.27) the frequency content also exhibited a greater spread in comparison to the at-grade case. The first major zone of frequency content was between 17-35Hz, followed by another peak at 52Hz and another smaller region of frequency content around 85Hz. In comparison, a large percentage of the frequency content present in the near field was not visible in the far field results. The lower frequency content was bound in the region 8-35Hz, with a significant eigenfrequency at 17Hz. A low amplitude region of high frequency content was also visible around 130Hz.

It was concluded from the frequency results that the near field vibration levels generated due the presence of an embankment were of much higher frequency in comparison to at-grade tracks. The frequency content of cuttings was also shifted to a higher spectrum than the at-grade case but less so than the embankment case. It was also concluded that the high frequency vibrations generated by the track were damped rapidly as they propagated through the

soil. Only the lower frequency waves, due to their longer wavelengths were able to propagate to larger distances.

8.7.5 Train type comparison

Figure 8.28 shows a comparison of VdB levels between all three train types at site 3. The 3 train speeds were within 3 km/h of each other thus allowing for reliable comparison. The trains produced a similar magnitude of vibration levels at each observation point. The TGV and Thalys trains were most similar whereas the Eurostar passage generated slightly less levels of vibration at distances less than 31m but slightly greater levels at distances greater than this. Regarding frequency content, the dominant frequencies and overall frequency ranges for all train types were very similar. This was because wheel spacing was identical, although the Eurostar has more wheels due to its superior overall length.

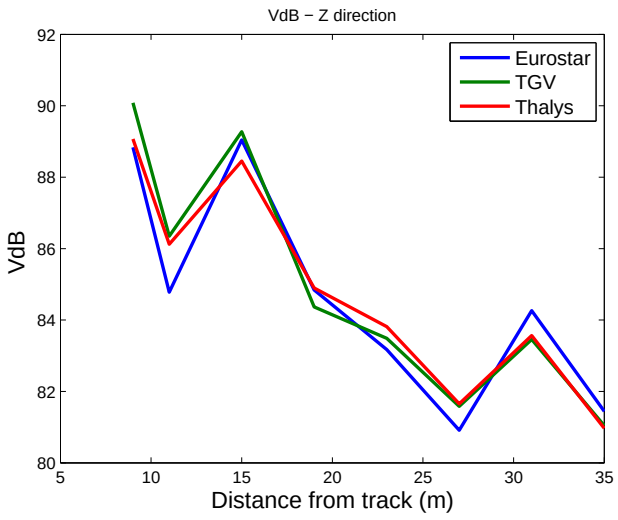

Figure 8.28 – Vertical vibration levels for various train types

8.7.6 Scattering due to abutments

Figure 8.29 compares the variation in vibration levels with increasing distance from the track for both the abutment and non-abutment cases. At distances close to the track there was a large discrepancy between the vibration levels, however as the distance was increased to 35m from the track, responses became similar. This shadow zone occurred because the ground vibrations could not pass directly from the track into the ground due to the presence of the abutment. Instead the vibrations were forced to pass around the abutment before reaching the receivers. This travel path was longer thus causing the waves to lose a greater percentage of their energy due to geometrical damping.

Figure 8.30 shows the difference in frequency content between the abutment and non-abutment cases. Although both responses were similar, the frequency spectrum for the abutment case was wider and a greater number of peaks were present. This occurred due to the complex wave scattering process induced by the abutment dimensions. When the waves generated by train passed through the track they were scattered due to the complex geometry of the abutment, thus generating a wider frequency spectrum.

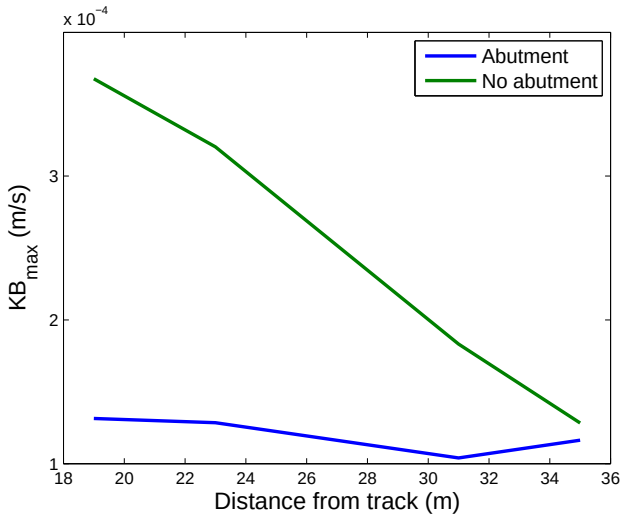

Figure 8.29 - Vertical vibration variation (abutment)

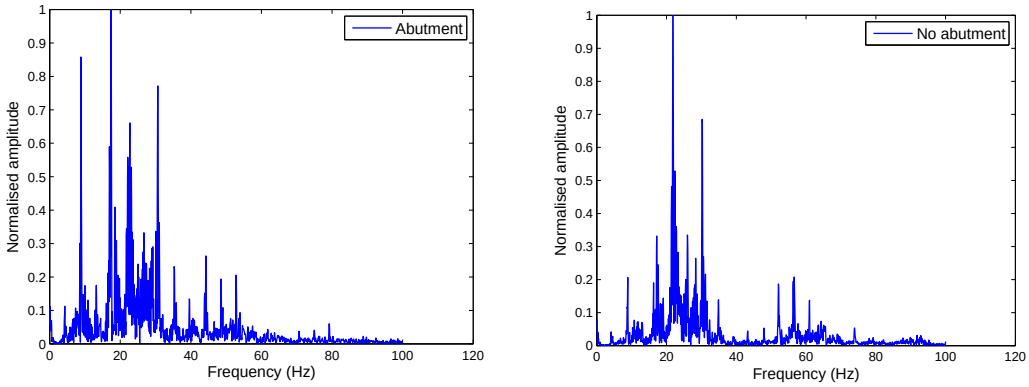

Figure 8.30 – Frequency spectrum comparison, (a) Left: abutment, (b) Right: no abutment

8.8 Conclusion

Field experiments were undertaken at six railway sites across Belgium and England. These experiments consisted of ground vibration monitoring to assess vibration levels due to train passage, and MASW tests to determine the

underlying soil properties. MASW tests were used to determine S-wave and P-wave velocities and the results were validated using seismic refraction analysis. Damping was calculated by optimising stiffness damping coefficients using a FE model. The purpose of the experimental campaign was two-fold. Firstly, to validate previously developed numerical models, results of which are presented in Chapter 9. Secondly, to provide insight into the vibration characteristics of three earthworks profiles: embankments, at-grade sections and cuttings.

Analysis of the field results revealed that:

1. Vertical component vibration levels are more dominant than horizontal vibration levels.

2. Cuttings generate elevated levels of ground vibration in comparison to at-grade and fill embankment track sections.

3. Embankments cause the generation of higher frequency content in comparison to at-grade track. Cuttings also generate higher frequency content than at-grade sections, albeit less than embankments.

4. The higher frequency components generated by all tracks is damped rapidly as the seismic waves propagate through the soil. Lower frequency components attenuate less quickly.

5. In the case of two parallel high speed lines, embankments cause a slight reduction in vibration levels in the free field on the side of train passage. Conversely, on the opposite side of train passage, they cause a slight increase in vibrations.

6. Embankments trap energy within them resulting in higher frequency vibration in comparison to the free field.

7. Thalys, TGV and Eurostar trains generate similar levels of ground vibration.

8. When abutments are present, the near field in close proximity to the abutment is shielded from vibration and experiences low vibration levels in comparison to the far field. Additionally, wave scattering due to the abutment generates vibration with a broader frequency spectrum in comparison to the free field.

Chapter 9. Numerical model validation

Once the vibration prediction models had been developed and the experimental data collected, the models were validated to verify that their output was similar to the vibration results recorded during field testing. Similar approaches to numerical model validation have been undertaken by (Galvin & Domínguez, 2009), (Kouroussis et al., 2011a) and (Lombaert & Degrande, 2009).

9.1 Validation of detailed prediction models

9.1.1 ABAQUS model validation

The ABAQUS model results were compared against field results from England, Belgium, and also using a peer reviewed data set also recorded in Belgium. All tracks were constructed from ballast and were modelled using the properties described in Table 9.1.

Ballasted track	Young's modulus (MPa)	Poisson's ratio	Density (kg/m^3)	Dimensions - x, y, z (m)
Rail	210,000	0.25	7,900	50 x 0.153 x 0.078
Sleepers	30,000	0.3	2,400	0.242 x 0.2 x 2.42
Ballast	1,000	0.35	1,800	50 x 0.3 x 3.92
Subballast	3,000	0.35	2,200	50 x 0.2 x 5.12
Subgrade	12.7,000	0.35	2,100	50 x 0.5 x 6.62

Table 9.1 – Ballasted track material properties

9.1.1.1 Eurostar 285 km/h (HS1)

Figure 9.1 - Figure 9.4 shows the predicted and recorded vertical vibration response from a Eurostar train travelling at 285 km/h in England on the HS1 line. For the 9m location all peaks were well resolved and the majority of bogie passages were predicted accurately in terms of timing and shape. Although nearly all bogie passage magnitudes were predicted with precision, the initial arrival of the driving car was overestimated by the numerical model. The 19m location was similar to the 9m case. Although the model accurately simulated the timing, shape and magnitude of nearly all wheel/bogie passages, there were several overestimations of vibration, the most notable being the end driving car.

This increase in discrepancy was likely due to the simplifications made regarding the underlying soil properties. The MASW technique used to classify

the soil properties was only capable of creating a 'best-fit' 1D soil site profile, near the point of hammer excitation. The 1D profile was then assumed to be representative of the 3D space. This meant that distances further away from the initial calculation point were more likely to be less representative of the approximated 1D profile. Therefore it was more difficult to replicate vibration levels with increasing distance from the track.

Regarding the frequency content comparison, the numerical model performed well. Although it was found to shift the frequency content to a slightly higher range than the experimental results, it modelled the general spectrum accurately.

One area where its performance was reduced was the replication of high frequency content, especially in the range greater than 50Hz. This was expected because the model was designed for simulating wave propagation predominantly below 50Hz. The fact that the experimental results exhibited frequency components outside this range was uncommon and thus difficult to anticipate.

For VdB, vibration levels were predicted competently at all distances from the track. At each location there was a slight over prediction of around 3-4dB.

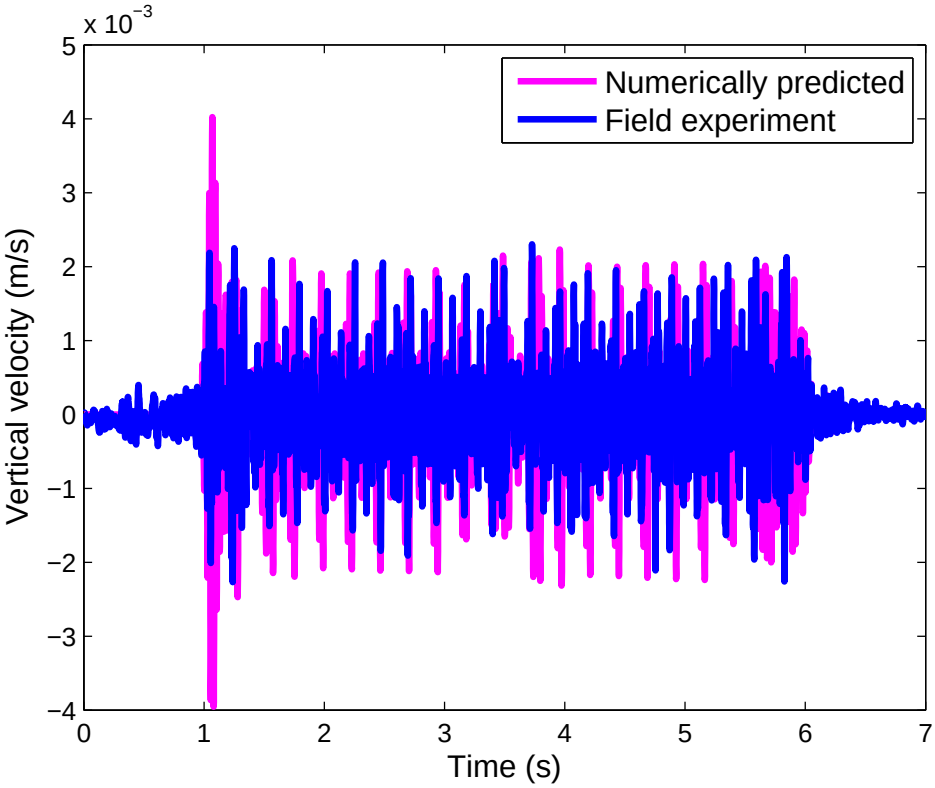

Figure 9.1 – Eurostar 285 km/h. Vertical velocity time history 9m from track centre

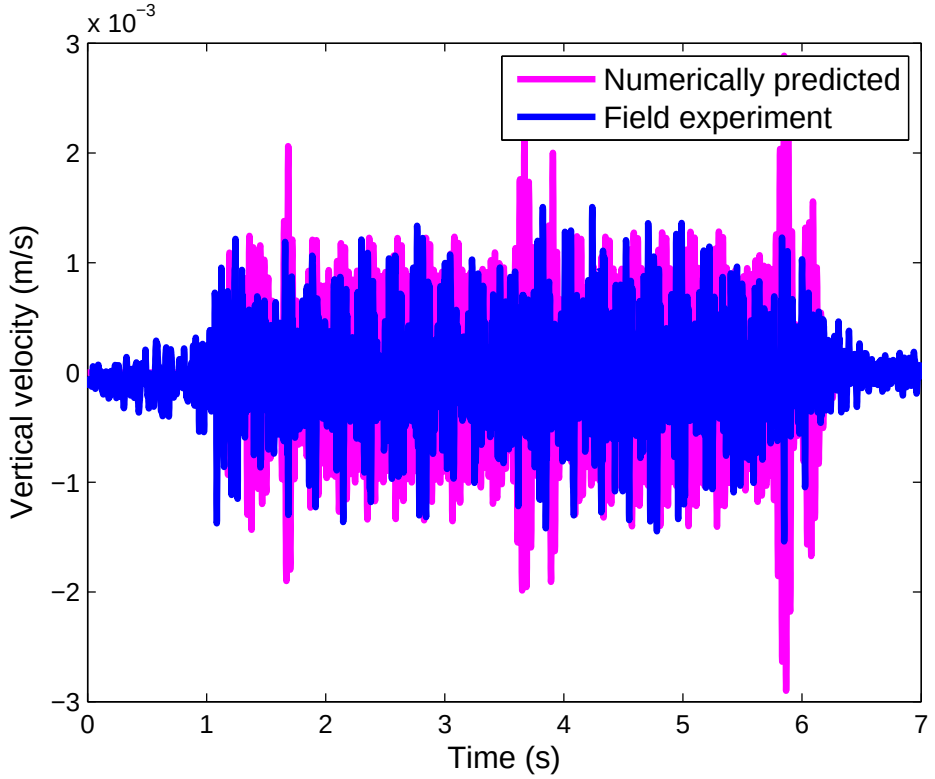

Figure 9.2 – Eurostar 285 km/h. Vertical velocity time history 19m from track centre

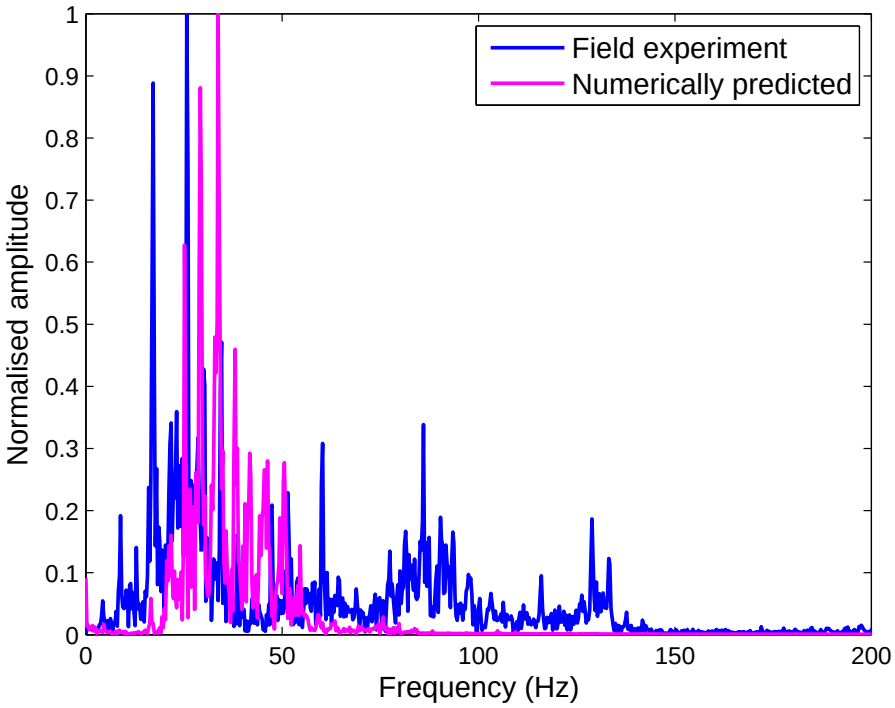

Figure 9.3 – Eurostar 285 km/h. Normalised vertical velocity frequency content at 9m from track

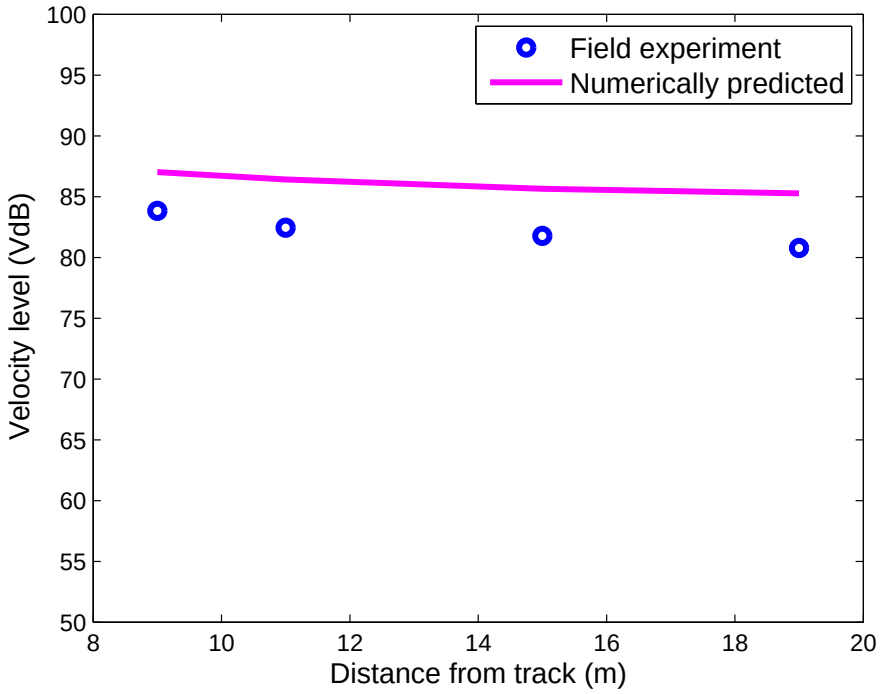

Figure 9.4 – Eurostar 285 km/h. VdB variation with distance from track

9.1.1.2 Thalys 300 km/h (Mons 2012)

Figure 9.5 - Figure 9.8 compares the predicted vibration response as generated by the ABAQUS model with the results collected in Belgium at the at-grade track section. Subfigures (a) and (b) show that the vertical velocity time histories of both receivers are similar. The predicted results can be seen to closely match the timing and shape of the experimental results. In general the replication of vibration magnitude was also strong which showed that the soil damping had been modelled accurately. Despite this, two peaks appear at the 11m location which were higher than those recorded during the field trials. The source of these peaks was unknown.

One area of discrepancy was the vibration response at times when the train is at large distance from the receiver (i.e. as the train approaches the receivers and as it fades away after the receivers). This discrepancy occurred because the numerical model was only capable of modelling a section of the overall railway track, the edges of which were bounded by an absorbing boundary. Therefore the response at far away locations was deliberately not simulated due to computational constraints. This was not of great concern because the magnitude of response experienced by the receivers due to the generation of excitation at such locations was very low in comparison to when the train was perpendicular to the receivers.

Frequency content was also predicted with accuracy. The main peaks were accurately simulated albeit at a slightly lowered range. This was possibly due to a discrepancy between the predicted and simulated train speeds.

Regarding the variation in PPV values, the numerical model also predicted these well with the computational results closely following the experimental ones. It was seen that the experimental PPV results showed an increase at 19m which was unexpected. This may have been due to experimental error and was thus difficult to account for within a numerical model. PPV was typically more difficult to predict at all locations than VdB because it is based on a single instantaneous response instead of a moving average. Therefore it was more likely to be effected by outliers within the dataset.

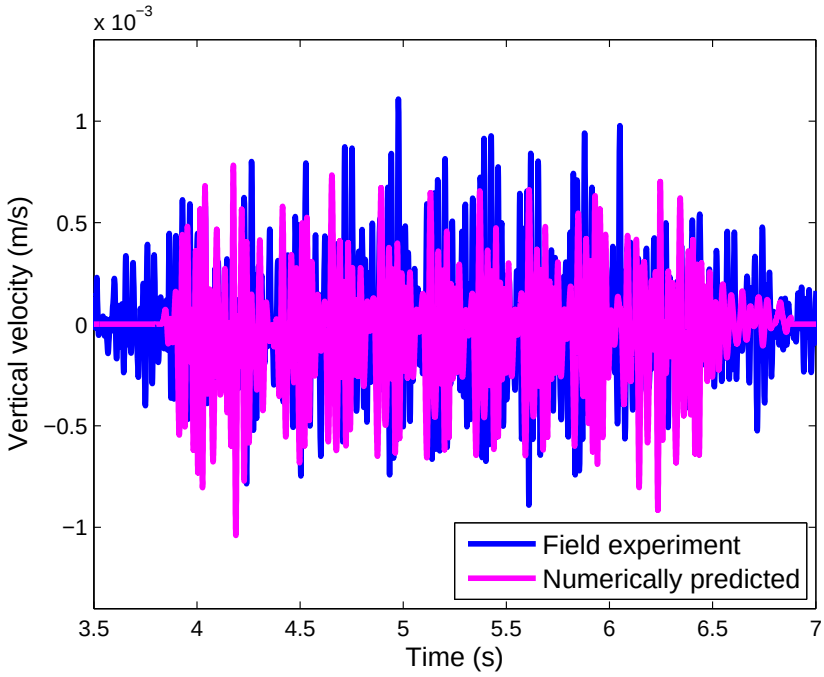

Figure 9.5 – Thalys 300 km/h. Vertical velocity time history 9m from track centre

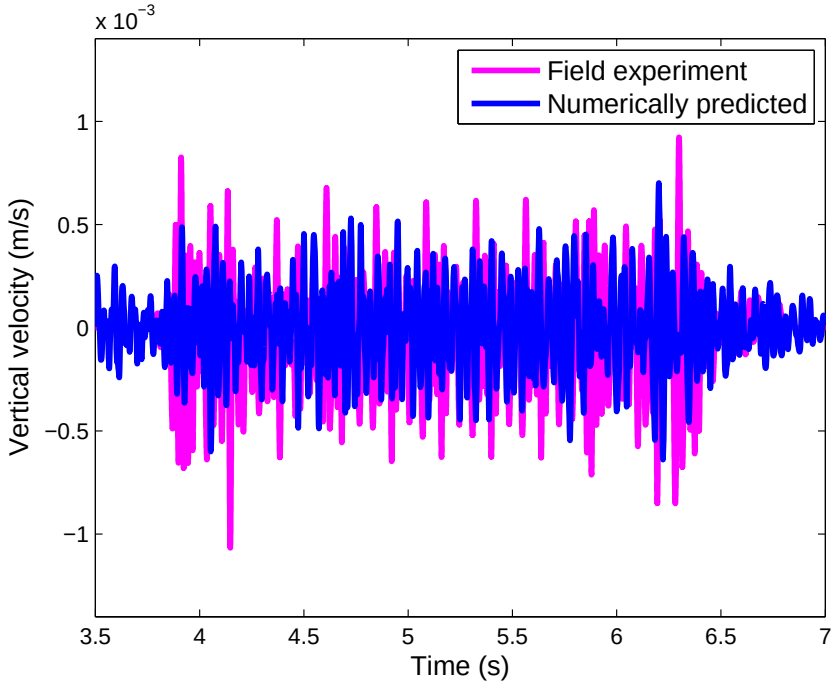

Figure 9.6 – Thalys 300 km/h. Vertical velocity time history 11m from track centre

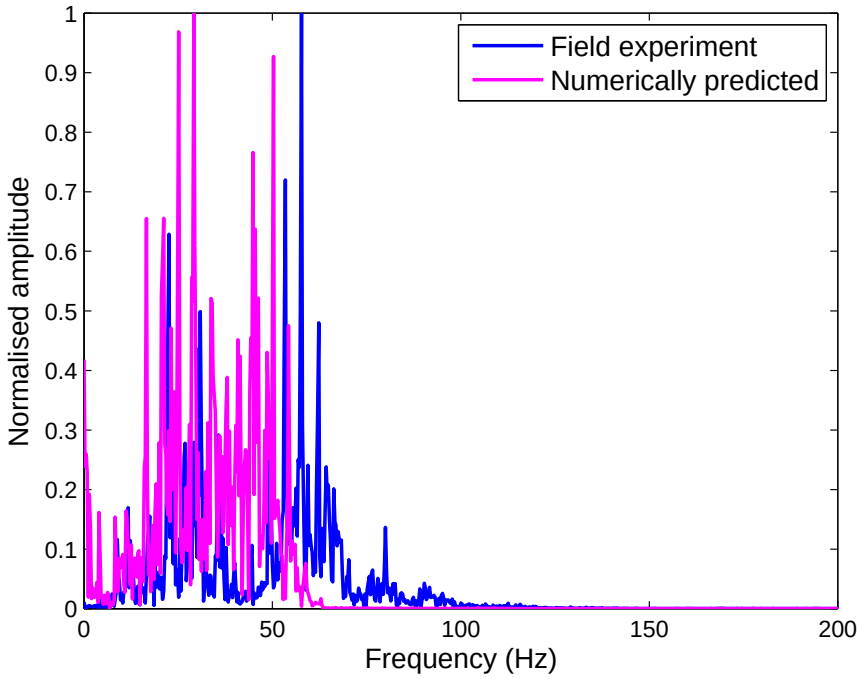

Figure 9.7 – Thalys 300 km/h. Normalised vertical velocity frequency content at 9m from track

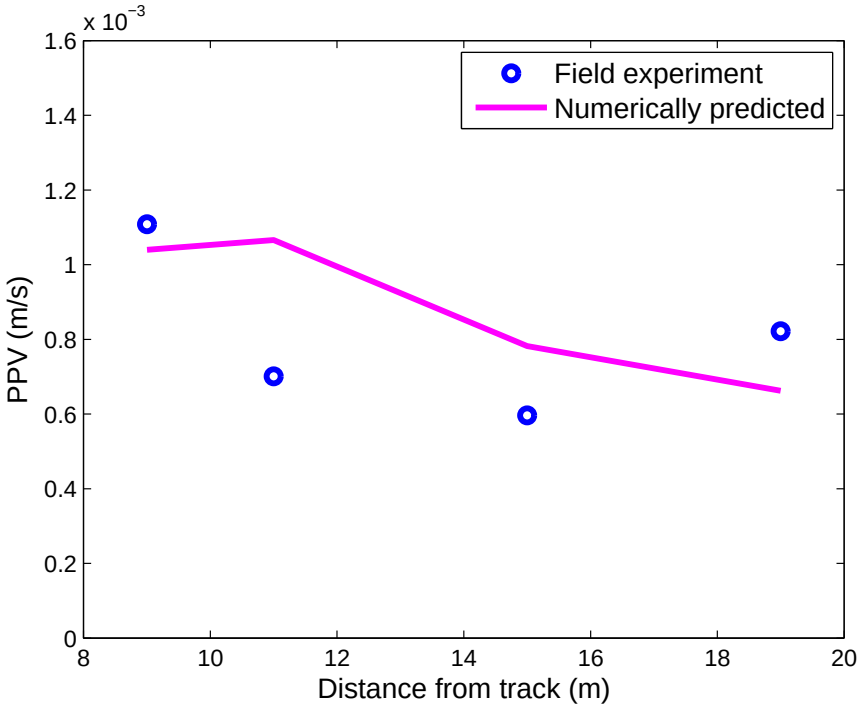

Figure 9.8 – Thalys 300 km/h. PPV variation with distance from track

9.1.1.3 Thalys 265 km/h (Mons 2005) (Peer reviewed data set)

Figure 9.9 - Figure 9.12 shows a comparison between numerical and experimental results for a Thalys high speed train travelling at 265 km/h. For this test, experimental results outside those described in Chapter 8 were used. Instead, results from (Kouroussis, 2005), were used to determine whether the numerical model would be capable of replicating field results collected by independent researchers.

For the tests performed by (Kouroussis, 2005), the railway structure was identical to that described in Table 9.1, however the soil properties were different. The soil consisted of three stratified layers, each of which are shown in Table 9.2.

Mons 2005	Soil description	Young's modulus (MPa)	Poisson's ratio	Density (kg/m^3)
Layer 1 (2.7m)	Silt	129	0.3	1600
Layer 2 (3.9m)	Sandy clay	227	0.3	2000
Layer 3 (inf)	Sand	659	0.3	2000

Table 9.2 – Mons 2005 soil description

It is seen that the numerical model performs well again. At both 7m and 19m from the track the model was able to accurately predict the timing, magnitude and shape of the velocity time history. Similarly, the frequency content was well resolved with the dominant frequencies being identified around 30Hz. The VdB results also showed a high correlation between predicted and experimental results. The predicted value at each location was within 2dB of the experimental value.

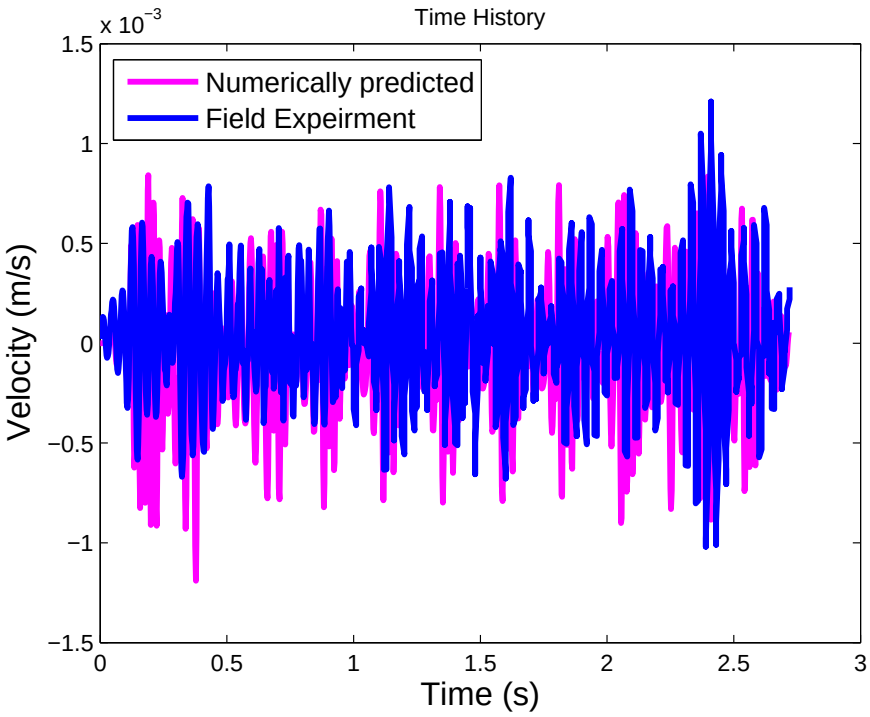

Figure 9.9 – Thalys 265 km/h. Vertical velocity time history 7m from track centre

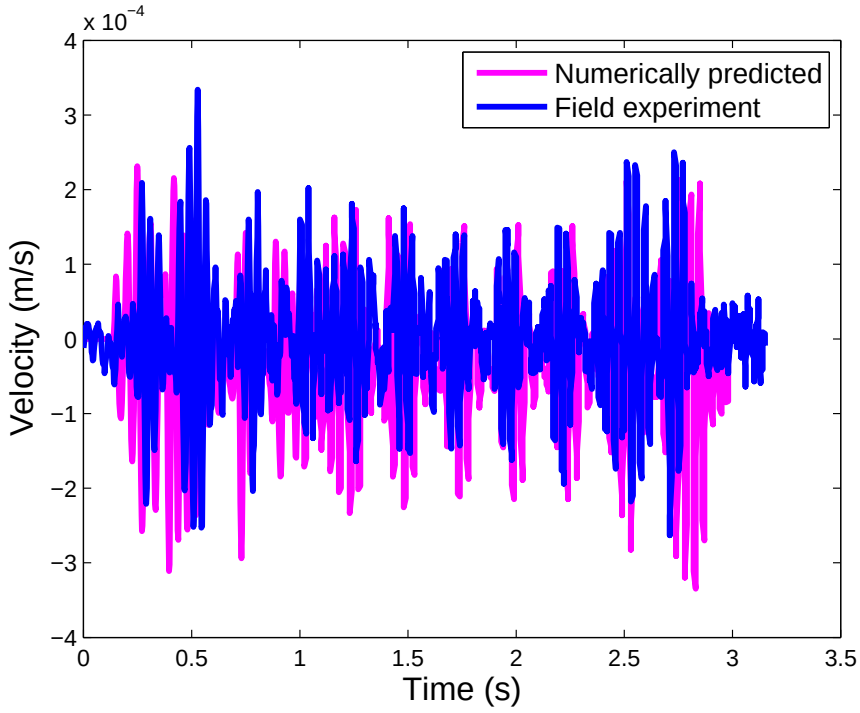

Figure 9.10 – Thalys 265 km/h. Vertical velocity time history 19m from track centre

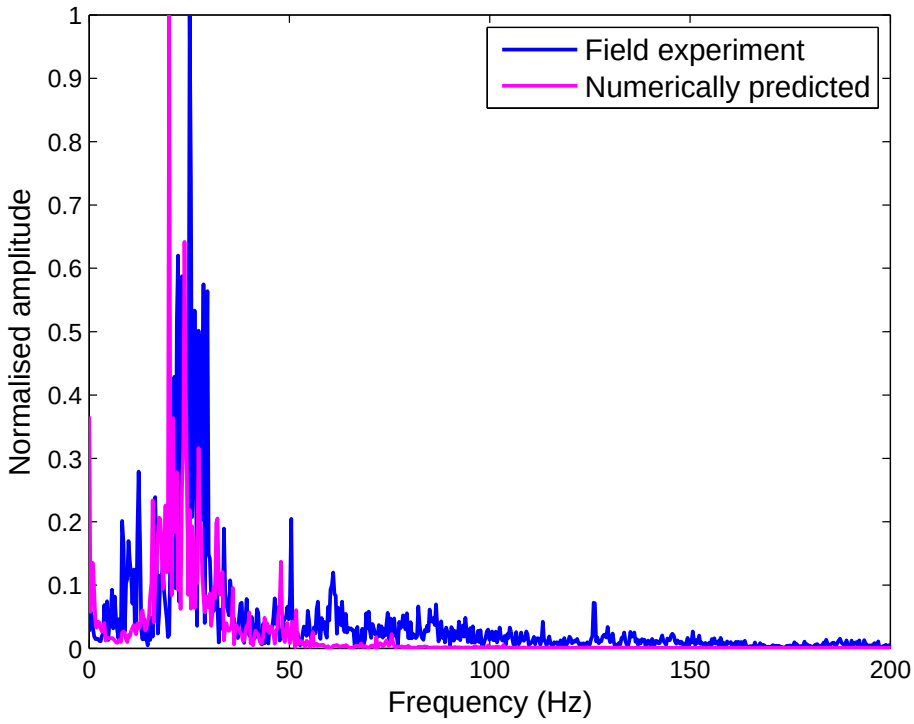

Figure 9.11 – Thalys 265 km/h. Normalised vertical velocity frequency content at 7m from track

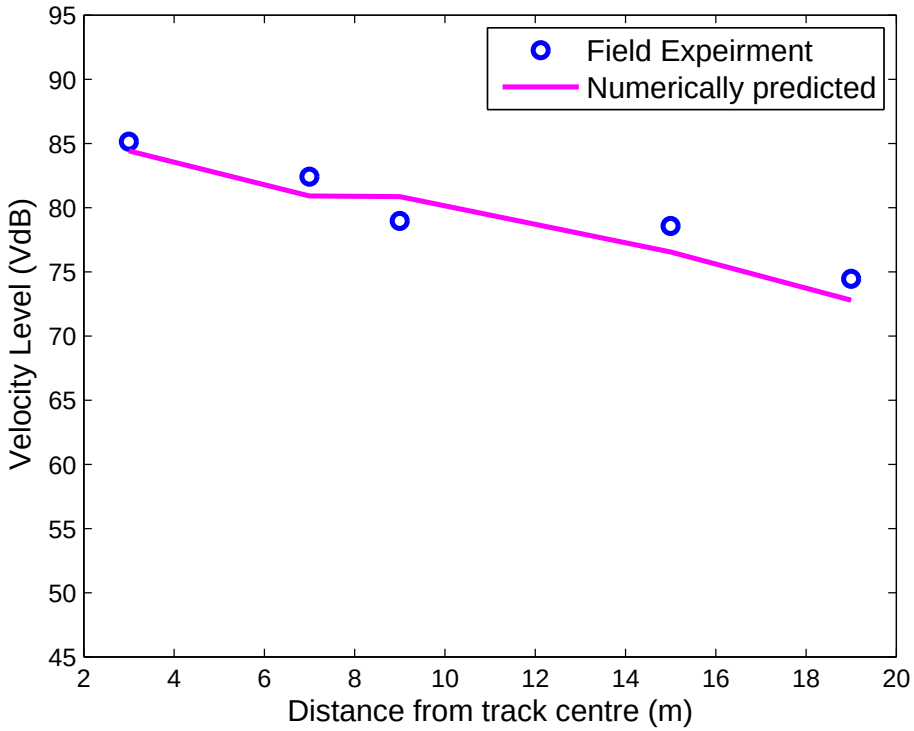

Figure 9.12 – Thalys 265 km/h. VdB variation with distance from track

9.1.2 LSDYNA model validation

9.1.2.1 Thalys 291 km/h (Mons 2012)

Figure 9.13 - Figure 9.16 shows a comparison between a recorded Thalys high speed train travelling at 291 km/h at the Mons 2012 test site, and one simulated using the LSDYNA prediction model. Similarly to the ABAQUS model velocity time histories the fading in and out of the train is deliberately ignored at all locations by the numerical model due to its truncation using absorbing boundaries. Despite this, the key, large magnitude velocities at receivers 9m and 19m were well resolved with regard to timing, shape and magnitude.

The frequency spectrum was also accurately modelled. Although the main Eigenfrequency was shifted to a slightly higher range by the numerical model, the main frequency range was well resolved. Regarding the PPV prediction, the model also performed well. The experimental PPV magnitudes were found to decrease with increasing distance from the track except at 19m where the magnitude unexpectedly rose. For the first three points the PPV values were predicted accurately however for the 19m point the value was under predicted.

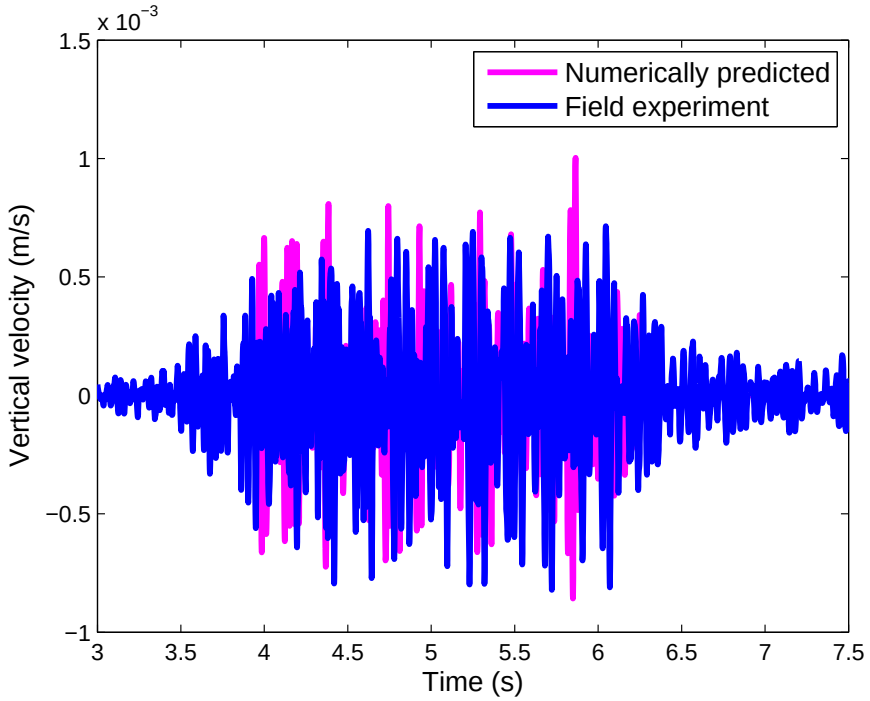

Figure 9.13 – Thalys 291 km/h. Vertical velocity time history 9m from track centre

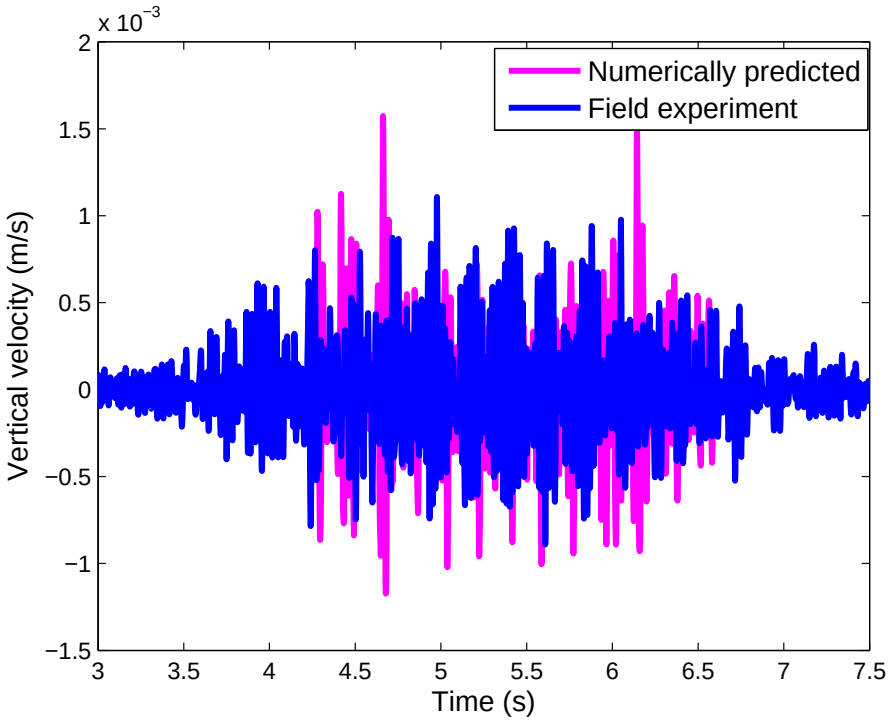

Figure 9.14 – Thalys 291 km/h. Vertical velocity time history 19m from track centre

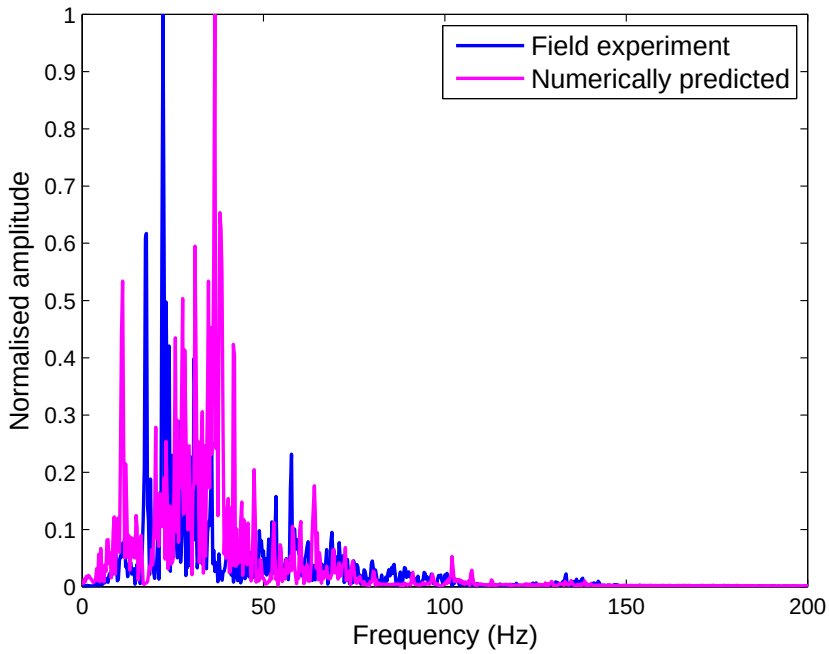

Figure 9.15 – Thalys 291 km/h. Normalised vertical velocity frequency content at 7m from track

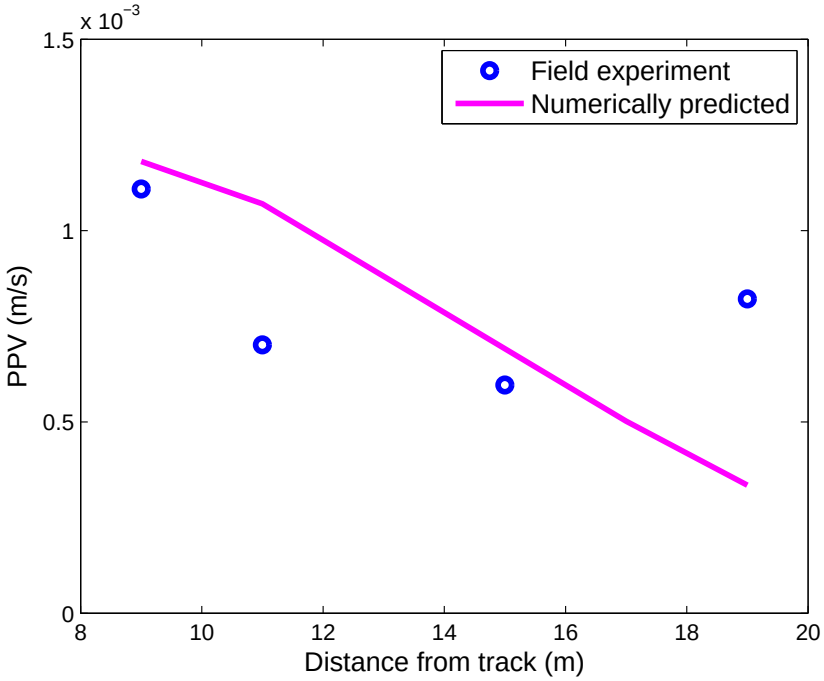

Figure 9.16 – Thalys 291 km/h. PPV variation with distance from track

9.1.3 Validation of empirical model

Empirical model results (Chapter 6) were compared to experimental results from four test sites. The two at-grade test sites outlined in Chapter 8 are denoted 'Mons 2012' and 'HS1 2012' to describe the Belgium and English test sites respectively. The other two sets of experimental data were taken from published literature. Both sets of data were recorded in Belgium are denoted 'Mons 2005' and 'Degrande 2001'. Information related to the recording of these results can be found in (Kouroussis, 2005), (Kouroussis et al., 2011a), (Degrande & Schillemans, 2001a) and (Degrande & Lombaert, 2001) respectively.

The empirical models developed in chapter Chapter 6 are only capable including a discrete number of layers in their calculation. Therefore the soil properties at each test site were translated from profiles with at least three layers into profiles with only 1-2 layers. This translation was performed using a thickness weight average technique as outlined in (Brahma & Mukherjee, 2010):

$$E_{eq} = \frac{\sum H_i E_i}{\sum H_i} \qquad \text{Equation 9.1}$$

Where E_{eq} = equivalent Young's modulus, H_i = each layer thickness and E_i = Young's modulus of each layer. After translation, the resulting soil properties for each site were as shown in Table 9.3 - Table 9.6.

	Original soil profile		Homogenous approximation		Two-layer approximation	
Mons 2012	**Thickness (m)**	**Young's modulus (MPa)**	**Thickness (m)**	**Young's modulus (MPa)**	**Thickness (m)**	**Young's modulus (MPa)**
Layer 1	1.8	113	10	316	3.8	125
Layer 2	2	135			6.2	434
Layer 3	5.2	434				
Layer 4	1	437				

Table 9.3 – Soil properties, Mons 2012

	Original soil profile		Homogenous approximation		Two-layer approximation	
HS1	**Thickness (m)**	**Young's modulus (MPa)**	**Thickness (m)**	**Young's modulus (MPa)**	**Thickness (m)**	**Young's modulus (MPa)**
Layer 1	1.5	114	10	318	1.5	114
Layer 2	7.6	354			8.5	354
Layer 3	0.9	5400				

Table 9.4 - Soil properties, HS1 2012

	Original soil profile		Homogenous approximation		Two-layer approximation	
Degrande	**Thick-ness (m)**	**Young's modulus (MPa)**	**Thick-ness (m)**	**Young's modulus (MPa)**	**Thick-ness (m)**	**Young's modulus (MPa)**
Layer 1	1.4	31	10	162	1.5	31
Layer 2	3.3	85			8.5	184
Layer 3	5.3	245				

Table 9.5 - Soil properties, Degrande 2001

	Original soil profile		Homogenous approximation		Two-layer approximation	
Mons 2005	**Thickness (m)**	**Young's modulus (MPa)**	**Thickness (m)**	**Young's modulus (MPa)**	**Thickness (m)**	**Young's modulus (MPa)**
Layer 1	2.7	129	10	347	2.7	129
Layer 2	3.9	227			7.3	428
Layer 3	3.4	659				

Table 9.6 - Soil properties, Mons 2005

9.1.3.1 Homogenous VdB

Figure 9.17 shows the results of the homogenous empirical neural network model developed in Chapter 6, computed using the soil properties described in Table 9.3 - Table 9.6. In addition to validating the model, results were compared to the model outlined by (Federal Railroad Administration, 2012) for benchmarking purposes.

It was found that the homogenous model performed well and was able to predict VdB values with strong accuracy for each test site. For the Mons 2012 test site the new empirical model closely matched the experimental results. Similar results were found for Degrande 2001 although there was an over prediction of vibration levels for the receivers at distances greater than 10m.

For the HS1 2012 and Mons 2005 results the new model was found to slightly over predict vibration levels at distances less than 20-25m from the track, and to over predict levels at further distances.

The model proposed by (Federal Railroad Administration, 2012)was found to overestimate vibration levels for nearly all receivers at all test sites. This is particularly true for Degrande 2001 where FRA 2012 was found to overestimate vibration levels by up to 20dB. In comparison to the new empirical model, FRA 2012 was found to offer lower levels of accuracy.

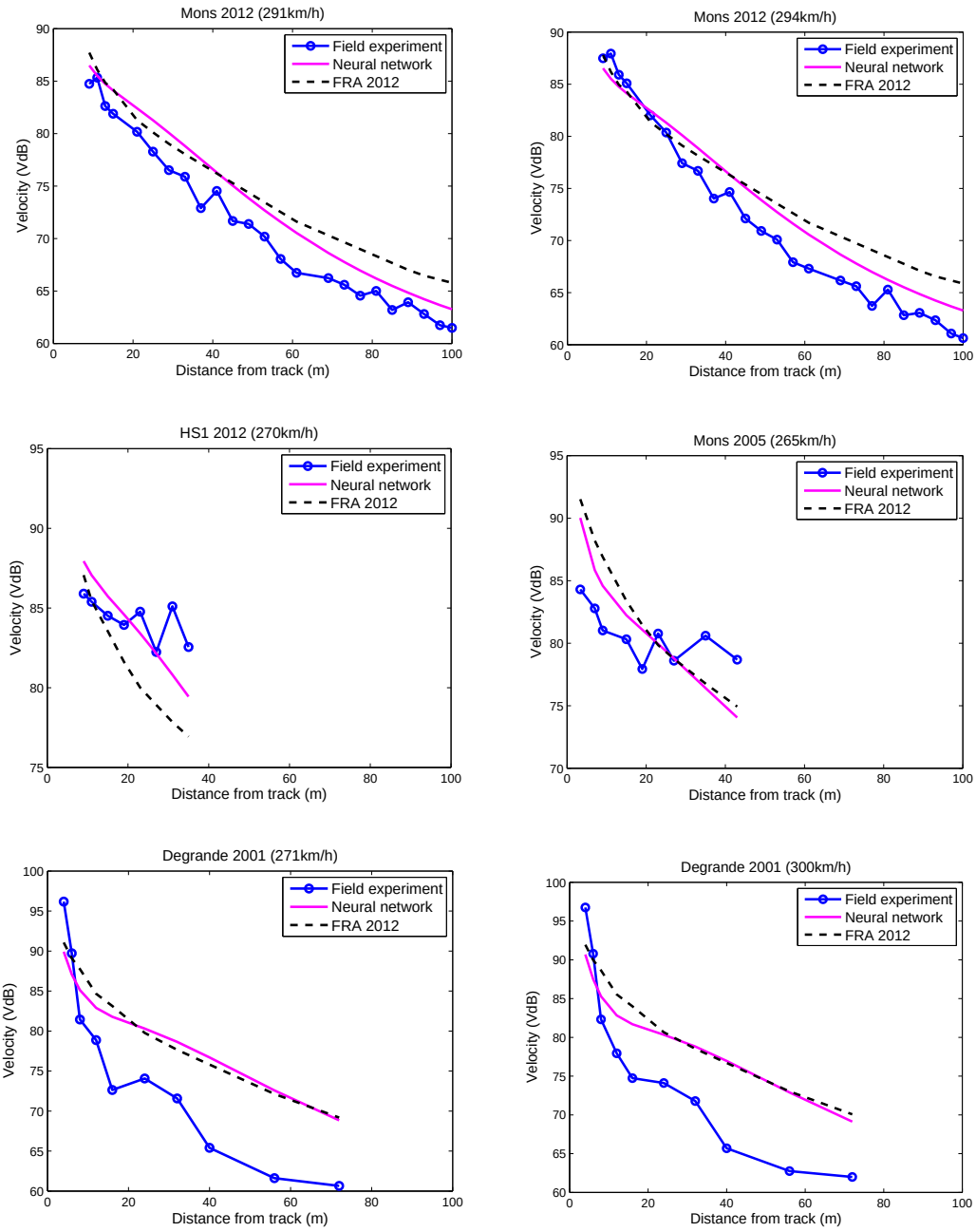

Figure 9.17 – Homogenous VdB results

9.1.3.2 Two layer VdB

The two layer VdB model also developed in Chapter 6 had additional degrees of freedom. Therefore it was tested to determine whether it was capable of improving the prediction accuracy of the homogenous model.

Figure 9.18 shows comparisons between the experimental results, FRA 2012 and the two layer empirical model. For Mons 2012 and Degrande 2001 in particular, the accuracy of the new model was high. The predicted VdB magnitudes and their variance with receiver distances from the track had a high correlation with the experimental results. The results for HS1 2012 and Mons 2005 remained similar to the predictions generated by the one layer model. Despite this, overall the prediction accuracy was found to be increased through the application of the two layer model in comparison to the one layer model. Additionally, both models were found to vastly outperform the predictions generated using FRA 2012.

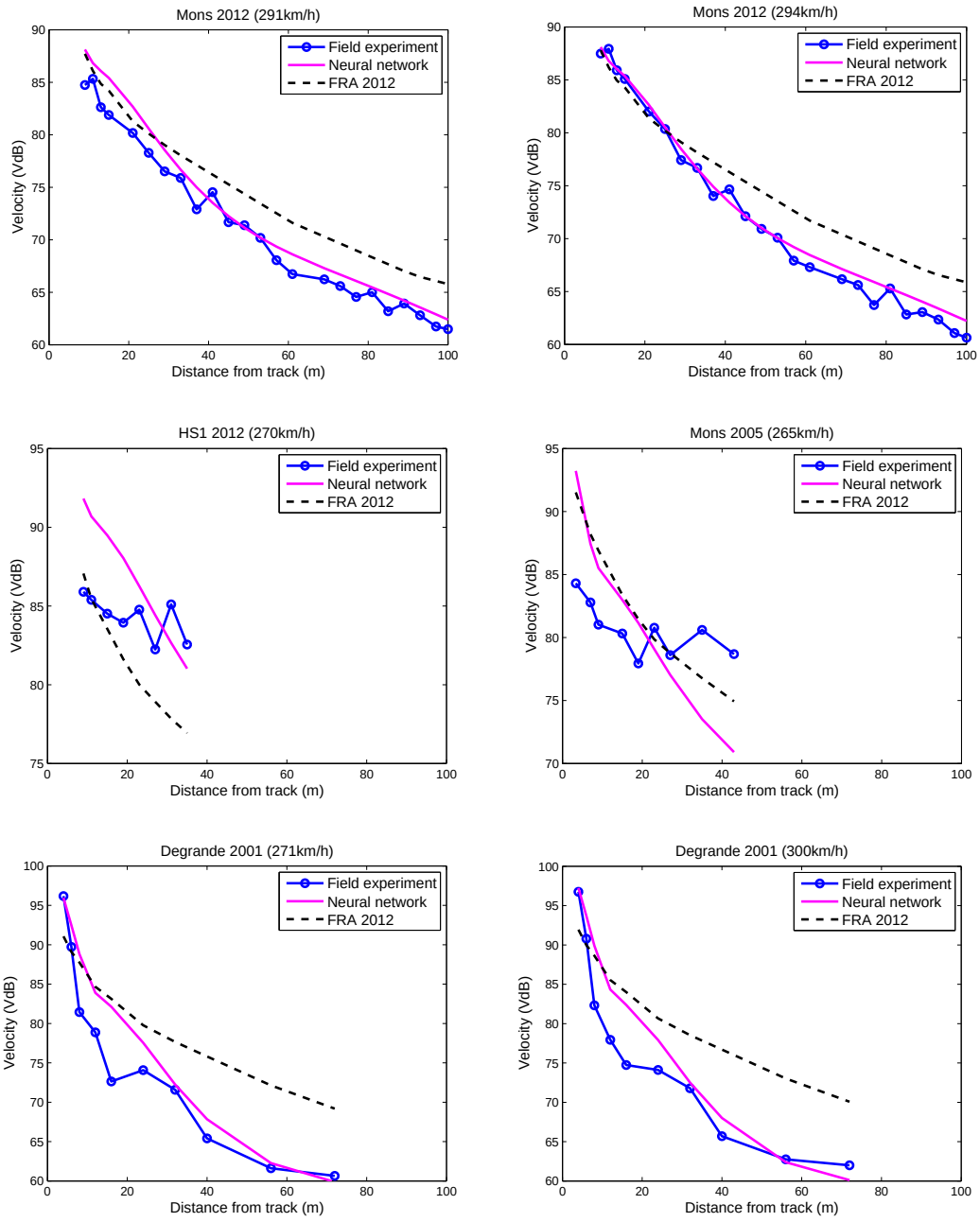

Figure 9.18 – Two layer VdB results

9.1.3.3 Two layer PPV

Figure 9.19 shows a comparison between the two layer empirical neural network model and the experimental results. For both PPV and KB_{max}, only a two layer model was developed.

It can be seen from the experimental results that in general PPV does not offer as uniform of a distribution as VdB. This is because PPV is a single instantaneous measurement rather than a moving average meaning it is more sensitive to global outliers. This effect was particularly clear for HS1 2012 and Mons 2005 where there were several distinct peaks and troughs in PPV values with increasing distance from the track. Theoretically, PPV should diminish with increasing distance from the track due to geometrical and material damping. Therefore these local increases in PPV were likely to be due to either localised soil artefacts or field experiment error.

Despite these fluctuations in experimental results the new empirical model was capable of accurately predicting the vibration levels at all test sites. It performed best for Mons 2012 and Degrande 2001 sites because they exhibited a clearer pattern in PPV attenuation and had fewer outliers. It was also capable of providing strong global approximations for Mons 2005 and HS1 2012 although was unable to predict the aforementioned local increases in PPV.

The PPV model was not be compared to the FRA 2012 empirical model because FRA 2012 is unable to predict PPV levels.

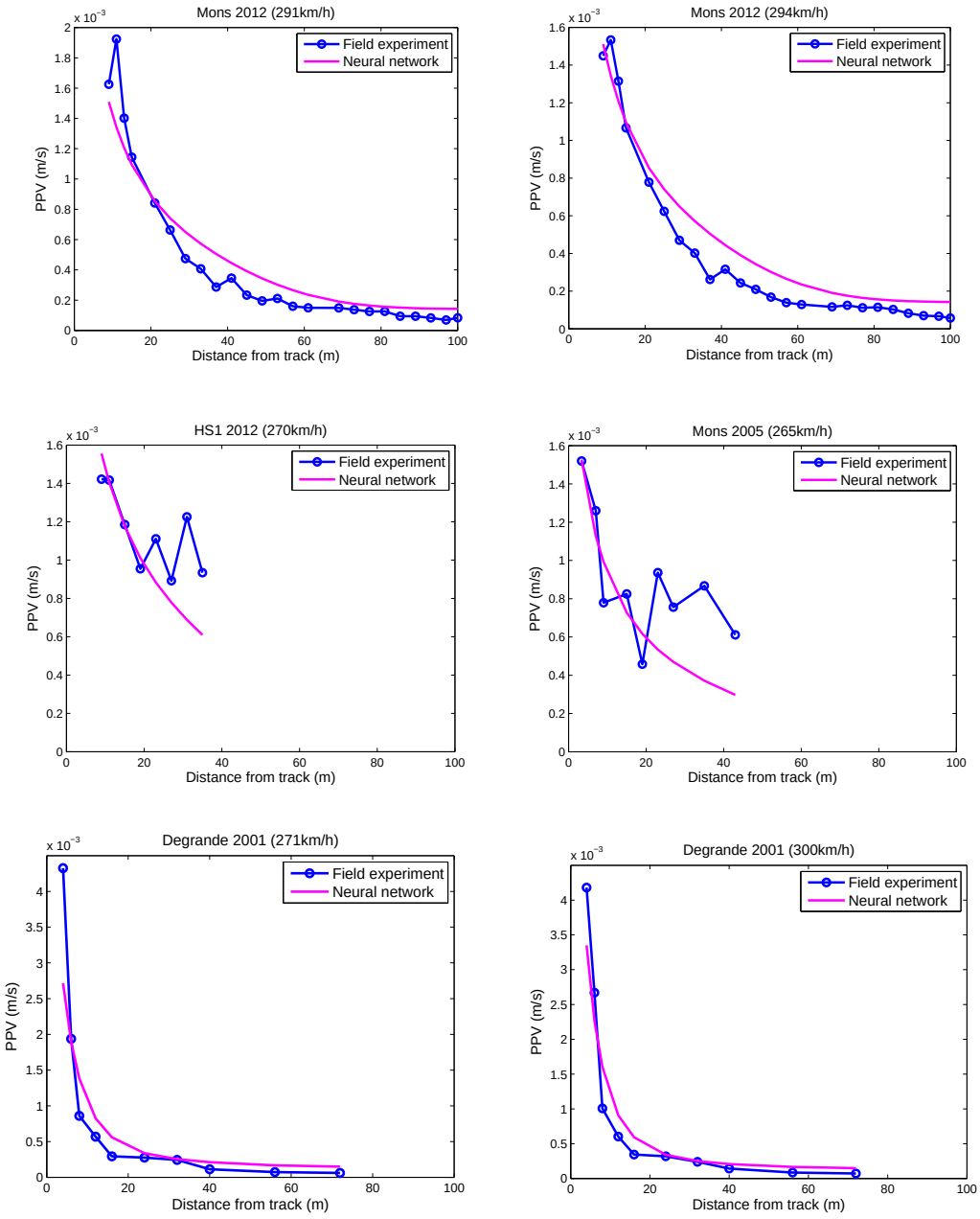

Figure 9.19 – Two layer PPV results

9.1.3.4 Two layer KB

Figure 9.20 shows comparisons between the neural network model and the experimental results recorded at all four sites. Similarly to the results presented for PPV and VdB, the model is capable of predicting vibration levels

with high accuracy. Once again the model performs best for Mons 20012 and Degrande 2001 data. Although the model is unable to predict the previously discussed local increases in vibration at HS1 2012 and Mons 2005 test sites, the predicted values closely followed the theoretical best fit line through all points. Therefore it was concluded to provide a strong approximation of the overall response.

The KB_{max} model could not be compared to the empirical model presented by (Federal Railroad Administration, 2012) because it is not capable of predicting KB_{max} levels.

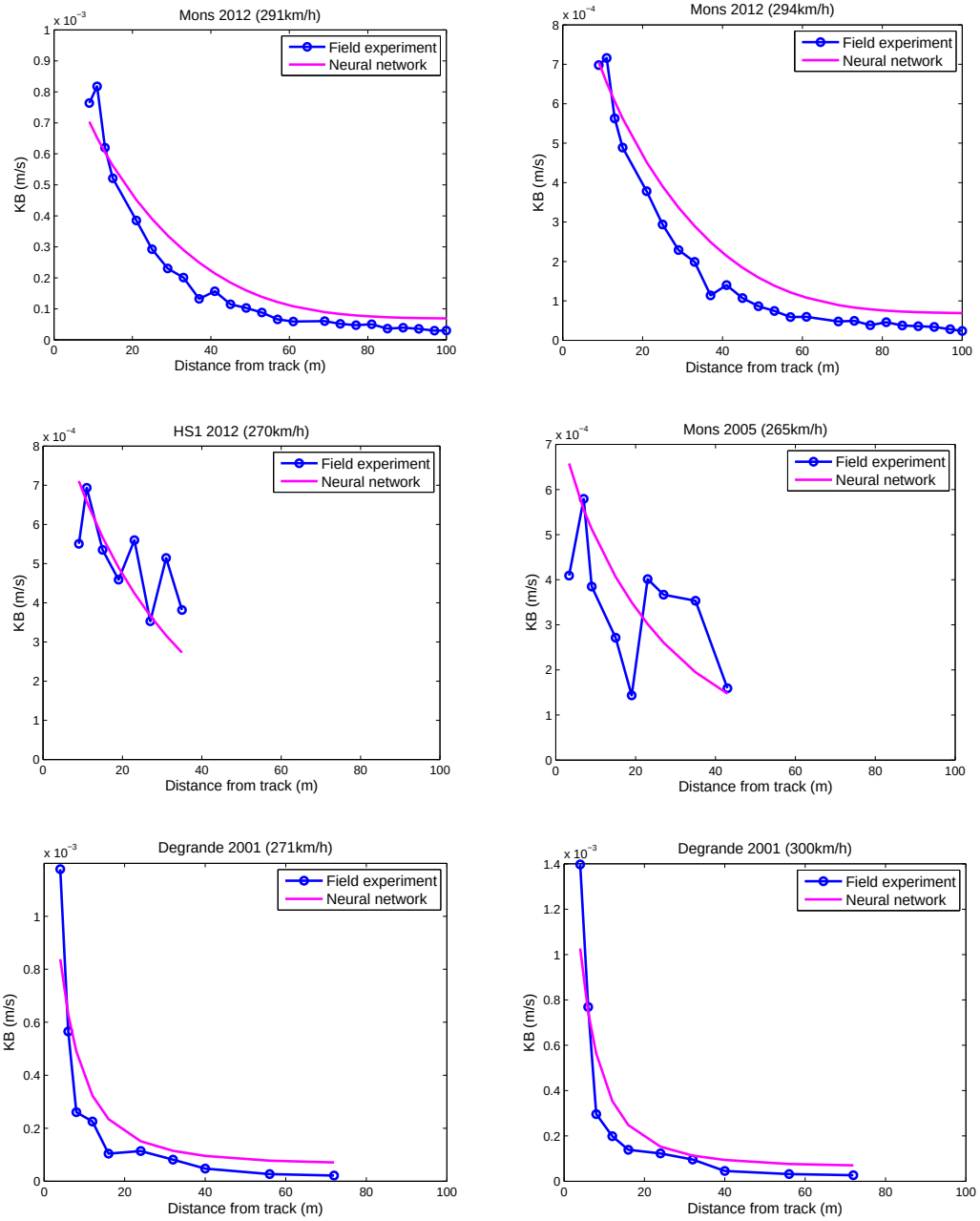

Figure 9.20 – Two layer KB_{max} results

9.2 Conclusions

Railway vibration assessments typically use a combination of scoping and detailed models to predict vibration levels. In this chapter the previously developed scoping and detailed models were tested against experimental data.

Firstly, the 3D finite element, ABAQUS and LSDYNA models developed in Chapter 3 and Chapter 4 were compared against field results collected in Chapter 8. They were also compared against peer reviewed data sets to prevent bias. Both detailed prediction models were shown to accurately predict the timing, shape and magnitude of vertical velocity time histories, at a variety of distances from the track. Results were presented for a variety of train speeds, train types and soil conditions. This ability to reliably estimate velocity response meant that each frequency spectrum was also accurately predicted. The ability of the numerical models to predict three international metrics (VdB, KB_{max}, and PPV) was also shown.

The neural network scoping models developed in Chapter 6 were also tested against a similar combination of experimental results. It was shown that both one and two layer models were capable of predicting vibration levels with accuracy. Despite this, it was shown that two layer models were capable of making higher accuracy predictions due to their extra degrees of freedom. For the two layer models, the ability to predict all three metrics was shown. For VdB prediction the neural network model was benchmarked against an alternative model and was shown to offer a significant performance benefit. This is an important finding because higher accuracy scoping models reduce the time and cost associated with deploying detailed 3D models.

In the next chapter the 3D FE models are used to investigate train speed, track type and embankments respectively.

Chapter 10. Numerical results – vibration effects

10.1 Background

The finite element ABAQUS model developed in Chapter 4 and validated in Chapter 9 was used to analyse several aspects of railway vibration. Firstly an investigation into train speed was undertaken to determine the effect of critical velocities on vibration levels. Secondly, three different track types were analysed to determine whether they offered any vibration reduction benefit. Lastly, the effect of embankment constituent material was analysed to determine its effect on vibration levels in the near and far field.

10.2 The effect of train speed

The dependence of vibration characteristics on moving load velocities was shown mathematically by (Fryba, 1972). It was shown that vibration levels increased if the moving load velocity approached the Rayleigh wave velocity of the surface over which it was traversing.

In the case of railways the train traverses over a complex configuration of track/ground materials that support its running wheels. The relationship between these materials and train speed effects the amplitude of the propagating vibrations. The majority of these track material wave speeds are much higher than typical train speeds. Despite this, under certain

circumstances it may be possible that the train speed is comparable to the two slowest track wave speeds: the underlying soil Rayleigh wave speed and the bending wave speed of the rails.

(Heckl, Hauck, & Wettschureck, 1996) presented a formula for the calculation of the bending wave speed in the rails (Equation 10.1). b_r is the bending stiffness of the rail, m_r is the mass per unit length of rail and s_e is the stiffness per unit length of elastic foundation. The relationship between elastic foundation stiffness (ballast) and rail bending wave speed is calculated analytically using Equation 10.1 and plotted in Figure 10.1.

$$V_{rb} = \sqrt[4]{\frac{4 s_e b_r}{m_r}} \qquad \text{Equation 10.1}$$

The dotted line defines the typical value of elastic stiffness (18 MPa), which results in a wave speed of 1225 km/h. This is much faster than typical high speed train velocities. The elastic stiffness of the track foundation is primarily determined by the ballast, however in the case of a very soft soil it may be lowered. Figure 10.1 shows the wave speeds also for values much less than the typical elastic stiffness. However, even at 2MPa the rail bending wave speed is 700 km/h which is still greater than current train speeds. Thus the possibility of the train velocity becoming comparable to the rail bending wave speed is unlikely and can be ignored. Therefore this chapter will focus on the other possible wave speed that the train may become comparable to (i.e. the critical velocity associated with the underlying soil).

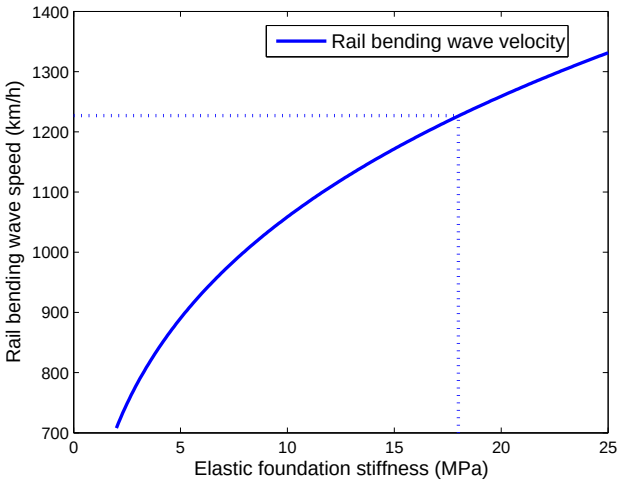

Figure 10.1 - The effect of elastic foundation stiffness on rail bending wave speed

10.2.1 Previous investigations into train speed

To analyse the effect of soil critical velocities, (Krylov, 1995) presented an analytical model and quantified that trains travelling at the critical velocity may produce vibration levels 70dB greater than slower trains. Through field experiments and an alternative analytical model, (Auersch, 2008c) divided the vibration response of a train travelling at critical velocity into two components: the response generated due to the moving load effect, and the response due to the critical velocity effect. It was found that the critical velocity effect was more dominant than the moving load effect.

A numerical model has also been presented by (El Kacimi et al., 2013) which showed that for low speeds the ground deformation under the train wheels was relatively symmetrical, however at increasing speeds this symmetry was lost. (Ju & Lin, 2004) made similar findings regarding critical velocities and

presented two methods for vibration isolation that were effective for high speed trains, but not for lower speeds.

10.2.2 Numerical analysis of critical velocities

The effect of train speed with respect to the underlying soil Rayleigh wave speed was investigated using the previously outlined ABAQUS model. Figure 10.2, Figure 10.3 and Figure 10.4 present a birdseye perspective of the variation in displacement for a 4 axle Thalys high speed passenger train travelling at speeds:

1. Lower than the Soil Rayleigh wave speed, 150 km/h, ($V < V_R$)
2. Equal to the soil Rayleigh wave speed, 330 km/h, ($V = V_R$)
3. Greater than the soil Rayleigh wave speed, 400 km/h ($V > V_R$)

	Young's modulus (MPa)	Poisson's ratio	Density (kg/m^3)
Homogenous soil	50	0.37	1900

Table 10.1 – Homogenous soil properties

In each case the direction of train passage was right to left and the Rayleigh wave speed of the soil was 91.7 m/s (330 km/h). At a speed of 150 km/h (Figure 10.2), both front axles were clearly visible however the trailing

two axles were less so. The wave pattern surrounding the four axles was relatively evenly spread and circular in shape. Behind the trailing axles some minor flaring of the displacement response was visible.

When the velocity was increased to the Rayleigh wave speed (Figure 10.3) and higher (Figure 10.4), the wave patterns changed radically. The wave pattern ahead of the initial two wheels was more conical (triangular) in shape and the individual wave fields were more tightly bunched together. Similarly, the relatively even distribution of the wave field surrounding the entire four axles was broken into two distinct areas, one surrounding the leading two axles and one surrounding the trailing two axles. The displacement levels directly beneath each wheel also changed, with the trailing axles of each bogie becoming more pronounced in comparison to the front axle of each bogie.

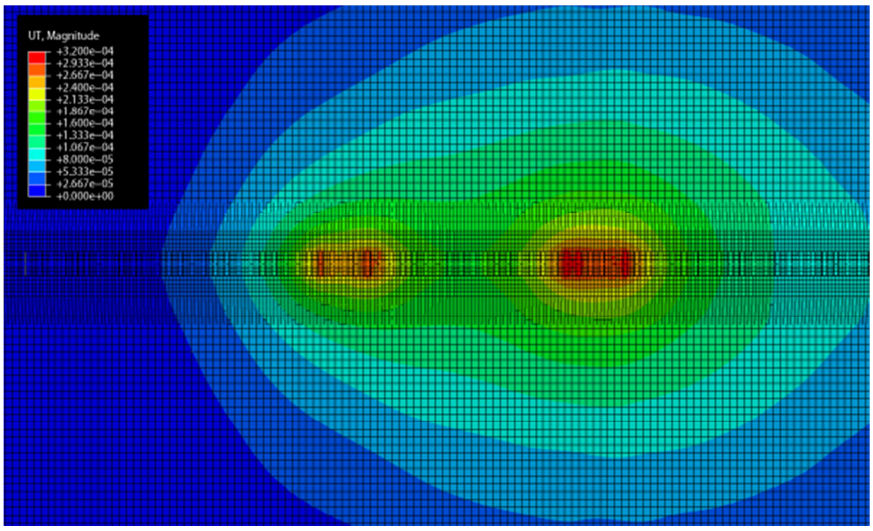

Figure 10.2 - Sub-Rayleigh, Thalys train passage, 42 m/s (150 km/h)

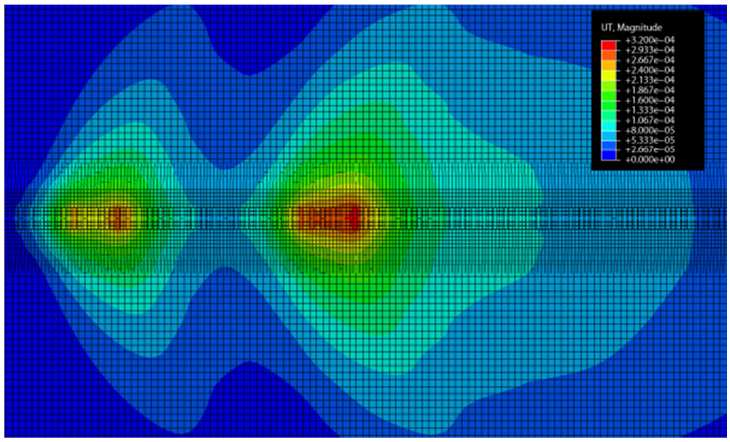

Figure 10.3 - Critical velocity, Thalys train passage 91.7 m/s (330 km/h)

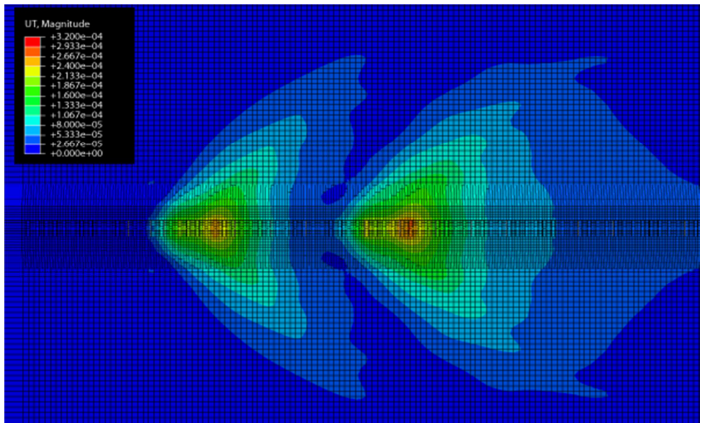

Figure 10.4 - Super Rayleigh velocity, Thalys train passage 111 m/s (400 km/h)

The effect of train speed on sub-surface wave propagation patterns was also investigated. Figure 10.5, Figure 10.6 and Figure 10.7 show displacement levels for a 4 axle Thalys high speed passenger train travelling the same three speeds described earlier. Each figure displays results for a cut made through the centre of the track.

The wave patterns were consistent with those presented in Figure 10.2, Figure 10.3 and Figure 10.4. As the train speed increased the patterns became increasingly conical in shape. Similarly, the pressure bulb induced by each bogie became more pronounced as the speed increased.

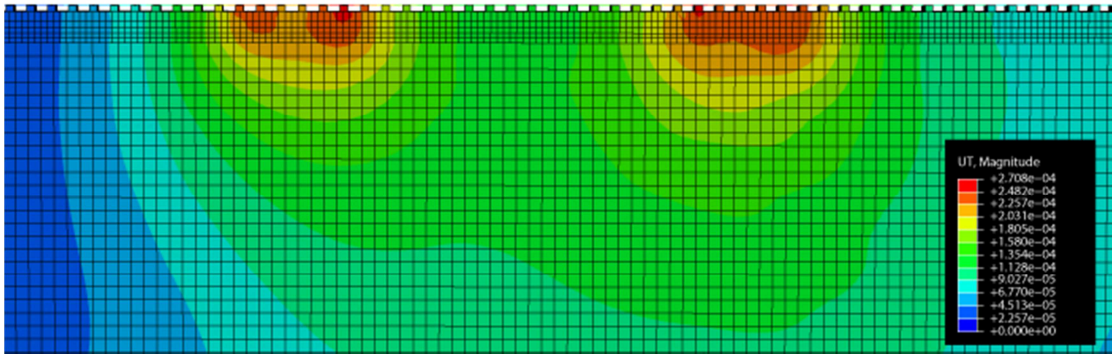

Figure 10.5 - Sub-Rayleigh, Thalys train passage, 42 m/s (150 km/h)

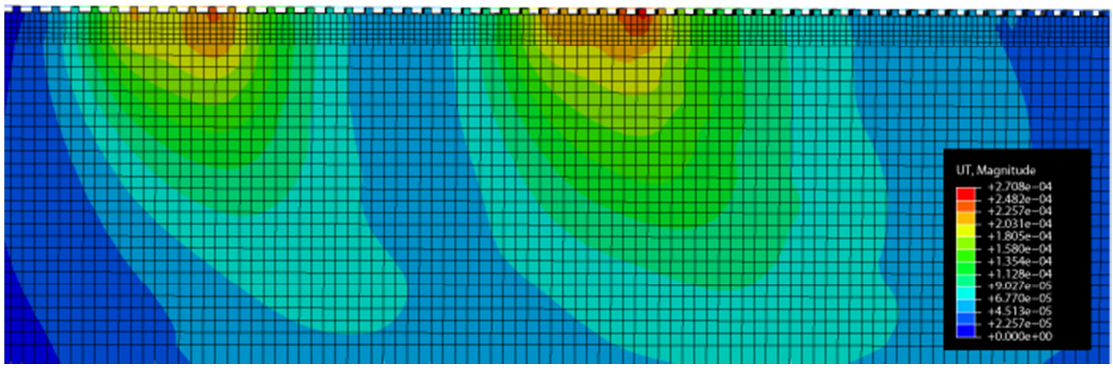

Figure 10.6 - Critical velocity, Thalys train passage 91.7 m/s (330 km/h)

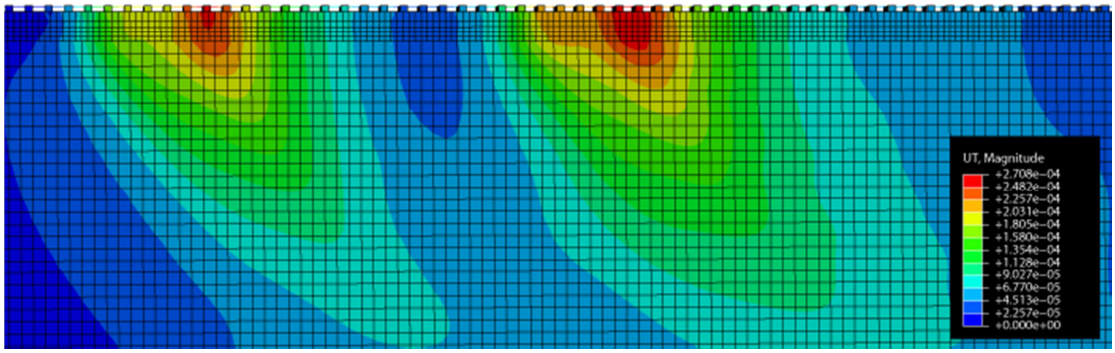

Figure 10.7 - Super Rayleigh velocity, Thalys train passage 111 m/s (400 km/h)

Table 10.2 and Table 10.3 compare soil vibration levels, using three separate metrics, for two individual receiver locations. The near receiver location was 5.5m from the track centre and the far receiver was 19m from the track centre. All metrics showed that the vibration levels increased at both locations as speed increased from 150km/h to 400km/h. VdB registered the lowest percentage increase as it was based on a log scale calculation, however PPV and KB max both exhibited significant increases. This was particularly true at the near receiver where the vibration levels for KB max increased by 377% when the speed was increased. Although the vibration levels also increased significantly for the far receiver, they did so at a lower rate in comparison to the near receiver. Therefore it was clear that vibrations within and close to the track structure were more critical than those in the far field.

Near				
	Sub-Rayleigh	Rayleigh	Super-Rayleigh	Total increase (%)
PPV (m/s)	8.98E-04	2.10E-03	2.90E-03	223.00
KB_{max} (m/s)	2.51E-04	7.54E-04	0.0012	377.35
VdB	79.7954	87.7845	91.1053	14.17

Table 10.2 - Vibration increases in the near field

Far				
	Sub-Rayleigh	Rayleigh	Super-Rayleigh	Total increase (%)
PPV (m/s)	4.60E-04	7.16E-04	9.81E-04	113.44
KB_{max} (m/s)	1.63E-04	2.78E-04	3.92E-04	140.58
VdB	73.7868	77.6721	80.7426	9.43

Table 10.3 - Vibration increases in the far field

10.3 Track type comparison

10.3.1 Background

Elevated ground vibrations from high speed trains can occur in both the near and far fields. As shown previously, when considering the effect of critical velocities the near field experiences a larger increase in vibration levels in comparison to the increase experienced in the far field. Therefore the effect of critical velocities on vibration levels within the track structure was investigated further. This was undertaken by developing three different track type models and comparing the vibration levels for each.

10.3.2 Currently available track types

Ballasted track has been the most common track type used for railway applications for several hundred years. It is a popular material because it is sustainable, hard, durable and provides a cushion for the periodically placed sleepers. This cushioning however can cause excessive track movement, which leads to track alignment irregularities. Correction of such problems requires regular maintenance which means ballasted tracks have high lifecycle costs.

High train speeds generate elevated track forces causing ballasted track to degrade more quickly, resulting in more regular maintenance. Using a discounted cash flow analysis (Schilder & Diederich, 2007), ballasted track can be seen to have high lifecycle costs (Figure 10.8). To improve its performance

track designers use techniques such as optimising rail head geometry, replacing wooden sleepers with concrete ones and inserting geosynthetics between layers (Bezin, Farrington, Penny, Temple, & Iwnicki, 2010). These measures have helped to reduce overall maintenance costs.

Rather than modifying the traditional ballasted track, designers have developed alternative tracks which are more suited for high speed rail. The decline in use of ballasted tracks and the rise in popularity of alternative slab tracks (on Japanese networks) is shown in Figure 10.9.

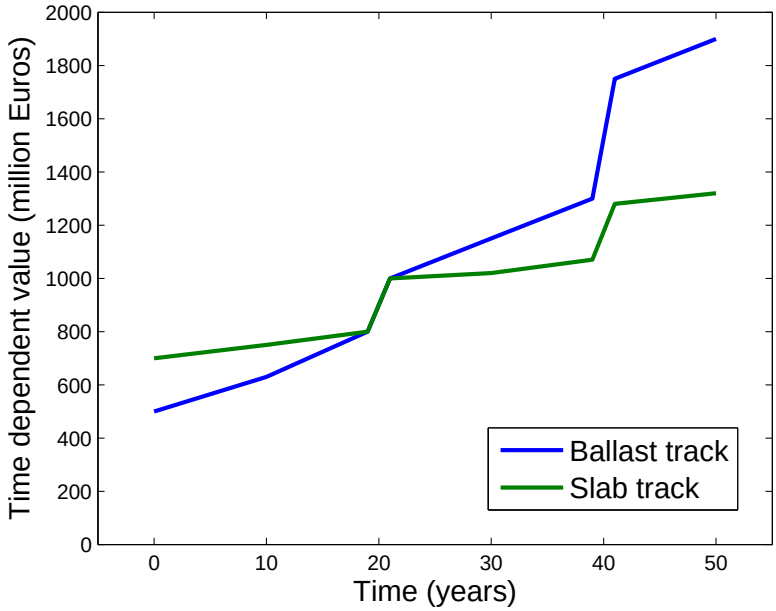

Figure 10.8 - Ballast and slab lifecycle costs (reproduced from (Schilder & Diederich, 2007))

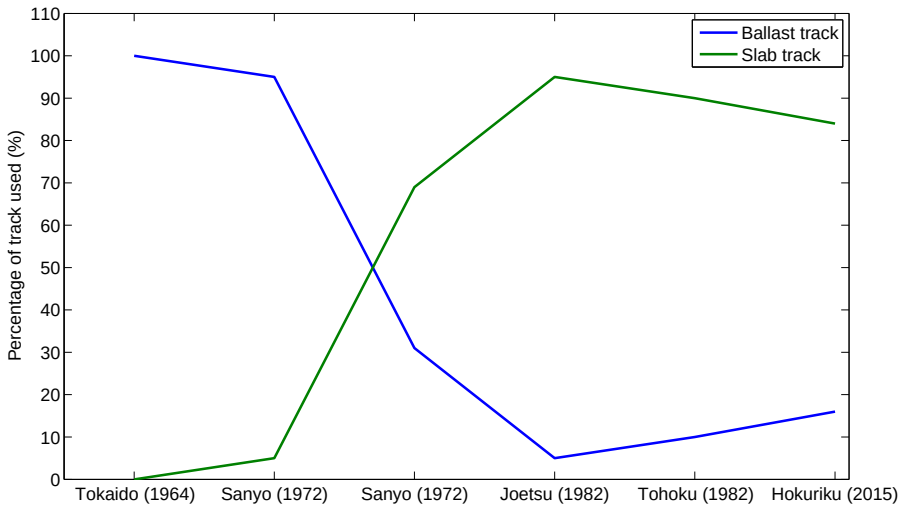

Figure 10.9 - The use of ballasted and slab tracks in Japanese rail (reproduced from (Kao, 2013))

Precast reinforced concrete slab track such as (Ando, Sunaga, Aoki, & Haga, 2001) and (Esveld & Markine, 2000) are manufactured off-site and transported to the construction site. This controlled prefabrication process allows for high quality control and rapid installation upon reaching the new line.

An alternative is the in-situ slab concrete track (Freudenstein, 2010) which is cast at the construction site. Prefabrication is not required thus reducing costs. Despite this, a disadvantage is that quality control is lower than precast tracks, due to weather conditions and a dependence on high quality workmanship.

Another form of in-situ slab concrete track is embedded rail systems (INNOTRACK, 2008). Rather than the rail being supported discretely using

sleepers, the rail is embedded in the concrete slab. The concrete is poured and cast using a slip forming machine which improves quality control but is more expensive in comparison than the construction of other in-situ tracks.

The majority of high speed rail track alternatives are concrete based however other material such as metal have been used. A two layer steel track has been outlined by (Bezin & Farrington, 2010). The bottom layer consists of concrete encased steel beams which support the upper steel layer on which the rails are placed. The installation process is fast however steel is more expensive than concrete meaning construction costs are high.

10.3.3 Previous research

A variety of authors have proposed numerical models to predict vibration levels from ballasted railway tracks. (Sheng, 1999a) proposed an analytical model where the track resting on the ground was approximated as an infinite layered beam resting on a number of infinite parallel homogenous elastic layers.

(X Lei & Rose, 2008) presented an alternative analytical method for ballast modelling. The model was used to determine the ability of an asphalt trackbed over soft subgrade to reduce vibration levels. Numerous FE approaches have also been proposed for ballast track vibration modelling (Galvin et al., 2010a), (L. A. Yang et al., 2009), (Kouroussis et al., 2011a)).

In contrast, (Xiaoyan Lei & Zhang, 2011) and (Jun, Dan, & Qing-yuan, 2008) outlined finite element approaches to modelling traditional concrete slab track behaviour. (Xiaoyan Lei & Zhang, 2011) showed that increasing the slab track structure stiffness improved track vibration performance. (Shamalta & Metrikine, 2003) developed an alternative analytical model capable of simulating vertical vibration from embedded rail slab tracks. Track stresses and displacement were then analysed as a function of train speed.

(Galvin, Romero, & Domínguez, 2010b) investigated the effect of ballasted and non-ballasted tracks on ground vibration levels using a FE/BE model. It was found that the track type had an effect on ground vibrations and it was also shown that floating slab tracks can be used to reduce vibration levels. Other than (Galvin et al., 2010b) and one other piece of literature (Santamaria, Vadillo, & Oyarzabal, 2011), documentation related to the comparison between track types is scarce.

10.3.4 The development of railway track models

Three track types were chosen for comparison: a traditional ballasted track, a slab track and a metal track. Each track model was developed through modification of the ABAQUS model outlined in Chapter 4. The multi-body excitation model and soil model were unchanged. As the ballasted track was identical to that developed in Chapter 3, Chapter 4 and Chapter 9 it is not further described. The properties outlined in Table 10.1 were used to describe the soil.

10.3.5 Slab track model development

The slab track model was composed of five components. The bottom frost protection layer (FPL) supported the hydraulically bonded layer (HBL), which in turn supported the concrete base layer (CBL). The rails were supported by the concrete sleepers which were embedded within the concrete base layer.

Material properties, dimensions and layout are shown in Table 10.4 and Figure 10.10. The FPL, HBL and CBL were truncated in the direction of train passage using infinite elements. Similarly, only half of each component was modelled due to symmetry.

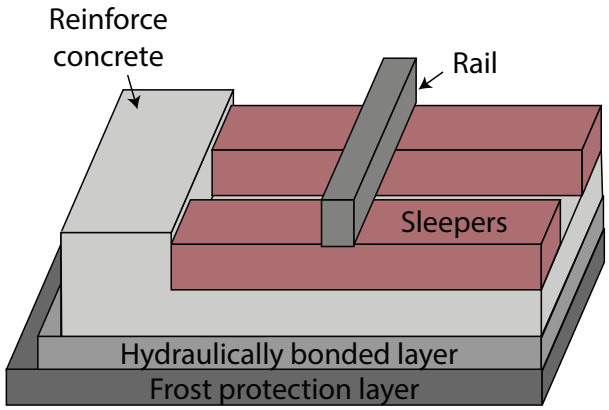

Figure 10.10 - Half-symmetry concrete slab track

Part		Rail	Concrete sleeper	Concrete base layer	Hydraulic base layer	Frost protection layer
Density (kg/m³)		7,900	2,400	2,400	2,400	2,400
Elastic Modulus (MPa)		210,000	30,000	20,000	5,000	1,200
Poisson's ratio		0.25	0.3	0.2	0.2	0.2
Dimensions (m)	**x**	50	0.2	50	50	50
	y	0.153	0.15	0.1	0.3	0.5
	z	0.078	1.6	1.6	1.9	5.2

Table 10.4 – Slab track material properties

10.3.6 Metal track model development

The metal track was modelled as a rail resting on a metal baseplate, which was in turn supported by metal I-section sleepers. The sleepers were directly supported by a concrete section and were also supported laterally through their connection to longitudinal asymmetric steel beams (ABS's). The ASB's and concrete sections were supported by a 100mm hardcore base section (Figure 10.11).

The U, I and ASB metal beam sections could not be modelled directly because the small elements sizes required to model their slim dimensions, enforced a very low timestep criteria for the explicit simulations. To overcome this, each beam section component was transformed into one larger solid section. The material properties (Young's modulus and density) of each section

were reduced to account for the new volume of material. Therefore the overall material properties were unchanged. They are shown in Table 10.5.

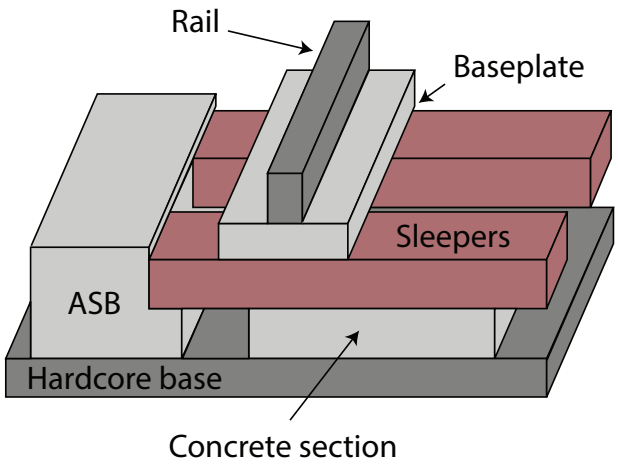

Figure 10.11 - Half-symmetry metal track layout

Part		Rail	Baseplate	Sleepers	ASB ground-plate	Concrete and channel section	Hard-core base
Density (kg/m³)		7,900	3,987	1,498	1,796	2,400	2,300
Elastic Modulus (MPa)		210,000	56,800	89,300	18,400	34,000	10,000
Poisson's ratio		0.25	0.3	0.3	0.3	0.3	0.3
Dimensions (m)	**x**	50	0.2	0.2	50	50	50
	y	0.153	0.1	0.4	0.3, 0.15*	0.15	0.1
	z	0.078	0.36	1.135	0.33, 0.1*	0.7	1.5335
* Cross section composed of 2 joint rectangles (1st number = larger rectangle)							

Table 10.5 – Metal track material properties

10.3.7 Track type vibration performance comparison

The three track type models were subject to a Thalys high speed train excitation running at four different speeds, 250, 300, 330, and 400 km/h. The Rayleigh wave speed of the soil was 330 km/h meaning that two of the train speeds were less than this value, one equal to it and one greater than it.

Figure 10.12, Figure 10.13 and Figure 10.14 show VdB vibration levels with increasing distance from the track centre, for the ballasted, metal and slab tracks respectively. For each plot the track structure with the relevant FE mesh has been superimposed. The receiver nodes were all located on the ground surface below the track structure. For all tracks it was found that vibration levels rose considerably with train speed. For the ballasted track, at the track centre the vibration level rose by 5dB when the train speed was increase from 250 km/h to 400 km/h. This difference increased to approximately 8dB at a point 4.2m away from the centre. Similar increases due to speed were found for the metal and slab tracks.

One notable difference between the three track types was that the vibration levels at the track centre were slightly greater for the ballasted track in comparison to the other tracks. The lowest vibration levels were experienced by the slab track, for which at all speeds experienced a 2-3 dB reduction when compared to the metal track. Even greater reductions were made in comparison to the ballasted track.

Furthermore, analysis of the ballasted and metal track showed that for the 250 km/h train the vibration level at the track centre was 96dB for both. In comparison, for the 400 km/h train the vibration level for the metal track was 2dB less than that for the ballasted thus leading to the conclusion that it was less affected by increases in train speed.

A noticeable observation found for each track at all speeds was that a local maxima was present at the point where the base sublayer met the soil. It was proposed that this peak was caused by a small release of vibration energy produced by the increased freedom of movement for the nodes at this point.

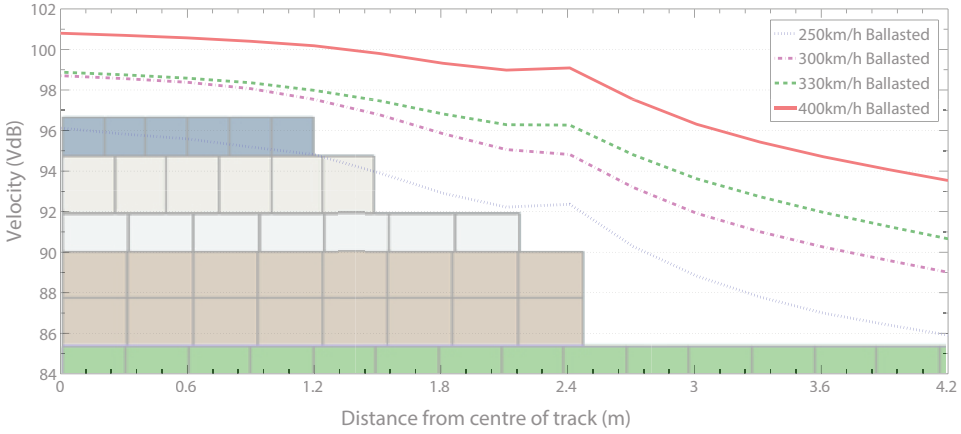

Figure 10.12 - Ballast track vibration

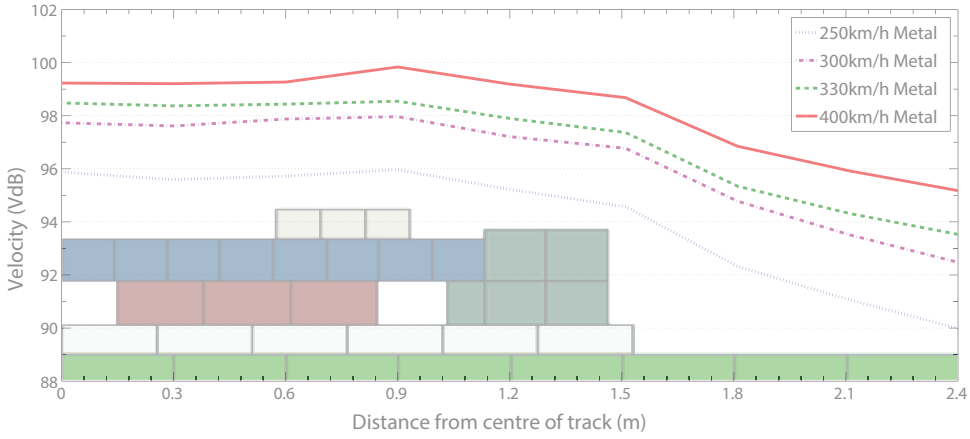

Figure 10.13 - Metal track vibration

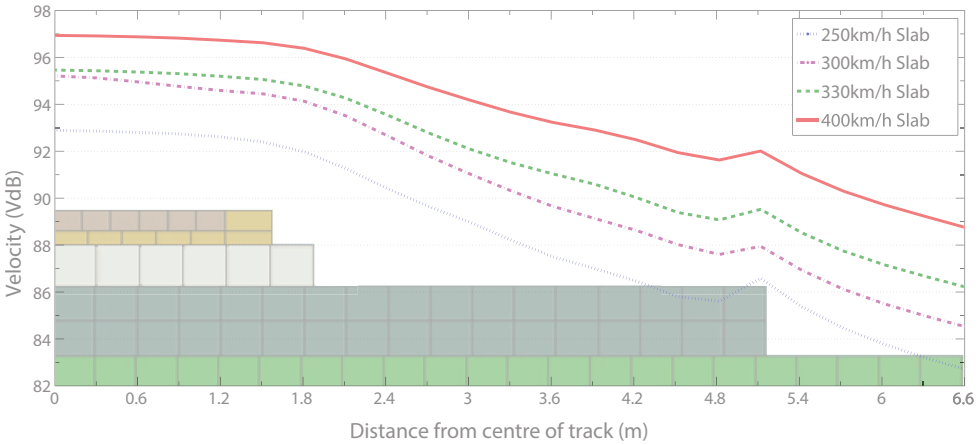

Figure 10.14 - Slab track vibration

10.4 The role of embankment structures on vibration propagation

To examine the role of embankments in vibration propagation, two embankment conditions were compared to the case of no embankment. The embankments investigated were both 1.5m high with a slope angle of 30 degrees.

They were formed from two materials with contrasting stiffness characteristics as detailed in Table 10.6. Physically these properties describe materials that are stiffer and softer than the top layer of supporting soil respectively. It must be noted that the material parameters were chosen to illustrate the envelope of the difference in embankment behaviour, rather than to replicate the physical reality of a specific soil type.

	Young's modulus (MPa)	Poisson's ratio	Density (kg/m^3)
Soft embankment	6	0.23	1300
Stiff embankment	600	0.35	2150

Table 10.6 – Embankment material properties

The effect of each embankment on vibration levels at various track locations was investigated. Firstly, the near field (locations within the track structure) was analysed for the purposes of examining the effect of embankment conditions on track degradation. Secondly, far field (locations outwith the track structure) vibration response was investigated to determine the potential for vibration to cause damage to structures in close proximity to the track.

For both investigations the natural soil was modelled as a 15m deep, homogenous, linear elastic material with physical properties as described in Table 10.7. The train speed was kept constant at 300 km/h.

	Young's modulus (MPa)	Poisson's ratio	Density (kg/m^3)
Homogenous soil	129	0.3	1600

Table 10.7 – Soil properties underlying embankment

10.4.1 The effect on near field vibrations

Displacement criteria was used to analyse the level of ballast deformation due to the passage of a Thalys high speed train. The passage of each individual wheel is clearly visible in Figure 10.15. Vertical deflection for the case of no embankment is less than the soft embankment but greater than the case of the stiff embankment. Similarly, there is a strong contrast in maximum deflection levels between the stiff and soft cases, with the peak displacement for the soft embankment being 63% greater.

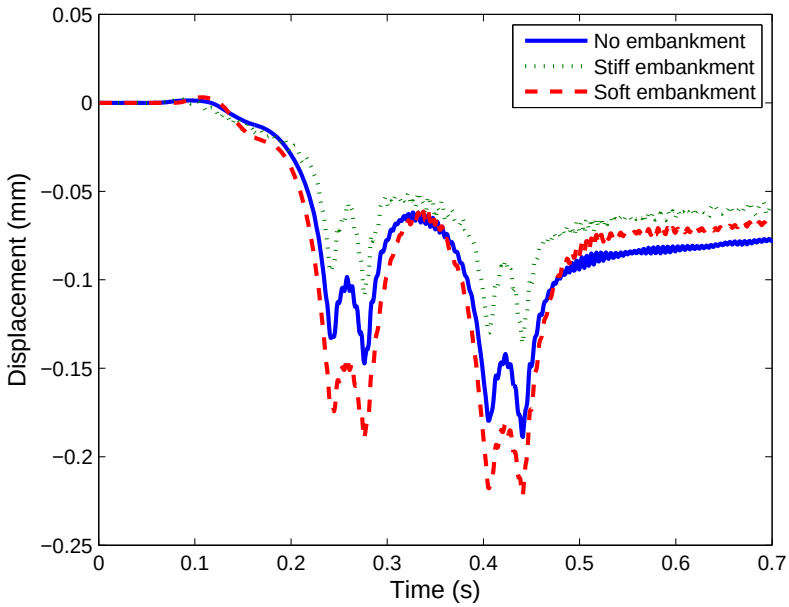

Figure 10.15 - Ballast vertical deflection

This increased deflection has two primary causes. Firstly the softer embankment has less compressional strength thus allowing the same load to penetrate further into the material. Secondly, the embankment to soil material interface has a seismic reflection coefficient (R_c) (Equation 10.2) of 0.28 thus causing wave energy to be reflected from the natural soil surface back into the embankment, thus trapping energy within its structure. This is consistent with Snell's law and causes a waveguide effect. The opposite is observed for the stiff case because the embankment-soil interface has a reflection coefficient of -0.55, thus encouraging high levels of energy transmission from embankment to soil.

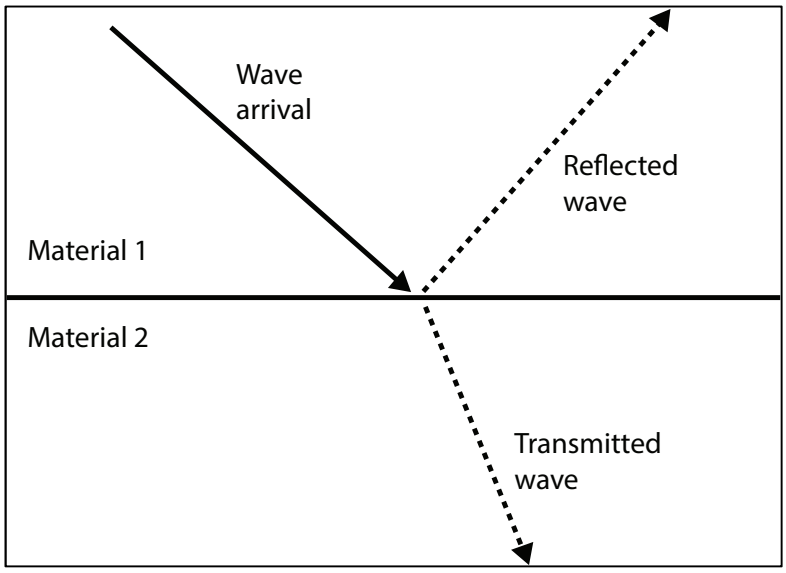

Figure 10.16 - Seismic reflection/transmission

$$R_c = \frac{\rho_1 v_1 - \rho_2 v_2}{\rho_1 v_1 + \rho_2 v_2} \qquad \text{Equation 10.2}$$

Where, ρ_1 = density of upper material, v_1 = wave velocity in upper material, ρ_2 = density of lower material, and v_2 = wave velocity in lower material.

10.4.2 The effect on far field vibrations

Far field vibrations are important for determining the probability of structural damage to nearby buildings. Therefore in accordance with (International Standards Organisation, 1999), PPV criteria were used to analyse vibration intensity at varying distances from the embankment.

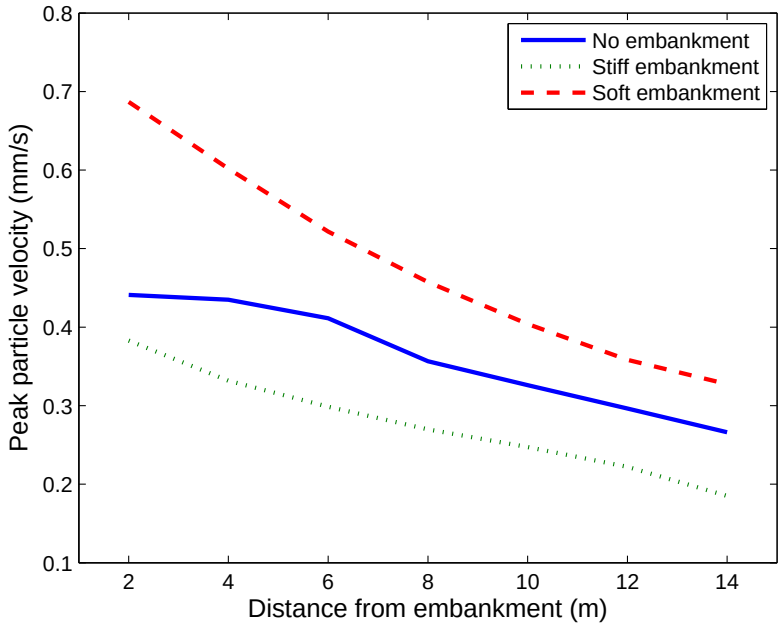

Figure 10.17 - The effect of embankment material on far field response

Figure 10.17 shows vibration levels at seven equally spaced receivers, ranging between 2-14m from the embankment footing. As expected, PPV decreases with distance from the embankment. Despite this, when embankment stiffness is increased from soft to stiff, an average decrease in PPV of 72% in the surrounding soil is observed. Furthermore, a stiff embankment causes a significant decrease in vibration propagation while the soft embankment causes an increase of similar magnitude. Therefore it can be concluded that the addition of an embankment formed from a stiffer material than the underlying soil reduces far field vibration. Similarly, an embankment that is soft in comparison to the surrounding soil increases far field vibrations.

10.5 Conclusions

The finite element ABAQUS model developed in Chapter 4 and validated in Chapter 9 was used to analyse several aspects of railway vibration. Firstly train speed was investigated and it was found that as the train approached the Rayleigh wave speed of the underlying soil (i.e. the critical velocity) vibration levels increased significantly. This was found for all three vibration metrics tested (PPV, KB_{max} and VdB). It was found that greater increases in all metrics occurred close to the track structure and diminished with increasing distance from the track.

Three different track types were also analysed to assess their vibration performance when subject to critical velocities. It was found that ballasted track generated the highest levels of vibration and was also more sensitive to changes in train speed. Slab track experienced the lowest levels in vibration and was least effected by speed. The vibration performance of the metal track lay between that of the slab and ballasted tracks.

Lastly, the effect of embankment constituent material was analysed to determine its effect on vibration levels in the near and far field. It was found that stiffer embankments resulted in a reduction in vibration in both the near and far field, in comparison to soft embankments. It was concluded that this was in-part due to the contrast in material properties between the embankment and underlying soil.

Having shown that the vibration levels generated due to train passage can be large, particularly at high speeds, Chapter 11 seeks to investigate the effectiveness of several vibration mitigation techniques.

Chapter 11. Vibration mitigation solutions

11.1 Wave barrier background

Techniques to mitigate vibration propagation can be divided into two categories: active and passive isolation. Active isolation refers to the isolation of vibration within locations either close to or inside the track structure, such as floating slab track (Tayabji & Bilow, 2001), rail pads (Thompson, 2009) or resilient wheels (Kouroussis, Verlinden, & Conti, 2011c). Passive isolation refers to screening vibration through measures placed at locations in close proximity to vibration sensitive sites rather than in close proximity to the track.

Wave barriers are a form of passive vibration isolation which offer high isolation performance and do not require direct access to the railway line during construction. To maximize performance, trench properties such as size, shape (Zakeri, Esmaeili, & Mosayebi, 2013) and infill material must be selected relative to the excitation frequency(s). Despite this, few researches have investigated the effect of trench properties and their ability to mitigate moving excitations, which emit a broad band of frequencies, as is the case of a high speed train.

Early research by (Woods, 1968) illustrated that open trenches were capable of reducing vibration amplitudes for a stationary excitation. It was shown that trench depth and its distance from the source have a significant influence on isolation. More recently a 2D frequency domain Boundary Element

Method (BEM) was used to investigate the performance of open and in-filled trenches for the purpose of vibration isolation (Beskos, Dasgupta, & Vardoulakis, 1986). The advantage of using BEM rather than FEM meant that no absorbing boundary condition was required at model edges. For a well formed harmonic excitation it was found that both trench depth and breadth play an important role in vibration isolation.

(Y. Yang & Hung, 1997) presented an alternative approach through the use of a frequency domain finite/infinite element method (FEM). All trenches were modelled with respect to the soil Rayleigh wavelength from a 31Hz pulse source. It was found that an acoustic impedance ratio of 8:1 between soil material and trench infill material was optimal.

Due to the wide range of geometrical dimensions that effect trench screening ability, (Di Mino, Giunta, & Di Liberto, 2009), and (Alzawi & Hesham El Naggar, 2011) used 2D models similar to (Y. Yang & Hung, 1997) to develop an artificial neural network to investigate each individual parameter. It was found that trench efficiency is improved by placing the trench at greater distances from the track.

Although such an approach allows for a rapid analysis of optimal trench properties, the underlying method is based on approximating a physical 3D space using a 2D numerical model. A disadvantage of 2D modelling is that the trench must be assumed to be infinite in length and the multi-path 3D wave-field is reduced to 2D. Thus the effect of trench length cannot be investigated and only two out of three velocity components can be modelled.

A 3D analytical solution based upon the Green's solution of Lamb's problem was developed to approximate the ability of in-filled trenches to reduce vibration (Gao, Shi, Feng, & Qiu, 2008). It was found that stiff backfill materials perform better than soft backfill materials. A limitation of this analytical approach is that it is only valid for a narrow range of assumptions.

(Shrivastava & Kameswara Rao, 2002) proposed a more versatile, implicit 3D FEM model to test the ability of open and in-filled trenches to screen vibration. A fixed boundary condition was used rather than an absorbing boundary, thus possibly allowing reflections to contaminate the solution; and a stationary excitation with narrow frequency content was utilized. Therefore the results have only limited relevance to the railway industry, because a moving train acts as a series of moving point sources of different amplitude and frequency rather than a single point/line load. The variation of source location and frequency content can have a significant effect on trench performance. In addition, trench length cannot be properly investigated because the source location is fixed.

(Karlstrom & Bostrom, 2007) overcame the challenges associated with a stationary excitation and investigated trench performance for a constant point load moving at different speeds. It was found that low frequency vibration (typically caused by a low velocity source) was effectively screened but high frequency vibration (high velocity source) levels were amplified by trench presence.

In practice, early forms of the gas cushion trench wave barrier were utilized at several locations in Sweden such as Gnarp, Stockholm, Uppsala and Saffle in the 1980's (Massarsch, 2005). In Gnarp a 50m long trench with a depth of 6.5m was used to reduce the transmission of railway vibration into a residential building by 70%. Similarly, in Stockholm a 95m long trench with a depth of 6.5m was used to reduce the transmission of railway vibration into a temple by 65%. More recently, advanced gas cushion wave barriers have been developed capable of being installed under a wider range of soil conditions and to greater depths. Such barriers have been installed to protect a two storey residential building in Dusseldorf. In this case the gas cushion was 75m long, extended to a depth of 12m and provided a significant reduction in vibration levels (Massarsch, 2005). Using a similar technique, a polystyrene wave barrier with concrete side panels was also used to effectively reduce vibration levels at a test track in Brussels (François et al., 2012).

Using a similar methodology to (Ahmad & Al-Hussaini, 1991) the effect trench depth, width, length and distance from the track on the ability of screen vibration was investigated. The relationships found between these parameters were used to show that substantial savings could be made by optimizing wave barrier geometry based upon geotechnical conditions and excitation frequency.

11.2 Trench Modelling

The efficiency of a trench to isolate vibration is a function of its geometrical dimensions in relation to the dominant frequency(s) of the

propagating wave(s). Approximately 2/3 of total wave energy is transmitted via surface waves (e.g. Rayleigh) meaning it is common to define trench dimensions in terms of Rayleigh wavelength. To avoid the ratio of trench geometry to excitation frequency skewing results, previous researchers such as (Y. Yang & Hung, 1997) have focused on utilizing stationary point excitations of single frequency, thus making it trivial to define trench dimension based upon this single frequency.

A single frequency source defined in this manner is an unrealistic approximation of typical high speed train passage. To achieve a more realistic approximation of the physical problem, a single Thalys high speed train passenger car was used as the excitation mechanism and modelled using the multi-body excitation model described in Chapter 4. The frequency content of this excitation source at a point 18m (observation point) from the track is presented in Figure 11.1. Although the frequency content was spread over a range predominately below 50Hz, and varied with distance from the track (Lombaert & Degrande, 2009), the dominant frequency was 12 Hz - which was used to calculate the Rayleigh wavelength and subsequent trench dimensions.

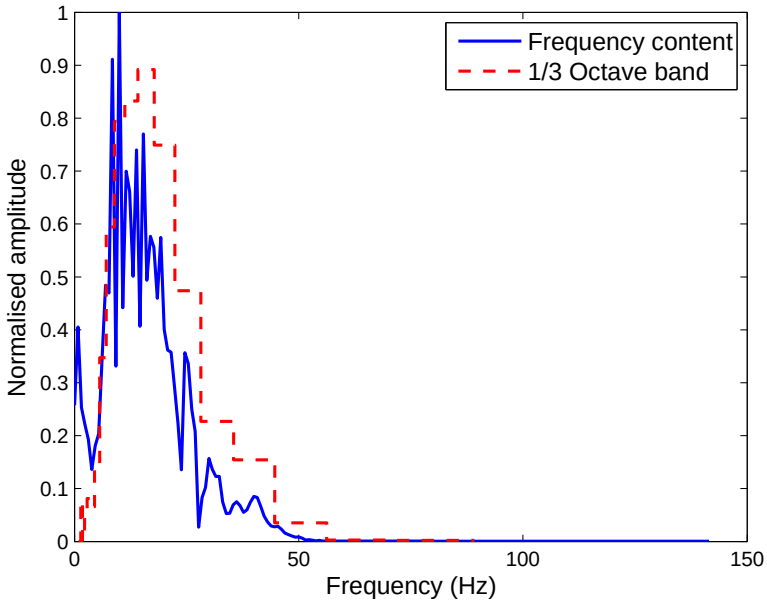

Figure 11.1 - Soil frequency spectrum due to a single passenger car axle (18m from track)

Based on this frequency value, the Rayleigh wavelength for the homogenous soil model was 7.7m. If a different soil was investigated the Rayleigh wavelength value would change because a change in soil material properties would generate different Rayleigh wave speeds and corresponding Rayleigh wavelengths. Similarly, this wavelength would change depending on train speed, track type and several other factors. This makes it difficult to calculate a range of typical Rayleigh wavelengths.

Trench geometry was defined using the notation:

$$d = D/\lambda_R$$

$$w = W/\lambda_R$$

Equation 11.1

$$l = L/\lambda_R$$

$$s = S/\lambda_R$$

where ‘D’ is trench depth, ‘W’ is trench width, ‘L’ is trench length and ‘S’ is the distance between track and trench as shown in Figure 11.2.

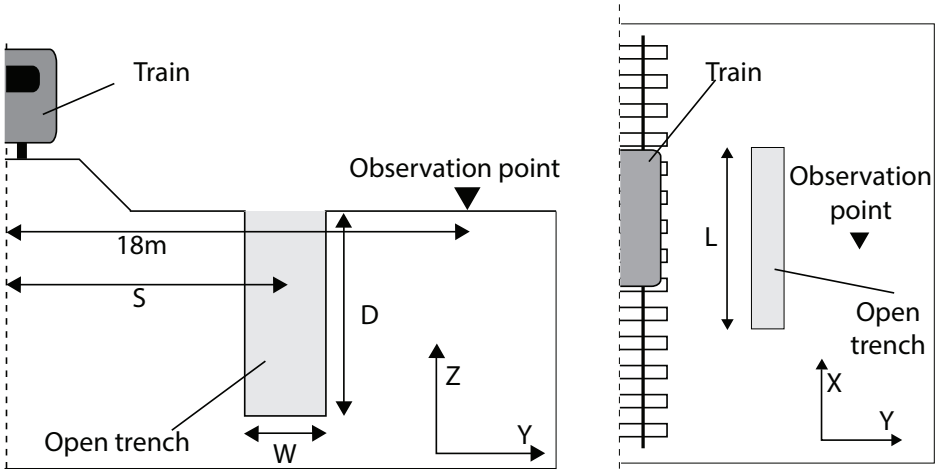

Figure 11.2 - Trench geometry schematic, (left: side-on view, right: Birdseye view)

Unless otherwise stated the trench dimensionless quantities were: d=1, w=1/3, l=6 and s=1.5. For this particular example this translates to a trench with dimensions, D = 7.7m, W = 2.54m, L = 46.2m (nearly the full width of track) and S = 11.55m.

All wave barriers were treated as open trenches. This is physically impractical as trenches require in-fill material to fulfill safety and stability criteria. A common engineering solution is to fill trenches with low density gas cushions (Kanda, Ishii, & Yoshioka, 2006) or polyurethane (Alzawi & Hesham El Naggar, 2011). Rather than introduce additional approximations for in-fill material properties it was found that open trenches provided an effective condition under which to analyse trench geometry. This assumption has been shown to be valid, as low density materials offer screening performance similar to open trenches – provided that the acoustic impedance ratio (the level of reflection determined using Equation 10.2) between soil and trench in-fill is at least 8 (Massarsch, 2005).

To assess the ability of each geometric trench permutation to isolate vibration, velocity levels were monitored and averaged over a $1m^2$ surface area located approximately 18m from the track. Trench performance was then evaluated using a reduction ratio approach similar to that used in (Y. Yang & Hung, 1997), and (Hung & Ni, 2007):

$$A_r \frac{RMS_{trench}}{RMS_{default}} \qquad \text{Equation 11.2}$$

Where RMS_{trench} is the root mean squared amplitude of the vibration level recorded in the presence of a wave barrier, and $RMS_{default}$ is the root mean squared amplitude of the vibration level recorded when no wave barrier is present. The root mean squared amplitude for each was calculated using a one

second time window. Physically this implies that if a trench does not exist then Ar = 1, and in contrast, if the trench isolates 100% of the vibration, then Ar = 0.

Firstly an initial simulation was performed in the presence of a solid homogenous half-space (i.e. without the presence of a trench). At 19m from the track, the RMS values were 0.068, 0.14 and 0.072 mm/s in the x, y and z directions respectively. Therefore for this case the vertical vibration was approximately twice that of the horizontal vibration. The vertical vibration was thus the critical condition and was more likely to cause structural damage than the horizontal components. This finding was complimentary to the field experiment results presented in Chapter 8.

11.3 Numerical results

11.3.1 The Effect of Trench Width

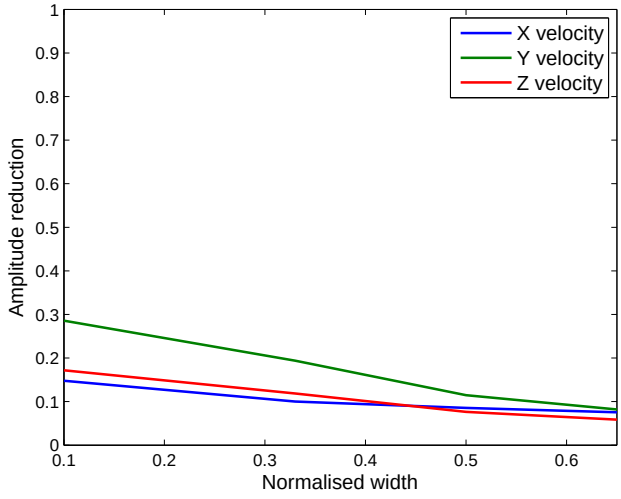

Figure 11.3 - The effect of trench width on amplitude reduction ratio (0.0 = 100% isolation, 1.0 = 0% isolation)

Figure 11.3 shows the effect of trench width on vibration reduction ratio for the vertical velocity component (red) and both horizontal components (blue and green). A range of width parameters varying between w=0.1 and w=0.65 were tested and all were found to offer high levels of screening. Despite this, for all three vibration components there is only minimal reduction when the trench width parameter is increased from w=0.1 to w=0.65. Therefore it can be concluded that trench width has little effect on the overall ability of a trench to screen vibration.

11.3.2 The Effect of Trench Depth

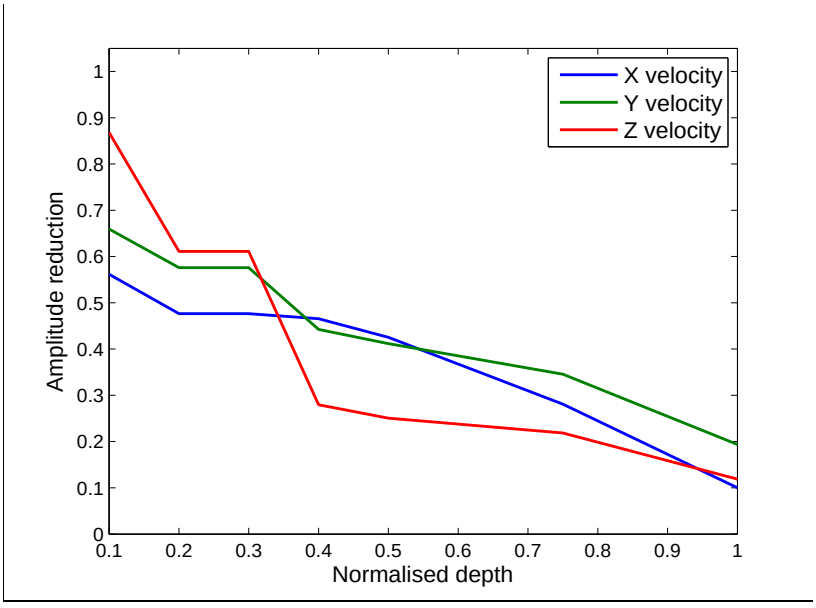

Figure 11.4 - The effect of trench depth on amplitude reduction ratio

Trench depth can be seen to have a greater impact on amplitude reduction ratio in comparison to trench width.

Figure 11.4 shows that amplitude reduction performance increases rapidly with depth for a series of seven depth parameters varying between d=0.1-1.0.

Regarding vertical vibration, depth parameters greater than 0.4 offer large reductions which is important because vertical vibration is typically more dominant than horizontal vibrations for the case of railway traffic. When the trench normalized depth is increased from 0.1 to 1, the amplitude reduction capability increases by 83%. This is consistent with results presented by (Jesmani et al. 2008) (Jesmani, Shafie, & SadeghiVileh, 2008).

Horizontal vibrations also reduce as normalized depth is increased, albeit more steadily. For both cases, an increase in normalized depth from 0.1 to 1, results in approximately a 0.45 improvement in amplitude reduction performance.

Depth has a significant influence on vibration screening because Rayleigh waves carry 67% of total wave energy and decay exponentially with depth. Therefore as trench depth increases less Rayleigh wave energy passes under the trench thus improving the trench vibration reduction ability.

11.3.3 The Effect of Trench Distance from Railway Line

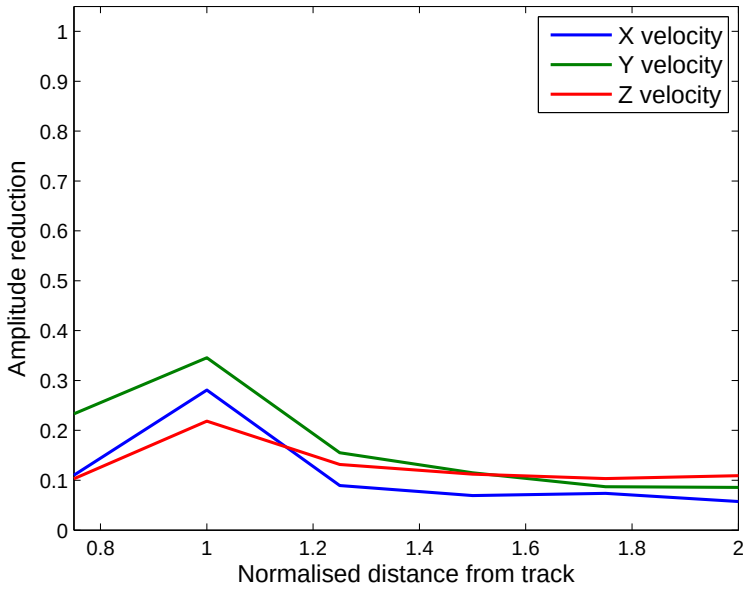

Figure 11.5 - The effect of trench distance from track on amplitude reduction ratio

Figure 11.5 shows the relationship between amplitude reduction ratio and the distance between trench and track. The minimum trench distance parameter tested was s=0.75 and the maximum was s=2.0. Distance parameters below s=0.7 were not considered because such trenches would be located too close to the line and possibly interfere with the supporting track material.

Trench performance is affected by distance from the track if the distance is less than or equal to one Rayleigh wavelength. For horizontal vibration, if a normalized distance is chosen greater than 1.25 then vibration levels will be much reduced in comparison to a normalized distance of 1. For vertical vibration, reduction is also observed but to a lesser extent. Therefore distance parameters above s=1.25 are desirable due to their higher reduction ratios.

Greater distances are more effective due to the dominance of body waves in regions very close to the track. In such regions body waves carry a high percentage of the total wave energy and decay slowly with depth. Therefore the body waves readily pass under the trench and are thus unaffected by its presence. As the trench moves further from the track the influence of body waves decreases and Rayleigh waves are predominant.

11.3.4 The Effect of Trench Length

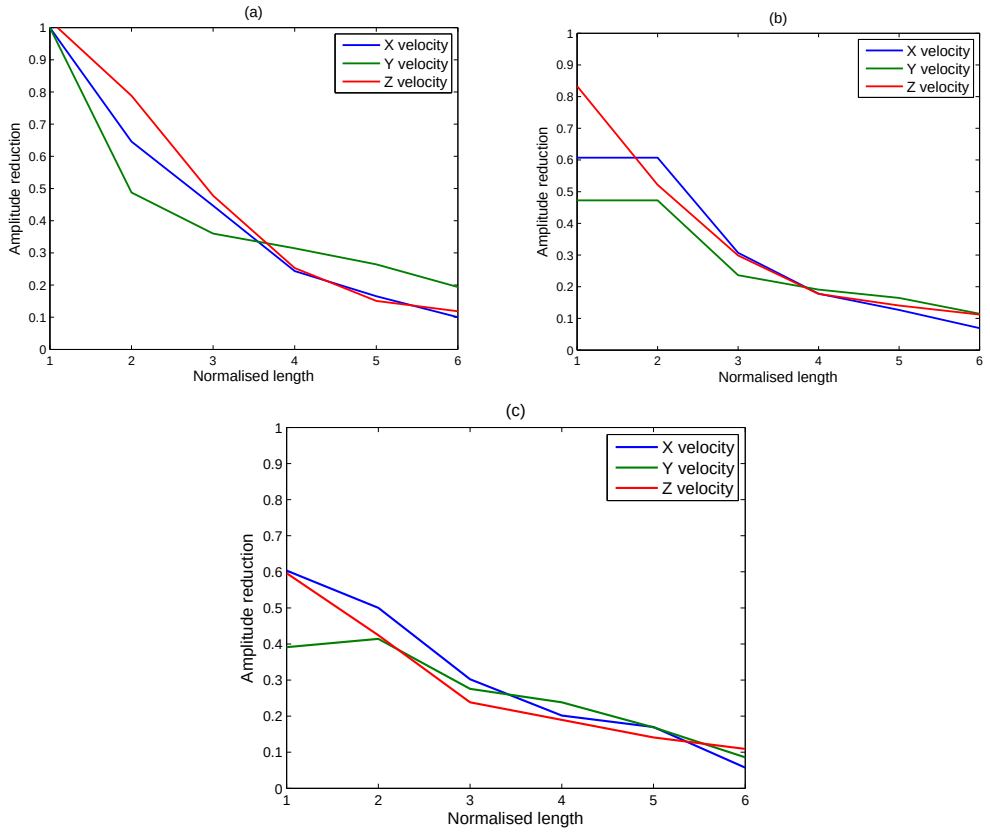

Figure 11.6 - The effect of trench length parameters on amplitude reduction ratio, (a) Left: s=1, (b) Right: s=1.5, (c) Bottom: s=2

Figure 11.6 shows that trench length plays an important role in vibration isolation. When the normalized trench length is 1 the reduction ratio in all three component directions is also 1 meaning that the trench is having no effect. As the trench length is increased, greater reduction is observed and when l=6, (nearly the full length of the track) a reduction in vibrations of about 85% is found. This is caused because there is no longer a direct path between the railway line and receiver - meaning that the only wave travel path is under the trench. This is important because Rayleigh waves decay exponentially with depth meaning that only a small percentage can pass under the excavation. Therefore the unimpeded response at the receiver location is likely to be a combination of compression, shear and Rayleigh waves that passed under the trench, all carrying low levels of energy.

When the trench distance from the track is increased to s=1.5, (Figure 10b) vibration levels are reduced for short trench lengths but are similar to the s=1 case for greater trench lengths. Similarly, when s=2 (Figure 10c), vibration levels are reduced for short trench lengths in comparison to when s=1 and s=1.5, but are similar to s=1 and s=1.5 at greater trench lengths. This effect is true for all three vibration component directions because when the trench is located in close proximity to the track it is easier for the Rayleigh waves to travel around the excavation and reach the observation point. Therefore it can be concluded that if trenches are placed further away from the track and closer to the structure they are shielding, trench length can be reduced while maintaining performance.

11.3.5 Practical considerations

A number of important practical aspects emerge from this research. In particular trench depth has been shown to have greater impact on vibration isolation performance than trench width. Despite this, when planning trench isolation strategies both construction feasibility and costs must also be considered.

For the case of vibration isolation trenches - the depth to width ratio is too large to utilize conventional backhoe excavation methods, so hydro vacuum excavation techniques are typically employed. Hydro vacuum excavation simultaneously uses high pressure water to break down soil deposits and a vacuum to remove it.

Excavated trenches must be in-filled to fulfil safety and stability criteria. Polyurethane foam is a suitable material because of its low density and hence low acoustic impedance, plus its ease of installation. The polyurethane resin is typically laid using gravity fed spraying and has an expansion ratio of 1000% (10x).

To determine the effect of trench geometry on project cost, overall construction costs were divided into two components: excavation costs and infill costs. Hydro vacuum excavation costs were been assumed to cost \$310/m^3 for labour, plant and spoil disposal costs. Polyurethane foam was

assumed as the infill material and costs were calculated to be \$650/m^3 for labour, plant and materials. Therefore the total cost per cubic metre is \$960.

For the default trench described in the 'trench modelling' sub-section (d=1 (7.7m), w=1/3 (2.54m), l=6 (46.2m)), the total trench size is 904m^3 resulting in an installation cost of \$868,000. Despite this, as trench width has been found to be a non-critical parameter then reducing the width to w=1/30 (i.e. total width = 0.25m) results in a barrier size of 89m^3 and a total cost of \$85,500. This saving of \$782,500 only leads to a small drop in performance. Similarly if the depth is reduced to d=0.4 (3.08m), \$518,000 is saved while maintaining a similar isolation performance for vertical vibrations.

To minimize costs even further, a trench with both optimized depth and width geometry was tested (d=0.4 and w=1/30). It was found that vibrations were reduced by 80% in the vertical direction and 30% and 57% in the x and z horizontal directions respectively. This optimized trench geometry offers similar performance to the default trench but for \$34,200. As vertical vibration is dominant in the case of high speed rail, for this specific example vibration levels can be reduced by approximately 80% at a cost 96% cheaper than the original solution.

11.3.6 Frequency content comparison

Figure 11.7 shows the normalised frequency spectrum and 1/3 octave band for the optimized trench at 18m from the track. When compared to the case of

no trench (figure 5), the frequency spectrum for both responses is relatively similar. Despite this, the trench damps out some of the frequencies located outside the range of 10-15Hz and an additional peak at 2Hz is present. This 2Hz peak is possibly due to Rayleigh waves reflecting against the trench, back to the track symmetry condition and back against the trench again.

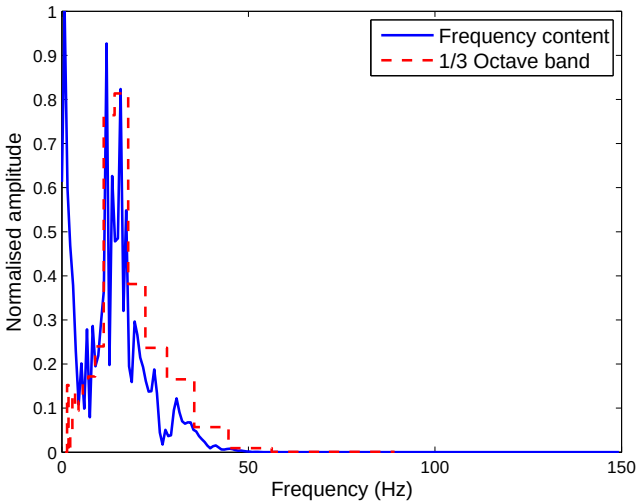

Figure 11.7 - Frequency spectrum and 1/3 octave band for an optimized trench (18m from track)

11.4 Vibration isolation using resiliently bound ballast

Resiliently bound ballast (RBB) is a material recently developed as an alternative to traditional ballast that improves on its mechanical behaviour and stiffness. It is a mixture of standard ballast and recycled tire derived aggregate (TDA) bound using a resilient epoxy binder. It is designed to permit the minute movement of ballast stone particles relative to each other while preventing abrasion between them.

Similar ballast strengthening techniques exist such as XiTrack, a polymer injection solution (Woodward, Kennedy, Medero, & Banimahd, 2011), which although it can be used on new tracks, is typically used to remediate sections of track with excessive displacements. The RBB material is principally designed for the deployment on new lines (or for ballast renewal), rather than remediation, with the added benefit of reducing the environmental impact of car tyres. RBB is not typically injected in-situ into existing ballast track in the same manner as XiTrack.

RBB has been shown to improve on the cohesive strength of traditional ballast and one usage has been proposed to use it to improve ballast durability at the sleeper/ballast interface. It has also been suggested that RBB may aid in the reduction of railway vibrations and thus is of interest to high speed rail track designers from an environmental assessment viewpoint.

To determine the effectiveness of RBB to isolate vibrations, the ABAQUS model developed in Chapter 4 was adapted to enable the simulation of both traditional and RBB ballast. The properties used to describe both materials are shown in Table 11.1. The resiliently bound ballast can be seen to be much stiffer than the traditional ballast.

	Young's modulus (MPa)	Poisson's ratio	Density (kg/m^3)
Traditional ballast	200	0.32	1650
Resiliently bound ballast	690	0.32	1710
Homogenous soil	50	0.37	1900

Table 11.1 – Ballast and soil material properties

11.4.1 The effect of ballast height on vibration isolation

Ballast height varies depending on railway standards and regulations in different countries. In the UK, the typical ballast height is 0.3m, however on some projects (e.g. HS2) this may be reduced due to environmental reasons. Similarly, it is not uncommon for ballast height to be greater than 0.3m on some European lines. Therefore the effect of traditional ballast and RBB height on vibration levels was investigated (Figure 11.8). Six heights were analysed: 0.15m, 0.3m, 0.45m, 0.6m, 0.75m and 0.9m.

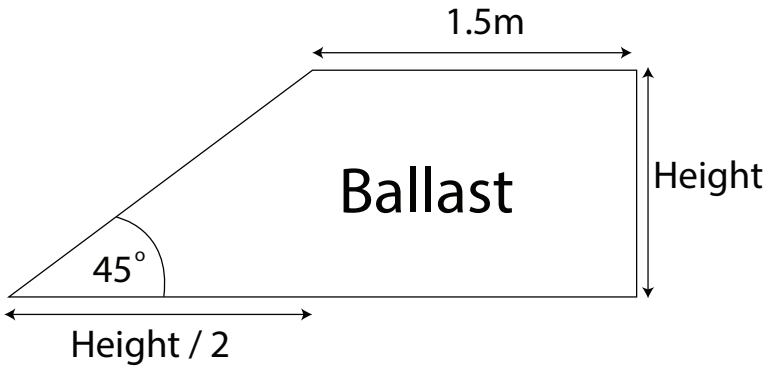

Figure 11.8 - Ballast height schematic

Each ballast height model was subject to a Thalys high speed train travelling at critical velocity (330 km/h) over a homogenous soil. The soil had material properties as shown in Table 11.1. To enable a fair comparison of ballast performance, the subgrade and subballast dimensions were held constant.

11.4.2 Near field vibration

Figure 11.9 shows the effect of ballast height on vibration levels (PPV) at soil locations 0.4m and 1.6m from the track centre. These locations represent two points directly beneath the ballast, at the ballast/soil interface. It should be noted that the vibration levels are greater at the 1.6m location because although it is further from the track centre, it is closer to the rail.

It can be seen that for both receivers that the RBB causes a reduction in vibration levels. Further, the divergence between blue and green lines shows that reduction performance is magnified when RBB thickness is increased.

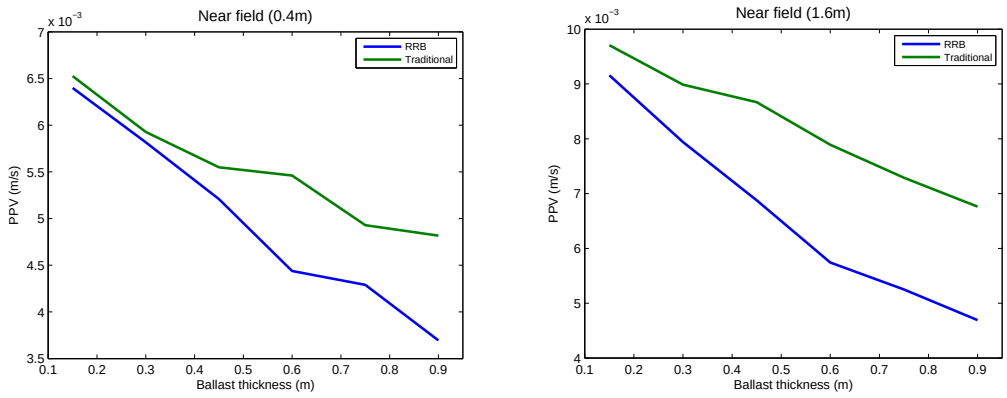

Figure 11.9 - Near field PPV, (a) Left = 0.4m, (b) Right = 1.6m

Figure 11.10 shows the frequency spectrum of a receiver at the bottom of a 0.15m thick section of both ballast types, at a distance of 0.9m from the track centre. It is seen that the RBB transmits a greater percentage of high frequency content through it in comparison to the traditional ballast. The low frequency eigenfrequencies are similar for both figures, however a large

percentage of the high frequency content has been dampened by the unbound discrete nature of the traditional ballast. Additionally, the total energy for the RBB case is divided over a greater frequency range whereas for the traditional case it is more concentrated at lower frequencies. Therefore the RBB eigenfrequencies that match the train excitation frequencies (typically <20Hz) are likely to cause lower levels of vibration in comparison to the traditional ballast.

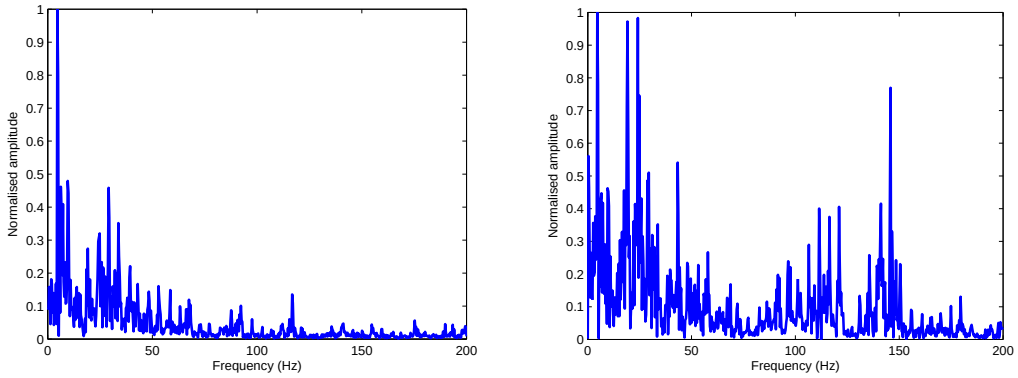

Figure 11.10 - Under-ballast frequency spectrums, (a) Left: traditional, (b) Right: RBB

11.4.3 Far field vibration

Figure 11.11 compares the performance of the RBB and traditional ballast at distances greater than 8m from the track. It is seen that for the 10m, 15m and 20m distances the RBB offers a reduction in vibration. This is true for all ballast thicknesses however for the 10m and 15m cases the percentage increase in performance over the traditional ballast is improved with increasing

ballast height. As the distance from the track increases, the performance difference between ballast heights becomes negligible.

The effect of ballast height is clearly apparent at 5m from the track where the 0.15m high RBB section is found to increase the vibration levels. This finding is isolated and possibly occurs because the receiver is close to the edge of the subgrade. Despite this, it is not a major concern because all other distances both in the far and near (Figure 11.9) fields exhibit reductions when the RBB is utilised.

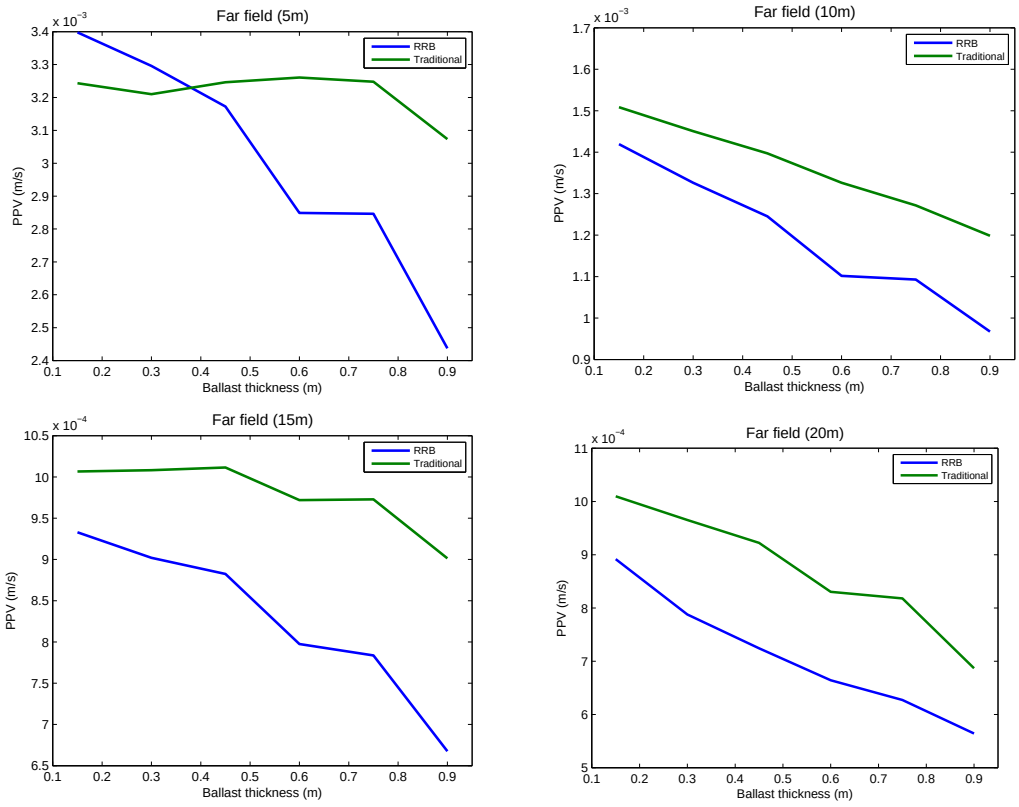

Figure 11.11 - Far field PPV at various distances from the track, (a) Top left: 5m, (b) Top right: 10m, (c) Bottom left: 15m, (d) Bottom right: 20m

11.5 Conclusions

The installation of wave barriers and resiliently bound ballast are two techniques that are potentially capable of reducing railway vibrations. Wave barriers provide an effective method to screen railway vibrations but their installation cost is high. In an attempt to minimize construction costs, numerical investigations were undertaken using the ABAQUS model to determine the relationship between trench geometry and vibration isolation performance.

Numerous simulations were performed and for each run one of the wave barrier dimensions was altered. Therefore the effect of each individual parameter on vibration levels was determined. It was found that trench depth had the most significant influence on vibration reduction with isolation performance increasing rapidly with depths greater than 40% of the soil Rayleigh wavelength. In contrast trench width was found to have little effect, with both narrow and wide trenches shown to be effective in screening vibration. Therefore it was recommended that trench depth should be at least d=0.4 and that width and distance should be minimised with respect to construction cost. Using these recommendations it was shown that for a theoretical wave barrier design, high screening performance (80%) could be maintained for substantially reduced investment.

The efficiency of a newly developed 'resiliently bound ballast' material to actively isolate vibrations within the track structure was also investigated. It was found that the new material offered increased performance over traditional

ballast in both the near and far fields. In the near field and at distances close to the track it was found that increasing ballast height provided increased vibration protection but the effect was less pronounced with increasing distance from the track. It was also found that the increased stiffness of the new ballast served to dampen lower frequency vibration components but magnified higher frequency ones.

Chapter 12. Conclusions

12.1 Overall conclusions

Over the last 30 years, the deployment of high speed rail technology has grown rapidly, which, in turn, has led to the generation of elevated ground borne vibrations in urban environments. These vibrations can have a negative impact on both the track structure and communities located close to high speed lines. The focus of this thesis has been on the prediction of these vibration levels in the free field, rather than those within the track structure. The work undertaken and key findings can be summarised in the following points:

1. A fully coupled, 3D, explicit FE model was developed to aid in detailed vibration assessments. Railway track components were modelled explicitly in three dimensions, thus facilitating an accurate description of track force propagation from wheel to soil. A multi-body dynamics approach was used to describe the wheel, bogie and car body interaction and the wheel was connected to the track using a non-linear Hertzian contact spring. Lastly, rail irregularity was simulated using a quality classification system derived from field experiments.

2. The FE model was implemented within two, commercial finite element software packages: ABAQUS and LSDYNA. Their pre-programmed algorithms for mesh creation, computation parallelisation, part interactions and absorbing boundary conditions reduced the complexity

of model development and execution. To compare the suitability of each package for railway vibration modelling, their element libraries and absorbing boundary conditions were tested. It was found that LSDYNA's perfectly matched layer solution offered higher absorption performance than ABAQUS' infinite element solution. Despite this, the ABAQUS solution was less computationally intense, meaning both solutions were found to be acceptable. To tailor the codes for railway modelling, they were modified to enable the simulation of moving multi-body loads. Although LSDYNA was found to offer a more straightforward implementation, both packages offered efficient solutions.

3. FDTD modelling approaches have been used commercially to model railway vibration and are attractive partly because they offer a more computationally efficient method in comparison to the FE method. Due to the commercial nature of previous approaches, few details are available relating to the modelling techniques used. Despite this, it was known that previous models utilise low performance absorbing boundary conditions, thus not maximising computational efficiency. Therefore the suitability of a SSG FDTD approach for railway modelling was evaluated. In the process a new PML absorbing boundary condition was developed and found to outperform other alternative conditions, especially for evanescent waves. Despite this, the SSG FDTD model tested provided a poorer approximation of vibration levels than the FE models previously developed. Furthermore, reduced performance was

caused by the parameter averaging between material interfaces that are necessary to maintain numerical stability.

4. Detailed vibration assessments require higher accuracy soil properties in comparison to scoping assessments. For scoping assessments, existing soils data is typically sufficient, provided it is in a format compatible with the numerical model to be used. Therefore a range of correlations were reviewed for the purpose of relating traditional soil parameters with FE properties. Using this information, new correlations were developed for sands, clays and silts. For detailed assessments, new soil investigations may be required. Various types of investigation are available, however it was found that bender element tests, resonant column tests and MASW tests yielded soil properties that were the most conducive to obtaining properties usable with FE simulation.

5. Field experiments were performed on six high speed rail sites across Belgium and England. Vibration levels were recorded up to 100m metres from the track and soil properties were determined using a MASW approach. Three earthworks profiles were investigated and it was found that cuttings generated higher vibration amplitudes than embankments and at-grade sections. Embankments were found to generate higher frequency vibrations in comparison to cuttings and at-grade sections. Additionally, it was found that Thalys, TGV and Eurostar trains generated similar levels of vibration and that railway abutments serve to shield soil locations in the near field. As well as for investigating embankment

vibrations, the results were also used in combination with previously published data sets to validate the predicted vibration levels from the ABAQUS and LSDYNA models.

6. The FE model developed for detailed assessment was compared against the field experiment results and also against peer reviewed data sets. Therefore it was tested on a range of train speeds, soil properties, train types and distances from the track. The numerical model was found to accurately predict the timing, shape and magnitude of vertical velocity time histories, at all distances from the track. It was also able to predict three international metrics and frequency spectrums with precision.

7. The FE prediction model was also used to investigate the effect of train speed on vibration levels. It was found that as the train approached the Rayleigh wave speed of the underlying soil, vibration levels (PPV, KB_{max} and VdB) increased significantly. This increase was more pronounced at locations within the track structure than locations in the free field. Three different track types were also analysed to assess their vibration performance when subject to critical velocities. It was found that ballasted track generated the highest levels of vibration and was also more sensitive to changes in train speed. Slab track experienced the lowest levels in vibration and was least effected by speed. The vibration performance of the metal track was between that of the slab and ballasted tracks. Lastly, the effect of embankment constituent material was analysed and it was found that stiffer embankments resulted in a

reduction of vibration in both the near and far field, in comparison to soft embankments.

8. Wave barriers and a 'resiliently bound ballast' material were assessed to determine their ability to reduce railway vibrations. Firstly, investigations into optimal wave barrier dimensions were performed using the ABAQUS model. It was found that trench depth had the most significant influence on vibration reduction, with isolation performance increasing rapidly at depths greater than 40% of the soil Rayleigh wavelength. In contrast trench width was found to have little effect, with both narrow and wide trenches shown to be successful in screening vibration. Therefore it was recommended that trench depth should be at least d=0.4 and that width and distance should be minimised with respect to construction cost. Using these recommendations it was shown that for a theoretical wave barrier design, high screening performance (80%) could be maintained for substantially reduced investment. Secondly, the ability of a 'resiliently bound ballast' material to actively isolate vibrations within the track structure was investigated. It was found that the new material offered increased performance over traditional ballast in both the near and far fields. In the near field and at distances close to the track, it was found that increasing ballast height improved vibration attenuation but the effect was less pronounced with increasing distance from the track. It was also found that the increased

stiffness of the new ballast served to dampen lower frequency vibration components but magnified higher frequency ones.

9. A scoping model was developed using a neural network approach for the purpose of quickly predicting vibration levels along long track sections. Most scoping models ignore soil properties in their calculation, however the new model was able to use soil information to improve prediction accuracy. Firstly, a sensitivity analysis was undertaken and it was found that Young's modulus and damping had a more dominant effect on PPV values, in comparison to Poisson's ratio and density. Using Young's modulus, damping and train speed data, a two soil layer ABAQUS model was used to construct a vast database of railway vibration records. These records acted as the basis for a neural network model and when tested, the new model was shown to have strong prediction capabilities and to significantly outperform a commonly used alternative model.

12.2 Limitations of current work

1. All finite element modelling undertaken in this work was assumed to be linear elastic. As high speed rail typically generates vibrations that fall within the threshold of small strain behaviour, this assumption is a valid one. Despite this, under rare circumstances it is possible that vibration levels within the track structure may exceed this threshold and behave non-linearly. Although the current models outlined in this thesis are not

capable of simulating these non-linear effects, it is possible to incorporate a variety of such behaviours using the existing libraries within the commercial software packages ABAQUS and LSDYNA.

2. The models developed in this thesis are capable of modelling vibration levels on at-grade and embankment track sections. Due to environmental considerations it is also common for high speed rail tracks to be constructed within tunnels. To model such tunnel sections, the models within this thesis must be heavily modified.

3. The accuracy of the numerical models is highly dependent on the accuracy of soil input parameters. If the soil properties for a particular region are completely unknown then site investigation may be required. If this is the case then it is likely that data collection will become the limiting factor in vibration prediction.

4. The numerical models have been developed using commercial software accessed with an academic license. If they were used in a commercial setting then a commercial license is required, thus drastically increasing project cost. Additionally, the models have long run times despite running on a computer cluster. In a commercial setting it would be expensive from both cost and time perspectives to deploy a large number of models.

5. Although the models used in this thesis have been shown to have high accuracy prediction capabilities, their performance is governed by the

accuracy of soil input parameters. Therefore if there is significant experimental error in the determination of the soil properties then model prediction ability will be reduced.

12.3 Recommendations for future work

Recommendations for future work can be divided into three main areas:

12.3.1 Numerical modelling

1. The performance of absorbing boundary conditions available for the finite element method is lower than those available in the finite difference method. Alternative perfectly matched layer stretching functions and the applicability of higher order PML's (for use within FE modelling) should be investigated. If these techniques are able to significantly reduce domain sizes and computational times then the finite element method may become a more attractive approach for seismic wave propagation applications such as railway vibration modelling and near surface full waveform inversions.

2. The excitation mechanism chosen for this work was broken down into a system of equations for each train wheel. To improve on this model, each entire carriage can be modelled, thus including additional pitch and yaw excitation mechanisms into the excitation model. Although this has the potential to improve accuracy, it is

likely to require a substantially longer track section thus increasing the modelling domain (and computational requirements).

3. The wheel/rail Hertzian contact spring used to couple the vehicle/track simulates vertical excitation and should be modified to include lateral forces. Although vertical vibrations have been shown to be more dominant than their horizontal counterparts, their inclusion would increase prediction accuracy.

4. The rail irregularity model could be upgraded to include wheel irregularities. This may allow for a better representation of the dynamic high frequency content associated with the wheel/rail interface.

5. Regarding the finite difference time domain modelling, additional investigations should be made in an attempt to overcome the challenges posed by material interfaces and the coupling of wheel and track. If these challenges were overcome then the FDTD method would be a highly attractive alternative modelling technique for railway applications.

6. Regarding neural network model development, additional ABAQUS models should be run to allow for a wider range of input parameters. Primarily this should focus on including more soil layers.

12.3.2 Experimental field work

1. Additional field work should be undertaken to obtain results for a wider range of trains, soil properties, train speeds…etc. If so, a results database could be constructed. This data would be useful for understanding railway vibrations in greater detail and for further validation of numerical models.

2. Future train vibration measurements should be undertaken using accelerometers (weather permitting) because their ability to record low frequency content is superior to geophones. Therefore they are better equipped to record bogie passage frequencies.

3. Further investigation should be undertaken into damping coefficient calculation. New techniques such as (Rix, Lai, & Wesley-Spang, 2000) have been proposed and could be useful alternatives for Rayleigh damping calculation.

12.3.3 Analysis

1. The neural network model should be analysed and validated further using a wider variety of field results. In particular its ability to predict alternative, yet commonly used, vibration metrics such as VDV should be tested.

2. Analysis of the vibration characteristics of a greater variety of railway tracks should be undertaken. This includes a variety of newly proposed slab tracks and metal tracks .

3. There are a vast range of vibration metrics available for assessing vibration levels. Similarly, each country uses a different approach to vibration calculation. Research should be undertaken into determining the most applicable railway vibration metrics for the purpose of developing universal metrics.

12.4 Acknowledgements

The work undertaken in this thesis could not have been achieved without the help from numerous individuals and organisations:

Prof. Michael Forde (1st supervisor, the University of Edinburgh) – His daily support and unwavering positivity kept the project exciting and fast moving throughout the duration. His academic experience and extensive knowledge of both key academic and industrial contacts was pivotal in steering this research. Without him this research would have not been possible.

Dr. Antonis Giannopolous (2nd supervisor, the University of Edinburgh) – His consistent support and adept knowledge of numerical modelling techniques,

especially the FDTD method, were vital in developing all numerical models associated with this thesis.

Mr Weizhi Fan, Dr. Craig Warren, Mr. Dominic Ahiaga-Dagbui (the University of Edinburgh) – Their input into many aspects of numerical modelling added great value to this work.

Dr. Georges Kouroussis (Université de Mons), **Prof. Ian Main, Mr Colin Kay** (the University of Edinburgh), **Mr. Michael Hayward** (CTRL), **Mr. Paul Hawthorn** (CTRL), **Mr. Debruxelles** (INFRABEL) – Their insights and support in undertaking experimental field work was pivotal in collecting the data underpinning many chapters of this thesis.

Prof. Peter Woodward, Prof. Omar Laghrouche, Dr. Abdellah Elkacimi, Dr. Gabriela Medero (Heriot Watt University) – Their insight, suggestions and collaborative efforts provided great assistance through the PhD research process.

Advisory board (Mr. Peter Boyd (AECOM), **Mr. Niall Fagan** (HS2)**, Mr. John Lane** (RSSB), **Mr. Andrew Went** (HS2), **Mr. Andrew Curzon** (BBRail), **John Amoore** (Network Rail), **Dermot Kelly** (BBRail), **Paul Richards** (Network Rail)**)** – Their guidance, support and constant feedback ensured that the project was relevant to the railway industry.

MEng students (Aidan Johnson, David Long, Sam Melling, Weizhi Fan, Jialiang Yu, Scott McGee, Colin Swan, David Winning, Jamie Robb, Jools Peters, Aly Sim, Henry Milewski, Punit Bhudia – University of Edinburgh)

Engineering and Physical Sciences Research Council (EPSRC) – Without funding from grant EP/H029397/1, this research would not have not been possible.

The University of Edinburgh – Without the facilities and resources provided by University this work would not have been possible.

Natural Environment Research Council (NERC) – The experimental equipment kindly provided free of charge was pivotal in performing field work.

12.5 Thesis outcomes

12.5.1 Published journal papers

1. Connolly, D., Giannopoulos, A., Forde, M.C, (2013). Numerical modelling of ground borne vibrations from high speed rail lines on embankments. Soil dynamics and Earthquake Engineering 2013, vol 46, p13-19. http://www.sciencedirect.com/science/article/pii/S026772611200262X
2. Connolly, D., Giannopoulos, A., Fan, W., Woodward, P.K., Forde, M.C, (2013). Optimising low acoustic impedance back-fill material wave barrier dimensions to shield structures from ground borne high speed rail vibrations. Construction and building materials 2013, vol 44, p557-564.

http://www.sciencedirect.com/science/article/pii/S0950061813002419

12.5.2 Awards/prizes

1. Institution of Civil Engineers – Graduate and student paper competition (1st - Scotland final 2012)
2. Scottish Geotechnical Group – Visual presentation competition (1st Scotland final 2012)
3. British Geological Association - Selected as the UK representative for the European Young Engineer Conference (2013)
4. Institution of Civil Engineers – Graduate and student paper competition (1st - Edinburgh final 2012)
5. Richard Brown scholarship – Edinburgh University research scholarship award (2011)
6. Moray endowment award – Promotion of new initiatives in research award (2011)
7. Natural Environment Research Council - Seismic equipment acquisition award (2012)
8. Engineering for a better environment (Short-listed) – Hawley award (2012)

12.5.3 Conference papers

Connolly, D., Giannopoulos, A., Fan, W., Forde, M., (2013). Ground vibration isolation on high speed rail lines. International conference for young geotechnical engineers 2013, Paris, France.

Kouroussis, G., Connolly, D., Forde, M., Verlinden, O., (2013). An experimental study of embankment conditions on high speed railway ground vibrations. Railway Engineering 2013, London, UK.

Connolly, D., Peters, J., Sim, A., Fan, W., Giannopoulos, A., Forde, M., (2013). Rapidly assessing high speed rail vibrations using a new empirical prediction model. Railway Engineering 2013, London, UK.

Connolly, D., Kouroussis, G., Fan, W., Percival, M., Verlinden, O., Giannopoulos, A., Forde, M., (2013). An experimental analysis of embankment vibrations due to high speed rail. Railway Engineering 2013, London, UK.

Connolly, D., Forde, M., Giannopoulos, A., Woodward, P. (2012). The effect of high speed railway embankment conditions on vibration levels in the near and far field. Rail Research UK Annual Conference 2012. London, England.

Connolly, D., Giannopoulos, A., Forde, M. Woodward, P. (2012). Evaluating & isolating ground borne vibrations in buildings from high speed trains. Structural faults and repair 2012. Edinburgh, Scotland.

Connolly, D., Giannopoulus, A., Forde, M. (2012). A new and improved pml implementation for ground vibration modelling due to high speed train passage. Annual Conference on Computational Mechanics 2012. Manchester, UK.

A.Giannopoulos, S. Melling and D. Connolly. (2012). A second order PML implementation for FDTD seismic modelling. Near Surface Geophysics conference 2012. Paris, France.

Connolly, D., Giannopoulos, A., Forde, M., Woodward, P. (2011). Alternative methods to predict ground borne vibrations on structures on different soils. International conference in railway engineering 2011. London, England

Chapter 13. References

Abarbanel, S., & Gottlieb, D. (1997). A Mathematical Analysis of the PML Method. *Journal of Computational Physics*, *134*(2), 357–363. doi:10.1006/jcph.1997.5717

Ahmad, S., & Al-Hussaini, T. (1991). Simplified Design for Vibration Screening by Open and In-Filled Trenches. *Journal of the Geotechnical Engineering Division, ASCE*, *117*(1), 67–88.

Aki, K., & Richards, P. (2002). *Quantitative seismology* (2nd ed., pp. 1–720). University Science Books.

Alzawi, A., & Hesham El Naggar, M. (2011). Full scale experimental study on vibration scattering using open and in-filled (GeoFoam) wave barriers. *Soil Dynamics and Earthquake Engineering*, *31*(3), 306–317. doi:10.1016/j.soildyn.2010.08.010

Ando, K., Sunaga, M., Aoki, H., & Haga, O. (2001). Tracks Development of Slab Tracks for Hokuriku Shinkansen Line. *Quarterly report of Railway Technical Research Institute*, *42*(1), 35–41.

Asmussen, B. (2011a). *Review of existing standards , regulations and guidelines , as well as laboratory and field studies concerning human exposure to vibration. Deliverable D1.4. Railway Induced Vibration Abatement Solutions.* (pp. 1–72).

Asmussen, B. (2011b). *Test procedures for the determination of the dynamic soil characteristics. Deliverable D1.1. Railway Induced Vibration Abatement Solutions* (pp. 1–107).

Asmussen, B. (2011c). *Protocol for free field measurement of mitigation effects. Deliverable D1.2. Railway Induced Vibration Abatement Solutions* (pp. 1–25).

Asmussen, B. (2012). *Definition of reference cases typical for hot-spots in Europe with existing vibration problems. Deliverable D1.5. Railway Induced Vibration Abatement Solutions* (pp. 1–16).

Astley, R. (2000). Infinite elements for wave problems: a review of current formulations and an assessment of accuracy. *International Journal for Numerical Methods in Engineering*, *49*, 951–976.

ASTM D4015 - 07. (2007). *Standard Test Methods for Modulus and Damping of Soils by Resonant-Column Method. American Society for Testing and materials* (pp. 1–22).

Athanasopoulos, G., Pelekis, P., & Anagnostopoulos, G. (2000). Effect of soil stiffness in the attenuation of Rayleigh-wave motions from field measurements. *Soil Dynamics and Earthquake Engineering*, *19*(4), 277–288. doi:10.1016/S0267-7261(00)00009-9

Auersch, L. (1996). Dynamic plate-soil interaction — finite and infinite, flexible and rigid plates on homogeneous, layered or Winkler soil. *Soil Dynamics*

and Earthquake Engineering, *15*(1), 51–59. doi:10.1016/0267-7261(95)00021-6

Auersch, L. (2005). The excitation of ground vibration by rail traffic: theory of vehicle-track-soil interaction and measurements on high-speed lines. *Journal of Sound and Vibration*, *284*, 103–132. doi:10.1016/j.jsv.2004.06.017

Auersch, L. (2008a). Dynamic interaction of various beams with the underlying soil – finite and infinite, half-space and Winkler models. *European Journal of Mechanics - A/Solids*, *27*, 933–958. doi:10.1016/j.euromechsol.2008.02.001

Auersch, L. (2008b). The Influence of the Soil on Track Dynamics and Ground-Borne Vibration. *Noise and vibration mitigation - Numerical notes on fluid mechanics* (pp. 122–128).

Auersch, L. (2008c). The effect of critically moving loads on the vibrations of soft soils and isolated railway tracks. *Journal of Sound and Vibration*, *310*(3), 587–607. doi:10.1016/j.jsv.2007.10.013

Bahrekazemi, M. (2004). *Train-Induced Ground Vibration and Its Prediction (PhD thesis)*. Stockholm University.

Baldi, G., Bellotti, R., Ghionna, V., Jamiolkowski, M., & Presti, D. (1989). Modulus of sands from CPT's and DMT's. *12th International conference on Soil Mechanics and Foundation Engineering* (pp. 165–170).

Balendra, T., Chua, K., Lo, K., & Lee, S. (1989). Steady-state vibration of subway-soil-building system. *Journal of Engineering Mechanics*, *115*(1), 145–162.

Banimahd, M. (2008). *Advanced finite element modelling of coupled train-track systems: A geotechnical perspective (PhD thesis)*. *Built Environment*. Heriot Watt University.

Banimahd, M., Kennedy, J., Woodward, P., & Medero, G. (2010). Behaviour of train – track interaction in stiffness transitions. *Proceedings of the Institution of Civil Engineers*, *1*, 1–10. doi:10.1680/tran.10.00030

Basu, U. (2003). Perfectly matched layers for time-harmonic elastodynamics of unbounded domains: theory and finite-element implementation. *Computer Methods in Applied Mechanics and Engineering*, *192*, 1337–1375. doi:10.1016/S0045-7825(02)00642-4

Basu, U. (2009). Explicit finite element perfectly matched layer for transient three-dimensional elastic waves. *International Journal for Numerical Methods in Engineering*, *77*, 151–176. doi:10.1002/nme

Becache, E., Ezziani, A., & Joly, P. (2003). Mathematical and Numerical Modeling of Wave Popagation in Linear Viscoelastic Media. *Mathematical and Numerical Aspects of Wave Propagation* (pp. 916–921).

Berenger, J.-P. (1994). A perfectly matched layer for the absorption of electromagnetic waves. *Journal of Computational Physics*, *114*(2), 185–200. doi:10.1006/jcph.1994.1159

Berg, P., Nielsen, P., & Skovgaard, O. (1994). *Analytical reference solutions, in Helbig, K. Modelling the earth for oil exploration* (pp. 421–427).

Bergmann, L. (1948). *Ultrasonics and their Scientific and Technical Applications*. Wiley, New York.

Beskos, D., Dasgupta, B., & Vardoulakis, I. (1986). Vibration isolation using open and filled trenches. Part 1: 2D homogeneous soil. *Computational Mechanics*, *1*, 43–63.

Bettess, P. (1992). *Infinite elements*. Penshaw press.

Bettess, P., & Zienkiewicz, O. . (1977). Diffraction and refraction of surface waves using finite and infinite elements. *Journal for Numerical Methods in Engineering*, *11*(8), 1271–1290.

Bezin, Y., & Farrington, D. (2010). A structural study of an innovative steel–concrete track structure. *Proceedings of the Institution of Mechanical Engineers, Part F: Journal of Rail and Rapid Transit*, *224*(4), 245–257. doi:10.1243/09544097JRRT340

Bezin, Y., Farrington, D., Penny, C., Temple, B., & Iwnicki, S. (2010). The dynamic response of slab track constructions and their benefit with respect to conventional ballasted track. *Vehicle System Dynamics*, *48*, 175–193. doi:10.1080/00423111003693201

Biglari, M., & Ashayeri, I. (2011). An empirical model for shear modulus and damping ratio of unsaturated soils. *Unsaturated soils: Theory and practice*, *1*, 591–595.

Bode, C. (2002). Soil–structure interaction in the time domain using halfspace Green's functions. *Soil Dynamics and Earthquake Engineering*, *22*(4), 283–295. doi:10.1016/S0267-7261(02)00020-9

Bohlen, T., & Saenger, E. (2006). Accuracy of heterogeneous staggered-grid finite-difference modeling of Rayleigh waves. *Geophysics*, *71*(4), T109–T115. doi:10.1190/1.2213051

Bovey, E. (1983). Development of an impact method to determine the vibration transfer characteristics of railway installations. *Journal of Sound and Vibration*, *87*(2), 357–370.

Bowness, D., Lock, a, Powrie, W., Priest, J., & Richards, D. (2007). Monitoring the dynamic displacements of railway track. *Proceedings of the Institution of Mechanical Engineers, Part F: Journal of Rail and Rapid Transit*, *221*(1), 13–22. doi:10.1243/0954409JRRT51

Brahma, P., & Mukherjee, S. (2010). A Realistic Way to Obtain Equivalent Young ' s Modulus of Layered Soil. *Indian Geotechnical Conferece* (pp. 305–308).

Brekhovskikh, L., & Godin, O. (1998). *Acoustics of Layered media I: Planes and Quasi-plane waves* (pp. 1–242). Springer-Werlag, Berlin.

Briggs, G., & Kolosov, O. (1992). *Acoustic Microscopy* (2nd ed., pp. 1–384). Clarendon Press, Oxford.

British Geological Association. (2013). Retrieved from http://www.bgs.ac.uk/

BSI. (1999). *BS 7385-2:1993 - Evaluation and measurement for vibration in buildings. Part 2: Guide to damage levels from groundborne vibration. British Standards Institution* (pp. 1–16).

BSI. (2004). *BS 14688-2:2004 - Geotechnical investigation and testing - Identification and classification of soil - Part 2: Principles for a classification. British Standards Institution* (Vol. 3, pp. 1–22).

BSI. (2008). *BS 6472-1:2008 Guide to evaluation of human exposure to vibration in buildings Part 1 : Vibration sources other than blasting. British Standards Institution* (pp. 1–28).

BSI. (2012). *BS EN ISO 22476-3:2005 + A1:2011 - Geotechnical investigation and testing - Field testing - Part 3 : Standard penetration test. British Standards Institution* (pp. 1–26).

Cao, Z. G., Cai, Y. Q., Sun, H. L., & Xu, C. J. (2011). Dynamic responses of a poroelastic half-space from moving trains caused by vertical track irregularities. *International Journal for Numerical and Analytical Methods in Geomechanics*, *35*, 761–786. doi:10.1002/nag

Carter, B., & Bentley, S. (1991). *Correlations of soil properties* (pp. 1–130). Pentech Press.

Caughey, T. (1960). Classical Normal Modes in Damped Linear Dynamic Systems. *Journal of Applied Mechanics*, *27*(2), 269–271.

Cerjan, C., Kosloff, D., Kosloff, R., & Resheq, M. (1985). A nonreflecting boundary condition for discrete acoustic and elastic wave equations. *Geophysics*, *50*(4), 705–708.

Chatterjee, P., Degrande, G., Jacobs, S., Charlier, J., Bouvet, P., & Drassenx, D. (2003). Experimental Results Of Free Field And Structural Vibrations Due To Underground Railway Traffic. *10th International congress on sound and vibration* (pp. 1–8).

Chebli, H., Othman, R., Clouteau, D., Arnst, M., & Degrande, G. (2008). 3D periodic BE–FE model for various transportation structures interacting with soil. *Computers and Geotechnics*, *35*(1), 22–32. doi:10.1016/j.compgeo.2007.03.008

Chen, Y. (2001). Response of an Infinite Timoshenko Beam on a Viscoelastic Foundation To a Harmonic Moving Load. *Journal of Sound and Vibration*, *241*(5), 809–824. doi:10.1006/jsvi.2000.3333

Cheng, Z., Thacker, J., Pilkey, W., Hollowell, W., & Reagan, S. (2001). Experiences in reverse-engineering of a Finite element automobile crash model. *Finite Elements in Analysis and Design*, *37*, 843–860.

Chew, W., & Lui, Q. (1996). Perfectly Matched Layers for Elastodynamics: A New Absorbing Boundary Condition. *Journal of Computational acoustics*, *4*, 341–359.

Chew, W., & Weedon, W. (1994). A 3D perfectly matched medium from modified maxwell's equations with stretched coordinates. *Microwave and Optical Technology Letters*, *7*(13), 599–604.

Chin, C., Duann, S., & Kao, T. (1988). SPT-CPT correlations for granular soils. *1st International symposium on Penetration Testing* (pp. 295–339).

Collino, F., & Tsogka, C. (2001). Application of the perfectly matched absorbing layer model to the linear elastodynamic problem in anisotropic heterogeneous media. *Geophysics*, *66*, 294–307.

Connolly, D., Giannopoulos, A., & Forde, M. . (2013). Numerical modelling of ground borne vibrations from high speed rail lines on embankments. *Soil Dynamics and Earthquake Engineering*, *46*, 13–19. doi:10.1016/j.soildyn.2012.12.003

Correia, D., & Jin, J. (2005). On the Development of a Higher-Order PML, *53*(12), 4157–4163.

Das, B. (2008). *Advanced Soil Mechanics* (pp. 1–600). CRC Press.

De Hoop, A. (1960). A modification of cagniard's method for solving seismic pulse problems. *Applied Scientific Research, Section B*, *8*(1), 349–356.

Degrande, G., & Lombaert, G. (2001). An efficient formulation of Krylov's prediction model for train induced vibrations based on the dynamic reciprocity theorem. *The Journal of the Acoustical Society of America*, *110*(3), 1379–1390. doi:10.1121/1.1388002

Degrande, G., & Schillemans, L. (2001a). Free Field Vibrations During the Passage of a Thalys High-Speed Train At Variable Speed. *Journal of Sound and Vibration*, *247*(1), 131–144. doi:10.1006/jsvi.2001.3718

Degrande, G., & Schillemans, L. (2001b). Free Field Vibrations During the Passage of a Thalys High-Speed Train At Variable Speed. *Journal of Sound and Vibration*, *247*(1), 131–144. doi:10.1006/jsvi.2001.3718

Dehghani, H., & Ataee-pour, M. (2011). Development of a model to predict peak particle velocity in a blasting operation. *International Journal of Rock Mechanics and Mining Sciences*, *48*(1), 51–58. doi:10.1016/j.ijrmms.2010.08.005

Dejong, J. (2007). *Site characterization - Guidelines for estimating Vs based on In-situ tests. Soil interaction laboratory, UCDavis* (pp. 1–22).

Di Mino, G., Giunta, M., & Di Liberto, C. M. (2009). Assessing the Open Trenches in Screening Railway Ground-Borne Vibrations by Means of Artificial Neural Network. *Advances in Acoustics and Vibration*, *2009*(i), 1–12. doi:10.1155/2009/942787

Dickensen, S. (1994). *Dynamic response of soft and deep cohesive soils during the Loma Prieta earthquake of October 17, 1989. PhD thesis*. University of California.

Ditzel, A., & Herman, G. (2004). The influence of a rail embankment on the vibrations generated by moving trains. *Journal of Sound and Vibration*, *271*, 937–957. doi:10.1016/S0022-460X(03)00772-7

Drossaert, F., & Giannopoulos, A. (2006). Complex frequency shifted convolution PML for FDTD modelling of elastic waves. *Wave Motion*, *44*, 593–604.

Drossaert, F. H., & Giannopoulos, A. (2007). A nonsplit complex frequency-shifted PML based on recursive integration for FDTD modeling of elastic waves. *Geophysics*, *72*(2), T9. doi:10.1190/1.2424888

El Kacimi, A., Woodward, P. K., Laghrouche, O., & Medero, G. (2013). Time domain 3D finite element modelling of train-induced vibration at high speed. *Computers & Structures*, *118*, 66–73. doi:10.1016/j.compstruc.2012.07.011

Esveld, C., & Markine, V. (2000). *Slab track design for high speed. Esveld Consulting Services* (pp. 1–11).

Federal Railroad Administration. (2005). *High speed ground transportation noise and vibration impact assessment. U.S. Department of Transportation* (pp. 1–235).

Federal Railroad Administration. (2012). *High-Speed Ground Transportation Noise and Vibration Impact Assessment. U.S. Department of Transportation* (pp. 1–248).

Findeis, H., & Peters, E. (2004). Disturbing effects of low-frequency sound immissions and vibrations in residential buildings. *Noise and Health*, *6*(23), 29–35.

FRA. (2013). Federal Railroad Administration. Retrieved from www.fra.dot.gov/

François, S., Schevenels, M., Thyssen, B., Borgions, J., & Degrande, G. (2012). Design and efficiency of a composite vibration isolating screen in soil. *Soil Dynamics and Earthquake Engineering*, *39*(39), 113–127. doi:10.1016/j.soildyn.2012.03.007

Freudenstein, S. (2010). RHEDA 2000: ballastless track systems for high-speed rail applications. *International Journal of Pavement Engineering*, *11*(4), 293–300. doi:10.1080/10298431003749774

Fryba, L. (1972). *Vibration of Solids and Structures Under Moving Loads* (pp. 1–524). Groningen, The Netherlands: Noordhoff International Publishing.

Galis, M., Moczo, P., & Kristek, J. (2008). A 3-D hybrid finite-difference — finite-element viscoelastic modelling of seismic wave motion. *Geophysics Journal International*, *175*, 153–184. doi:10.1111/j.1365-246X.2008.03866.x

Galvin, P., & Domínguez, J. (2009). Experimental and numerical analyses of vibrations induced by high-speed trains on the Córdoba–Málaga line. *Soil Dynamics and Earthquake Engineering*, *29*(4), 641–657. doi:10.1016/j.soildyn.2008.07.001

Galvin, P., Romero, A., & Domínguez, J. (2010a). Fully three-dimensional analysis of high-speed train–track–soil-structure dynamic interaction. *Journal of Sound and Vibration*, *329*(24), 5147–5163. doi:10.1016/j.jsv.2010.06.016

Galvin, P., Romero, A., & Domínguez, J. (2010b). Vibrations induced by HST passage on ballast and non-ballast tracks. *Soil Dynamics and Earthquake Engineering*, *30*(9), 862–873. doi:10.1016/j.soildyn.2010.02.004

Gao, G., Shi, G., Feng, S., & Qiu, C. (2008). 3D analysis of in-filled trench as passive barriers for ground vibration isolation. *Science in China Series G: Physics, Mechanics and Astronomy*, *51*(10), 1573–1585. doi:10.1007/s11433-008-0151-1

Garg, V., & Dukkipati, R. (1984). *Dynamics of railway vehicle systems* (pp. 1–407). Toronto: Academic Press.

Giannopoulos, A. (2011). Unsplit implementation of Higher-Order PMLs. *IEEE Transactions on Antennas and Propagation*, (6), 1–7.

Graves, R. W. (1996). Simulating Seismic Wave Propagation in 3D Elastic Media Using Staggered-Grid Finite Differences. *Bulletin of the Seismological Society of America*, *86*(4), 1091–1106.

Griffin, M. (1998). A Comparison of Standardized Methods for Predicting the Hazards of Whole-Body Vibration and Repeated Shocks. *Journal of Sound and Vibration*, *215*(4), 883–914. doi:10.1006/jsvi.1998.1600

Hall, L. (2003). Simulations and analyses of train-induced ground vibrations in finite element models. *Soil Dynamics and Earthquake Engineering*, *23*, 403–413. doi:10.1016/S0267-7261(02)00209-9

Hamilton, E. (1980). Geoacoustic modeling of the sea floor ooze. *Journal of Acoustic Society of America*, *68*(5), 1313–1340.

Hanazato, T, Ugai, K., Mori, M., & Sakaguchi, R. (1991). Three-dimensional analysis of traffic-induced ground vibrations. *Journal of Geotechnical and Geoenvironmental Engineering*, *117*(8), 1133–1151.

Hardin, B., & Black, W. (1963). Vibration modulus of normally consolidated clay. *Journal of the soil mechanics and foundation division*, *89*, 33–65.

Hasancebi, N., & Ulusay, R. (2006). Empirical correlations between shear wave velocity and penetration resistance for ground shaking assessments. *Bulletin of Engineering Geology and the Environment*, *66*(2), 203–213. doi:10.1007/s10064-006-0063-0

Heaton, J. (2008). *Introduction to Neural Networks with Java* (2nd ed., p. 380). Heaton Research.

Heckl, M., Hauck, G., & Wettschureck, R. (1996). Structure-Borne Sound and Vibration From Rail Traffic. *Journal of Sound and Vibration*, *193*(1), 175–184. doi:10.1006/jsvi.1996.0257

Hegazy, Y., & Mayne, P. (1995). Statistical correlations between Vs and CPT data for different soil types. *(CPT'95), Symposium on Cone Penetration Testing* (pp. 173–178).

Hemsley, J. (2000). *Design Applications of Raft Foundations* (pp. 1–608). ICE Publishing.

Hendry, M., Barbour, L., & Hughes, D. a. (2010). Track displacement and energy loss in a railway embankment. *Proceedings of the ICE - Geotechnical Engineering*, *163*(1), 3–12. doi:10.1680/geng.2010.163.1.3

Hibbitt, Karlsson, & Sorensen. (2010). *ABAQUS User's Manual (Version 6.10)*. Providence, RI, USA.

Higdon, R. L. (1986). Absorbing Boundary Conditions for Difference Approximations to the Multi-Dimensional Wave Equation. *Mathematics of Computation*, *47*(176), 437. doi:10.2307/2008166

Holequest. (2013). Holequest. Retrieved from www.holequest.co.uk

Holm, G., Andreasson, B., Bengtsson, P., Bodare, A., & Eriksson, H. (2002). *Mitigation of Track and Ground Vibrations by High Speed Trains at Ledsgard, Sweden. Report 10. Svensk Djupstabilisering* (pp. 1–60).

Howarth, H., & Griffin, M. (1991). The annoyance caused by simultaneous noise and vibration from railways. *Journal of the Acoustical Society of America*, *89*(5), 2317–2323.

HS2. (2012). *Safeguarding and Property & Compensation maps: general notes on draft safeguarded area. HS2* (pp. 1–38).

Hung, C., & Ni, S. (2007). Using multiple neural networks to estimate the screening effect of surface waves by in-filled trenches. *Computers and Geotechnics*, *34*(5), 397–409. doi:10.1016/j.compgeo.2007.06.005

Hussein, M. F. M., & Hunt, H. E. M. (2007). A numerical model for calculating vibration from a railway tunnel embedded in a full-space. *Journal of Sound and Vibration*, *305*(3), 401–431. doi:10.1016/j.jsv.2007.03.068

Hustedt, B., Operto, S., & Virieux, J. (2004). Mixed-grid and staggered-grid finite-difference methods for frequency-domain acoustic wave modelling. *Geophysical Journal International*, *157*(3), 1269–1296. doi:10.1111/j.1365-246X.2004.02289.x

Imai, T. (1977). P and S-wave velocities of the ground in Japan. *Ninth International conference of Soil Mechanics and Foundation Engineering* (pp. 257–260).

Imai, T., & Tonouchi, K. (1982). Correlation of N-value with S-wave velocity and shear modulus. *Proceedings of the 2nd European symposium of penetration testing* (pp. 57–72).

INNOTRACK. (2008). *Design and Manufacture of Embedded Rail Slab Track Components. Project no. TIP5-CT-20060031415. INNOTRACK* (pp. 1–133).

International Standards Organisation. (1999). *DIN 4150-3 - Effects of vibration on structures. International Standards Organisation* (pp. 1–34).

International union of Railways. (1994). *UIC code 719R: Earthworks and trackbed layers for railway lines*. UIC, Paris, France.

International Union of Railways. (2011). High speed lines in the world. *World*, (July), 1–10.

Ishibashi, I., & Zhang, X. (1993). Unified dynamic shear moduli and damping ratios of sand and clay. *Soils and Foundations*, *33*(1), 182–191.

ISO. (1999). *DIN 4150-2 - Human exposure to vibration in buildings. International Standards Organisation* (pp. 1–63).

Iyisan, R. (1996). Correlations between shear wave velocity and in-situ penetration test results. *Teknik Dergi*, *7*(2), 1187–1199.

Jafari, M., Shafiee, A., & Razmkhah, A. (2002). Dynamic properties of fine grained soils in south of Tehran. *Journal of Seismology and Earthquake Engineering*, *4*(1), 25–35.

Jesmani, M., Shafie, M., & SadeghiVileh, R. (2008). Finite Element Analysis of Active Isolation of Deep Foundation in Clayey Soil by Rectangular Trenches. *Electronic Journal of Geotechnical Engineering*, *13*.

Jofriet, J., & McNeice, G. (1971). Finite Element Analysis of Reinforced Concrete Slabs. *Journal of the Structural Division*, *97*(3), 785–806.

Johnson, K. (1985). *Contact mechanics* (pp. 1–468). Cambridge, UK: Cambridge University Press.

Jones, S. (2010). *Ground Vibration from Underground Railways: How Simplifying Assumptions Limit Prediction Accuracy (PhD thesis)*. University of Cambridge.

Ju, S. H., & Lin, H. (2004). Analysis of train-induced vibrations and vibration reduction schemes above and below critical Rayleigh speeds by finite element method. *Soil Dynamics and Earthquake Engineering*, *24*, 993–1002. doi:10.1016/j.soildyn.2004.05.004

Jun, X., Dan, H. E., & Qing-yuan, Z. (2008). Analysis theory of spatial vibration of high-speed train and slab track system. *Journal of Central South University of Technology*, *15*, 121–126. doi:10.1007/s11771

Kagawa, T. (1993). Moduli and damping factors of soft marine clays. *Journal of Geotechnical Engineering*, *118*(9), 1360–1375.

Kallivokas, L. F., Fathi, a., Kucukcoban, S., Stokoe, K. H., Bielak, J., & Ghattas, O. (2013). Site characterization using full waveform inversion. *Soil Dynamics and Earthquake Engineering*, *47*, 62–82. doi:10.1016/j.soildyn.2012.12.012

Kanda, H., Ishii, H., & Yoshioka, O. (2006). Field Measurement and its analysis of "Hybrid Vibration Isolation Wall" using gas cushions. *Transportation Research Board Annual Meeting*.

Kao, T. C. (2013). Elements, standards and parameters for design. *Transportation Research Board 2013* (pp. 1–44).

Kargarnovin, M. (2004). Dynamics of Timoshenko beams on Pasternak foundation under moving load. *Mechanics Research Communications*, *31*(6), 713–723. doi:10.1016/j.mechrescom.2004.05.002

Karl, L. (2005). *Dynamic Soil Properties out of SCPT and Bender Element Tests with Emphasis on Material Damping (PhD thesis)*. Ghent University.

Karlstrom, A., & Bostrom, A. (2006). An analytical model for train-induced ground vibrations from railways. *Journal of Sound and Vibration*, *292*, 221–241. doi:10.1016/j.jsv.2005.07.041

Karlstrom, A., & Bostrom, A. (2007). Efficiency of trenches along railways for trains moving at sub- or supersonic speeds. *Soil Dynamics and Earthquake Engineering*, *27*(7), 625–641. doi:10.1016/j.soildyn.2006.12.005

Katou, M., Matsuoka, T., Yoshioka, O., Sanada, Y., & Miyoshi, T. (2008). Numerical simulation study of ground vibrations using forces from wheels of a running high-speed train. *Journal of Sound and Vibration*, *318*, 830–849. doi:10.1016/j.jsv.2008.04.053

Kenney, J. (1954). Steady-state vibrations of beam on elastic foundation for moving load. *Journal of Applied Mechanics*, *76*, 359–364.

Ketcham, S., Moran, M., Lacombe, J., Greenfield, R., & Anderson, T. (2005). Seismic Source Model for Moving Vehicles. *IEEE Transactions on Geoscience and Remote Sensing*, *43*(2), 248–256.

Khandelwal, M., & Singh, T. N. (2006). Prediction of blast induced ground vibrations and frequency in opencast mine: A neural network approach. *Journal of Sound and Vibration*, *289*, 711–725. doi:10.1016/j.jsv.2005.02.044

Knothe, K., & Grassie, S. (1993). Modelling of railway track and vehicle/track interaction at high frequencies. *Vehicle System Dynamics*, *22*, 209–262.

Knothe, K., & Wu, Y. (1998). Receptance behaviour of railway track and subgrade. *Archive of Applied Mechanics*, *68*(7-8), 457–470. doi:10.1007/s004190050179

Komatitsch, D., & Martin, R. (2007). An unsplit convolutional perfectly matched layer improved at grazing incidence for the seismic wave equation. *Geophysics*, *72*(5), SM155–SM167. doi:10.1190/1.2757586

Kouroussis, G. (2005). *Mesures de vibrations induites sur l'environnement par le passage de trains a grande vitesse. Faculte Polytechnique De Mons* (pp. 1–84).

Kouroussis, G., Conti, C., & Verlinden, O. (2012). Investigating the influence of soil properties on railway traffic vibration using a numerical model. *Vehicle System Dynamics*, *51*(3), 1–22.

Kouroussis, G., Verlinden, O., & Conti, C. (2009a). Ground propagation of vibrations from railway vehicles using a finite/infinite-element model of the soil. *Proceedings of the Institution of Mechanical Engineers, Part F: Journal of Rail and Rapid Transit*, *223*(4), 405–413. doi:10.1243/09544097JRRT253

Kouroussis, G., Verlinden, O., & Conti, C. (2009b). Ground propagation of vibrations from railway vehicles using a finite/infinite-element model of the soil. *Proceedings of the Institution of Mechanical Engineers, Part F: Journal of Rail and Rapid Transit*, *223*(4), 405–413. doi:10.1243/09544097JRRT253

Kouroussis, G., Verlinden, O., & Conti, C. (2011a). Free field vibrations caused by high-speed lines: Measurement and time domain simulation. *Soil Dynamics and Earthquake Engineering*, *31*(4), 692–707. doi:10.1016/j.soildyn.2010.11.012

Kouroussis, G., Verlinden, O., & Conti, C. (2011b). A two-step time simulation of ground vibrations induced by the railway traffic. *Proceedings of the Institution of Mechanical Engineers, Part C: Journal of Mechanical Engineering Science*, *226*(2), 454–472. doi:10.1177/0954406211414483

Kouroussis, G., Verlinden, O., & Conti, C. (2011c). Efficiency of resilient wheels on the alleviation of railway ground vibrations. *Proceedings of the Institution of Mechanical Engineers, Part F: Journal of Rail and Rapid Transit*, *226*(4), 381–396. doi:10.1177/0954409711429210

Koziol, P., Mares, C., & Esat, I. (2008). Wavelet approach to vibratory analysis of surface due to a load moving in the layer. *International Journal of Solids and Structures*, *45*, 2140–2159. doi:10.1016/j.ijsolstr.2007.11.008

Kramer, S. (1996). *Geotechnical earthquake engineering* (pp. 1–653). Prentice Hall.

Krylov, V. V. (2001). *Noise and Vibration from High-Speed Trains*. (V. V Krylov, Ed.) (pp. 1–435). Thomas Telford Ltd. doi:10.1680/navfht.29637

Krylov, V. (1995). Generation of ground vibrations by superfast trains. *Applied Acoustics*, *44*(2), 149–164. doi:10.1016/0003-682X(95)91370-I

Krylov, V., Dawson, A., Heelis, M., & Collop, A. (2000). Rail movement and ground waves caused by high-speed trains approaching track-soil critical velocities. *Proceedings of the Institution of Mechanical Engineers, Part F: Journal of Rail and Rapid Transit*, *214*(2), 107–116. doi:10.1243/0954409001531379

Kuppelweiser, H., & Ziegler, A. (1996). A tool for predicting vibration and structure-borne noise immissions caused by railways. *Journal of Sound and Vibration*, *193*(1), 261–267.

Lamb, H. (1904). On the propagation of tremors over the surface of an elastic solid. *Philosophical Transactions of the Royal Society of London. Series A, Containing Papers of a Math. or Phys. Character (1896-1934)*, *203*, 1–42. doi:10.1080/15265161.2011.596400

Lan, H., & Zhang, Z. (2011). Comparative study of the free-surface boundary condition in two-dimensional finite-difference elastic wave field simulation. *Journal of Geophysics and Engineering*, *8*(2), 275–286. doi:10.1088/1742-2132/8/2/012

Larsson, R., & Mulabdic, M. (1991). Shear moduli in Scandinavian clays; measurements of initial shear modulus with seismic cones - empirical correlations for the initial shear modulus in clay. *Transport Reasearch Board* (pp. 1–127).

Lee, C., & Tsai, B. (2008). Mapping Vs30 in Taiwan. *Terrestrial Atmospheric and Oceanic Sciences*, *19*(6), 671–682. doi:10.3319/TAO.2008.19.6.671(PT)1.

Lee, S. (1990). Regression models of shear wave velocities in Taipei basin. *Journal of the Chinese Institution of Engineers*, *13*(5), 519–1990.

Lei, X, & Noda, N. (2002). ANALYSES OF DYNAMIC RESPONSE OF VEHICLE AND TRACK COUPLING SYSTEM WITH RANDOM IRREGULARITY OF TRACK VERTICAL PROFILE. *Journal of Sound and Vibration*, *258*, 147–165. doi:10.1006/jsvi.5107

Lei, X, & Rose, J. G. (2008). Numerical Investigation of Vibration Reduction of Ballast Track with Asphalt Trackbed over Soft. *Journal of Vibration and Control*, *14*(12), 1885–1902. doi:10.1177/1077546308091213

Lei, Xiaoyan, & Zhang, B. (2011). Analysis of Dynamic Behavior for Slab Track of High-Speed Railway Based on Vehicle and Track Elements, (April), 227–240. doi:10.1061/(ASCE)TE.1943-5436.0000207.

Li, D., Meddah, a, Hass, K., & Kalay, S. (2006). Relating track geometry to vehicle performance using neural network approach. *Proceedings of the Institution of Mechanical Engineers, Part F: Journal of Rail and Rapid Transit*, *220*(3), 273–281. doi:10.1243/09544097JRRT39

Liu, G., & Quek, S. (2003). *The Finite Element Method - A practical course* (pp. 1–365). Oxford, UK: Butterworth-Heinemann.

Lombaert, G., & Degrande, G. (2009). Ground-borne vibration due to static and dynamic axle loads of InterCity and high-speed trains. *Journal of Sound and Vibration*, *319*, 1036–1066. doi:10.1016/j.jsv.2008.07.003

Lombaert, G., Degrande, G., & Clouteau, D. (2001). The influence of the soil stratification on free field traffic-induced vibrations. *Archive of Applied Mechanics*, *71*(10), 661–678. doi:10.1007/s004190100174

Luco, J., & Apsel, R. (1983). On the greens functions for a layered half-space -part 1. *Bulletin of the seismological society of america*, *73*(4), 909–929.

Lunne, T., Robertson, P., & Powell, J. (1997). *Cone penetrating testing* (pp. 1–312). Spons Press.

Madshus, C., Bessason, C., & Harvik, L. (1996). Prediction model for low frequency vibration from high speed railways on soft ground. *Journal of Sound and Vibration*, *193*(1), 195–203.

Malischewsky, P. G. (2005). Comparison of approximated solutions for the phase velocity of Rayleigh waves (Comment on "Characterization of surface damage via surface acoustic waves"). *Nanotechnology*, *16*(6), 995–996. doi:10.1088/0957-4484/16/6/N01

Martin, R., Komatitsch, D., & Ezziani, A. (2008). An unsplit convolution perfectly matched layer improved at grazing incidence for seismic wave propagation in poroelastic media. *Geophysics*, *73*(4), T51–T61.

Martin, R., Komatitsch, D., Gedney, S. D., & Bruthiaux, E. (2010). A High-Order Time and Space Formulation of the Unsplit Perfectly Matched Layer for the Seismic Wave Equation Using Auxiliary Differential Equations (ADE-PML). *Computer Modeling in Engineering and Sciences*, *56*(1), 17–40.

Massarsch, K. R. (2005). Vibration Isolation using Gas-filled Cushions. *Geo-Frontiers* (pp. 1–22). Austin, Texas.

Mayne, P. (2006). Undisturbed sand strength from seismic cone tests. *Geomechanics & Geoengineering*, *1*(4), 239–257.

Mayne, P., & Rix, G. (1993). Gmax-qc Relationships for Clays. *ASTM Geotechnical Testing Journal*, *16*(1), 54–60.

Mayne, P., & Rix, G. (1995). Correlations Between Shear Wave Velocity and Cone Tip Resistance in Clays. *Soils and Foundations*, *35*(2), 107–110.

Mazilu, T., Dumitriu, M., Tudorache, C., & Sebeşan, M. (2011). Using the Green's functions method to study wheelset/ballasted track vertical interaction. *Mathematical and Computer Modelling*, *54*(1-2), 261–279. doi:10.1016/j.mcm.2011.02.009

Mead, D. . (1970). Free wave propagation in periodically supported infinite beams. *Journal of Sound and Vibration*, *11*, 187–197.

Melke, J., & Kraemer, S. (1983). Diagnostic methods in the control of railway noise and vibration. *Journal of Sound and Vibration*, *87*(2), 377–386.

Metrikine, a. V., & Popp, K. (2000). Steady-state vibrations of an elastic beam on a visco-elastic layer under moving load. *Archive of Applied Mechanics*, *70*(6), 399–408. doi:10.1007/s004199900071

Metrolinx. (2010). *GO electrification study final report (Appendix 8E). Metrolinx* (pp. 1–40).

Millard, S., Shaw, M., Giannopoulos, A., & Soutsos, M. (1998). MODELING OF SUBSURFACE PuLSED RADAR FOR NONDESTRUCTIVE TESTING OF

STRUCTURES By S. G. Millard,t M. R. Shaw,z A. Giannopoulos,3 and M. N. Soutsos 4. *Journal of Materials in Civil Engineering*, *10*(3), 188–196.

Monjezi, M., Ghafurikalajahi, M., & Bahrami, a. (2011). Prediction of blast-induced ground vibration using artificial neural networks. *Tunnelling and Underground Space Technology*, *26*(1), 46–50. doi:10.1016/j.tust.2010.05.002

Nazari, S., Saljooghi, S., Shahbazi, M. M., & Akbari, H. R. (2010). Application of artificial neural networks in solving inversion problem of surface wave method on pavements. *2nd International conference on engineering optimization* (pp. 1–8).

Nazarian, S., & Milind, D. (1993). Automated surface wave method: Field testing. *Journal of Geotechnical Engineering*, *119*(7), 1094–1111.

Nelson, J., & Saurenman, H. (1987). A prediction procedure for rail transportation groundborne noise and vibration. *Transportation Research Record: Journal of the Transportation Research Board*, (1143), 26–35.

Newmark, N. (1959). A method of computation for structural dynamics. *Journal of Engineering Mechanics*, *85*, 67–94.

Nielsen, J., & Igeland, A. (1995). Vertical Dynamic Interaction Between Train and Track Influence of Wheel and Track Imperfections. *Journal of Sound and Vibration*, *187*(5), 825–839. doi:10.1006/jsvi.1995.0566

Nour, A., Slimani, A., Laouami, N., & Afra, H. (2003). Finite element model for the probabilistic seismic response of heterogeneous soil profile. *Soil Dynamics and Earthquake Engineering*, *23*(5), 331–348. doi:10.1016/S0267-7261(03)00036-8

O'Brien, J., & Rizos, D. (2005). A 3D BEM-FEM methodology for simulation of high speed train induced vibrations. *Soil Dynamics and Earthquake Engineering*, *25*, 289–301. doi:10.1016/j.soildyn.2005.02.005

O'Riordan, N., & Phear, A. (2001). Design and construction of ballasted track formation and subgrade for high speed lines. *International Conference of Railway Engineering-2001*. London, UK: Engineering Technics Press, ISBN:0-947644-45-8.

Ohta, Y., & Goto, N. (1978). Empirical shear wave velocity equations in terms of characteristic soil indexes. *Earthquake Engineering & Structural Dynamics*, *6*(2), 167–187.

Okumura, Y., & Kuno, K. (1991). Statistical analysis of field data of railway noise and vibration collected in an urban area. *Applied acoustics*, *33*, 263–280.

Paoletti, L., Hegazy, Y., Monaco, S., & Piva, R. (2010). Prediction of shear wave velocity for offshore sands using CPT data – Adriatic sea. *2nd International Symposium on Cone Penetration Testing* (pp. 1–8). Huntington Beach, California.

Park, C., Miller, R., & Xia, J. (1999). Multichannel analysis of surface waves. *Geophysics*, *64*(3), 800. doi:10.1190/1.1444590

Park Seismic. (2013). Multichannel analysis of surface waves. Retrieved from www.masw.com

Patil, S. . (1987). Natural Frequencies of a Railroad Track. *Journal of Applied Mechanics*, *54*, 299–304.

Paulsen, P., & Kastka, J. (1995). Effects of combined noise and vibration on annoyance. *Journal of Sound and Vibration*, *181*(2), 295–314.

Payton, R. (1967). Transient motion of an elastic half-space due to a moving surface line load. *International Journal of Engineering Science*, *5*(1), 49–79.

Pitilakis, K., Raptakis, D., Lontzetidis, K., & T, T.-V. (1999). Geotechnical and geophysical description of EURO-SEISTEST, using field, laboratory tests and moderate strong motion recordings. *Journal of Earthquake Engineering*, *3*(3), 381–409.

Pouillon, S., Rys, J., Samyn, F., & Vanhonacker, T. (2009). *Edinburgh tram network - Newhaven Road to Haymarket - Ground borne noise and vibration study. D2S International*.

Powrie, W., Yang, L., & Clayton, C. (2007). Stress changes in the ground below ballasted railway track during train passage. *Proceedings of the Institution*

of Mechanical Engineers, Part F: Journal of Rail and Rapid Transit, *221*(2), 247–262. doi:10.1243/0954409JRRT95

Prasad, B. (2009). *Fundamentals Of Soil Dynamics And Earthquake Engineering* (pp. 1–584). PHI Learning.

Rahman, M., & Barber, J. R. (1995). Exact Expressions for the Roots of the Secular Equation for Rayleigh Waves. *Journal of Applied Mechanics 2*, *62*, 250–252.

Rahman, M., & Michelitsch, T. (2006). A note on the formula for the Rayleigh wave speed. *Wave Motion*, *43*(3), 272–276. doi:10.1016/j.wavemoti.2005.10.002

Rainer, J., & Pernica, G. (1988). Effect of train induced vibration on houses - a case study. *National research council Canada*.

Richards, O., & Baker, M. (2008). GridPP and the Edinburgh Compute and Data Facility. *UK All Hands Meeting*. University of Edinburgh.

Rix, G., Lai, C., & Wesley-Spang, A. (2000). In situ measurement of damping ratio using surface waves. *Journal of Geotechnical and Geoenvironmental Engineering*, *126*(5), 472–480.

Robertson, P., Campanella, G., & Wightman, A. (1983). SPT-CPT correlations. *Journal of Geotechnical Engineering*, *109*(11), 1449–1459.

Rollins, K., Evans, M., Diehl, N., & Daily, W. (1998). Shear Modulus And Damping Relationships For Gravels. *Journal of Geotechnical and Geoenvironmental Engineering*, *124*(5), 396–405.

Rossi, F., & Nicolini, A. (2003). A simple model to predict train-induced vibration: theoretical formulation and experimental validation. *Environmental Impact Assessment Review*, *23*(3), 305–322. doi:10.1016/S0195-9255(03)00005-2

RPS. (2004). *Crossrail Groundborne Noise and Vibration Prediction - Validation on DLR Greenwich. Technical report 1E315-G0E00-00002. RPS Group Plc* (pp. 1–56).

Rucker, W., & Auersch, L. (1999). A user friendly prediction tool for railway induced ground vibrations: Emission - Transmission - Immission. *Noise and vibration mitigation* (Vol. 3, pp. 129–135). doi:10.1039/b104835j

Ryall, M., Parke, G., & Harding, J. (2000). *The Manual of bridge engineering* (pp. 1–1012). Thomas Telford Ltd.

Saenger, E., Gold, N., & Shapiro, S. (2000). Modeling the propagation of elastic waves using a modified finite-difference grid. *Wave Motion*, *31*, 77–92.

Salvador, P., Real, J., Zamorano, C., & Villanueva, A. (2011). A procedure for the evaluation of vibrations induced by the passing of a train and its application to real railway traffic. *Mathematical and Computer Modelling*, *53*(1-2), 42–54. doi:10.1016/j.mcm.2010.07.016

Santamaria, J., Vadillo, E. G., & Oyarzabal, O. (2011). Dynamic comparison of different types of slab track and ballasted track using a flexible track model. *Proceedings of the Institution of Mechanical Engineers , Part F : Journal of Rail and Rapid Transit*, *000*, 1–20. doi:10.1177/0954409711401516

Schevenels, M., Lombaert, G., Degrande, G., & Clouteau, D. (2007). The wave propagation in a beam on a random elastic foundation. *Probabilistic Engineering Mechanics*, *22*(2), 150–158. doi:10.1016/j.probengmech.2006.09.003

Schevenels, M., Lombaert, G., Degrande, G., & François, S. (2008). A probabilistic assessment of resolution in the SASW test and its impact on the prediction of ground vibrations. *Geophysical Journal International*, *172*(1), 262–275. doi:10.1111/j.1365-246X.2007.03626.x

Schilder, R., & Diederich, D. (2007). Installation Quality of Slab Track – A Decisive Factor for Maintenance. *RTR Special* (pp. 76–78). Austria.

Seed, H., Idriss, I., & Arango, I. (1983). Evaluation Of Liquefaction Potential Using Field Performance Data. *Journal of Geotechnical Engineering*, *109*, 458–482.

Seed, H., Wong, R., Idriss, I., & Tokimatsu, K. (1987). Moduli and Damping Factors for Dynamic Analyses of Cohesionless Soils. *Journal of Geotechnical Engineering*, *112*(11), 1016–1032.

Shamalta, M., & Metrikine, A. V. (2003). Analytical study of the dynamic response of an embedded railway track to a moving load. *Archive of Applied Mechanics*, *73*, 131 – 146. doi:10.1007/s00419-002-0248-3

Sheng, X. (1999a). Ground Vibration Generated By a Harmonic Load Acting on a Railway Track. *Journal of Sound and Vibration*, *225*(1), 3–28. doi:10.1006/jsvi.1999.2232

Sheng, X. (1999b). Ground Vibration Generated By a Load Moving Along a Railway Track. *Journal of Sound and Vibration*, *228*(1), 129–156. doi:10.1006/jsvi.1999.2406

Sheng, X. (2004). A theoretical model for ground vibration from trains generated by vertical track irregularities. *Journal of Sound and Vibration*, *272*(3-5), 937–965. doi:10.1016/S0022-460X(03)00782-X

Sheng, X., Jones, C. J. C., & Thompson, D. J. (2003). A comparison of a theoretical model for quasi-statically and dynamically induced environmental vibration from trains with measurements. *Journal of Sound and Vibration*, *267*, 621–635. doi:10.1016/S0022-460X(03)00728-4

Shrivastava, R., & Kameswara Rao, N. (2002). Response of soil media due to impulse loads and isolation using trenches. *Soil Dynamics and Earthquake Engineering*, *22*(8), 695–702. doi:10.1016/S0267-7261(02)00060-X

Sisman, H. (1995). *An investigation on relationships between shear wave velocity and SPT and pressuremeter test results (MSc thesis)*. Ankara University.

Smith, I., & Griffiths, D. (1997). *Programming the finite element method* (pp. 1–648). NY: Wiley.

Statsoft. (2008). Statistica. Retrieved from http://www.statsoft.co.uk/

Stoll, R. D. (1979). Experimental studies of attenuation in sediments. *Journal of Acoustic Society of America*, *66*(4), 1152. doi:10.1121/1.383309

Subramanian, N. (2011). *Design of Steel Structures: Theory and Practice* (pp. 1–864). OUP India.

Suiker, a. S. J., De Borst, R., & Esveld, C. (1998). Critical behaviour of a Timoshenko beam-half plane system under a moving load. *Archive of Applied Mechanics*, *68*(3-4), 158–168. doi:10.1007/s004190050153

Tayabji, S., & Bilow, D. (2001). Concrete Slab Track State of the Practice. *Transportation Research Record: Journal of the Transportation Research Board*, *1742*, 87–96.

Thompson, D. (2009). *Railway Noise and Vibration. Mechanisms, modelling and means of control* (pp. 1–532). Elsevier Ltd.

Thornely-Taylor, R. . (2004). The Prediction Of Vibration , Groundborne And Structure-Radiated Noise From Railways Using Finite Difference Methods – Part I - Theory. *Proceedings of the Institute of Acoustics* (Vol. 26, pp. 1–11).

Thornely-Taylor, R. . (2013). Personal communication.

Timoshenko, S. (1953). *The collected papers of Stepan Prokopovitch Timoshenko 1878-1972* (pp. 1–642). London ; New York: McGraw-Hill.

Tran, K. T., & McVay, M. (2012). Site characterization using Gauss–Newton inversion of 2-D full seismic waveform in the time domain. *Soil Dynamics and Earthquake Engineering*, *43*, 16–24. doi:10.1016/j.soildyn.2012.07.004

Triepaischajonsak, N. (2011). *The influence of various excitation mechanisms on ground vibration from trains (PhD thesis)*.

Triepaischajonsak, N., Thompson, D. J., Jones, C. J. C., Ryue, J., & Priest, J. a. (2011). Ground vibration from trains: experimental parameter characterization and validation of a numerical model. *Proceedings of the Institution of Mechanical Engineers, Part F: Journal of Rail and Rapid Transit*, *225*(2), 140–153. doi:10.1177/09544097JRRT370

Trinder, M., & Wood, C. (2009). *Epsom railway station - Noise and vibration assessment. Acoustic Consultants* (pp. 1–30).

Trochides, A. (1991). Ground-borne vibrations in buildings near subways. *Applied Acoustics*, *32*, 289–296.

Tsiambaos, G., & Sabatakakis, N. (2010). Empirical estimation of shear wave velocity from in situ tests on soil formations in Greece. *Bulletin of Engineering Geology and the Environment*, *70*(2), 291–297. doi:10.1007/s10064-010-0324-9

URS. (2010). *Docklands light rail project, Seagrave Road environmental statement, Vol 3 - Appendix F: Noise and Vibration. URS Corporation* (pp. 1–68).

Verbraken, H., Lombaert, G., & Degrande, G. (2011). Verification of an empirical prediction method for railway induced vibrations by means of numerical simulations. *Journal of Sound and Vibration*, *330*(8), 1692–1703. doi:10.1016/j.jsv.2010.10.026

Verlinden, O., Kouroussis, G., & Conti, C. (2005). EASYDYN: A framework based on free symbolic and numerical tools for teaching multibody systems. *Multibody dynamics 2005, ECCOMAS Thematic Conference* (pp. 1–19). Madrid, Spain.

Virieux, J. (1986). P-SV wave propagation in heterogenous media: Velocity-stress finite-difference method. *Geophysics*, *51*, 889–901.

Virieux, J., & Operto, S. (2009). An overview of full-waveform inversion in exploration geophysics. *Geophysics*, *74*(6), WCC1–WCC26. doi:10.1190/1.3238367

Wang, J., Jin, X., & Cao, Y. (2011). High speed Maglev train-guideway-tunnel-soil modelling of ground vibration. *Journal of rail and rapid transit*. doi:10.1177/0954409711424823

Wathelet, M. (2008a). www.Geopsy.org.

Wathelet, M. (2008b). An improved neighborhood algorithm: Parameter conditions and dynamic scaling. *Geophysical Research Letters*, *35*(9), 1–5. doi:10.1029/2008GL033256

Whitlock, J., Fitzgerald, C., & Peakall, S. (2012). *City Rail Link - Noise and Vibration Assessment Report No. 001 R07 2012068A. Marshall Day Acoustics* (pp. 1–83).

With, C., Bahrekazemi, M., & Bodare, A. (2006). Validation of an empirical model for prediction of train-induced ground vibrations. *Soil Dynamics and Earthquake Engineering*, *26*(11), 983–990. doi:10.1016/j.soildyn.2006.03.005

Witten, I., & Frank, E. (2005). *Data Mining: Practical Machine Learning Tools and Techniques* (2nd ed., pp. 1–560). Morgan Kaufmann.

Wolf, J. (1994). *Foundation vibration analysis using simple physical models* (p. 423). Prentice-Hall, Englewood Cliffs, USA.

Woods, R. (1968). Screening of surface waves in soils. *Journal of the Soil Mechanics and Foundation Division, ASCE*, *94*, 951–979.

Woodward, P. K., Kennedy, J., Medero, G. M., & Banimahd, M. (2011). Application of in situ polyurethane geocomposite beams to improve the passive shoulder resistance of railway track. *Proceedings of the Institution of Mechanical Engineers, Part F: Journal of Rail and Rapid Transit*, *226*(3), 294–304. doi:10.1177/0954409711423460

Xia, H., Cao, Y. M., & De Roeck, G. (2010). Theoretical modeling and characteristic analysis of moving-train induced ground vibrations. *Journal of Sound and Vibration*, *329*(7), 819–832. doi:10.1016/j.jsv.2009.10.007

Yamashita, S., Fujiwara, T., Kawaguchi, T., Mikami, T., Nakata, Y., & Shibuya, S. (2007). International Parallel Test on the Measurement of G max Using Bender Elements. *International Society for Soil Mechanics and Geotechnical Engineering - Technical Committee 29* (pp. 1–76).

Yang, L. A., Powrie, W., & Priest, J. A. (2009). Dynamic Stress Analysis of a Ballasted Railway Track Bed during Train Passage. *Journal of Geotechnical and Geoenvironmental Engineering*, *135*(5), 680. doi:10.1061/(ASCE)GT.1943-5606.0000032

Yang, Y. (2003). Train-induced wave propagation in layered soils using finite/infinite element simulation. *Soil Dynamics and Earthquake Engineering*, *23*(4), 263–278. doi:10.1016/S0267-7261(03)00003-4

Yang, Y., & Hung, H. (1997). A parametric study of wave barriers for reduction of train-induced vibrations. *International Journal for Numerical Methods in Engineering*, *40*, 3729–3747.

Yuan, D., & Nazarian, S. (1993). Automated surface wave method: Inversion technique. *Journal of Geotechnical Engineering*, *119*(7), 1112–1126.

Zakeri, J., Esmaeili, M., & Mosayebi, S. (2013). Numerical investigation of the effectiveness of a step-shaped trench in reducing train-induced vibrations.

Proceedings of the Institution of Mechanical Engineers, Part F: Journal of Rail and Rapid Transit, *0*(0), 1–9. doi:10.1177/0954409712473094

Zhai, W. (1996). Two simple fast integration methods for large-scale dynamic problems in engineering. *International journal for numerical methods in engineering*, *39*(1994), 4199–4214.

Zhang, J., Andrus, R., & Juang, C. (2005). Normalized Shear Modulus and Material Damping Ratio Relationships. *Journal or Geotechnical and Geoenvironmental Engineering*, *131*(4), 453–464.

Zhang, W., & Shen, Y. (2010). Unsplit complex frequency-shifted PML implementation using auxiliary differential equations for seismic wave modeling. *Geophysics*, *75*(4), T141–T154. doi:10.1190/1.3463431

Zhao, J., Labiouse, V., Dudt, J., & Mathier, J. (2010). *Rock Mechanics in Civil and Environmental Engineering* (pp. 1–884). CRC Press.

Appendix A – Experimental information

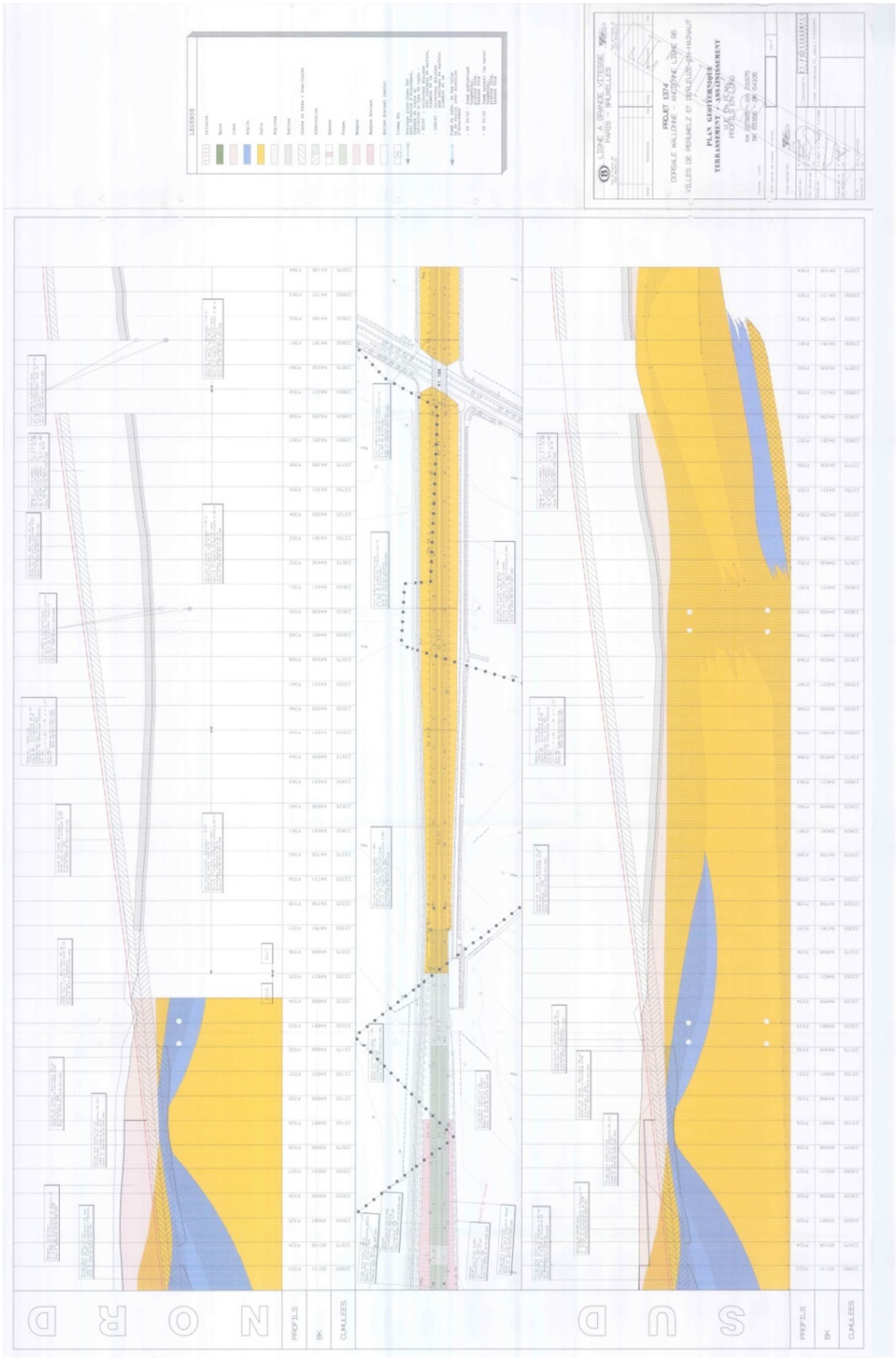

Figure A1 – Belgian at-grade soil map

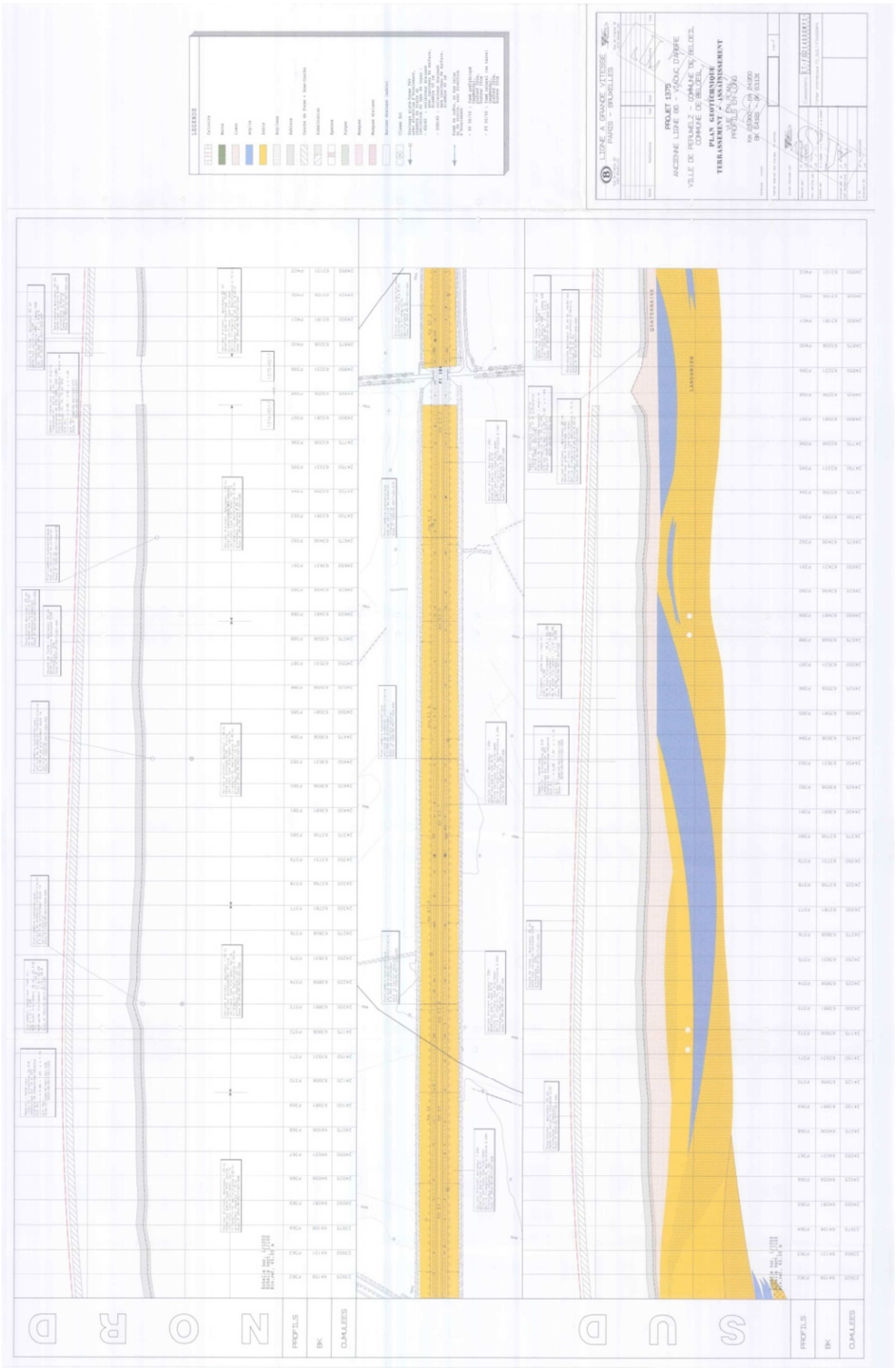

Figure A2 – Belgian embankment soil map

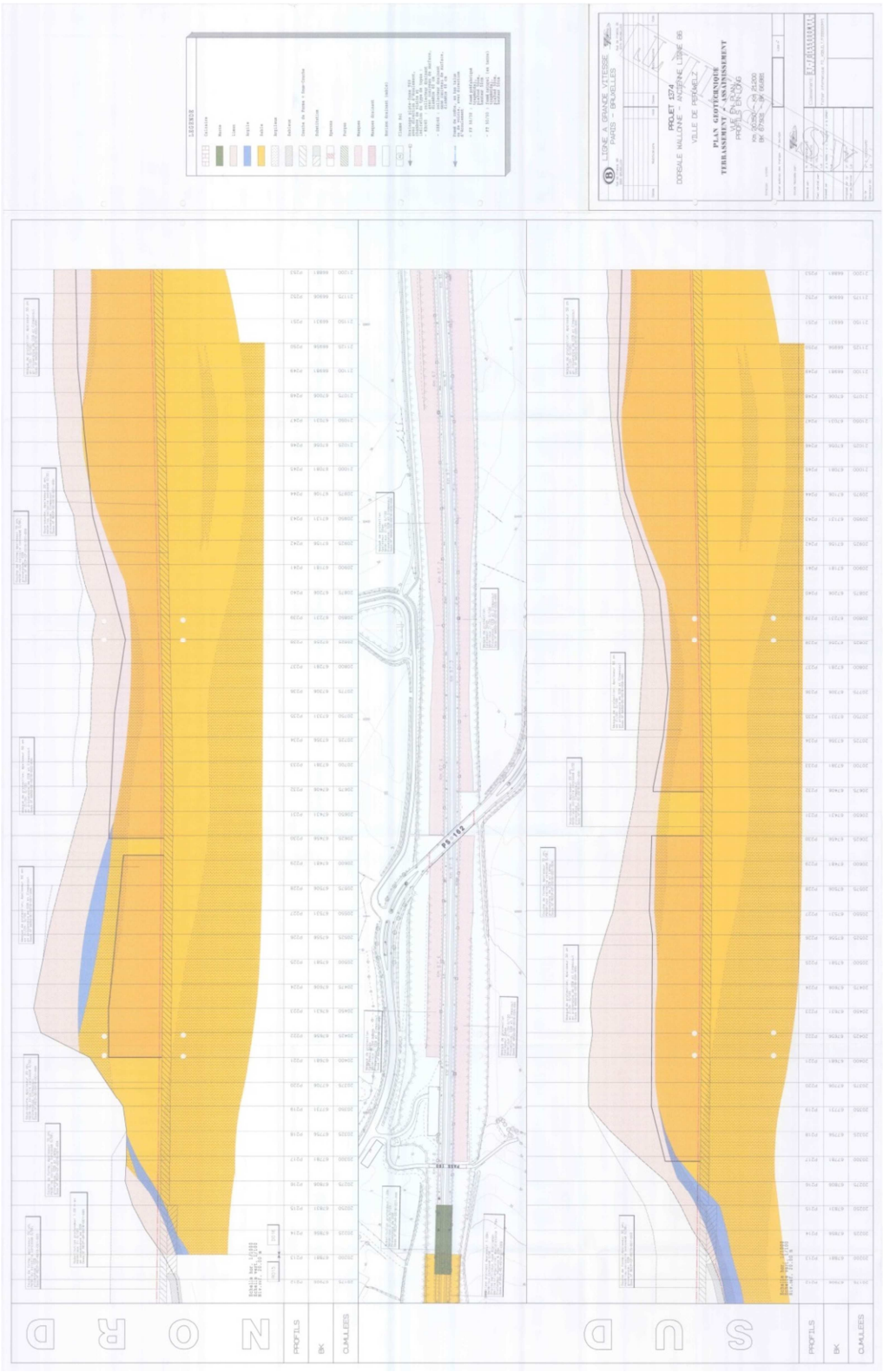

Figure A3 – Belgian cutting soil map

British Geological Survey
NATURAL ENVIRONMENT RESEARCH COUNCIL

Site	Borehole Number
CTRL GI DATA - Entire NDATA19 data set	SA1938

Boring Method	Diameter	Ground Level (mOD)	Client	Job Number
Cable Percussion		58.50	UR/LCE	Issue 1
	Location	**Dates**	**Engineer**	**Sheet**
	582935 E 154555 N	14/06/1994	RLE	1/3

Depth (m)	Sample / Tests	Casing Depth (m)	Water Depth (m)	Field Records	Level (mOD)	Depth (m) (Thickness)	Description	Legend	Water
							Brown clayey; fine to coarse SAND. (possible HEAD)		
0.20	K2					(0.50)			
0.20	V1								
0.50	V3				58.00	0.50	Firm brown sandy (fine and medium) very silty CLAY. (possible HEAD);Below 1.00m; becoming clayey (fine and medium) SAND with a little angular to subrounded; fine to coarse flint gravel.		
0.50	K4								
0.50-1.00	B7								
1.00	V5					(1.00)			
1.00	K6								
1.50-1.95	SPT N=11	1.40		1,1/2,2,3,4	57.00	1.50	Very dense yellow brown silty fine and medium; SAND with occasional localised green brown clayey sand lenses. (FOLKESTONE BEDS);From 1.50m to 2.00m; clayey.;From 1.50m to 2.50m; medium dense.;Below 9.50m; silt fraction insignificant.;At 18.50m; orange brown.;		
1.50-1.95	D8								
1.50-1.95	B9								
2.00	K11								
2.00	V10								
2.50-2.82	CPT 50/170	2.40	2.20	2,7/12,19,19					
2.50-2.95	B12								
3.00	K14								
3.00	V13								
3.50-3.78	SPT 50/125	3.20	3.30	3,9/22,28					
3.50-3.77	D15								
3.50-3.95	B16								
4.00	V17								
4.00	K18								
4.50-4.80	SPT 50/150	4.40	4.30	2,12/26,24					
4.50-4.75	D19								
4.50-4.95	B20								
5.00	V21								
5.00	K22								
5.50-5.82	SPT 50/170	5.50	5.40	6,17/37,13					
5.50-5.95	D23								
5.50-5.95	B24								
6.00	V25								
6.00	K26								
6.50-6.80	SPT 50/152	6.50	6.30	8,23/46,4					
6.50-6.73	D27								
6.50-6.95	B28								
7.00	V29								
7.00	K30								
7.50-7.84	SPT 50/185	7.50	7.20	6,15/26,24					
7.50-7.76	D31								
7.50-7.95	B32								
8.00	V33								
8.00	K34								
8.50-8.71	SPT 50/60	8.50	8.30	12,32/50					
8.50-8.71	D35								
8.50-8.95	B36								
9.00	K38								
9.00	V37								
9.50-9.83	SPT 50/175	9.50	9.30	2,8/14,21,15					
9.50-9.82	D39								
9.50-9.95	B40								

Remarks
1) An inspection pit was excavated by hand to 1.20m depth. ;2) water was added to assist boring from 2.00m to 19.00m and 21.00m to 23.00m which may have masked any groundwater strike; however when the borehole was left standing for 0.75 hoursat 21.00m a water level of 17.80m was recorded.;3) Insitu tests for gas composition and water quality were carried out during borehole construction. ;4) On completion of boring; a 50mm standpipe piezometer was installed with the slotted section from 22.50m to 19.50m and wrapped in a Terram filter the following detail: From 23.00m to 19.00m; gravel filter response zone; from 19.00m to 17.00m; bentonite seal; from 17.00m to 0.50m; cement/bentonite grout;;and from 0.50m to ground level concrete and a flush stopcock cover.

Scale (approx)	Logged By
1:50	SMC

Figure No.

Figure A4 – England at-grade soil map

V

Specifications

INPUT/OUTPUT, INC.

	SM-6/U-B			
Frequency				
Natural frequency (f_n)	8 Hz	10 Hz	14 Hz	
Tolerance	±0.5 Hz	±5%	±5%	
Maximum tilt angle for specified f_n	20°	25°	25°	
Typical spurious frequency	150 Hz	170 Hz	190 Hz	
Distortion				
Distortion with 0.7 in/s p.p coil-to-case velocity	<0.2%	<0.2%	<0.2%	
Distortion measurement frequency	12 Hz	12 Hz	14 Hz	
Maximum tilt angle for distortion specification	15°	20°	20°	
Damping				
Open-circuit damping	0.315	0.25	0.18	
Damping calibration-shunt resistance	2,257 Ω	1,339 Ω	645 Ω	
Damping with shunt	0.6	0.6	0.6	
Tolerance with shunt	±5%	±5%	±5%	
Resistance				
Standard coil resistance	375 Ω	375 Ω	375 Ω	
Tolerance	±5%	±5%	±5%	
Sensitivity				
Open-circuit sensitivity	28.8 V/m/s	28.8 V/m/s	28.8 V/m/s	(0.73 V/in/s)
Tolerance	±5%	±5%	±5%	
$R_tB_cf_n$	6,000 ΩHz	6,000 ΩHz	6,000 ΩHz	
Moving mass	11.1 g	11.1 g	11.1 g	(0.39 oz)
Maximum coil excursion p.p.	4 mm	4 mm	4 mm	(0.16 in)
Physical Characteristics				
Diameter	25.4 mm	25.4 mm	25.4 mm	(1 in)
Height	36 mm	36 mm	36 mm	(1.42 in)
Weight	81 g	81 g	81 g	(2.85 oz)
Operating temperature range	–40°C to +100°C	–40°C to +100°C	–40°C to +100°C	(–40°F to +212°F)
Limited Warranty Period*	2 years	2 years	2 years	

* Warranty excludes damage caused by high-voltage and physical damage to the element case.

All parameters are specified at +20°C in the vertical position unless otherwise stated.

Figure A5 - Geophone specification - part 1

V

Specifications (cont.) INPUT/OUTPUT, INC.

SM-6 LOW FREQUENCY GEOPHONE	A-Coil	B-Coil
Frequency		
Natural frequency (f_n)	4.5 Hz	4.5 Hz
Tolerance	±0.5 Hz	±0.5 Hz
Maximum tilt angle for specified f_n	0°	0°
Typical spurious frequency	140 Hz	140 Hz
Distortion		
Distortion with 0.7 ips p.p. coil-to-case velocity	<0.3%	<0.3%
Distortion measurement frequency	12 Hz	12 Hz
Maximum tilt angle for distortion specification	0°	0°
Damping		
Open-circuit damping	0.265	0.56
Open-circuit damping tolerance	±5%	±5%
Resistance		
Standard coil resistance	375 Ω	375 Ω
Tolerance	±5%	±5%
Sensitivity		
Open-circuit sensitivity	28.0 V/m/s (0.71 V/in/s)	28.8 V/m/s (0.73 V/in/s)
Tolerance	±5%	±5%
$R_eB_cf_n$	3,875 ΩHz	6,000 ΩHz
Moving mass	16.1 g (0.57 oz)	11.1 g (0.39 oz)
Maximum coil excursion p.p.	4 mm (0.16 in)	4mm (0.16 in)
Physical		
Diameter	25.4 mm (1 in)	25.4 mm (1 in)
Height	36 mm (1.42 in)	36 mm (1.42 in)
Weight	81 g (2.85 oz)	81 g (2.85 oz)
Operating temperature range	–40°C to +100°C (–40°F to +212°F)	–40°C to +100°C (–40°F to +212°F)
Limited Warranty Period*	1 year	1 year

* Warranty excludes damage caused by high-voltage and physical damage to the element case.

All parameters are specified at +20° C in the vertical position unless otherwise stated.

Figure A6 - Geophone specification - part 2

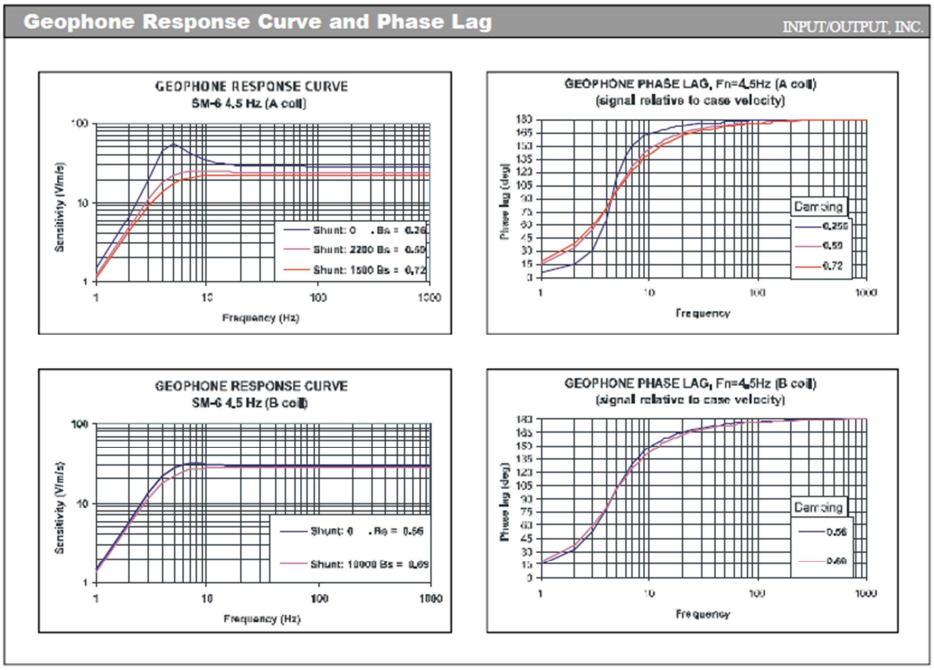

Figure A7 - Geophone specification - part 2

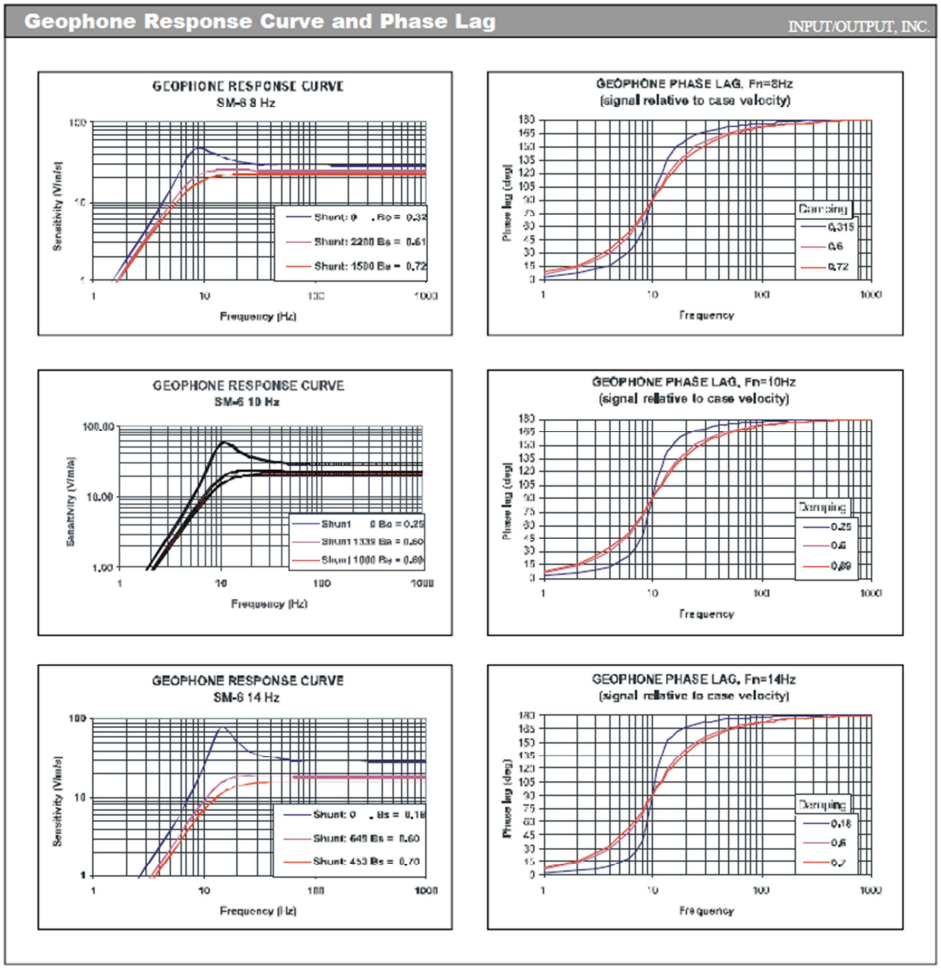

Figure A8 - Geophone specification - part 3

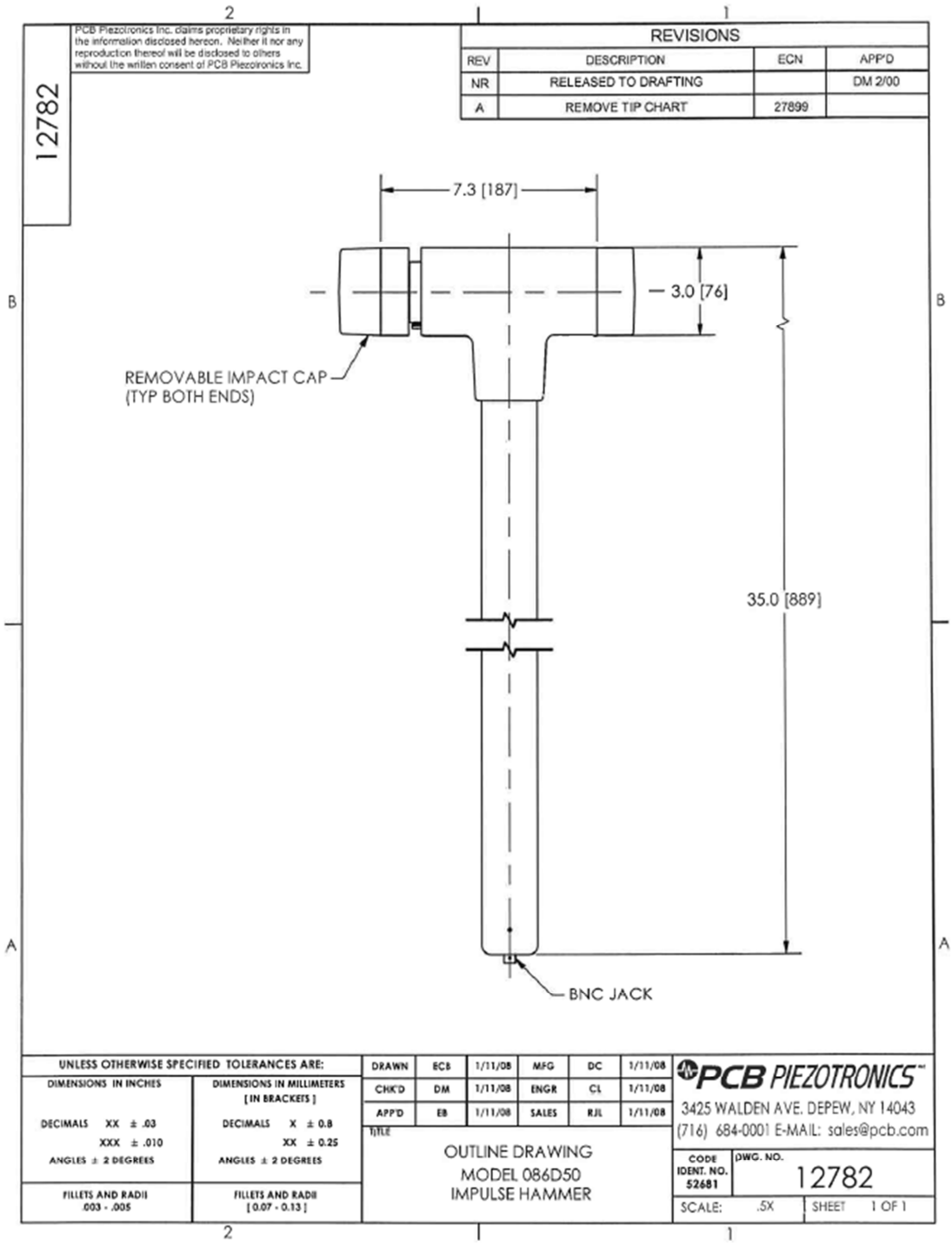

Figure A9 - Hammer specification - part 1

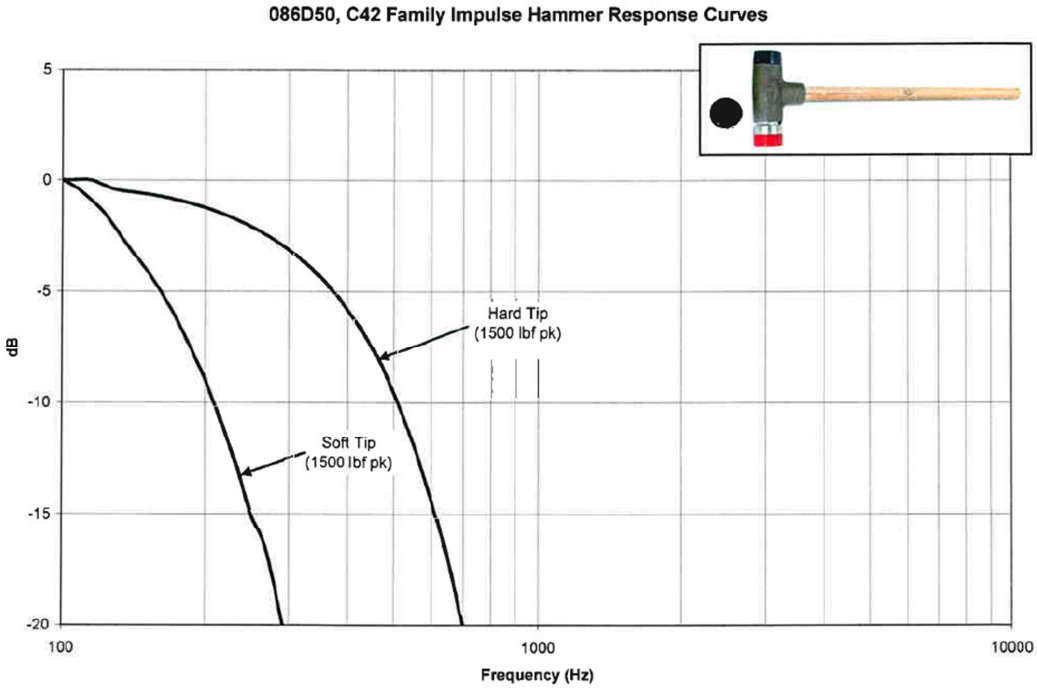

Figure A10 - Hammer specification - part 2

Model Number 086D50	IMPACT HAMMER, ICP®			Revision F ECN #: 32971
Performance	**ENGLISH**	**SI**		
Sensitivity (±15 %)	1 mV/lbf	0.23 mV/N		
Measurement Range	±5000 lbf pk	±22240 N pk		
Resonant Frequency	≥5 kHz	≥5 kHz		
Non-Linearity	≤1 %	≤1 %		
Electrical				
Excitation Voltage	20 to 30 VDC	20 to 30 VDC		
Constant Current Excitation	2 to 20 mA	2 to 20 mA		
Output Impedance	<100 Ohm	<100 Ohm	[1]	
Output Bias Voltage	8 to 14 VDC	8 to 14 VDC		
Discharge Time Constant	≥2000 sec	≥2000 sec	[1]	
Physical				
Sensing Element	Quartz	Quartz		
Sealing	Hermetic	Hermetic		
Hammer Mass	12.1 lb	5.5 Kg		
Head Diameter	3.0 in	7.6 cm		
Tip Diameter	3.0 in	7.6 cm		
Hammer Length	35 in	89 cm		
Electrical Connection Position	Bottom of Handle	Bottom of Handle		
Electrical Connector	BNC Jack	BNC Jack		

All specifications are at room temperature unless otherwise specified.
In the interest of constant product improvement, we reserve the right to change specifications without notice.
ICP® is a registered trademark of PCB group, Inc.

Optional Versions (Optional versions have identical specifications and accessories as listed for standard model except where noted below. More than one option maybe used.)
T - TEDS Capable of Digital Memory and Communication Compliant with IEEE P1451.4

Output Bias Voltage	8.5 to 15 VDC	8.5 to 15 VDC

Notes
[1] Typical.

Supplied Accessories
084A31 Tip - soft plastic, brown (1)
084A32 Tip - hard plastic, red (1)
HCS-2 Calibration of Series 086 instrumented impact hammers (1)

Entered: LLH	Engineer: BAM	Sales: WDC	Approved: LLH	Spec Number:
Date: 05/20/2010	Date: 05/12/2010	Date: 05/12/2010	Date: 05/20/2010	12993

PCB PIEZOTRONICS VIBRATION DIVISION

3425 Walden Avenue
Depew, NY 14043
UNITED STATES
Phone: 800-828-8840
Fax: 716-684-0987
E-mail: info@pcb.com
Web site: www.pcb.com

Figure A11 - Hammer specification - part 3